Search for New Resonances in Lepton-Antilepton Final States in Proton-Proton Collisions at $\sqrt{s} = 13\,\mathrm{TeV}$ with the ATLAS Experiment

Dissertation zur Erlangung des Grades

Doktor der Naturwissenschaften

am Fachbereich Physik, Mathematik und Informatik
der Johannes Gutenberg-Universität in Mainz

Simon Schmitz
geboren in Trier

Mainz, den 09.05.2018

1. Berichterstatter:
2. Berichterstatter:
Datum der mündlichen Prüfung: 22.10.2018

Kurzfassung

Das Standardmodell der Teilchenphysik beschreibt die Wechselwirkungen der elementaren Teilchen und den Aufbau der Materie. Die meisten Prozesse des Mikrokosmos lassen sich damit erfolgreich erklären. Es gibt jedoch ungeklärte Phänomene, die darauf hinweisen, dass das Standardmodell nicht vollständig ist. Oft liegt eine theoretische Lösung in der Erweiterung des Standardmodells um zusätzliche Eichbosonen. Diese Eichbosonen könnten sich unter anderem durch einen Zerfall in ein Lepton und ein Antilepton manifestieren. Die Untersuchung des invarianten Massenspektrums dieser Lepton-Antilepton-Paare könnte daher zur Beobachtung einer neuen Resonanz führen. Die potentiellen Eichbosonen sind neutral, könnten eine Masse im TeV Bereich haben und heißen Z'-Bosonen. Diese Arbeit konzentriert sich auf die Suche nach solch neuen Resonanzen unter Verwendung spezifischer theoretischer Modelle sowie eines modellunabhängigen Ansatzes.
Die zugrunde liegenden Daten für diese Suche wurden in Proton-Proton-Kollisionen am Large Hadron Collider bei einer Schwerpunktsenergie von $\sqrt{s} = 13\,\text{TeV}$ erzeugt. Die Daten wurden vom ATLAS-Detektor aufgezeichnet und entsprechen einer integrierten Luminosität von $36.1\,\text{fb}^{-1}$. Die Untergründe für eine mögliche Resonanz in den Lepton-Antilepton-Endzuständen wurden sowohl mit Monte-Carlo-Simulationen als auch mit datengetriebenen Methoden abgeschätzt. Mögliche Diskrepanzen zwischen dem invarianten Massenspektrum in den Daten und den abgeschätzten Untergründen wurden mit statistischen Methoden ausgewertet. Es wurde keine signifikante Abweichung von der Vorhersage des Standardmodells festgestellt. Eine untere Grenze von 4.35 TeV auf die Masse des Z'-Bosons wurde unter der Annahme eines sequentiellen Standardmodells mit einem Kredibilitätsintervall (*credibility interval*) von 95 % extrahiert. Unter der Annahme von E_6-motivierten Modellen konnten untere Grenzen von 3.80 bis 4.06 TeV auf die Masse des Z'-Bosons mit einem Kredibilitätsintervall von 95 % extrahiert werden. Mit einem modellunabhängigen Ansatz wurden obere Grenzen auf den Wirkungsquerschnitt multipliziert mit dem Verzweigungsverhältnis für Zerfälle in Lepton-Antilepton Paare der Produktion von Z'-Bosonen in einem begrenzten Phasenraum extrahiert. Dies ermöglicht es Theoretikern, Lepton-Antilepton-Endzustände innerhalb anderer spezifischer theoretischer Modelle mit potentiell verschiedenen Zerfallsbreiten neu zu interpretieren. Schließlich wurde eine Suche nach neuen exotischen Resonanzen durchgeführt, die im inklusiven Lepton-Antilepton-Spektrum versteckt sein könnten. Um solche potentiellen Resonanzen aufzudecken, wurde das inklusive Spektrum der Lepton-Antilepton-Paare untersucht, wenn zusätzliche Jets vorhanden sind. Es wurden keine signifikanten Abweichungen von der Erwartung des Standardmodells festgestellt.

Abstract

The Standard Model of particle physics describes the interactions of elementary particles and the structure of matter. Most processes of the microcosm can be successfully explained with it. However, there are unexplained phenomena indicating that the Standard Model is not complete. Often a theoretical solution lies in extending the Standard Model by additional gauge bosons. These gauge bosons could manifest themselves amongst others through a decay into a lepton and an antilepton. Hence, investigating the invariant mass spectrum of these lepton-antilepton pairs could lead to the observation of a new resonance. The potential gauge bosons are neutral, could have a mass in the TeV range and are called Z' bosons. This thesis focuses on the search for such new resonances using specific theoretical models as well as a model-independent approach.
The underlying data for this search has been produced in proton-proton collisions at the Large Hadron Collider at a center of mass energy of $\sqrt{s} = 13\,\text{TeV}$. The data has been recorded by the ATLAS detector and corresponds to an integrated luminosity of $36.1\,\text{fb}^{-1}$. The backgrounds for a possible resonance in the lepton-antilepton final states have been estimated with Monte-Carlo simulations as well as data-driven methods. Statistical tools have been used to evaluate possible discrepancies between the invariant mass spectrum in data and the estimated backgrounds. No significant deviation from the Standard Model prediction has been found. A lower limit of 4.35 TeV on the Z' boson mass has been extracted assuming a sequential Standard Model with a credibility interval of 95 %. Assuming E_6-motivated models lower limits from 3.80 to 4.06 TeV on the Z' boson mass have been extracted with a credibility interval of 95 %. With a model-independent approach upper limits on the production cross section multiplied with the branching ratio for decays in lepton-antilepton pairs of Z' bosons have been extracted within a restricted phase space. This enables theorists to reinterpret lepton-antilepton final states within other specific theoretical models with potentially different decay widths. Finally a search for new exotic resonances which might be hidden in the inclusive lepton-antilepton spectrum has been performed. To uncover such potential resonances the inclusive spectrum of lepton-antilepton pairs has been investigated when additional jets are present. No significant deviations from the Standard Model expectation were discovered.

Contents

Chapter 1

Introduction

The beginning of elementary particle physics reaches back to the 6th century BCE when *Leucippus* and his student *Democritus* first developed the idea that matter is composed out of elementary particles. They invented the theory of *atomism* driven by the assumption that an understanding of the smallest components of matter leads to the explanations of everything that builds up on these components. Within the theory of atomism the term *atom* was characterized. It was assumed that atoms exist in an infinite variety of different shapes and sizes and that they are indestructible and immutable. In the 19th century *John Dalton* used the concept of atoms to explain that chemical elements always react with each other in proportions of small integer numbers. That time, it was still believed that atoms were the fundamental particles of nature.
In 1897, however, *J. J. Thomson* performed experiments that showed that cathode rays were made up out of particles that were much lighter than the least massive known atom [1] which is hydrogen. The cathode ray particles, at that time, were measured to be around a thousand times lighter than hydrogen. This was the discovery of the electron, the first particle from which it is believed until today that it has no substructure. Knowing that atoms were no fundamental particles many experiments have been performed to investigate their structure. In 1907 *Ernest Rutherford* conducted his "gold foil experiment" where alpha particles were scattered on a thin gold foil [2]. The experiment revealed that atoms are mainly empty space with most of its mass concentrated in the atomic nucleus. By 1914 additional experiments lead to the concept of atoms having a dense positively charged nucleus surrounded by electrons which are of negative charge. In 1917 Rutherford proved that the nucleus of the hydrogen atom is present in heavier nuclei as well. These findings are often described as the discovery of the proton, a positively charged particle that should later be unveiled to have a substructure. Shortly after, the discovery of the existence of isotopes lead Rutherford to theorize the neutron. It was discovered in 1932 by *James Chadwick* [3]. Until then, only the electromagnetic interaction and the gravity were known as fundamental forces from which only the former interaction could contribute to explain atoms and their isotopes. Further investigations of the atoms and the atomic nuclei uncovered the nuclear force. It was not a fundamental force itself but the first sign of the fundamental strong force. In the following the exploration of isotopes and radioactivity began to strive.
In the 1950s the development of particle accelerators moved forward such that inelastic scattering experiments on protons and atomic nuclei could be performed.

The highest collision energies reached at that time were around a few hundred MeV and led to discoveries of several unstable particles with short lifetimes. New improvements of particle accelerators resulted in an increase of the collision energies while improvements of the particle detectors made the discovery of more unstable particles possible. This period characterized the term "particle zoo".
In 1969 the aforementioned substructure of the proton was discovered in deep inelastic scattering of electrons on protons at *SLAC (**S**tanford **L**inear **A**ccelerator **C**enter)* [4, 5]. The discovery was a success for the quark model [6, 7] that was theorized in order to explain the particle zoo and finally lead to the formulation of the Standard Model of particle physics. The substructure of the proton as well as of hadrons in general was made up out of quarks which are fundamental particles. The quarks discovered at SLAC were the up, down and strange quark. Another fundamental particle of the Standard Model is the gluon, the mediator of the strong interaction. It was discovered indirectly in 1979 in so called "three-jet events" at *DESY (**D**eutsches **E**lektron **Sy**nchrotron)* [8, 9, 10, 11]. Four years later the mediators of the weak interaction, the $W^{\pm}$ bosons and the Z boson, have been discovered at *CERN (**C**onseil **E**uropéen pour la **R**echerche **N**ucléaire)* [12, 13, 14, 15]. The last missing quark and heaviest particle of the Standard Model, the top quark, was discovered in 1995 at the *Fermi National Accelerator Laboratory* [16, 17, 18, 19]. The final piece of the Standard Model was to be discovered in 2012. It was the Higgs boson, a particle theorized in 1964, that was discovered with experiments at the *LHC (**L**arge **H**adron **C**ollider)* at CERN [20, 21].
From the beginning of the 20th century until now elementary particle physics evolved through observations carried out by experiments as well as theoretical predictions leading to new experiments. At present, many experiments are performed and theories are constructed to further develop the knowledge of elementary particle physics. Although the Standard Model describes most of the observations in the microcosm successfully there are phenomena that can not be explained with it. This is a strong hint to undiscovered physics beyond the Standard Model. Gravity, dark matter and dark energy, neutrino masses and the matter-antimatter asymmetry are only the most prominent examples of physical observations that can not be explained in the context of the Standard Model. The aim of this thesis is a contribution to the ongoing search to reveal the physics beyond the Standard Model. Especially the Z' boson, a theoretically predicted particle, shall be the focus of this work. The Z' boson is a heavier version of the Standard Model's Z boson and may be of significance in clarifying unexplained phenomena. An opportunity to search for the Z' boson is the spectrum of lepton-antilepton pairs which is a final state that the Z' boson theoretically decays into. This is a promising search since a final state of a lepton and an antilepton is relatively easy to reconstruct compared to other final states. Additionally a search for more general resonances not bound to a theoretical model is carried out. The search for Z' bosons is also performed in final states with additional jets which is a scenario predicted by other theoretical models. The technical environment to conduct these searches is the ATLAS Experiment at the LHC at CERN.
The contents of this thesis are divided in the parts theory, experiment and analysis. The theory is discussed in chapter 2 where first an introduction to the Standard Model of particle physics is given. Subsequently the physics of proton-proton collisions as produced by the LHC as well as the theories aiming to describe the physics

beyond the Standard Model are discussed. The experiment is described in chapter 3 where the technical facilities all around the ATLAS experiment are introduced. The analysis of the data recorded by the ATLAS detector is presented in chapter 4. Also part of the analysis is the interpretation of the analyzed data in a model-specific and a model-independent approach which is addressed in chapter 5. Chapter 6 focuses on a search for more exotic resonances. The last chapter will give a summary of the findings as well as an outlook on future research directions regarding the Z' boson.

Chapter 2

Theoretical Principles

This chapter describes the theoretical foundations needed for the research conducted within this analysis. First the Standard Model of particle physics (SM) [22] will be introduced in words before a more mathematical perspective is given. Subsequently the physics of proton-proton collisions is discussed. Finally physics beyond the Standard Model (BSM) will be discussed with an emphasis put on models describing hypothetical resonances in lepton-antilepton final states. All formulations follow the review [23]. Within this thesis the convention $\hbar = c = 1$ is used.

2.1 The Standard Model of Particle Physics

The SM is a theory describing the most fundamental matter and interactions formulated by the theoretical framework of quantum field theory. Broadly speaking the SM assembles all known elementary particles which are the fundamental *fermions*, the fundamental *gauge bosons* and the *Higgs boson*. All particles of the SM are considered to be point-like and carry "charges" corresponding to the interactions they are affected by. The fundamental interactions described by the SM are the electromagnetic, the weak and the strong interaction. The fourth fundamental interaction, gravity, is not included in the SM. The charges corresponding to the electromagnetic, the weak and the strong interaction are the electric charge, the weak isospin and the color charge, respectively.

Fermions
The fermions of the SM build up the matter and can be seen in figure 2.1. They are subdivided into quarks and leptons as well as into three generations. According to the spin-statistics theorem fermions have a half-integer spin and respect the Pauli exclusion principle. The classification of the fermions follows the charges they carry and hence the interactions they are affected by. Quarks interact via all three interactions of the SM and therefore carry a color charge, a weak isospin and an electric charge. The color charge can be red (r), green (g), blue (b), antired ($\bar{r}$), antigreen ($\bar{g}$) or antiblue ($\bar{b}$). In contrast to the quarks, leptons do not carry a color charge. The electron, the muon and the tau carry both electric charge and a weak isospin while the corresponding neutrinos only carry a weak isospin. Hence, they only interact via the weak force and are extremely difficult to detect. Each fermion has a corresponding antifermion with inverted quantum numbers, which are included in the SM as well.

Gauge Bosons

The gauge bosons of the SM are the mediators of the interactions of the SM and can be seen in figure 2.1. According to the spin-statistics theorem the gauge bosons have an integer spin and do not respect the Pauli exclusion principle. The mediator of the electromagnetic interaction is the photon which is a massless particle. The weak interaction is mediated by the W^+, W^- and Z boson. All three boson are massive while the Z boson is more massive than the $W^\pm$ bosons. In contrast to the Z boson the $W^\pm$ bosons carry an electric charge and hence couple to the electromagnetic interaction. The gluon is a massless particle and mediates the strong interaction. It carries a combination of a color and an anticolor which is why the gluon can interact with itself. Due to different color combinations, eight different gluons exist in the SM.

Higgs Boson

The Higgs boson is the final piece of the SM particle content. In contrast to the gauge bosons it has spin zero and is therefore denoted as scalar boson. The Higgs boson explains how the other elementary particles gain their masses. It couples to every elementary particle with mass and explains why the photon has zero mass while the W^+, W^- and Z boson have very high masses. The Higgs boson itself is massive which is why it interacts with itself.

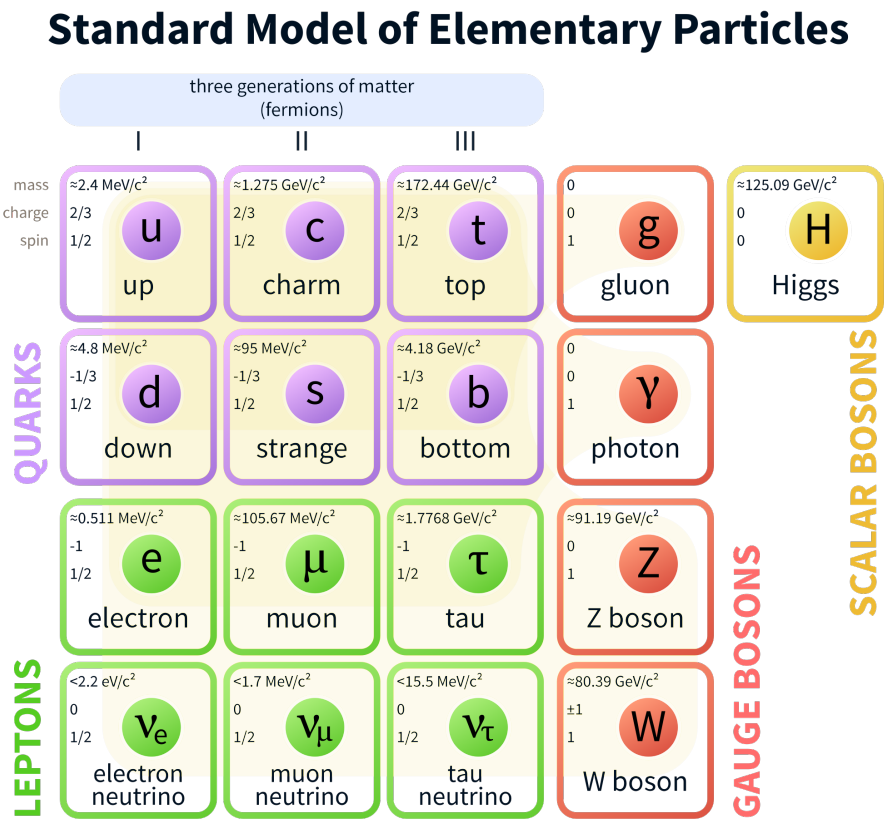

Figure 2.1: Elementary particles of the Standard Model. [24]

Composite Particles
The ordinary matter of the universe is constituted only out of the charged fermions of the first generation which is the up quark, the down quark and the electron. The charged fermions from the second and third generation have very short half-lives and finally decay into the particles of the first generation. Neutrinos, on the other hand, do not decay and traverse space and time. The quarks form color-neutral compositions which are either two quarks with a color and an anticolor or three quarks with the colors r, g and b or $\bar{r}$, $\bar{g}$ and $\bar{b}$, respectively. Compositions out of three quarks are called *baryons* for which the proton and the neutron are examples. Compositions out of two quarks are called *mesons*, for instance pions or kaons. The general term for color-neutral quark compositions is *hadron*.

2.1.1 The Standard Model Lagrangian

The SM is formulated as a gauge quantum field theory using the Lagrangian formalism [25]. The Lagrangian density of the SM can be divided into four different parts as the following equation implies.

$$\mathcal{L}_{\mathrm{SM}} = \mathcal{L}_{\mathrm{YM}} + \mathcal{L}_{\mathrm{ferm}} + \mathcal{L}_{\mathrm{H}} + \mathcal{L}_{\mathrm{Yuk}} \tag{2.1}$$

The part $\mathcal{L}_{\mathrm{YM}}$, denoted after Chen-Ning Yang and Robert Mills who introduced the Yang-Mills theory [26], describes the gauge bosons and their interactions. $\mathcal{L}_{\mathrm{ferm}}$ describes the propagation of the fermions and their interactions with the gauge bosons. The part $\mathcal{L}_{\mathrm{H}}$ introduces the Higgs field which is necessary since a Yang-Mills theory requires massless gauge bosons. Observations, however, show that the gauge bosons have mass which the Higgs field allows through interactions with the gauge bosons. The last term $\mathcal{L}_{\mathrm{Yuk}}$ characterizes the interactions of the fermions with the Higgs boson which gives rise to the fermion masses via Yukawa couplings.
The Yang-Mills part of the SM Lagrangian density can be expressed via

$$\mathcal{L}_{\mathrm{YM}} = -\frac{1}{4} W^i_{\mu\nu} W^{i,\mu\nu} - \frac{1}{4} B_{\mu\nu} B^{\mu\nu} - \frac{1}{4} G^a_{\mu\nu} G^{a,\mu\nu} \tag{2.2}$$

where

$$W^i_{\mu\nu} = \partial_\mu W^i_\nu - \partial_\nu W^i_\mu - g\epsilon^{ijk} W^j_\mu W^k_\nu, \qquad i,j,k \in \{1,2,3\}, \tag{2.3}$$

$$B_{\mu\nu} = \partial_\mu B_\nu - \partial_\nu B_\mu, \tag{2.4}$$

$$G^a_{\mu\nu} = \partial_\mu G^a_\nu - \partial_\nu G^a_\mu - g_s f^{abc} G^b_\mu G^c_\nu, \qquad a,b,c \in \{1,...,8\}, \tag{2.5}$$

are the field strength tensors of the gauge fields W^i_μ, B_μ and G^a_μ respectively. $W^i_{\mu\nu}$ is the field strength tensor of the non-abelian $\mathrm{SU}(2)_I$ group with the weak isospin I^i_{w}. The gauge coupling of this group is g and ϵ^{ijk} are the group's structure constants. $B_{\mu\nu}$ is the field strength tensor of the abelian $\mathrm{U}(1)_Y$ group with the weak hypercharge Y^i_{w}. The gauge coupling of this group will be denoted with g'. Due to the abelian character of the $\mathrm{U}(1)_Y$ the structure constants vanish. $G^a_{\mu\nu}$ is the field strength tensor of the non-abelian $\mathrm{SU}(3)_c$ group with the color charge c. The gauge coupling of this group is g_s and f^{abc} are the group's structure constants. W^i_μ and B_μ can be identified with the electroweak boson fields while G^a_μ is the gluon field. The self-interactions of the gauge bosons are reflected in the last term of equation 2.3 and

equation 2.5.
The interaction of the gauge fields with the fermions is described via

$$\mathcal{L}_{\text{ferm}} = i\overline{\Psi}_L \not{D} \Psi_L + i\overline{\psi}_{l_\text{R}} \not{D} \psi_{l_\text{R}} + i\overline{\Psi}_Q \not{D} \Psi_\text{Q} + i\overline{\psi}_{u_\text{R}} \not{D} \psi_{u_\text{R}} + i\overline{\psi}_{d_\text{R}} \not{D} \psi_{d_\text{R}}. \tag{2.6}$$

Ψ is used as a notation to bundle the fermion fields ψ. $L = (\nu_{l_\text{L}}, l_\text{L})^\text{T}$ are the left-handed $\text{SU}(2)_I$ doublets of charged leptons $l \in \{e, \mu, \tau\}$ and neutrinos $\nu_l \in \{\nu_e, \nu_\mu, \nu_\tau\}$. Similarly, $Q = (u_\text{L}, d_\text{L})^\text{T}$ are the left-handed $\text{SU}(2)_I$ doublets of up-type quarks $u \in \{u, c, t\}$ and down-type quarks $d \in \{d, s, b\}$. l_R, u_R and d_R are the right-handed $\text{SU}(2)_I$ singlets. As can be seen right-handed neutrinos have been left out since at high-energy colliders they do not play any role. The Feynman slash notation $\not{D} = \gamma^\mu D_\mu$ contains the covariant derivative D_μ which introduces the actual interaction.

$$D_\mu = \partial_\mu + igI^i_\text{w} W^i_\mu + ig' Y_\text{w} B_\mu + ig_s T^a_c G^a_\mu \tag{2.7}$$

$I^i_\text{w} = \frac{\sigma^i}{2}$, where σ^i are the Pauli matrices, are the generators of the left-handed $\text{SU}(2)_I$ doublets. For the right-handed $\text{SU}(2)_I$ singlets I^i_w is zero since they do not undergo weak interactions. Y_w is the generator of the $\text{U}(1)_Y$ part of the electroweak gauge group and is related to the electric charge Q by the Gell-Mann-Nishijima relation $Q = I^3_\text{w} + \frac{Y_\text{w}}{2}$. $T^a_c = \frac{\lambda^a}{2}$, where λ^a are the Gell-Mann matrices, are the generators of the $\text{SU}(3)_c$ quark triplets. For the leptons T^a_c is zero since they do not undergo strong interactions. In the well established theory of quantum electrodynamics (QED) [27] the coupling structure of the photon is proportional to $Q\overline{\psi}\not{A}\psi$. The description in equation 2.6 does not reduce trivially to the QED formulation. However, using the Gell-Mann-Nishijima relation it is possible to recover the structure of QED by identifying the photon field A_μ and the Z boson field Z_μ as linear combinations of W^3_μ and B_μ. This leads to the relation

$$\begin{pmatrix} Z_\mu \\ A_\mu \end{pmatrix} = \begin{pmatrix} \cos\theta_\text{w} & -\sin\theta_\text{w} \\ \sin\theta_\text{w} & \cos\theta_\text{w} \end{pmatrix} \begin{pmatrix} W^3_\mu \\ B_\mu \end{pmatrix} \tag{2.8}$$

where θ_w denotes the weak mixing or Weinberg angle. θ_w can be determined by relating the elementary charge e to the coupling constants g and g' by the equation

$$e = \frac{gg'}{\sqrt{g^2 + g'^2}} = g \sin\theta_\text{w} = g' \cos\theta_\text{w}. \tag{2.9}$$

The remaining fields

$$W^\pm_\mu = \frac{(W^1_\mu \mp iW^2_\mu)}{\sqrt{2}} \tag{2.10}$$

can be related to the charged weak gauge bosons $W^\pm$ of charge $\pm e$.

2.1.2 The Higgs Mechanism

The Higgs part of the SM Lagrangian can be expressed via

$$\mathcal{L}_\text{H} = (D_\mu \Phi)^\dagger (D^\mu \Phi) - V(\Phi). \tag{2.11}$$

This extends the previously introduced particle content by the complex scalar $\text{SU}(2)_I$ doublet $\Phi = (\phi^+, \phi^0)^\text{T}$ of weak hypercharge $Y_{\text{w},\Phi} = 1$, so that ϕ^+ carries charge $+e$

and ϕ^0 is neutral. The potential $V(\Phi)$ describes the self-interaction of Φ and can be freely chosen under the constraint that the Lagrangian remains gauge invariant and renormalizable. The potential

$$V(\Phi) = -\mu^2(\Phi^\dagger\Phi) + \frac{\lambda}{4}(\Phi^\dagger\Phi)^2 \tag{2.12}$$

fulfills these constrains and allows for the generation of particle masses. μ^2 and λ are free real parameters. However, vacuum stability requires $\lambda > 0$. In order to enforce a non-vanishing vacuum expectation value (vev) Φ_0 of Φ the sign of μ^2 is deliberately taken positive. This configuration gives the potential its characteristic "mexican hat" shape. The vev can be computed by minimizing $V(\Phi)$ which yields the condition

$$\Phi_0^\dagger\Phi_0 = \frac{v^2}{2} \qquad \text{with} \qquad v = 2\sqrt{\frac{\mu^2}{\lambda}}. \tag{2.13}$$

Requiring the vev to be electrically neutral results in a vanishing upper component of Φ_0. Hence, Φ_0 is fixed up to a phase and is chosen to be $\Phi_0 = \left(0, \frac{v}{\sqrt{2}}\right)^{\mathrm{T}}$. Choosing the vev Φ_0 of Φ reflects the spontaneous breakdown of the $\mathrm{SU}(2)_I \times \mathrm{U}(1)_Y$ symmetry to the unbroken electromagnetic U(1) symmetry. The following equation shows a reparameterization of the field Φ in terms of perturbation around the vev:

$$\Phi = \begin{pmatrix} \phi^+ \\ \phi^0 = \left(\frac{v+H+i\chi}{\sqrt{2}}\right). \end{pmatrix} \tag{2.14}$$

In this equation H represents the real physical Higgs field and can be understood as a vacuum excitation. The fields ϕ^+ and χ are complex and real, respectively, and can be understood as Goldstone bosons. However, these Goldstone fields are not physical since a gauge transformation letting them vanish can always be found. This gauge transformation is known as the "unitary gauge" (U-gauge). Broadly spoken, from the four degrees of freedom of Φ three are absorbed by the gauge bosons $W^\pm$ and Z while the remaining is the Higgs boson. Using equation 2.14 and the covariant derivative 2.7 with $I^i_{\mathrm{w},\Phi} = \frac{\sigma^i}{2}$, $Y_{\mathrm{w},\Phi}$ and $T^a_{c,\Phi} = 0$ to insert into the Higgs Lagrangian 2.11 one finds

$$\begin{aligned} \mathcal{L}_{\text{H,U-gauge}} = &\frac{1}{2}(\partial H)^2 + \frac{g^2}{4}(v+H)^2 W^+_\mu W^{-,\mu} + \frac{g^2}{8\cos^2\theta_{\mathrm{w}}}(v+H)^2 Z_\mu Z^\mu \\ &+ \frac{\mu^2}{2}(v+H)^2 - \frac{\lambda}{16}(v+H)^4. \end{aligned} \tag{2.15}$$

This equation contains bilinear terms in the gauge fields $W^\pm$ and Z and in the Higgs field H. These terms correspond to mass terms for the weak gauge bosons $W^\pm$ and Z as well as for the Higgs boson H. Identifying these masses with

$$M_W = \frac{gv}{2}, \quad M_Z = \frac{M_W}{\cos\theta_{\mathrm{w}}} \quad \text{and} \quad M_H = \sqrt{2\mu^2} \tag{2.16}$$

one can completely eliminate the parameters μ^2, λ and v and finally gets

$$\begin{aligned}\mathcal{L}_{\text{H,U-gauge}} = &\frac{1}{2}(\partial H)^2 - \frac{1}{2}M_H^2 H^2 + M_W^2 W_\mu^+ W^{-,\mu} + \frac{1}{2}M_Z^2 Z_\mu Z^\mu \\ &+ g M_W H W_\mu^+ W^{-,\mu} + \frac{g^2}{4} H^2 W_\mu^+ W^{-,\mu} \\ &+ \frac{g M_Z}{2\cos\theta_\text{w}} H Z_\mu Z^\mu + \frac{g^2}{4\cos^2\theta_\text{w}} H^2 Z_\mu Z^\mu \\ &- \frac{g M_H^2}{4 M_W} H^3 - \frac{g^2 M_H^2}{32 M_W^2} H^4 + \text{const.}\end{aligned} \tag{2.17}$$

with a not spelled out but irrelevant constant.

2.1.3 Yukawa Couplings

Yukawa couplings of the Higgs doublet Φ to the fermions are allowed due to the renormalizability and the gauge invariance of the SM Lagrangian. The most general form of these interactions is

$$\mathcal{L}_\text{Yuk} = -\overline{\Psi}_L G_l \psi_{l_\text{R}} \Phi - \overline{\Psi}_Q G_u \psi_{u_\text{R}} \widetilde{\Phi} - \overline{\Psi}_Q G_d \psi_{d_\text{R}} \Phi + \text{h.c.}, \tag{2.18}$$

where "h.c." means hermitian conjugate. $\widetilde{\Phi} = i\sigma^2\Phi^* = ((\phi^0)^*, -\phi^-)^\text{T}$ denotes the charge-conjugate Higgs doublet with quantum numbers opposite to Φ. The matrices G_f with $f \in \{l, u, d\}$ represent arbitrary 3×3 matrices. This introduces a large number of free parameters. However, most of them are not physical and can be eliminated by field redefinitions. As can be seen the non-diagonal elements of G_f mix the left- and right-handed parts of the different generations of fermion type f leading to the fact that each term of $\mathcal{L}_\text{Yuk}$ involves terms that are bilinear in the fermion fields. These mixing terms cause a fermion of flavor f_i ($i \in \{1,2,3\}$) of the ith generation to oscillate into the flavor f_j ($j \in \{1,2,3\}$) of the other generations ($j \neq i$). This is possible even during a free propagation in space and time. The oscillation can be removed by transforming the existing "flavor basis" $(\psi_{f_{\tau,1}}, \psi_{f_{\tau,2}}, \psi_{f_{\tau,3}})$ of left-handed ($\tau = \text{L}$) and right-handed ($\tau = \text{R}$) fields into a "mass basis" $(\hat{\psi}_{f_{\tau,1}}, \hat{\psi}_{f_{\tau,2}}, \hat{\psi}_{f_{\tau,3}})$ with a unitary matrix U according to

$$\hat{\psi}_{f_{\tau,i}} = U_{ij}^{f_\tau} \psi_{f_{\tau,j}}. \tag{2.19}$$

In this process the matrices G_f receive the diagonal form

$$U^{f_\text{L}} G_f (U^{f_\text{R}})^\dagger = \frac{\sqrt{2}}{v} \text{diag}\{m_{f_1}, m_{f_2}, m_{f_3}\}. \tag{2.20}$$

The diagonal value m_{f_i} is the mass of the fermion f_i and can be chosen non-negative by convention. Applying this field redefinition on the whole SM Lagrangian one has to transform the left-handed neutrino fields with the same unitary matrix as for the charged leptons. This is possible for mass-degenerate neutrinos such as massless neutrinos. The effects of applying the redefinition on the whole SM Lagrangian can be summarized in the following three facts:

1. The coupling matrices G_f are replaced by the diagonal form 2.20.

2. The fermion fields $\psi_{f_{\tau,i}}$ are replaced by the counterparts $\hat{\psi}_{f_{\tau,i}}$.

3. As a remnant of the U matrices the Cabibbo-Kobayashi-Maskawa (CKM) [28, 29] matrix $V = U^{u_L}(U^{u_L})^\dagger$ appears in fermion chains of type $\overline{\hat{\psi}}_{u_L}...V\hat{\psi}_{d_L}$ and as $V^\dagger$ in fermion chains of type $\overline{\hat{\psi}}_{d_L}...V^\dagger\hat{\psi}_{u_L}$.

As can be seen only charged-current interactions receive modifications by V while neutral-current interactions remain unchanged. In the following the use of the mass basis is assumed so that the hats on the fermionic fields can be omitted. As a result of the unitary gauge the Yukawa Lagrangian takes the simple form

$$\mathcal{L}_{\text{Yuk,U-gauge}} = -\sum_f m_f(\overline{\psi}_{f_L}\psi_{f_R} + \overline{\psi}_{f_R}\psi_{f_L})\left(1 + \frac{H}{v}\right), \tag{2.21}$$

where f runs over all fermion flavors of all generations. The Yukawa Lagrangian shows that the Higgs boson couples to each fermion f of mass m_f with the strength $y_f = \frac{m_f}{v}$. Also the coupling is a pure scalar rather than a pseudo-scalar admixture proportional to γ_5.

2.1.4 The Free Parameters of the Standard Model

The most general SM Lagrangian with massless neutrinos as formulated in the sections above depends on 18 parameters which need to be determined by experiments. The choice of the free parameters is arbitrary. For convenience, however, the following parameters are usually chosen:

- electromagnetic coupling constant $\alpha = \frac{e^2}{4\pi}$
- strong coupling constant $\alpha_s = \frac{g_s^2}{4\pi}$
- weak gauge boson masses M_W and M_Z
- Higgs boson mass M_H
- fermion masses m_f (9 parameters)
- CKM matrix (3 mixing angles + 1 phase)

2.2 Perturbative Quantum Chromo Dynamics

Quantum Chromo Dynamics (QCD) [30] is the quantum field theory of the strong interaction and is incorporated in the SM Lagrangian introduced in section 2.1.1. In contrast to the electromagnetic interaction mediated by uncharged photons the strong interaction is mediated by gluons carrying a color charge which results in the color confinement. This leads to the fact that in hadronic collisions like at the LHC the effects of QCD are omnipresent. The most interesting hadronic collisions at the LHC involve large momentum exchanges such that the perturbative expansion of QCD (pQCD) has to be applied. In pQCD an observable $\mathcal{O}$ is truncated with the power-series expansion

$$\mathcal{O} = \mathcal{O}_0 + \mathcal{O}_1\alpha_s + \mathcal{O}_2\alpha_s^2 + ... \quad \text{with} \quad \alpha_s = \frac{g_s^2}{4\pi} \tag{2.22}$$

to expect meaningful estimates as long as $\alpha_s \ll 1$. An exemplary observable usually truncated with the power-series expansion is the cross section σ of a process. It can be written as

$$\sigma = \sigma_{\mathrm{LO}} + \underbrace{\sigma_{\mathrm{NLO}}}_{\mathcal{O}(\alpha_s)} + \underbrace{\sigma_{\mathrm{NNLO}}}_{\mathcal{O}(\alpha_s^2)} + ... \tag{2.23}$$

where σ_{LO} is the leading order (LO) term, σ_{NLO} the next-to-leading order (NLO) term and σ_{NNLO} the next-to-next-to leading order (NNLO) term of the cross section. This can be illustrated with Feynman diagrams [31]. Feynman diagrams are pictorial representations of mathematical expressions. They were invented by Richard Feynman in 1949 in the framework of quantum electrodynamics (QED) in order to illustrate the quantum field theoretical interactions of particles in a simple manner. Feynman diagrams are read from left to right which implies the direction of time. As an example, the production of Z/γ^* bosons can be described using Feynman diagrams as shown in figure 2.2. In this case the Z/γ^* is produced by a quark-antiquark

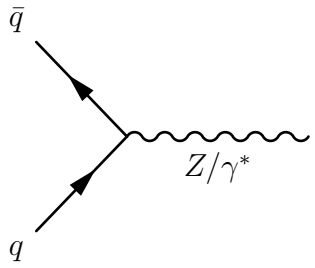

Figure 2.2: Feynman diagram of the production of a Z/γ^* boson through the interaction of a quark-antiquark pair at leading order.

pair. In Feynman diagrams, fermions are represented by straight lines with arrows. If the arrow points to the right a fermion is represented while an arrow pointing to the left represents an antifermion. Bosons are represented by waved lines with the exception of the gluon which is represented by a curled line as can be seen in the Feynman diagrams 2.3. A point of contact by at least three lines is called a vertex. The LO Feynman diagram 2.2 has one vertex while the NLO Feynman diagrams 2.3 have two vertices. It has to be pointed out that the vertices where the Z/γ^* couples to, are electroweak couplings denoted by the constant α. The vertices where the gluon couples to are strong couplings denoted by the constant α_s. The LO Feynman diagram is hence of the order $\mathcal{O}(\alpha)$ while the NLO Feynman diagrams are of the order $\mathcal{O}(\alpha\alpha_s)$. The NNLO Feynman diagrams of the Z/γ^* production are of the order $\mathcal{O}(\alpha\alpha_s^2)$ respectively. The Feynman diagrams shown so far are *tree diagrams*. At NLO or higher orders, however, one can get diagrams where it is possible to go along particle lines and return to the starting point without backtracking. Such Feynman diagrams are called *loop diagrams*. An example is shown in figure 2.4. In order to calculate the cross section of Z/γ^* production all diagrams that one is able to calculate are usually taken into account. Therefore the Feynman diagrams need to be translated in the corresponding mathematical expressions from which the scattering amplitudes can be calculated. *Fermi's golden rule* [32, 33, 34] can then be applied to calculate the cross section.
Another important example of the power-series expansion in pQCD is the β function which determines the running of the coupling constant α_s through the renormaliza-

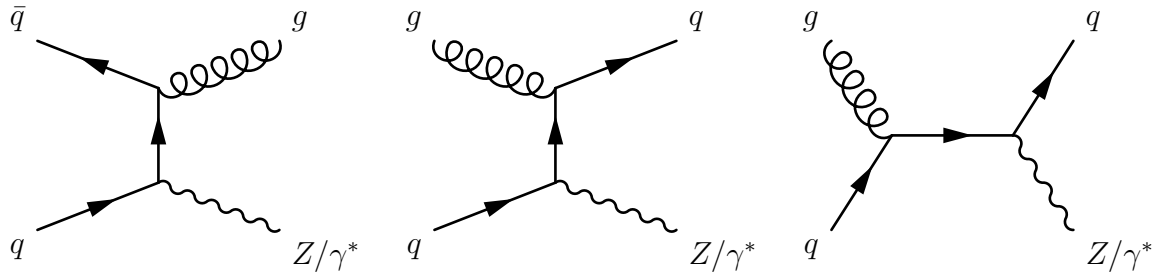

Figure 2.3: Three exemplary Feynman diagrams of the production of a Z/γ^* at next-to-leading order.

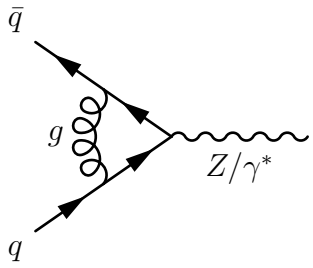

Figure 2.4: Loop diagram showing the production of a Z/γ^* boson.

tion group equation

$$Q^2\frac{\partial\alpha_s}{\partial Q} = \beta(\alpha_s) \quad \text{with} \quad \beta(\alpha_s) = -\alpha_s^2(b_0 + b_1\alpha_s + \mathcal{O}(\alpha_s^2)). \tag{2.24}$$

The coefficients b_0 and b_1 depend on the number of quark flavors n_F with masses smaller than the scale Q as follows:

$$b_0 = \frac{33 - 2n_F}{12\pi} \qquad b_1 = \frac{153 - 19n_F}{24\pi^2}. \tag{2.25}$$

Maintaining only the leading term b_0, equation 2.24 is solved by

$$\alpha_s(Q^2) = \frac{\alpha_s(\mu^2)}{1 + b_0 \ln\left(\frac{Q^2}{\mu^2}\right)\alpha_s(\mu^2)}. \tag{2.26}$$

This relates the strength of the coupling α_s at a scale Q to the strength of α_s at a scale μ assuming both scales are in the perturbative regime. As long as $n_F < 17$ the coupling becomes weaker at higher scales Q. In other words it describes the fact, that the QCD color charge decreases when the distance decreases. As a consequence, for high scales Q, QCD becomes almost a free theory which is known as *asymptotic freedom*. The opposite effect is the so called *color confinement*. The strong coupling constant can rise arbitrarily for small values of Q. Since the gluons carry a color charge itself and hence couple to the quarks, lower scales Q can be related to a larger separation of the quarks. At some point, although, the binding of the quarks collapses under the production of new quark-antiquark pairs with a stronger binding.

2.3 Proton-Proton Collisions

Protons are non-elementary particles consisting of quarks and gluons. The quantum numbers of the proton are determined by three *valence quarks*. The valence quarks

interact among each other via virtual quark-antiquark pairs called *sea quarks* and virtual gluons. In the following, these color charged constituents of the protons will be called "partons". Due to the composite nature of a proton, a collision of two protons usually leads to a complex picture of different processes as shown in figure 2.5. Only the minority of proton-proton collisions at the LHC involves processes with a large momentum exchange. Such a process is called *hard scattering process* and is illustrated by the large red dot in figure 2.5. The hard scattering process is the interaction of two partons originating from the protons pictured as dark green ellipses. However, before the hard scattering happens, the original partons can produce other partons by parton splitting or gluon radiation. Since this occurs before the hard scattering process it is called *initial state radiation* (ISR). If such processes occur after the hard scattering process it is called *final state radiation* (FSR). The products of the hard scattering process displayed as smaller red dots undergo further parton splitting and parton radiation which is called the *parton shower*. The ISR, FSR and the parton shower is illustrated by the blue parts in the figure. In the final process the colored partons combine into colorless hadrons which is called *hadronization* and shown in light green. These hadrons may enter the detector or decay into other particles before entering the detector which is shown in dark green. Apart from the hard scattering process a secondary process takes place and is illustrated by the purple parts in the figure. This process is due to interactions of the remnant partons of the initial protons and is called *underlying event*. The interaction usually involves much smaller momentum exchanges than the hard scattering process but develops an additional individual parton shower resulting in a hadronization as well. The yellow parts of the figure indicate electromagnetic radiation of charged particles.

2.3.1 Cross Section Prediction

In order to describe the production of a final state X through the hard scattering process the factorization ansatz [36, 37, 38] can be used. The cross section for the production of X by the collision of two hadrons H_1 and H_2 can be written as

$$\begin{aligned}\sigma_{H_1H_2\to X} = &\sum_{i,j}\int \mathrm{d}x_1\mathrm{d}x_2 f_{i/H_1}(x_1,\mu_F) f_{j/H_2}(x_2,\mu_F) \\ &\times \hat{\sigma}_{ij\to X}\left(x_1P_1, x_2P_2, \alpha_s(\mu_R), \frac{Q}{\mu_F}\right) \quad \text{with} \quad i,j \in \{q,\bar{q},g\}.\end{aligned} \tag{2.27}$$

q, $\bar{q}$ and g are the acronyms for the partons that constitute the initial-state hadrons which in this case will be protons. At large scales Q the effects related to the binding of the partons can be neglected. As a result, the cross section factorizes into a product of *parton distribution functions* (PDFs) $f_{i/H}(x,\mu_F)$ at a factorization scale μ_F and the partonic cross section $\hat{\sigma}_{ij\to X}$. The PDFs are of non-perturbative origin while $\hat{\sigma}_{ij\to X}$ can be calculated perturbatively. PDFs model the probability to find a parton of flavor i in a proton with a fraction x of the proton's momentum P and will be discussed further in the following section. The squared partonic center-of-mass energy $\hat{s}$ is given by

$$\hat{s} = x_1x_2(P_1+P_2)^2. \tag{2.28}$$

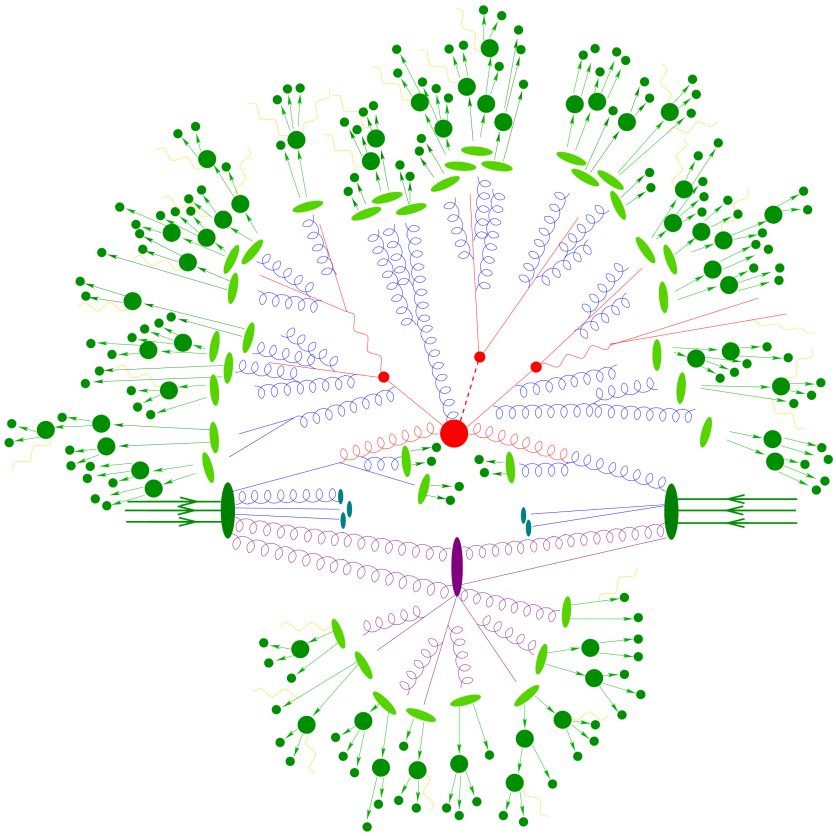

Figure 2.5: Illustration of a collision of two protons. [35]

Based on the framework of QCD the partonic cross section can be expanded as a power series of the coupling constant α_s. According to equation 2.23 the partonic cross section can be written as

$$\hat{\sigma}_{ij\to X} = [\hat{\sigma}_{\mathrm{LO}} + \underbrace{\hat{\sigma}_{\mathrm{NLO}}}_{\mathcal{O}(\alpha_s(\mu_R^2))} + \underbrace{\hat{\sigma}_{\mathrm{NNLO}}}_{\mathcal{O}(\alpha_s^2(\mu_R^2))} + ...]_{ij\to X} \tag{2.29}$$

where μ_R denotes the renormalization scale. Theoretically, all orders of the power series can be calculated which would lead to an invariant cross section under μ_R and μ_F. Practically, however, terms of orders larger than NLO are very difficult to calculate. Therefore, the cross section is usually described only by the LO and NLO terms which leads to a dependence on μ_R and μ_F. The choice of μ_R and μ_F as well as the finite order of the cross section results in a systematic uncertainty. In order to avoid large logarithms in the perturbative calculation of the cross section, μ_R and μ_F are usually chosen on the scale of the momentum exchange of the hard scattering process. When calculating the LO, NLO and NNLO coefficients of the partonic cross section the corresponding QCD evolution of the PDFs has to be used as will be shown in the next section.

2.3.2 Parton Distribution Functions

As introduced in the previous section PDFs model the probability to find a parton of a specific flavor in a proton with a fraction x of the proton's momentum. The fraction x of the parton is usually called *Bjorken-x* variable. Due to the repeated applicability

of the factorization ansatz a PDF can be defined via evolution equations. The initial state PDFs $f_i(x, \mu_F)$ can be evolved to the appropriate scales using the DGLAP equations

$$\mu_F^2 \frac{\partial f_i(x,\mu_F)}{\partial \mu_F^2} = \sum_{j=\{q,\bar{q},g\}} \int_x^1 \frac{dz}{z} \frac{\alpha_s}{2\pi} P_{ij}(z) f_{j/H}(x/z, \mu_f) \quad \text{with} \quad i \in \{q, \bar{q}, g\}. \tag{2.30}$$

P_{ij} are the Altarelli-Parisi splitting functions. They can be expanded in perturbation theory according to

$$P_{ij}(z, \alpha_s) = [P_{\mathrm{LO}}(z) + \frac{\alpha_s}{2\pi} P_{\mathrm{NLO}}(z) + ...]_{ij} \tag{2.31}$$

and are known up to NNLO. Expressions for these functions can be found in [23]. Assuming an initial parton with a specific momentum, the splitting functions describe the probability of emitting a parton with a fraction of the initial parton's momentum. More precisely, at leading order, the splitting function $P_{ij}(z)$ describes the probability of finding a parton of type i emitted by a parton of type j carrying a fraction z of the momentum of j. A visualization of the splitting functions can be seen in figure 2.6. It has to be pointed out, that $P_{\bar{q}g} = P_{qg}$, $P_{g\bar{q}} = P_{gq}$ and $P_{\bar{q}\bar{q}} = P_{qq}$.

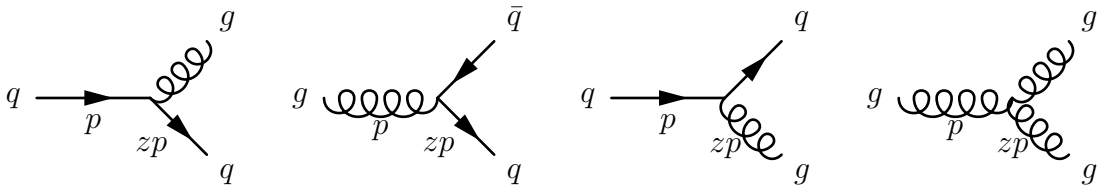

(a) $P_{qq}(z)$ (b) $P_{qg}(z)$ (c) $P_{gq}(z)$ (d) $P_{gg}(z)$

Figure 2.6: Feynman diagrams of the Altarelli-Parisi splitting functions at leading order. p indicates the momentum of the incoming parton.

In order to determine a PDF, no unique approach exists. However, the fundamental experimental input for all PDF determinations is deep-inelastic-scattering (DIS) as well as collider data. The DIS data has been obtained through fixed-target lepton-hadron scattering and through the HERA electron-proton collider at DESY. Additionally, $p\overset{(-)}{p}$ collider experiments have yielded more input data. At such colliders the lighter quarks are usually probed via the production of $W^{\pm}$ and Z bosons through the interaction of a quark and an antiquark. Gluons and heavy quarks can for instance be probed via gluon-gluon, quark-gluon or quark-quark interactions resulting in two jets. Additional processes can be found in table 18.1 in reference [39]. There are different PDF determination groups using different techniques and different experimental input. Usually though, the PDF is obtained by a global fit of the input data. In a first step, the quark, antiquark and gluon distributions are parameterized at a scale Q_0. The parameterizations usually differ among the different PDF fitting groups. Equation 2.32 shows an exemplary parameterization used by

the HERAFITTER project [40, 41, 42]:

$$\begin{aligned} xg(x) &= A_g x^{B_g}(1-x)^{C_g} - A'_g x^{B'_g}(1-x)^{C'_g} \\ xu_v(x) &= A_{u_v} x^{B_{u_v}}(1-x)^{C_{u_v}}(1+E_{u_v}x^2) \\ xd_v(x) &= A_{d_v} x^{B_{d_v}}(1-x)^{C_{d_v}} \\ x\overline{U}(x) &= A_{\overline{U}} x^{B_{\overline{U}}}(1-x)^{C_{\overline{U}}} \\ x\overline{D}(x) &= A_{\overline{D}} x^{B_{\overline{D}}}(1-x)^{C_{\overline{D}}} \end{aligned} \tag{2.32}$$

$xg(x)$ is the gluon distribution and $xu_v(x)$ and $xd_v(x)$ represent the valence quark distributions with $u_v(x) = u(x) - \bar{u}(x)$ and $d_v(x) = d(x) - \bar{d}(x)$. $\overline{U}(x) = \bar{u}(x)$ and $\overline{D}(x) = \bar{d}(x) + \bar{s}(x)$ are the up- and down-type antiquark distributions. Note that at the starting scale Q_0 there are no heavy quarks. In the next step the DGLAP equations are solved to obtain the PDFs at any scale $Q > Q_0$. In the final step the 19 parameters A_i, B_i, C_i and E_i with $i \in \{g, u_v, d_v, \overline{U}, \overline{D}\}$ of this parameterization are determined by a global fit on the input data. Figure 2.7 shows the MSTW 2008 NLO PDFs multiplied by Bjorken-x and as a function of the Bjorken-x for different scales Q. As can be seen in both plots, the largest contribution at high

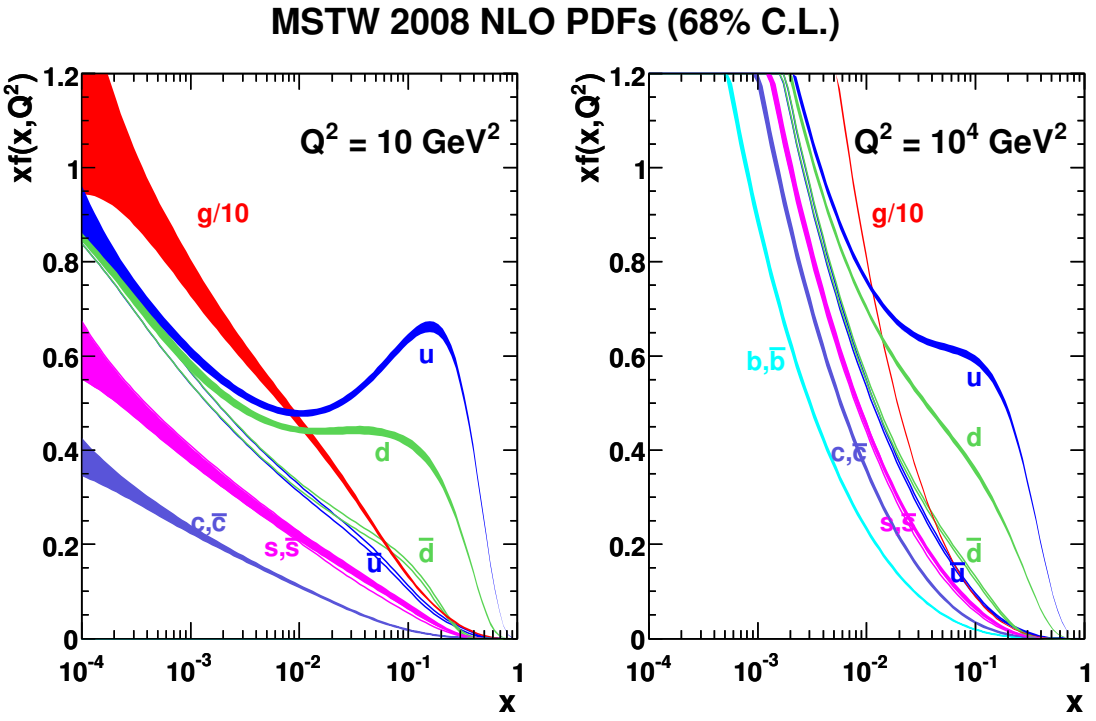

Figure 2.7: MSTW 2008 NLO PDFs for quarks, antiquarks and gluons at a scale of $Q^2 = 10\,\mathrm{GeV}^2$ (left) and $Q^2 = 10^4\,\mathrm{GeV}^2$ (right). [43]

Bjorken-x comes from u and d quarks which are dominantly valence quarks. The contribution of the sea quarks rises with larger scales Q due to gluons resolving in quark-antiquark pairs more often.
Each PDF is not only illustrated by its central value but by a band describing the PDF uncertainty due to the input data. This PDF uncertainty can be estimated with the so called "eigenvector method" based on the Hessian formalism. A global PDF

fit is based on the minimization of a χ^2 function. The usual approach to estimate uncertainties for such a fit is by constructing the quadratic expansion of χ^2 which is known as the error matrix or Hessian matrix. From the Hessian matrix orthogonal eigenvector basis PDFs can be extracted. These eigenvector basis PDFs can be used to describe the deviation from the global minimum of χ^2. Therefore, the eigenvectors are moved in an up and down direction. As a result, each eigenvector variation leads to a varied PDF which are known as the PDF error set. More information about the uncertainty determination of PDFs and especially the Hessian method can be found in [44].

2.3.3 Parton Shower and Hadronization

Due to the large momentum exchange in the hard scattering process the resulting partons lead to large non-zero virtualities. Additionally the strong coupling constant increases with the distance of the partons. Both facts enhance the probability of QCD radiation in form of gluon emission similarly to the QED radiation in form of photons of electrically charged particles. The emitted gluons in turn will radiate quark-antiquark pairs which leads to a parton shower. An exact calculation of the parton shower is practically impossible such that an approximation scheme is used. This scheme only includes the dominant contributions to the parton shower which are collinear parton splitting or gluon radiation of low energy. The evolution of the parton shower can be described with the DGLAP evolution equations from which the *Sudakov form factor* can be derived. It can be written as

$$\Delta_i(q_1^2, q_2^2) = \exp\left\{ - \sum_{j=\{q,\bar{q},g\}} \int_{q_2^2}^{q_1^2} \frac{\mathrm{d}q^2}{q^2} \int_{\frac{Q_0^2}{q^2}}^{1-\frac{Q_0^2}{q^2}} \frac{\alpha_s}{2\pi} \mathrm{d}z P_{ij}(z) \right\} \tag{2.33}$$

$$\text{with} \quad i \in \{q, \bar{q}, g\}$$

and expresses the probability that a parton is not splitting into other partons or radiating gluons during the evolution from the scale q_1^2 to q_2^2. The starting scale for the evolution of the parton shower is usually chosen as the scale Q^2 of the hard scattering process. A natural cutoff scale of the parton shower is given by $Q_0^2 \approx 1\,\mathrm{GeV}$ since partons can not be separately resolved at this scale. In order to describe the generation of a parton shower one solves the equation $\Delta_i(Q^2, q^2) = R$ where R is a random number in the interval $[0, 1]$. The equation is solved again with the determined scale q^2 as the new starting scale. This is repeated as long as the scales have fallen below Q_0^2. Due to the running of the coupling constant α_s (see equation 2.26) an increase of the strong coupling at low values of the parton shower evolution scale is observed. As a result the parton shower leaves the perturbative regime and enters the non-perturbative stage at which the final state hadrons are formed. This is the hadronization of the proton-proton collisions and can be described via the *string model* or the *cluster model*. The string model [45] is based on the observation that the attraction of two color charges increases linearly with their distance from each other such as a quark-antiquark pair. This is due to the gluons which attract the quark and the antiquark similarly to a string. As soon as the energy of the gluon string becomes of the order of quark-antiquark masses it collapses along its length and forms new quark-antiquark pairs which can undergo the same process again or

being identified as the final state hadrons. The cluster model [46] is based on the observation of the preconfinement property of QCD. It shows that for evolution scales $q^2 \ll Q^2$ the partons of the shower are arranged in colourless clusters independent of the hard scattering process. As a result, at the cutoff scale Q_0^2 it is natural to identify these clusters as hadrons that decay into the final state hadrons.

2.3.4 Event Simulation

In order to compare the observations with the predictions of the theory simulations are used. These simulation are performed with the Monte Carlo (MC) method which is a technique for numerical integration based on random numbers. First the proton-proton collisions as described in the sections above need to be calculated through by a so called *event generator* in order to get to the final state particles of the proton-proton collisions. Within this thesis the event generators Pythia [47] and Sherpa [48] have been used. Both event generators are general-purpose event generators meaning that they can calculate the hard scattering process and model the parton shower, hadronization, underlying event as well as particle decays before reaching the detector. A difference between both event generators arises in the calculation of the hard scattering process. While Sherpa is able to calculate the hard scattering process with NLO precision Pythia can only calculate this process at LO. Therefore the event generator Powheg, which can calculate the hard scattering process with NLO precision, is usually interfaced into the Pythia event generator. Since the cross section of the hard scattering process can often be calculated at higher orders than the event generators can simulate this process a so called *k-factor* can be applied. Hence, this k-factor is a correction for the MC simulation expressed for instance via

$$k = \frac{\sigma_{\mathrm{NNLO}}}{\sigma_{\mathrm{NLO}}} \tag{2.34}$$

where σ_{NLO} is the cross section used in the simulation while σ_{NNLO} is the calculated higher order cross section. The k-factor can be regarded as a weight that each simulated event has to be applied with.

2.4 Physics Beyond the Standard Model

Despite the success of the SM in describing the observed elementary particles and their interactions there is evidence that the SM is not a complete description. Some phenomena remain unexplained by the SM which hints to physics beyond the Standard Model (BSM). Among other unexplained phenomena the following are the most prominent:

Gravity
Gravity, one of the four fundamental forces, is not incorporated in the SM. Adding a graviton as the boson mediating gravity to the SM does not recreate the experimental observations. Furthermore the theory describing gravity, the general relativity, seems to be incompatible with the SM.

Dark Matter and Dark Energy
Only about 5 % of the energy in the universe can be explained by the SM. This is the result of cosmological observations showing that about 26 % of the energy in the universe is dark matter while the remaining 69 % is dark energy [49]. Dark matter only interacts weakly or not at all with the SM matter. Dark energy is a constant energy density for the vacuum that currently is not much known of.

Neutrino Masses
The SM as presented in the previous section assumes that the neutrinos are massless particles. The discovery of neutrino oscillation [50], in contrast, shows that neutrinos do have mass. It is possible to incorporate mass terms for the neutrinos into the SM. However, this leads to new theoretical problems such that the mass terms need to be extremely small. Also it is not clear if the neutrino masses arise due to the same mechanism as for the other fundamental particles.

Matter-Antimatter Asymmetry
The SM predicts that matter and antimatter should have been created in almost the same amounts under the assumption that the initial conditions of the universe involve proportionate amounts of matter relative to antimatter. In contrast, it is observed that the universe is made out of mostly matter which is an asymmetry that the SM can not explain.

One of the most common ways to incorporate BSM physics into the SM is by introducing additional new heavy gauge bosons. Mathematically this compares to extending the gauge group of the SM by additional gauge groups. The concept behind this approach is known as "Grand Unified Theories" (GUTs). The idea of GUTs is to unify the electromagnetic, the weak and the strong interaction. The gauge group describing this scenario is characterized by several gauge bosons mediating the interaction but by only one unified coupling constant. The unification of the three gauge couplings is predicted above some high energy unification scale by many GUTs. The gauge couplings have been determined very precisely up to a scale M_Z equal to the Z boson mass which allows to test the gauge coupling unification by extrapolating the gauge couplings to higher scales. The GUTs assume that the three gauge couplings intersection at some scale M_X. Taking the SM as a basis the three gauge couplings do not meet at one scale. However, using the Minimal Supersymmetric Standard Model (MSSM) the unification works at a scale of around $M_X \sim 3 \times 10^{16}\,\text{GeV}$ [51]. This is a strong motivation for GUTs and BSM physics. The BSM models used in this analysis to search for new physics will be introduced in the following.

2.4.1 Sequential Standard Model

The sequential Standard Model (SSM) [52] is a simple approach to duplicate the SM bosons Z, W^+ and W^- of the weak interaction. This can be achieved by an extension of the SM gauge group $\text{SU}(3)_c \times \text{SU}(2)_I \times \text{U}(1)_Y$ by another SU(2) group. This results in a new additional triplet of heavy gauge bosons Z'_{SSM}, $W^{+\prime}_{\text{SSM}}$ and $W^{-\prime}_{\text{SSM}}$. These new gauge bosons are defined to have the same couplings to fermions as the SM bosons. The lower limit on the pole mass of a Z'_{SSM} derived with LHC

data corresponding to $3.2\,\mathrm{fb}^{-1}$ at $\sqrt{s} = 13\,\mathrm{TeV}$ can be seen in table 2.1.

2.4.2 E_6-motivated Model

The E_6 gauge group is a symmetry group that can break into the SM gauge group in a number of different ways. A common breakdown of the E_6 is

$$E_6 \rightarrow \mathrm{SO}(10) \times \mathrm{U}(1)_\psi \tag{2.35}$$

yielding the $\mathrm{U}(1)_\psi$ group implying an associated gauge boson Z'_ψ. The SO(10) breaks down further according to

$$\mathrm{SO}(10) \rightarrow \mathrm{SU}(5) \times \mathrm{U}(1)_\chi \tag{2.36}$$

yielding the $\mathrm{U}(1)_\chi$ group likewise implying an associated gauge boson Z'_χ. The SU(5) contains the SM gauge group $\mathrm{SU}(3)_c \times \mathrm{SU}(2)_I \times \mathrm{U}(1)_Y$. The new gauge boson of this model is created by a mixture of Z'_ψ and Z'_χ. The precise mixture is governed by the angle θ_{E_6} according to

$$Z'(\theta_{E_6}) = Z'_\psi \cos\theta_{E_6} + Z'_\chi \sin\theta_{E_6}. \tag{2.37}$$

The angle θ_{E_6} specifies the coupling strength of the Z' boson as well as its intrinsic width. Table 2.1 shows a summary of the commonly used Z' mixtures of the E_6-motivated model as well as the corresponding values for the Z'_{SSM}. The table also shows the lower limits on the pole masses of the various Z' models derived with LHC data corresponding to $3.2\,\mathrm{fb}^{-1}$ at $\sqrt{s} = 13\,\mathrm{TeV}$. It can be seen that the E_6-motivated model predicts much narrower Z' signals than the SSM. More details on E_6-motivated models can be found in [52] and [53].

Table 2.1: Summary of the bosons from the E_6-motivated model as well as from the sequential Standard Model together with their lower pole mass limit derived with LHC data corresponding to $3.2\,\mathrm{fb}^{-1}$ at $\sqrt{s} = 13\,\mathrm{TeV}$ for a credibility interval of 95 % [54].

	Z'_{SSM}	Z'_χ	Z'_{S}	Z'_{I}	Z'_η	Z'_{N}	Z'_ψ
Width [%]	3.0	1.2	1.2	1.1	0.6	0.6	0.5
θ_{E_6} [rad]	—	0.50π	0.63π	0.71π	0.21π	-0.08π	0π
Mass Limit [TeV]	3.36	3.05	3.00	2.94	2.80	2.80	2.74

2.4.3 The Hidden Valley Model

The hidden valley model has been introduced in [55] with the idea of the existence of a hidden sector that couples weakly to the SM via heavy gauge bosons. These models can be constructed by extending the SM gauge group by a non-abelian group G_v implying new particles called v-particles. It is assumed that all SM particles are charge-neutral under G_v whereas the v-particles are charged under G_v but charge-neutral under the SM gauge group. A heavy gauge boson carrying both G_v charges as well as SM charges could then act as a mediator between the SM and the hidden valley. This scenario is shown in figure 2.8 where a heavy gauge boson X created

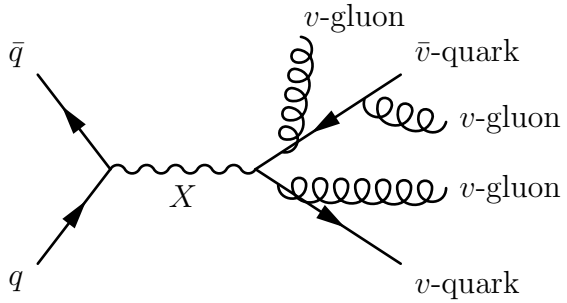

Figure 2.8: Feynman diagram of a quark-antiquark annihilation forming a heavy gauge boson X decaying into v-quarks which radiate v-gluons.

by a quark-antiquark annihilation decays into so called v-(anti)quarks $Q(\overline{Q})$. The v-quarks in turn can radiate v-gluons. The final state particles consisting of v-quarks and v-gluons assemble themselves into v-hadrons. Some of the v-hadrons are stable and will therefore be invisible. Some of them, however, decay into SM particles like quark-antiquark pairs or lepton-antilepton pairs. Thus they will be visible in the detector. An interesting decay for the analysis presented in this thesis is $Q\overline{Q} \to Z' \to f\bar{f}$ where f can be any SM fermion such as an electron or a muon. The mediator X in the Feynman diagram 2.8 could as well be a Z' boson. Additional information on the hidden valley model can be found in [56] and [57].

Chapter 3

The ATLAS Experiment

An outstanding possibility to explore lepton-antilepton final states in proton-proton collisions is given by the ATLAS experiment taking place at the *European Organization for Nuclear Research* (CERN) in Geneva Switzerland. This chapter discusses the experimental setup used for this analysis following the reviews [58] and [23].

3.1 The Large Hadron Collider

The Large Hadron Collider (LHC) is a superconducting dual ring accelerator and collider for hadrons at CERN. The LHC is installed in the 26.7 km long tunnel that was constructed for the *Large Electron-Positron Collider* (LEP) between 1984 and 1989 and has been designed to produce proton-proton collisions with a center-of-mass energy of up to 14 TeV. Further, a peak luminosity of $1.0 \times 10^{34}\,\mathrm{cm}^{-2}\mathrm{s}^{-1}$ has been aimed at when the LHC was designed. In order to reach this peak luminosity a high beam intensity is required. This excludes a design as a single ring collider with the use of antiprotons since the creation of a high intensive beam of antiprotons is technically very difficult compared to a beam of protons. As a result the LHC consists of two rings with counter-rotating beams using protons only. A schematic view of the LHC geometry can be seen in figure 3.1. The tunnel where the LHC rings are implemented has eight straight sections and eight arcs and is located approximately between 45 m and 170 m underground. Each straight section of the tunnel was originally designed to be a crossing point for the two beams. In case of the LHC, however, only four of the straight sections are used as crossing points. At these crossing points denoted with *IP1*, *IP2*, *IP5* and *IP8* the four detectors ATLAS, ALICE, CMS and LHCb are located. Two of the four remaining straight sections are equipped with a momentum cleaning and a betatron cleaning collimator denoted with *IR3* and *IR7* respectively. The momentum cleaning collimator is dedicated to remove particles with large longitudinal oscillation amplitudes, in other words protons with high momentum offsets. The betatron cleaning collimator is dedicated to remove particles with large transverse oscillation amplitudes also known as betatron amplitudes. At the straight section denoted with *IR4* the radio-frequency (RF) cavities used to accelerate the protons are implemented. *IR6* is the so called beam dump and used to eject the proton beams whenever it is necessary. The arcs on the other hand are equipped with superconducting dipole magnets keeping the proton beams in the ring. Figure 3.2 shows such a magnet where the two separate beam pipes requiring the dipole-type magnets can be seen. In order to keep the magnets

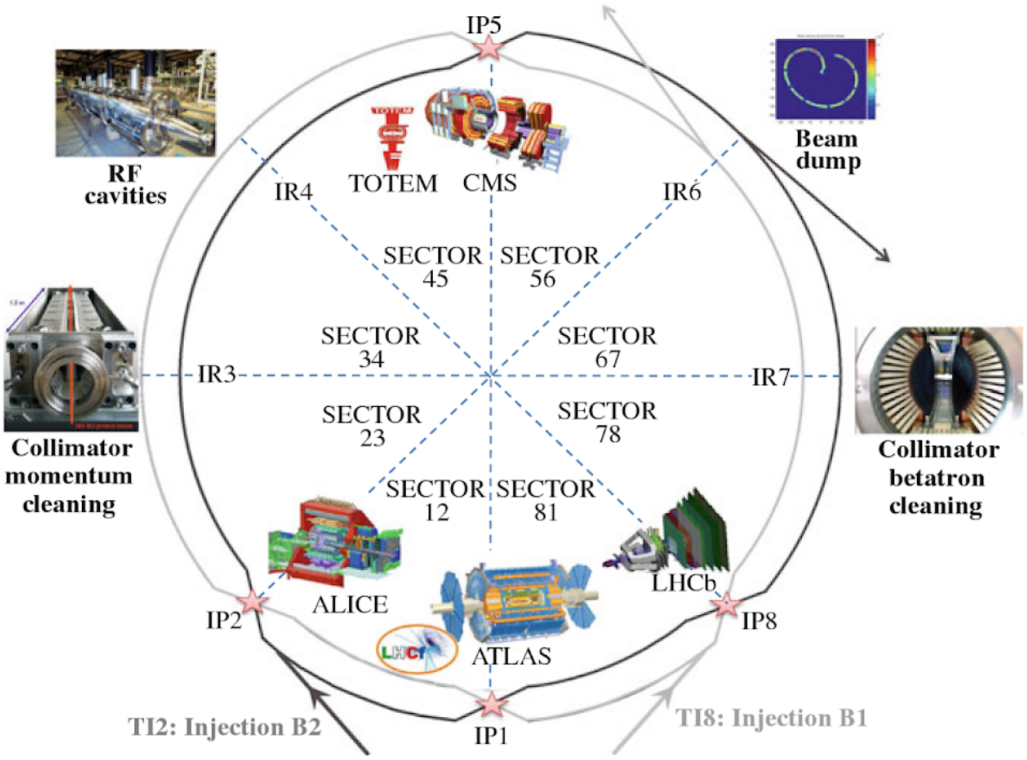

Figure 3.1: Schematic illustration of the geometry of the LHC. For simplicity the LHC is displayed as a circle, however, from one sector to another a straight section is in existence while within each sector an arc is implemented. [23]

cold enough to stay superconducting they are housed in a cryostat. The maximum magnetic field strength is 8.3 T and corresponds to a beam energy of 7 TeV. The injection of the beams occurs at *IP2* and *IP8* where the *Super Proton Synchrotron* (SPS) provides protons of the energy of 450 GeV. A proton beam is divided into 2808 bunches including a nominal number of 1.2×10^{11} protons each. The distance between two bunches is 25 ns.
The instantaneous luminosity L of the LHC is an important quantity that relates the cross section σ_{Process} of a process with the particle rate $\dot{N}_{\text{Events}}$ expected in the proton-proton collisions due to the process. This relation can be expressed via

$$\dot{N}_{\text{Events}} = L\sigma_{\text{Process}}. \tag{3.1}$$

Knowing the exact value of the luminosity L is thus indispensable. For beams with a Gaussian spatial transverse particle distribution the luminosity can be expressed as

$$L = \frac{N_1 N_2 f_{\text{rev}} n_{\text{b}}}{2\pi\sqrt{\sigma_{1x}^2 + \sigma_{2x}^2}\sqrt{\sigma_{1y}^2 + \sigma_{2y}^2}} \cdot F \cdot W. \tag{3.2}$$

N_1 and N_2 are the number of protons in the n_{b} colliding bunches. f_{rev} stands for the revolution frequency in the ring and σ_{1x} and σ_{2x} (σ_{1y} and σ_{2y}) are the transverse beam sizes at the interaction point in the horizontal (vertical) plane for beam 1 and beam 2. F is a luminosity reduction factor describing the effect of a finite crossing angle of the two beams at the interaction point. Due to the large number of stored bunches and the small bunch distance the beams can not be collided head on since this would lead to many secondary collisions upstream and downstream of

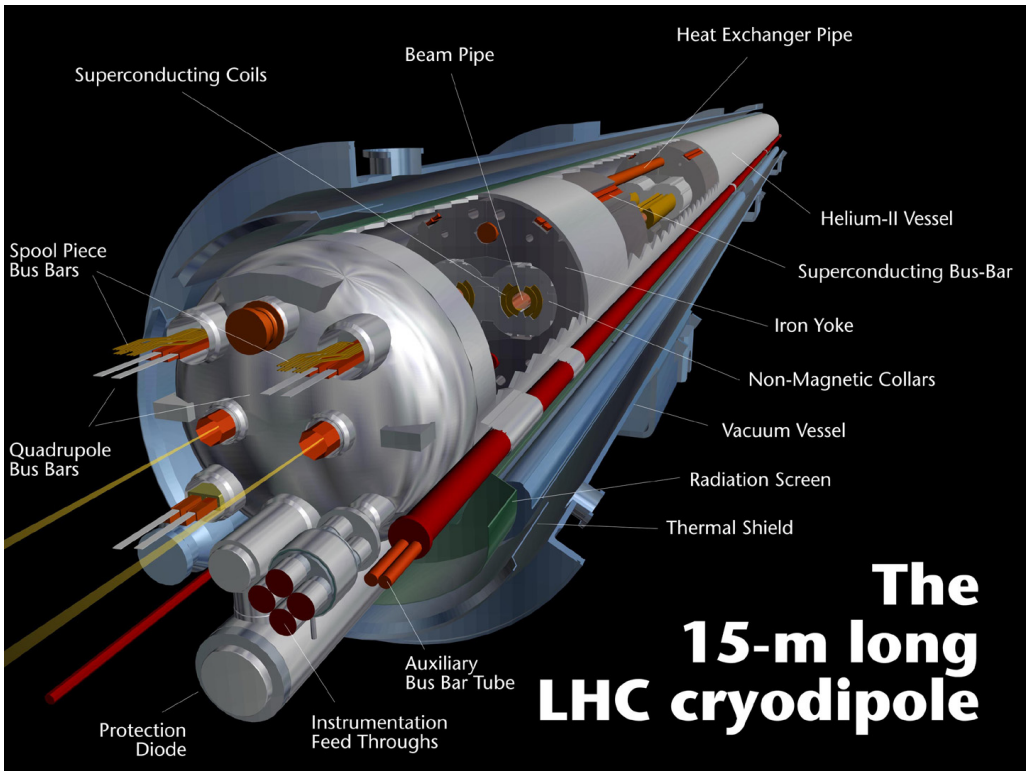

Figure 3.2: Schematical view of the superconducting dipole magnets of the LHC. [59]

the interaction point. This would also have a negative effect on the beam stability as well as the quality of the detector data analysis. Instead, the beams are crossed resulting in an angle ϕ between the two beams. The reduction factor F depends on this finite crossing angle as well as on the bunch length σ_s and the transverse beam sizes in the plane of crossing as mentioned above. These quantities define the reduction factor F according to

$$F = \frac{1}{\sqrt{1 + 2\frac{\sigma_s^2}{\sigma_{1x}^2 + \sigma_{2x}^2} \tan^2 \frac{\phi}{2}}}. \tag{3.3}$$

W is a reduction factor as well and describes a technical possibility to manually reduce the luminosity. This becomes relevant as soon as the luminosity at one of the interaction points at the LHC is too high to be handled by the corresponding detector. W can be expressed via

$$W = e^{\frac{-(d_1 - d_2)^2}{2(\sigma_1^2 + \sigma_2^2)}}. \tag{3.4}$$

d_1 (d_2) are the distances with respect to the nominal beam line and σ_1 (σ_1) are the beam sizes of beam 1 (beam 2) each in the direction of the beam offset. The reduction of the luminosity according to W can be achieved via an automatic accelerator-experiment real-time feedback system. The experiment has to compute and monitor the instantaneous luminosity which is communicated to an LHC application that adjusts the beam overlap at the interaction point accordingly. This is known as "luminosity levelling" and has to be applied for the detectors ALICE and LHCb. In case of ATLAS and CMS the detectors were able to handle the instantaneous luminosity achieved in the data taking periods from 2015 and 2016 without using

the luminosity leveling. In 2017, however, due to the higher instantaneous luminosity these two experiments had to use the luminosity leveling as well.

3.2 The ATLAS Detector

ATLAS (**A** **T**oroidal **L**HC **A**pparatu**S**) is a multi-purpose experiment covering extensive physics goals for which the ATLAS detector has been designed. The goal was to design the detector to cover the full solid angle so that also particles traversing the detector under a shallow angle with respect to the beam line can be detected. In order to achieve this, the ATLAS detector has a cylindric shape with a barrel and two end-cap sections. It has a width of 44 m, a diameter of 22 m and weighs 7000 t. The ATLAS detector is constructed onion-like with different detector components wrapping up the interaction point like layers. The inner most detector component is the tracking system embedded in a magnetic field. The next layer is the electromagnetic calorimeter followed by the hadronic calorimeter. The outer most detector component is the muon spectrometer. Figure 3.3 shows which components of the ATLAS detector are responsible for the detection of different particles. As can be

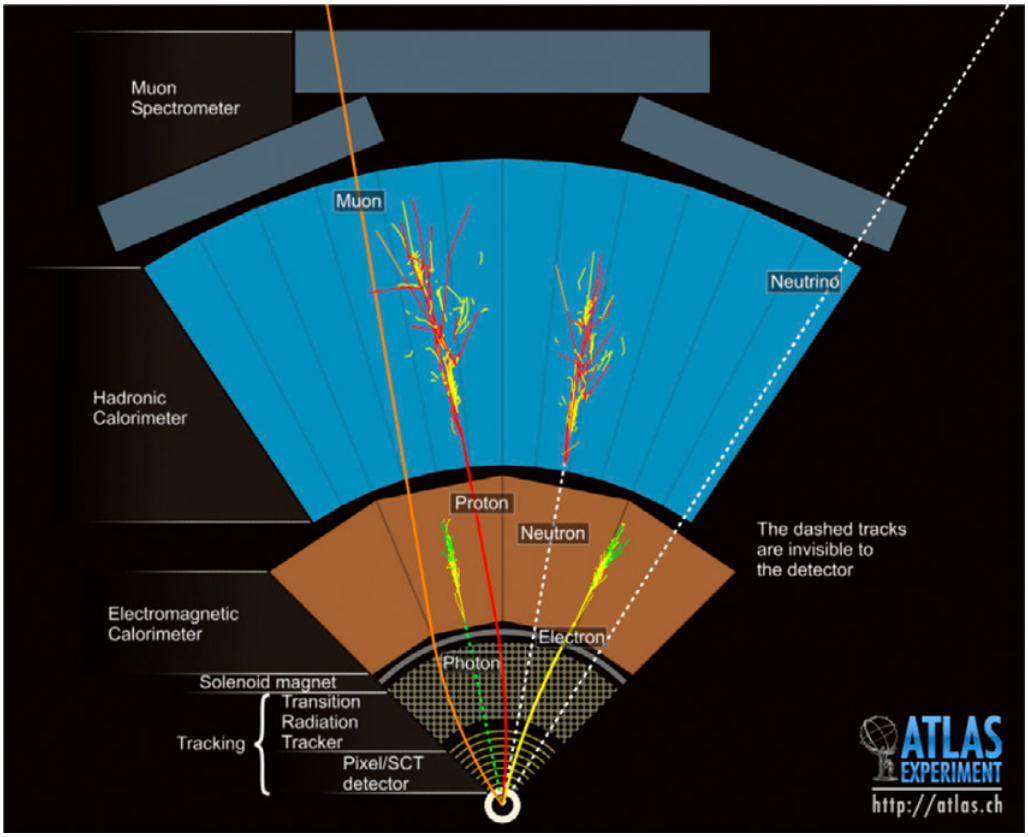

Figure 3.3: Illustration of the various components of the ATLAS detector and of different particle signatures as they manifest themselves in the detector. [60]

seen the tracking system can only detect charged particles. In the following component, the electromagnetic calorimeter, photons and electrons are detected via their cluster depositions. Hence, in the ATLAS detector, an electron can be defined as a track with a matching electromagnetic cluster while a photon can be defined as an electromagnetic cluster without a matching track. In the hadronic calorimeter

hadrons are detected. A charged hadron like the proton would be seen in the ATLAS detector as a track with a matching hadronic cluster. A neutral hadron like the neutron, in contrast, would be seen as a hadronic cluster without a matching track. The outer most component is especially constructed to detect muons. Since muons are minimum ionizing particles they only leave very small signatures in the calorimeters. However, a track would be seen in the tracking system as well as in the muon spectrometer. There are also particles like neutrinos that can not be detected by any detector component. It is only possible to calculate the missing transverse momentum as will be shown later. Figure 3.4 shows the full geometry of the ATLAS detector with all its components. The overall design of the ATLAS detector

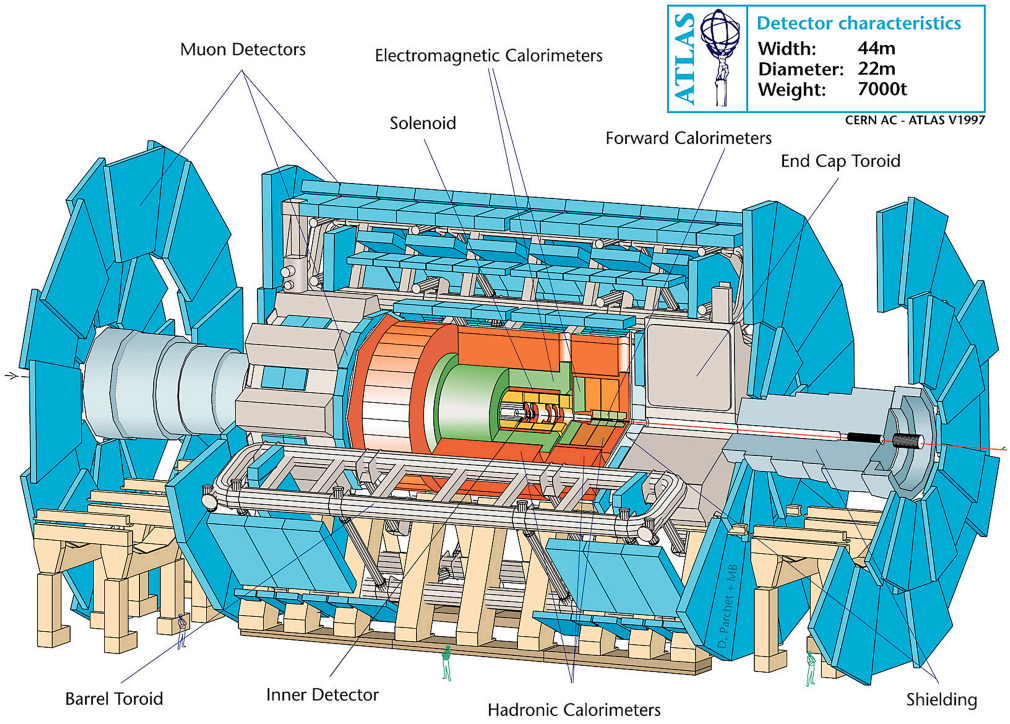

Figure 3.4: Layout of the ATLAS Detector. [61]

is driven by the magnetic field used to bend charged particles, especially muons, and thus enabling the measurement of their momenta. The momentum resolution is proportional to $B^{-1}L^{-2}$, where B is the strength of the magnetic field and L is the distance from the interaction point to the muon momentum measurement. The optimal momentum resolution can thus be achieved by choosing a strong magnetic field B or a long lever arm L or both. ATLAS approaches the momentum measurement with a large lever arm and a moderate magnetic field. CMS (**C**ompact **M**uon **S**olenoid) in contrast chose to build a small detector with a strong magnetic field. The magnetic field of the CMS detector is a solenoidal field with a strength of 3.8 T. The advantage of this kind of magnetic field is a large homogeneity inside the solenoid magnet. The disadvantage is the limited size due to cost reasons. The magnetic field of the ATLAS detector is a combination of a toroidal magnetic field of about 1 T for the muon spectrometer and a solenoidal magnetic field of about 2 T for the tracking system. A toroidal magnetic field has the advantage that the magnetic field is always perpendicular to the particle trajectories which simplifies the calculation of momentum. On the other hand a toroidal field is rather non-uniform

which complicates the reconstruction of the trajectories. However, the usage of two magnetic fields in the ATLAS detector allows for a larger size which is beneficial for the momentum measurement.

3.2.1 The ATLAS Coordinate System

In order to describe the space and positions of objects in the ATLAS detector, a coordinate system is needed. The interaction point is defined as the origin of the coordinate system. The z axis points along the beam line while the x-y plane is perpendicular to the beam line. The x-y plane is referred to as the "transverse plane" in the following. The x axis points from the interaction point to the center of the LHC ring while the y axis points upwards to the surface of the earth. Since the ATLAS detector has a cylindrical design it is useful to introduce cylindrical coordinates. The transverse plane is therefore described in terms of r-ϕ coordinates where r measures the distance from the beam line and ϕ denotes the azimuthal angle measured from the x axis around the beam line. The polar angle θ is defined from the positive z axis. Usually the polar angle is given in terms of the pseudo-rapidity η. The pseudo-rapidity is a massless approximation based on the rapidity y which is defined for a particle with energy E and longitudinal momentum $p_{\mathrm{L}} = |\boldsymbol{p}| \sin\theta$ along the beam as

$$y = \frac{1}{2} \ln \frac{E + p_{\mathrm{L}}}{E - p_{\mathrm{L}}}. \tag{3.5}$$

For massless particles the energy-momentum relation reduces to $E = |\boldsymbol{p}|c = |\boldsymbol{p}|$ with $c = 1$ as stated in chapter 2. In case the energies of particles produced in the collisions at the LHC are much smaller than their rest energies determined by their rest masses one can use this relation to approximate the pseudo-rapidity via

$$y \approx \eta = \frac{1}{2} \ln \frac{|\boldsymbol{p}| + p_{\mathrm{L}}}{|\boldsymbol{p}| - p_{\mathrm{L}}} = -\ln \tan\left(\frac{\theta}{2}\right). \tag{3.6}$$

At hadron colliders the usage of rapidity as well as the pseudo-rapidity is motivated by the fact that rapidity intervals Δy and differential cross sections $\frac{\mathrm{d}\sigma}{\mathrm{d}y}$ are Lorentz invariant under a boost along the beam direction. Furthermore, the particle density in inelastic proton-proton collisions is approximately constant when measured in equal rapidity intervals. Therefore, the components of the ATLAS detector are typically segmented in such intervals. The coordinate system of the ATLAS detectors with exemplary values of the pseudo-rapidity η is shown in figure 3.5.

3.2.2 Tracking Detectors

The tracking detectors are the first detectors that are encountered by particles emerging from the interaction point. The task of these detectors is the measurement of the particle trajectories to provide a precise reconstruction of the tracks of the particles. Also the measurement of the vertices of the particles as well as the impact parameters needs to be performed by the tracking detectors. The design and number of layers of the tracking system is a trade-off between the performance of the tracking detectors, the amount of material and the cost. For one thing, many layers result in a larger number of hits and thus increase the performance. However, many layers also increase the amount of material which cause enhanced effects of

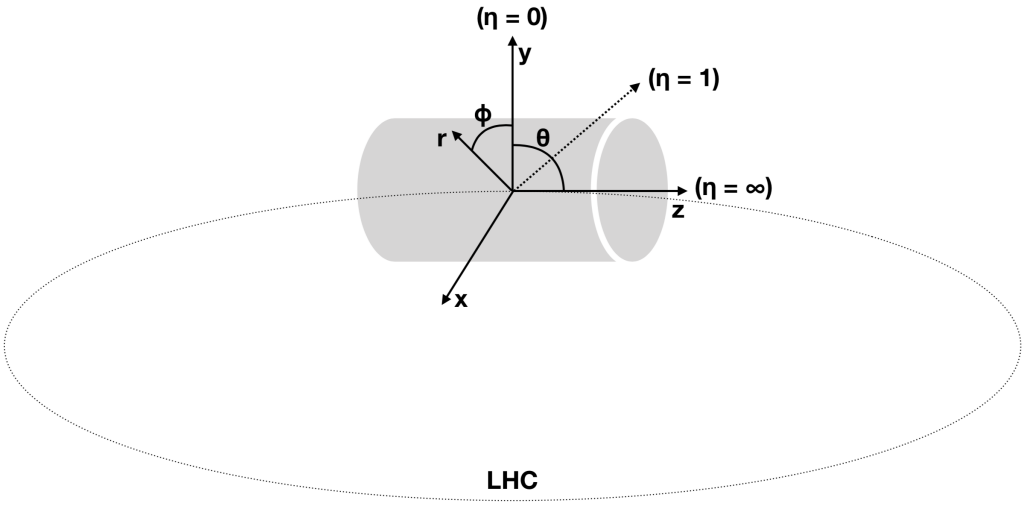

Figure 3.5: Coordinate System of the ATLAS detector.

multiple scattering and energy looses of the particles. The tracking system of the ATLAS detector [62] is divided in the subsystems IBL, Pixels, SCT and TRT as can be seen in figure 3.6.

IBL (Insertable B-Layer)
The IBL is the inner most tracking detector and is build around the beam pipe with a distance of 33 mm to the nominal beam line. The beam pipe itself has a radius of 22.5 mm. Most of the ATLAS tracking detectors are based on silicon pixel sensors. The silicon is doped such that it works like a diode. When operated in reverse-bias mode charged particles cause an ionization current that can be detected. The IBL consists of silicon pixel sensors based on two different technologies. A planar pixel technology is used in the barrel region while a 3D technology is used in the end-cap region. The size of the pixel sensors in the barrel (end-cap) region is $50 \times 250\,\mu\text{m}^2$ in r-$\phi \times z(r)$. The spatial resolution of the IBL in the barrel and end-cap region is $10\,\mu$m in the r-ϕ plane. In the $z(r)$ direction the spatial resolution is $75\,\mu$m in the barrel (end-cap) region. The silicon pixel sensors are arranged concentrically around the beam pipe and provide 12 million readout channels. The IBL allows a full coverage in ϕ and a coverage in $|\eta|$ of up to 2.9.

Pixel Detector
The pixel detector is located around the IBL ranging from a distance of 5.1 cm up to 12.3 cm in distance from the beam pipe. Like the IBL the pixel detector consists of sensors out of silicon segmented into cells with a size of $50 \times 400\,\mu\text{m}^2$. The value of $50\,\mu$m relates to the r-ϕ plane and the value of $400\,\mu$m relates to the $z(r)$ direction in the barrel (end-cap) region. A pixel cell also consists of a readout chip which is the limitation of the cell size since the area is required for the front-end electronics. The spatial resolution of the ATLAS pixel detector in the barrel and end-cap region is $10\,\mu$m in the r-ϕ plane. In the $z(r)$ direction the spatial resolution is $115\,\mu$m in the barrel (end-cap) region. The pixel cells are arranged into three concentric layers in the barrel and in form of discs in the end-caps such that three hits can be recorded for each particle trajectory. The entire pixel detector consists of 80 million readout channels and provides a full coverage in ϕ and a coverage of up to 2.5 in $|\eta|$.

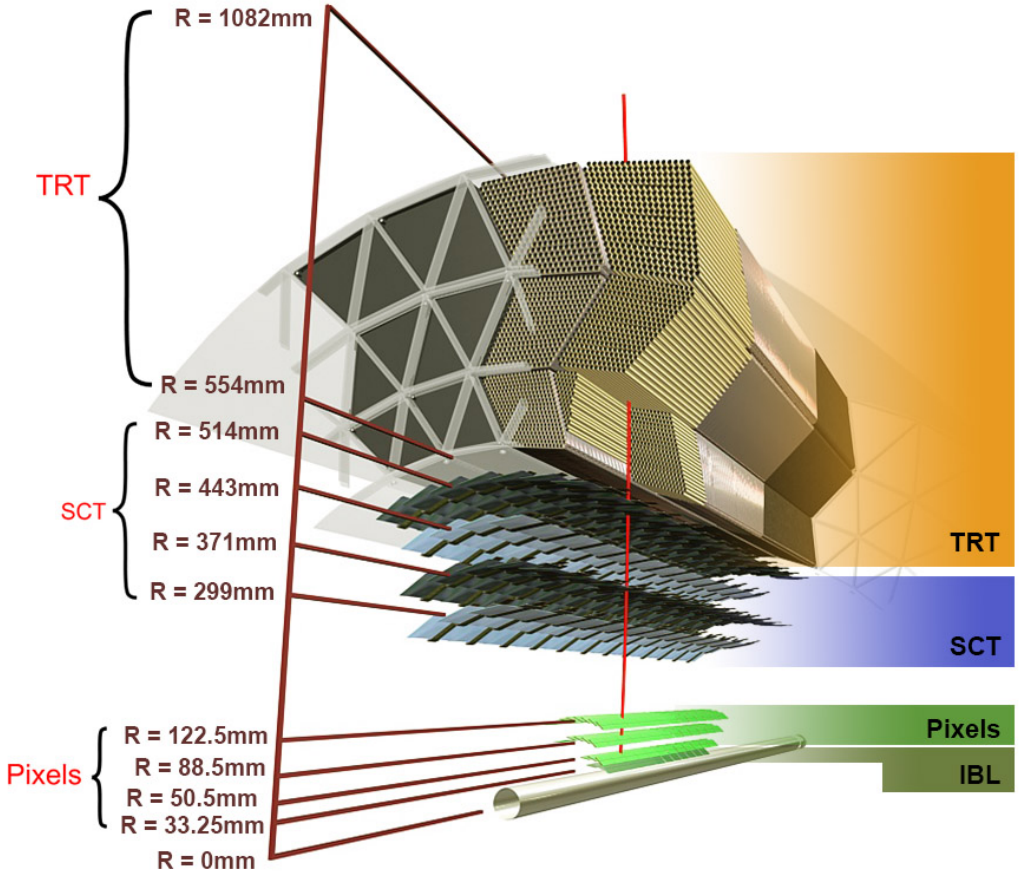

Figure 3.6: Schematic view of the ATLAS tracking detectors. [63]

SCT (Semiconductor Tracker)
The SCT surrounds the pixel detector ranging from a distance of 30 cm up to 51 cm from the beam pipe. The SCT consists of silicon sensors with a pitch of 80 μm. The sensors are arranged back to back and are rotated to each other by an angle of 40 mrad which enables a better measurement of the r-ϕ coordinate as well as the z and r coordinate in the barrel and the end-cap region, respectively. The spatial resolution of the SCT in the barrel and end-cap region is 17 μm in the r-ϕ plane. In the $z(r)$ direction the spatial resolution is 580 μm in the barrel (end-cap) region. In the barrel region the SCT consists of four concentric layers equipped with SCT modules on both sides. Hence, a maximum of eight hits can be recorded. In the end-cap region the SCT consists of nine single-sided equipped layers which enables to record up to nine hits. The entire SCT consists of 6.2 million readout channels and provides a full coverage in ϕ and a coverage of up to 2.5 in $|\eta|$.

TRT (Transition Radiation Tracker)
The TRT is the outer most tracking detector and ranges from a distance of 55 cm up to around 1.1 m in distance from the beam pipe. It consists of gas-filled straw tubes with a diameter of 4 mm and a central wire of 30 μm in diameter. The maximum length of the straws is 144 cm. The tubes are filled with a gas mixture of 70 % Xe, 27 % CO_2 and 3 % O_2. In the barrel region the straws are divided in two halves in the center and read out at both ends in order to reduce occupancy. In the straw

tubes a drift-time measurement is performed which provides an intrinsic spatial resolution of $< 120\,\mu$m for the r-ϕ coordinate. The spaces between the straw tubes are filled with polymer fibres, a radiator in which relativistic charged particles produce transition radiation when crossing from one medium into another medium with a different refraction index. The transition radiation photons will be absorbed in the straw tubes and produce large signals. In order to distinguish between ionisation in the gas due to charged particles and transition radiation due to photons the readout electronics of the TRT provide two thresholds. The lower threshold detects signals from ionization while the higher threshold detects the transition radiation which can be used as an additional information to identify particles. Overall the TRT consists of 0.3 million readout channels and up to 35 hits can be recorded. The TRT allows a full coverage in ϕ and a coverage in $|\eta|$ of up to 2.0.

3.2.3 Calorimetry Detectors

The calorimeter system is used to determine the energy and the momentum direction of electrons, photons and hadrons produced at the interaction point or produced as decay products of unstable particles. The ATLAS calorimeter system [64] consists of an electromagnetic calorimeter and a hadronic calorimeter and can be seen in figure 3.7. In order to optimize the energy resolution both calorimeter types are build in such a way that the electromagnetic and hadronic shower of a particle are fully contained in the corresponding calorimeter. In the energy reconstruction the material between the interaction point and the calorimeter system is taken into account since the shower of a particle can already start in the tracking system.

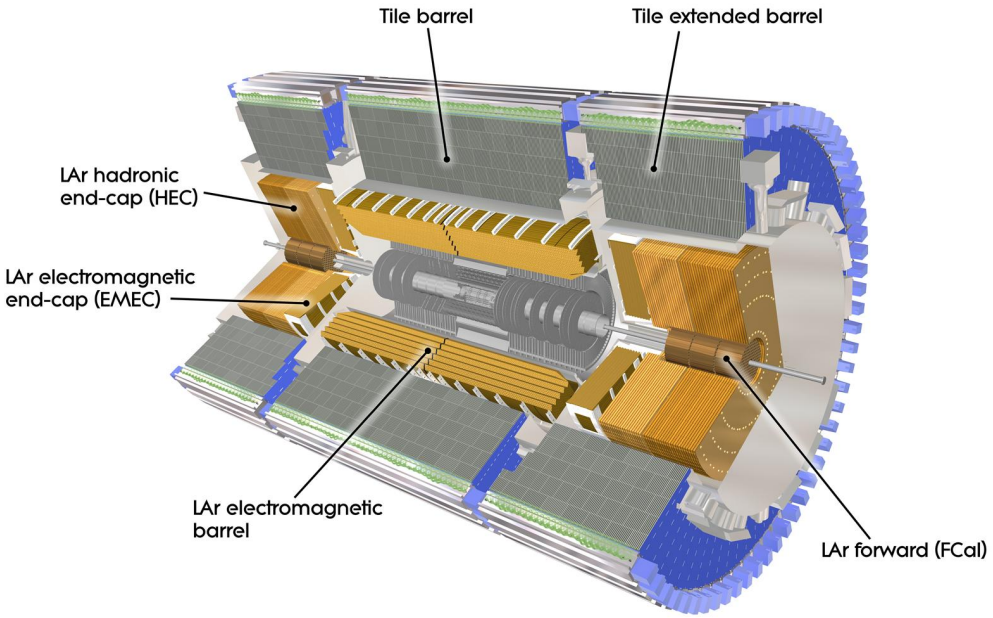

Figure 3.7: Schematic view of the ATLAS calorimetry detectors. [65]

The relative energy resolution $\frac{\Delta E}{E}$ of the calorimeters can be described by a stochastic coefficient c_s, a noise coefficient c_n and constant coefficient c_c via

$$\left(\frac{\Delta E}{E}\right)^2 = \left(\frac{c_s}{\sqrt{E}}\right)^2 + \left(\frac{c_n}{E}\right)^2 + (c_c)^2 . \tag{3.7}$$

The stochastic term describes the relative energy resolution due to fluctuations in the number of particles produced in the shower in the calorimeter. This number is proportional to the energy E. Thus the relative energy resolution due to this stochastic source is proportional to $\frac{1}{\sqrt{E}}$. The noise term describes the relative energy resolution due to the noise of the readout electronics of the detector which is independent of the deposited energy. Hence, a term proportional to $\frac{1}{E}$ appears. The remaining constant term describes the relative energy resolution due to different sources like shower tails that are not captured by the calorimeter, inhomogeneities of the detector, limited inter-calibration of detector segments and non-linearities in the signal response. Thus, the constant term limits the relative energy resolution at high energies. The resolution parameters c_s, c_n and c_c are all optimized in the design of the calorimeters.

Electromagnetic Calorimeters
The electromagnetic calorimeter system of the ATLAS detector consists of a barrel calorimeter (EMB) and an end-cap calorimeter (EMEC). Both electromagnetic calorimeters use a sampling technology for the measurement of the particle showers. The EMB and the EMEC use liquid argon (LAr) as active material and lead (Pb) as passive absorber material. The ionisation signal in the LAr volume due to a particle shower is proportional to the energy deposit and is read out in up to three layers via finely segmented electrodes. The first layer has a segmentation of 0.003×0.1 in $\eta \times \phi$ space. The very fine η segmentation provides a possibility to separate photons and pions and enables a photon direction measurement. The second layer has a segmentation of 0.025×0.025 in $\eta \times \phi$ space. Most of the shower energy is collected in this layer. The third layer has a segmentation of 0.05×0.025 in $\eta \times \phi$ space and is used to correct for leakage behind the electromagnetic calorimeters. Additionally, before the first layer of the electromagnetic calorimeters a thin presampler layer is located and used to correct for the energy loss upstream the calorimeter. The number of readout channels of the EMB is around 110 thousand. The EMEC has around 64 thousand readout channels. Both electromagnetic calorimeters uniformly cover the full ϕ region. The $|\eta|$ region is covered up to 1.475 by the EMB and from 1.375 to 3.2 by the EMEC. Both electromagnetic calorimeters have a radiation length $X_0 > 20\,\mathrm{gcm}^{-2}$ which ensures that the full electromagnetic showers are mostly covered. The resolution parameters of the EMB and EMEC have been measured to be around $c_s = 10\,\%\sqrt{\mathrm{GeV}}$ and $c_c = 0.7\,\%$. The noise term c_n of the electromagnetic calorimeters ranges from 10 to 50 MeV.

Hadronic Calorimeters
The hadronic calorimeter system of the ATLAS detector consists of a tile calorimeter in the barrel region and an end-cap calorimeter (HEC). Similarly to the electromagnetic calorimeters both hadronic calorimeters are designed as sampling calorimeters as well. The tile calorimeter uses scintillator as active material and iron plates as passive absorber material. The HEC uses LAr as active material and copper (Cu) as

passive material. The number of readout channels of the tile calorimeter is around 10 thousand. The HEC has around 5.6 thousand readout channels. Both hadronic calorimeters uniformly cover the full ϕ region. The $|\eta|$ region is covered up to 1.7 by the tile calorimeter and from 1.5 to 3.2 by the HEC. The energy resolution of the hadronic calorimeters due to the stochastic term is much lower than for the electromagnetic calorimeters. The reason for this is that hadronic showers usually involve a hadronic component, an electromagnetic component and a component consisting of muons and neutrinos. The latter component can not be detected by the hadronic calorimeter. This makes it more difficult to determine the number of particles in the hadronic shower compared to an electromagnetic shower and hence leads to a worse energy resolution. The resolution parameter c_s of the tile calorimeter and HEC have been measured to be around $52\,\%\sqrt{\text{GeV}}$ and $84\,\%\sqrt{\text{GeV}}$ respectively. The constant term of the hadronic calorimeters is around $c_c = 3\,\%$. The noise term of the tile calorimeter is around $c_n = 1.6\,\text{GeV}$ and ranges from 100 to 500 MeV for the HEC.

Forward Calorimeters
The forward calorimeters of the ATLAS detector consist of an electromagnetic part in the front and a hadronic part in the back. The intention of the hadronic part is a reduction of the lateral shower width. A sampling technology is used to measure the showers of the particles. The active material of the forward calorimeters is LAr. The passive absorber material is Cu in the electromagnetic part and tungsten (W) in the hadronic part. The electromagnetic part has around 2 thousand readout channels, the hadronic part around 1.5 thousand readout channels. The forward calorimeters uniformly cover the full ϕ region and the $|\eta|$ region from 3.1 to 4.9. The radiation length of the forward calorimeters is similar to the one of the electromagnetic calorimeters. The resolution parameters of the electromagnetic part are around $c_s = 28.5\,\%\sqrt{\text{GeV}}$ and $c_c = 3.5\,\%$. The resolution parameters of the hadronic part are around $c_s = 94\,\%\sqrt{\text{GeV}}$ and $c_c = 7.5\,\%$. The noise term of the forward calorimeters ranges from 100 to 500 MeV.

3.2.4 Muon Spectrometer

The ATLAS muon spectrometer is the outermost detector component and has the task to record the trajectories of muons. However, since a muon in a hadron environment is a clean signature for almost all discovery physics, the ATLAS muon spectrometer also has the task to trigger such events. The muon spectrometer of the ATLAS detector consists of the four different subsystems RPC (resistive-plate chamber), TGC (thin-gap chamber), MDT (monitored drift tubes) and CSC (cathode-strip chamber) [66]. Recording the particle tracks is done by the MDT and CSC while the RPC and TGC are used for triggering. Therefore the MDT and CSC are optimized for a good momentum resolution while the RPC and TGC are optimized for a fast response time. A schematic illustration of all subsystems can be seen in figure 3.8.

RPC and TGC
Both the RPC and TGC are gaseous detectors which detect muons via the ionization of the gas. The RPC consists of parallel arranged plates implementing electrodes made from a material with a high volume resistivity between 10^7 and 10^{12} Ωcm.

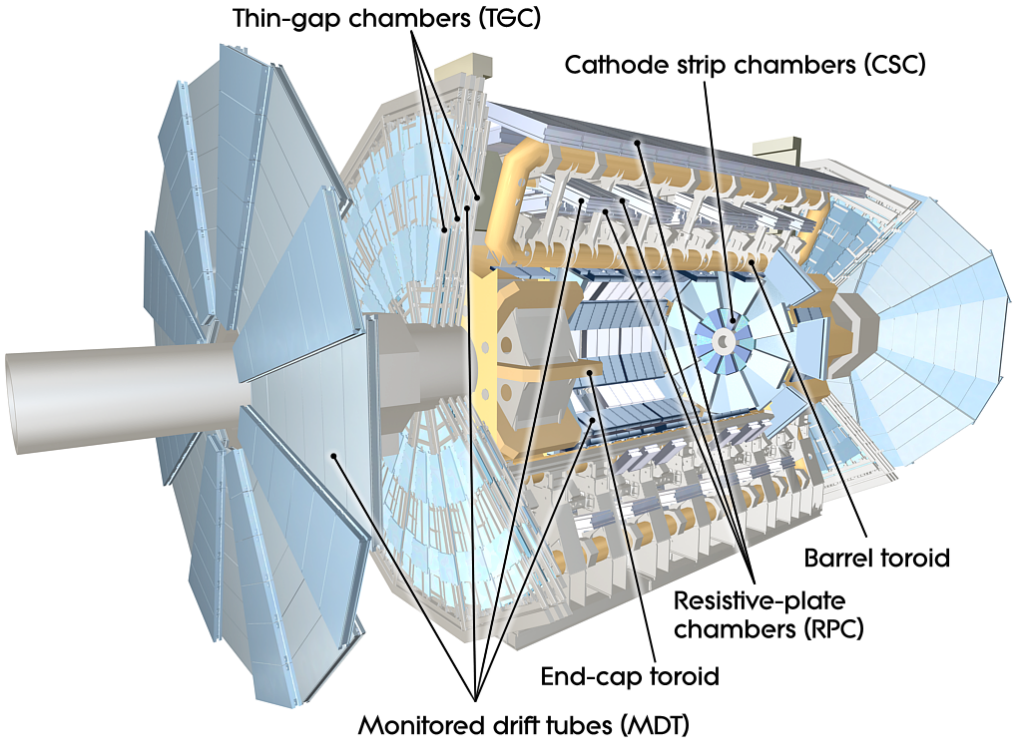

Figure 3.8: Schematic view of the components of the ATLAS muon spectrometer. [67]

The gas in the chambers of the RPC is a mixture of C_2H_2, F_4, C_4H_{10} and SF_6. The TGC is a multi-wire proportional chamber with a smaller wire-cathode gap than the wire-wire gap. The gas in the chambers of the TGC is a mixture of CO_2 and n-pentane. Both detectors cover the full ϕ space while the RPC covers the barrel region ($|\eta| < 1.05$) and the TGC covers the end-cap region ($1.05 < |\eta| < 2.4$).

MDT and CSC
The MDT is based on drift tubes which are gas-filled tubes containing a central wire. A muon ionizes the gas along their path and the created electrons drift to the wire where they experience a gas amplification close to the wire. The signal is then read out at both ends of the tubes. The CSC uses a more complex system based on arrays of anode wires crossed with copper cathode strips within a gas volume. This allows a 3D coordinate measurement. The gas volume of both, the MDT and CSC, is based on a mixture of Ar and CO_2. The CSC is especially useful at high rates or inhomogeneous B fields which is the case at high $|\eta|$ regions. Therefore the CSC covers the $|\eta|$ region between 2.0 and 2.7 while the MDT covers this region up to 2.0. Both detectors allow a full coverage of the ϕ space. In total the system of MDT and CSC provides 70 thousand channels allowing a spatial resolution of 60 μm.

3.2.5 Trigger and Data Acquisition System (TDAQ)

Since the LHC provides a bunch-crossing rate of about 40 MHz the raw data stream of the ATLAS detector reaches approximately 300 GByte/s. Hence, the storage of the entire raw data is impossible. In addition most of the interesting physics

processes have cross sections several orders of magnitude smaller than the inelastic proton-proton cross section. Therefore, a trigger system has been designed to only filter out events with interesting physics processes. The ATLAS trigger system is based on physics objects like electrons, photons, muons, hadronically decaying τ leptons, jets and missing transverse momentum (see section 3.3). As soon as these physics objects pass a certain threshold in transverse momentum p_{T} this indicates an interesting process. Weakly interacting particles, like neutrinos, can be triggered via missing transverse momentum. The trigger system of the ATLAS detector consists of two stages, the Level-1 trigger [68] and the High Level Trigger (HLT) [69]. The data acquisition (DAQ) system manages the data streams from the trigger system up to the data storage of the accepted events. A schematic connection of the Level-1 trigger, the HLT and the DAQ system can be seen in figure 3.9 and will be explained in the following.

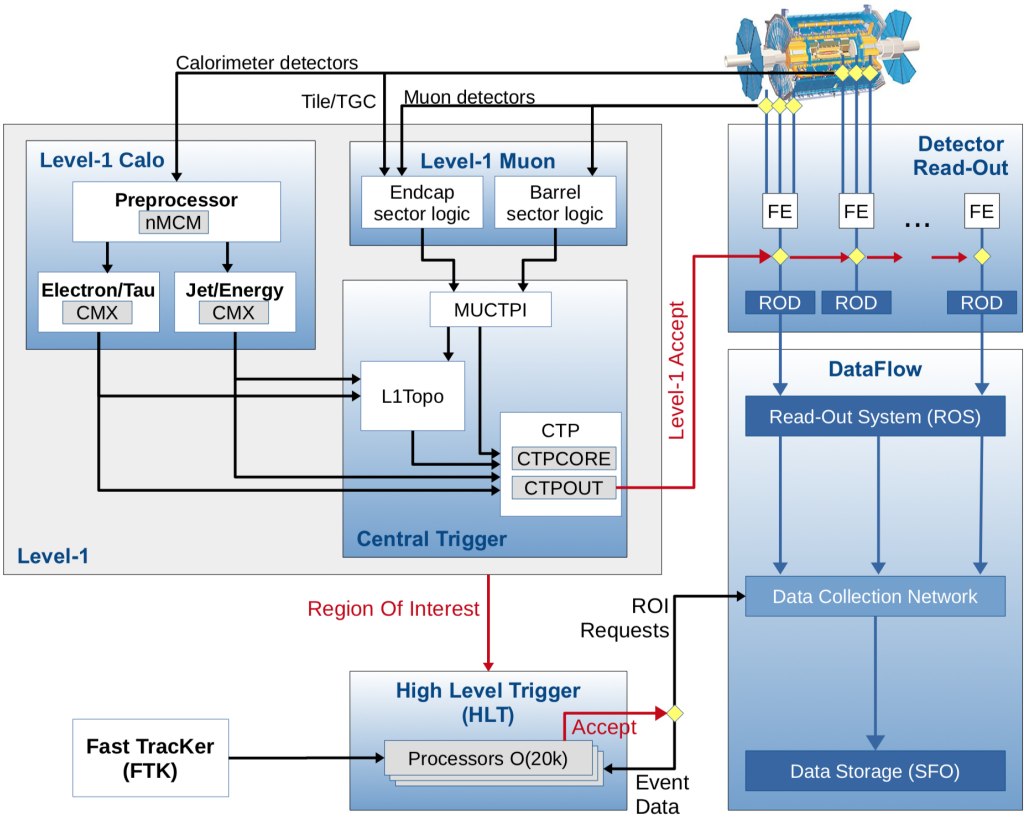

Figure 3.9: Schematic view of the ATLAS trigger system. [70]

Level-1 Trigger

The Level-1 trigger is a hardware-based system using custom electronics to process the signals recorded in the ATLAS detector. It consists of the three components *Level-1 Calo*, *Level-1 Muon* and *Central Trigger*. The Level-1 Calo has a cluster processor identifying electron and photon as well as hadron and tau candidates. The transverse momenta of these candidates can be discriminated against different thresholds. Similarly, there is a jet/energy processor which identifies jet candidates and discriminates their transverse momenta against different thresholds. The jet/energy processor also evaluates global energy sums like the missing transverse momentum. The information about the identified candidates are sent to the

Central Trigger. The Level-1 Muon checks for hit coincidences within a track in different stations of the muon spectrometer and identifies muon candidates. It can also discriminate the transverse momenta of the muon candidates against different thresholds and sends the information to the Central Trigger as well. The Central Trigger includes a trigger menu which is a set of triggers with different requirements on the events. Based on the information of the Level-1 Calo and the Level-1 Muon the Central Trigger creates a *Level-1 Accept* signal which is a "logical or" of all triggers from the trigger menu. For the Level-1 Accept signal the Level-1 trigger has a decision time of 2.5 μs. During this time all the event data is kept in the memories of the *Front-End Electronics (FE)* of the sub-detectors. Only if the Level-1 trigger accepts the event the data is transferred to the *Read Out System (ROS)*. The Level-1 trigger also builds a *Region Of Interest* (ROI) based on the trigger and the η and ϕ coordinates of the objects which caused the Level-1 Accept signal. The LHC bunch-crossing rate of about 40 MHz is reduce to about 100 kHz by the Level-1 trigger.

HLT
The HLT is a software-based system using sophisticated selection algorithms. The software algorithms can reject the event at any stage in the decision process. In such a case, the event data stored in the *Data Collection Network* is deleted. At a first stage the HLT requests event data from the Data Collection Network identified from the ROI. In contrast to the Level-1 trigger the HLT uses the full granularity detector information in the ROI enabling the highest precision. Additionally information from the tracking detectors are used. In case of an accept signal at this stage, a second stage reconstructs the full event using all available detector information. The fully reconstructed event with a mean size of around 1.6 MB is then sent to the *Data Storage*. For its decision the HLT has a processing time of about 200 ms. The Level-1 rate of 100 kHz is reduced further to about 200 Hz by the HLT.

All the data stored at the Data Storage is further processed in the LHC Computing Grid [71, 72]. The Grid is a network of different computing clusters all around the world divided in the categories Tier-0, Tier-1, Tier-2 and Tier-3. The CERN computing center is the only Tier-0 cluster and applies reconstruction and calibration algorithms to the data. Additional processing power can be requested from the Tier-1 clusters which also serve as storage space for the data. The product of the processing so far is the primary physics analysis format called Analysis Object Data (AOD). The Tier-2 clusters are mainly used for Monte-Carlo production but also provide processing power for physics analysis. From the AOD analysis specific files can be derived for the data and the Monte-Carlo simulations called DAOD. These files can be analyzed with the ROOT framework [73] and are usually stored at the Tier-3 clusters, such as the *mainzgrid*, where the physics analyses are performed.

3.2.6 Luminosity Measurement

In order to measure the cross section of a physics process via the number of recorded events of this process the recorded luminosity integrated over the data-taking period is used. Therefore equation 3.1 needs to be integrated over time such that the particle rate $\dot{N}_{\text{Events}}$ becomes a number of particles N_{Events} and the instantaneous luminosity

L transforms into an integrated luminosity $L_{\text{Int}} = \int L \mathrm{d}t$. This gives the relationship

$$N_{\text{Events}} = L_{\text{Int}} \sigma_{\text{Process}}. \tag{3.8}$$

Hence, when investigating cross sections the integrated luminosity recorded by the ATLAS detector needs to be estimated as described in the following. Since the instantaneous luminosity varies with time, it needs to be measured in real-time during data-taking. At the LHC the luminosity can either be determined from the beam parameters or by using a reference physics process with a theoretically well-known cross section which is calculable to a high precision. According to equation 3.2 the following proportionality of the average instantaneous luminosity L is given:

$$L \propto \frac{W}{2\pi \sqrt{\sigma_{x1}^2 + \sigma_{x2}^2} \cdot \sqrt{\sigma_{y1}^2 + \sigma_{y2}^2}}. \tag{3.9}$$

σ_{x1}^2, σ_{x2}^2, σ_{y1}^2 and σ_{y2}^2 are the Gaussian widths of the transverse profiles of the two beams. W is the luminosity reduction factor as described by equation 3.4. Denoting $\rho_1(x, y)$ and $\rho_2(x, y)$ as the transverse particle densities of beams 1 and beam 2 expression 3.9 can be derived from the overlap integral $\Omega(\rho_1, \rho_2)$ as follows:

$$L \propto \Omega(\rho_1, \rho_2) = \int \rho_1(x, y) \rho_2(x, y) \mathrm{d}x \mathrm{d}y. \tag{3.10}$$

The overlap integral $\Omega(\rho_1, \rho_2)$ can be measured at the interaction point of the ATLAS detector via the van der Meer method [74]. This method exploits that the luminosity varies when one of the beams is displaced by b_x and b_y in x and y direction respectively. Due to the normalization of the beam particle densities it is ensured that

$$\int \rho_1(x, y) \rho_2(x + b_x, y + b_y) \mathrm{d}x \mathrm{d}y \mathrm{d}b_x \mathrm{d}b_y = 1 \tag{3.11}$$

when variations in z direction and in time t are neglected. Therefore, only a particle rate $R(b_x, b_y) \propto L(b_x, b_y)$ needs to be measured in order to determine the overlap integral via

$$\Omega(\rho_1, \rho_2) = \frac{R(b_x = 0, b_y = 0)}{\int R(b_x, b_y) \mathrm{d}b_x \mathrm{d}b_y}. \tag{3.12}$$

A luminosity measurement via the van der Meer method needs special running conditions that are different from the nominal data-taking conditions. In these special runs the luminosity is measured in addition with the inelastic proton-proton particle rate such that both values can be directly mapped to each other. Under the nominal data-taking conditions the inelastic proton-proton particle rate is measured in order to conclude the current luminosity. Luminosity measurements at the ATLAS experiment are primarily performed with the ***Lu**minosity Measurement using **C**herenkov **I**ntegrating **D**etector* (LUCID) [75] and the ***B**eam **C**ondition **M**onitors* (BCM) [76] which deliver independent measurements.

3.2.7 Detector Simulation

In section 2.3.4 the simulation of proton-proton collisions has been described. Building upon this, a simulation of the ATLAS detector is needed as well in order to

compare the measurements of the ATLAS detector with the theoretical predictions. Therefore a software is needed that simulates the response of the detector components when the final state particles of the proton-proton collisions enter the detector. The simulation of the ATLAS detector is performed with the toolkit GEANT4 [77]. It is able to propagate the simulated final state particles through the detector considering the geometry and the materials of each detector component as well as the magnetic field inside the detector. The interaction of the final state particles with the detector, the production of additional particles especially in the electromagnetic and hadronic showers as well as the readout electronics are simulated. The sequence of the event simulation and the detector simulation is a full simulation of what is expected to take place from the collision of two protons provided by the LHC up to the electronical signals read out by the ATLAS detector. Each full simulation contains information at two levels, the *truth level* which denotes the state of the simulation when the final state particles have been produced and the *reconstruction level* which denotes the state when the particles have been reconstructed by the ATLAS detector.

3.2.8 Pile-Up

The proton-proton collisions provided by the LHC occur in intervals of 25 ns. The proper detection of all proton-proton collisions leads to a serious challenge for the ATLAS detector since many detector components have sensitivity windows larger than 25 ns. Additionally each collision of two proton bunches leads to several proton-proton collisions in one crossing of two proton bunches. Both of these circumstances lead to the effects of *pile-up*. The effects mentioned can be categorized following review [78] as below.

In-Time Pile-Up
Additional proton-proton collisions occurring in the same crossing of two proton bunches is referred to as *in-time pile-up*. This leads to a significant background for all physics objects in the detector. In the data taking period from 2015 (2016) an average of around 14 (25) proton-proton collisions took place in each crossing of two proton bunches [79]. The different numbers can be explained with the higher instantaneous luminosity at which the LHC operated in the 2016 data taking period.

Out-Of-Time Pile-Up
Additional proton-proton collisions occurring in the crossings of two proton bunches before or after the bunch crossing with the proton-proton collision of interest are referred to as *out-of-time pile-up*. This effect is strongly depending on the detector technology. The LAr calorimeter, for instance, is sensitive to around 250 ns after the collision of interest and many bunch crossings before which can result in reduced total pulse heights. Similarly, in the TRT for example, particles from the collision of interest can be masked by particles from other collisions passing through a tube.

The simulation of both effects is crucial to have the similar conditions in the simulation as found in reality. In order to do so the event simulation and detector simulation is run for single proton-proton interactions first. In the digitization step of the simulations multiple simulated proton-proton interactions are combined. The

particle hits in the detector are simply overlaid. Including the pile-up effects in the digitization step has the advantage that the pile-up conditions can be adapted without having to perform the whole simulation again.

3.3 Identifying Physics Objects

The physics objects reconstructed with the ATLAS detector are photons, electrons, muons, τ leptons, individual hadrons, jets, total energy and missing transverse energy. For the analysis presented in this thesis the objects electrons, muons, jets and missing transverse energy are relevant and will be discussed below.

3.3.1 Electrons

In the ATLAS detector an electron manifests itself by an energy deposition in the electromagnetic calorimeter matched to a track recorded in the tracking detectors. Identifying an electron runs through several steps in which the signature of an energy deposition and a matching track gets first reconstructed as an electron candidate. Subsequently identification and isolation criteria are defined for the electron candidate to be used in analyses to further constrain the candidate to a real electron. The following explanations are based on the review [80].

Reconstruction
The reconstruction of an electron in the central region of the ATLAS detector ($|\eta| < 2.47$) proceeds in several steps. The clusters in the electromagnetic calorimeter are reconstructed first. Subsequently the tracks in the tracking detectors are reconstructed followed by a procedure fitting electron-specific tracks. Lastly combinations of the clusters and tracks are performed to reconstruct the electrons. In the following the detailed procedure is described:

1. *Seed-Cluster Reconstruction:* A seed-cluster is an energy deposition in the electromagnetic calorimeter with a total cluster transverse energy above 2.5 GeV. The calorimeter's $\eta \times \phi$ space with smallest units of 0.025×0.025 is scanned over by a sliding window algorithm. A window size of 3×5 in terms of the smallest calorimeter units is used to search for seed-clusters. As soon as a seed-cluster is found a cluster algorithm [81] that allows for duplicates to be removed builds the full cluster.

2. *Track Reconstruction:* Tracks are reconstructed by recognizing the track pattern followed by fitting the track. The standard algorithm performing these steps uses a pion hypothesis for energy loss due to interactions with the detector material. This is complemented by an algorithm allowing up to 30 % energy loss to account for possible bremsstrahlung. If a track-seed of 3 hits in different layers of the tracking detectors with a transverse momentum larger than 1 GeV can not be extended to a full track with at least 7 hits but falls within one of the seed-clusters in the electromagnetic calorimeter a second attempt is performed using an electron hypothesis allowing a larger energy loss. The fits are performed with the ATLAS Global χ^2 Track Fitter [82].

3. *Electron-Specific Track Fit:* The obtained tracks are loosely matched to the electromagnetic clusters using the distance in η and ϕ between the position of the track in the middle layer of the calorimeter and the barycenter of the cluster. The matching accounts for energy loss due to bremsstrahlung and for the number of hits in the tracking system. Tracks with ≥ 4 hits and loosely associated electromagnetic clusters are refit using an optimized Gaussian Sum Filter [83], which takes into account the non-linear effects due to bremsstrahlung.

4. *Electron Candidate Reconstruction:* The final step is the electron candidate reconstruction for which the refitted track of the previous step is matched to the electromagnetic cluster with stricter conditions for the η and ϕ distances. If several tracks fulfill the matching conditions an algorithm using the cluster-track distance $R = \sqrt{\Delta\eta^2 + \Delta\phi^2}$ decides for the most optimal track. Finally the electromagnetic cluster is reformed using windows of size 3×7 (5×5) in units of the smallest calorimeter segments in the barrel (end-caps) of the electromagnetic calorimeter.

The four-momentum of an electron candidate is computed using both the information from the track as well from the electromagnetic cluster. The energy of the electron candidate is given by the electromagnetic cluster while the η and ϕ coordinates are calculated from the track with respect to the primary vertex.

Identification

The electron identification is based on algorithms which determine whether the reconstructed electron candidates are signal-like objects or background-like objects, such as hadronic jets or converted photons. Converted photons are electrons that are the result of pair production by a photon. The quantities used by the algorithms are related to the electron cluster and track measurements which include the shape of the calorimeter shower, track properties, information from the TRT and variables measuring effects due to bremsstrahlung in order to distinguish signal from background. Hadronic jets could potentially leave clusters and tracks that are similar to the ones of electrons. Hence, there is a probability that a hadronic jet could be mistaken for an electron candidate. The identification algorithms use likelihoods based on the discriminating quantities. Some exemplary quantities will be given below:

- *Hadronic Leakage:* Most of the time electrons deposit all of their energy in the electromagnetic calorimeter before reaching the hadronic calorimeter. If energy is deposited in the first layer of the hadronic calorimeter this can be used as an indication of a hadronic jet rather than an electron.

- *Shower Width:* The electromagnetic shower caused by hadronic jets or converted photons tends to be wider than the shower of electrons. Several discriminating quantities take advantage of this. One variable is constructed as the ratio of the energy measured in 3×7 and 7×7 calorimeter cells in $\eta \times \phi$ space such that the 3×7 window is centered in the 7×7 window. For electrons most of the energy is contained in the 3×7 cells while hadronic jets and converted photons usually deposit energy outside of the smaller window as well.

- *Hits in Pixel and SCT:* The number of Pixel and SCT hits can be used to discriminate between prompt electrons and converted photons. A converted photon does not leave hits in the detector before it converted. Prompt electrons, however, can leave hits starting from their origination. Thus, converted photons are assumed to have less hits in the tracking detectors than prompt electrons.

- *Track to Cluster η:* The matching of the tracks and clusters require the comparison of the η variable measured with the tracking detectors and the electromagnetic calorimeter resulting in a distribution $\Delta\eta$. In hadronic jets additional produced particles can bias the cluster position with respect to the matching track resulting in a wider $\Delta\eta$ distribution. For electrons this distribution is more narrow such that it can be used as a discriminating variable.

- $\frac{E}{p}$*:* The ratio of the energy measured in the electromagnetic calorimeter to the momentum determined by the tracking detectors is referred to as $\frac{E}{p}$. For electrons this value peaks at one and has a long tail for larger values. This tail reflects the energy loss due to bremsstrahlung in the tracking detectors. In the electromagnetic calorimeter, however, the radiated photons contribute to the electromagnetic cluster. Hadronic jets peak at lower values of $\frac{E}{p}$ since a significant fraction of their energy will also be deposited in the hadronic calorimeter.

A multivariate analysis (MVA) technique simultaneously evaluates the different quantities of the reconstructed electron candidates in order to decide for a signal-like or a background-like object. Therefore the algorithms use the probability density functions (PDFs) of the discriminating quantities for signal and for background objects. These PDFs can be gained from MC simulations. The information of the signal and background PDFs are finally combined into a discriminant $d_{\mathcal{L}}$ according to

$$d_{\mathcal{L}} = \frac{\mathcal{L}_{\mathrm{S}}}{\mathcal{L}_{\mathrm{S}} + \mathcal{L}_{\mathrm{B}}} \qquad \text{with} \qquad \mathcal{L}_{\mathrm{S(B)}}(\vec{x}) = \prod_{i=1}^{n} P_{\mathrm{S(B),i}}(x_i). \tag{3.13}$$

The vector $\vec{x}$ denotes the discriminating variables. $P_{\mathrm{S(B),i}}(x_i)$ is the value of the signal (background) PDF of the ith discriminant variable. Hence, $\mathcal{L}_{\mathrm{S(B)}}$ is the entire likelihood describing the probability of the reconstructed object being signal-like (background-like). $d_{\mathcal{L}}$ defines the degree of identification for which the three levels *LHLoose*, *LHMedium* and *LHTight* have been defined with signal efficiencies of 90 %, 80 % and 70 % respectively. The background rejection is strongest for *LHTight* and gets weaker towards *LHLoose*. In order to gain efficient data these criteria are already applied at some HLT triggers in a slightly softened version.

Isolation

The electron isolation is a further quantity used to discriminate if the reconstructed electron candidate is signal-like or background-like. The isolation variable describes the energy around the reconstructed electron candidate. It can be used to disentangle between prompt electrons from signals like $Z \to e^+e^-$ which are usually isolated and other non-isolated objects such as electrons originating from converted photons produced in hadron decays, electrons from heavy flavor hadron decays and light

hadrons mis-identified as electrons. For this purpose, two discriminating variables have been designed:

- *Calorimeter Isolation:* The calorimeter isolation value $E_{\mathrm{T}}^{\mathrm{cone0.2}}$ is the transverse energy contained in the cells around the reconstructed electron candidate cluster with a cone of $\Delta R = 0.2$ subtracted by the transverse energy in the cells defined by $\Delta\eta \times \Delta\phi = 0.125 \times 0.175$ around the barycenter of the cluster of the reconstructed electron candidate.

- *Track Isolation:* The track isolation $p_{\mathrm{T}}^{\mathrm{varcone0.2}}$ is the sum of the transverse momenta of all tracks within a cone of $\Delta R = \min\left(0.2, 10\frac{GeV}{E_{\mathrm{T}}}\right)$ around the reconstructed electron candidate track which is excluded together with additional tracks from converted bremsstrahlung-photons. The tracks included in the $p_{\mathrm{T}}^{\mathrm{varcone0.2}}$ have to emerge from the primary vertex of the hard scattering and fulfill the following criteria:

  - $E_{\mathrm{T}} > 1\,\mathrm{GeV}$
  - A combined seven hits in the pixel detector and the SCT with no more than two missing hits in total and one missing hit in the pixel detector. In addition, there has to be no more than one hit assigned to more than one track.
  - $|\Delta z_0 \sin\theta| < 3\,\mathrm{mm}$, where z_0 is the closest distance between the primary vertex and the lepton candidates track component along the beam line.

From $E_{\mathrm{T}}^{\mathrm{cone0.2}}$ and $p_{\mathrm{T}}^{\mathrm{varcone0.2}}$ the levels *LooseTrackOnly*, *Loose* and *Tight* have been designed. *LooseTrackOnly* reflects the weakest background rejection followed by *Loose* and *Tight* which has the strongest background rejection.

3.3.2 Muons

In the ATLAS detector a muon manifests itself by a track recorded in the tracking detectors as well as a track recorded in the muon spectrometer. Similarly to electrons, identifying a muon runs through several steps using information from the tracking detectors and the muon spectrometer to reconstruct a signature as a muon candidate. Subsequently identification and isolation criteria are defined for the muon candidate to be used in analyses to further constrain the candidate to a real muon. The following explanations are based on the review [84].

Reconstruction
The reconstruction of muons is performed independently in the tracking system and the muon spectrometer. The information from the individual subdetectors are then combined to form the muon tracks used in physics analyses. The reconstruction of muons in the tracking system is performed in the same way as for electrons but without the hypothesis of bremsstrahlung. In the muon spectrometer a search for hit patterns in each muon chamber is performed. In each MDT chamber and nearby trigger chamber, a Hough transform [85] is applied to search for hits aligned on a trajectory in the bending plane of the detector. A straight line is fitted to the found hits to reconstruct the hit segments of the MDT. The RPC and TGC measure the coordinate in the transverse plane which is orthogonal to the bending plane. The

segments in the CSC detector are reconstructed using a combinatorial search in the η and ϕ planes of the detector.
Muon track candidates are then built by fitting hits from segments in different layers. The algorithm used for the track reconstruction is based on a combinatorial search that starts by using as seeds the segments found in the middle layers of the detector where more trigger hits are available. The algorithm is then extended to use the segments from the outer and inner layers as seeds. The selection of the segments is based on hit-multiplicity as well as fit quality. The matching is performed using their relative positions and angles. At least two matching segments are required to build a track. In the transition region from the barrel to the end-cap, only one single high-quality segment with η and ϕ information is sufficient to build a track. A segment can be used to build several track candidates. However, an overlap removal algorithm is used to either select the best assignment to a single track or to allow the segment to be shared between two tracks. The hits associated to a track candidate are fitted using a global χ^2 fit. The energy loss of the muons in the calorimeters is taken into account in the fits. Finally, a combination of the information about the muon track from the tracking system, the muon spectrometer and the calorimeter is used to define four types of muons:

- *Combined Muons:* A track reconstruction is performed independently in the tracking system and the muon spectrometer. A combined track is formed with a global fit using both, the hits from the tracking system and the muon spectrometer. An outside-in strategy reconstructing the muon in the muon spectrometer first is used and then extrapolated inwards to match the track in the tracking system. As a complementary approach an inside-out strategy reconstructing the muon in the tracking system first is used before extrapolating outward to match the track in the muon spectrometer.

- *Segment-Tagged Muons:* A track reconstructed in the tracking system is classified as a muon once it is associated with at least one local track segment in the MDT or CSC. A segment-tagged muon is usually a muon with a low transverse momentum or falling in a reduced acceptance region such that only one layer of the muon spectrometer is crossed.

- *Calorimeter-Tagged Muons:* A reconstructed track in the tracking system is identified as a muon when a minimum-ionizing calorimeter signature can be matched to the muon track. This type of muon is beneficial in the region $|\eta| < 0.1$ where the muon spectrometer is not fully equipped due to cabling and services for the calorimeters and tracking system.

- *Extrapolated Muons:* A track in the muon spectrometer is extrapolated to the interaction point. This type of muon is used to extend the acceptance of muons into the region $2.5 < |\eta| < 2.7$ where the tracking system does not provide tracking information.

When producing these types of muons an overlap algorithm is used giving the preference to the combined muons in case a track is shared.

Identification
The muon identification is performed with quality requirements suppressing background muons mainly due to pion and kaon decays. Muon candidates originating

from in-flight decays of charged hadrons in the tracking system are usually characterized by a "kink" topology. As a result, it is expected that the fit quality of the combined muon track will be poor. Additionally the momentum measured in the tracking system and the muon spectrometer independently may not be compatible. The following variables offer a good discrimination between prompt muons and background muons:

- $\frac{q}{p}$ *Significance:* It is defined as the absolute value of the difference between the ratio of the charge q and momentum p of the muons measured in the tracking system and the muon spectrometer divided by the sum in quadrature of the corresponding uncertainties.

- ρ'*:* It is defined as the absolute value of the difference between the transverse momentum measured in the tracking system and the muon spectrometer divided by the p_{T} of the combined track.

- *Fit Quality:* The normalized χ^2 of the combined track fit is used to characterize the quality of the fit.

For a robust momentum measurement several requirements on the number of hits in the tracking system and muon spectrometer have to be fulfilled. In the tracking system at least one hit in the pixel detector, at least five hits in the SCT and fewer than three missing hits in all layers of the SCT and pixel detector are required. In the region $0.1 < |\eta| < 1.9$ at least 10 % of the TRT hits originally assigned to the track have to be included in the final fit. The following levels of identification for a muon are defined:

- *Medium:* The *medium* level provides the default selection for muons in ATLAS. It minimizes the systematic uncertainties associated with the muon reconstruction and calibration. For this identification level only combined muons and extrapolated muons are used. Combined muons are required to have at least three hits in at least two MDT layers. In the region $|\eta| < 0.1$ hits in at least one MDT layer but no more than one missing hit in an MDT layer is allowed. Extrapolated muons are required to have at least three hits in the MDT or CSC and are only employed in the region $2.5 < |\eta| < 2.7$ to extend the acceptance outside of the tracking system. The $\frac{q}{p}$ significance is required to be less than seven. In the region $|\eta| < 2.5$, about 0.5 % of the muons classified as *medium* are reconstructed with the inside-out strategy.

- *Loose:* The *loose* level is defined to maximise the reconstruction efficiency while providing good-quality muon tracks. It is specifically optimized for reconstructing Higgs boson candidates in the four-lepton final state [86]. All combined and extrapolated muons satisfying the *medium* requirements are included in the *loose* definition. Calorimeter-tagged and segment-tagged muons are restricted to $|\eta| < 0.1$. In the region $|\eta| < 2.5$ around 97.5 % of the *loose* muons are combined muons, around 1.5 % are calorimeter-tagged muons and the remaining are segment-tagged muons.

- *Tight:* The *tight* level is defined to maximize the purity of muons which costs some of the efficiency. Only combined muons with hits in at least two stations of the muon spectrometer and satisfying the *medium* selection are required.

The normalized χ^2 of the global fit has to be smaller than eight. A 2D criterion describing the variables ρ' and $\frac{q}{p}$ as of the muon p_{T} is used to ensure a stronger background rejection. This is especially important for muons with momenta smaller than 20 GeV where the mis-identification probability is higher.

- *High-p_T:* The *high-p_T* level maximizes the momentum resolution for tracks with transverse momenta above 100 GeV. This selection is optimized for searches for high mass resonances [87, 88] as presented in this thesis as well. Therefore, combined muons passing at least three hits in three MS stations are used. Specific regions of the muon spectrometer with a sub-optimal alignment are vetoed as precaution. While the reconstruction efficiency of *high-p_T* muons is reduced by about 20 % the p_{T} resolution of muons above 1.5 TeV is improved by about 30 %.

Isolation
Similarly to electrons the isolation of muons is a further quantity to discriminate the reconstructed muon candidate to be signal-like or background-like. Via the energy around the muon candidate it can be decided if the muon is produced through a decay of a heavy boson or through a semi-leptonic decay where the muon is produced in the proximity of other particles. For this discrimination the following two variables have been defined:

- *Calorimeter Isolation:* The calorimeter isolation value $E_{\mathrm{T}}^{\mathrm{topocone20}}$ is defined as the sum of the transverse energy of the topological clusters [89] in a cone with size $\Delta R = 0.2$ around the muon candidate after subtracting the energy deposit from the muon candidate itself.

- *Track Isolation:* The track isolation value $p_{\mathrm{T}}^{\mathrm{varcone30}}$ is defined as the scalar sum of the transverse momenta of all tracks in a cone of size $\Delta R = \min\left(\frac{10\,\mathrm{GeV}}{p_{\mathrm{T}}}, 0.3\right)$. The transverse momentum of a track entering the sum has to be at least 1 GeV.

As for the electrons the levels *LooseTrackOnly*, *Loose* and *Tight* have been designed using $E_{\mathrm{T}}^{\mathrm{topocone20}}$ and $p_{\mathrm{T}}^{\mathrm{varcone30}}$. *LooseTrackOnly* reflects the weakest background rejection followed by *Loose* and *Tight* which has the strongest background rejection.

3.3.3 Jets

The clusters of final state hadrons after the hadronization process are referred to as jets. The reconstruction of jets as described below follows the review [90]. In ATLAS the vast majority of jets is reconstructed with the anti-k$_t$ algorithm [91]. This jet finding algorithm is based on distances between objects. d_{ij} is the distance between two objects i and j while d_{iB} is the distance between object i and the beam. First the smallest of the distances is identified. If it is d_{ij} the two objects are recombined, if it is d_{iB} the object i is considered a jet and removed from the list of objects. The distances are recalculated which is repeated until no objects are left. The definition of the distances are

$$d_{ij} = \min(k_{t,i}^{-2}, k_{t,j}^{-2}) \frac{\Delta_{ij}^2}{R^2}, \tag{3.14}$$

$$d_{iB} = k_{t,i}^{-2} \tag{3.15}$$

where $\Delta_{ij}^2 = (y_i - y_j)^2 + (\phi_i - \phi_j)^2$. $k_{t,i}$, y_i and ϕ_i are the transverse momentum, rapidity and azimuth angle of object i, respectively. R is the radius parameter which has the value $R = 0.4$ for the jets used in this analysis. The inputs for the jet finding algorithm can be inner detector tracks, energy deposits in the calorimeter or a combination of both [92, 93]. Jets reconstructed from tracks have a low dependence on pile-up. This is due to the fact that only tracks originating from the primary vertex are used for the jet finding. However, since the ATLAS inner detector tracking is limited to $|\eta| < 2.5$ a jet reconstruction with energy deposits in the calorimeter is mostly used. These calorimeter jets are reconstructed from "topologically" clustered calorimeter cells which are known as *topo-clusters* [94]. The idea of this procedure is a topological noise suppression by removing specific cells as explained below. The results are topological cell clusters with shape and location information that can be used for the jet reconstruction. It is assumed that σ is the total noise of the cell which is the quadratic sum of the measured electronics and pile-up noise. The clustering algorithm starts to define topo-clusters from seed cells with energy deposits larger than 4σ. If neighboring cells of the seed cells have an energy deposit larger than 2σ they are added to the topo-cluster. Lastly, all adjacent cells of the topo-cluster are added. A cluster splitting algorithm separates topo-clusters based on local energy maxima in order to avoid overlaps. A topo-cluster has to have a positive energy in order to be considered for the jet reconstruction.

3.3.4 Missing Transverse Momentum

The missing transverse momentum is a quantity describing the momentum of particles that have left the detector uncaptured. Neutrinos, for instance, are known particles that only interact weakly and hence can leave the detector "unseen" and take away undetected particle momentum and energy. Unknown particles interacting rarely or not at all with the detector could as well be contributing to this quantity. The missing transverse momentum could simply be determined by summing up all calorimeter cells and tracks. However, an object based reconstruction has the advantage that object based calibrations can be applied. This results in a better resolution of the missing transverse momentum. As described in the review [95] the missing transverse momentum is the negative vector sum of transverse momenta $\vec{p}_{\mathrm{T}}$ of reconstructed physics objects. The physics objects considered in this calculation are electrons, photons, muons, τ-leptons and jets. All these contributions are referred to as hard terms while the soft term denotes any contributions that are not associated to one of the hard terms. Hence the missing transverse momentum can be expressed via

$$E_{x(y)}^{\mathrm{miss}} = E_{x(y)}^{\mathrm{miss},e} + E_{x(y)}^{\mathrm{miss},\gamma} + E_{x(y)}^{\mathrm{miss},\tau} + E_{x(y)}^{\mathrm{miss,jets}} + E_{x(y)}^{\mathrm{miss},\mu} + E_{x(y)}^{\mathrm{miss,soft}} \tag{3.16}$$

where each term is calculated separately along the x and y axes. The magnitude of the missing transverse momentum is then calculated via

$$E_{\mathrm{T}}^{\mathrm{miss}} = \sqrt{(E_x^{\mathrm{miss}})^2 + (E_y^{\mathrm{miss}})^2}. \tag{3.17}$$

Chapter 4

Analysis of Dilepton Final States

This chapter discusses all steps of the analysis of dilepton final states. A dilepton final state is synonymous for an event leading to two oppositely charged leptons l^+ and l^- of the same flavor. Within the scope of this analysis a lepton l is meant to be an electron e or a muon μ such that events leading to two oppositely charged electrons e^+ and e^- and events leading to two oppositely charged muons μ^+ and μ^- will be investigated. The word lepton will hence be used to indicate both an electron and a muon, i.e. $l \in \{e, \mu\}$. To further introduce simplicity the word lepton will be used to denote the negative charged lepton as well as the positive charged lepton, i.e. $l = l^+ = l^-$. In the course of this chapter the general strategy will be discussed first. Subsequently all background and signal processes relevant to this analysis will be examined. Afterwards a set of selection criteria will be introduced to select dilepton events from data and MC simulations. Finally the estimation of the backgrounds, the systematic uncertainties of the analysis as well as kinematic distributions will be discussed. The analysis has been performed with the ROOT framework [73].

4.1 Analysis Strategy

The analysis aims to find new physics in form of a yet unknown resonance. It is assumed that such a resonance exists due to a hypothetical particle that can decay into a pair of leptons of the same flavor and opposite electric charge. The process describing this scenario at leading order (LO) can be expressed in a Feynman diagram (see figure 4.1) and is called signal process. In order to search for such a signal process all other processes resulting in the same final state as well as processes

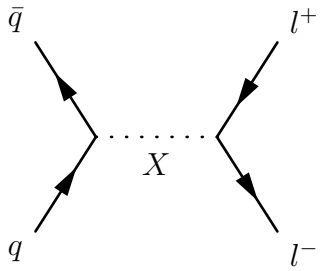

Figure 4.1: Feynman diagram of a quark-antiquark annihilation forming a yet unknown mediator X decaying into a lepton and an antilepton at leading order.

faking this final state need to be considered. These processes are called background processes. The approach is to compare the data with MC simulations of all these background processes. The MC simulations are only based on the known physics described by the Standard Model (SM). Hence a disagreement between the MC simulations and the data indicates physics beyond the Standard Model (BSM). However, the latter statement only holds true when assuming the detector behavior is fully understood. MC simulations of signal processes can then be used to quantify a potential resonance or generally any disagreement. The discriminating observable for this search is the invariant mass of the dilepton final state m_{ll}.

4.2 Background Processes

All known physical processes in proton-proton collisions leading to two leptons are considered to be background processes within this analysis. Due to inefficiencies of the detector it can happen that a non-lepton signature is misidentified as a lepton or that a lepton is not reconstructed at all. The latter case is rare due to high reconstruction efficiencies. Particles that are misidentified as leptons, however, constitute a significant background. Such particles are called fake leptons in contrast to correctly identified leptons which are called real leptons. Hence, all background processes can be divided into components with at least two real leptons in the final state as well as components with less than two real leptons and at least one fake lepton in the final state. The two components are called real background and fake background. The real and fake background processes are discussed in this section while the estimation of the resulting backgrounds can be found in section 4.5 and section 4.6 respectively.

4.2.1 Drell-Yan Process

The Drell-Yan process describes the annihilation of a quark and an antiquark with formation of a virtual Z boson or a virtual photon decaying into two leptons. The related Feynman diagram at leading order can be seen in figure 4.2.

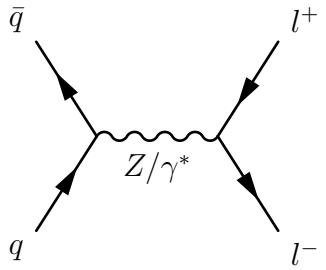

Figure 4.2: Feynman diagram of the leading order Drell-Yan process. It shows the annihilation of a quark and an antiquark with formation of a virtual Z boson or a virtual photon decaying into two leptons.

For the MC simulation of the Drell-Yan process the POWHEG BOX [96] event generator is used in combination with PYTHIA 8.186 [47] for the hadronization and parton shower. The hard scattering process is calculated at next-to-leading order (NLO) using the CT10 [97] parton distribution function (PDF) as well as the ATLAS AZNLO [98] tune. More details on this procedure can be found in [99]. The

simulated Drell-Yan sample is further corrected by applying k-factors. The NLO cross section is corrected to next-to-next-to-leading order (NNLO) by using the CT14NNLO [100] PDF. This is achieved by a dilepton mass-dependent k-factor calculated with VRAP 0.9 [101] for quantum chromodynamic (QCD) corrections and MCSANC 1.20 [102] for electroweak (EW) corrections. The Drell-Yan background also includes a contribution by photon-induced (PI) dilepton production. This happens through photon-photon scattering producing two charged leptons under the mediation of a charged lepton. The related Feynman diagrams at LO in the t- and u-channel can be seen in figure 4.3. The PI dilepton production is not taken

(a) t-channel (b) u-channel

Figure 4.3: Feynman diagrams of the leading order photon-induced dilepton production. It shows photon-photon scattering in the t- and u-channel mediated by a charged lepton decaying into two leptons.

into account in the calculation of the hard scattering process. To account for this contribution a mass-dependent k-factor included in the EW corrections, based on the MRST2004QED [103] PDF set, is used for its description. In order to ensure small statistical uncertainties over the entire dilepton invariant mass spectrum the MC simulation is generated as 20 separate samples each covering a specific invariant mass range of the spectrum. Each MC sample with the corresponding values of the cross section, the number of generated events and the integrated luminosity calculated via equation 3.8 can be found in table 4.1. The separation of the MC simulation into samples covering a specific mass range is especially important for the region of high invariant masses.

4.2.2 Top Quark Processes

A top quark decays into a W^+ boson and a bottom quark with a probability of more than 99 %. The resulting W^+ boson decays into a positive charged lepton and the corresponding lepton neutrino in about 11 % for each generation. A Feynman diagram of this process can be seen in figure 4.4. This implies that processes with a top and an antitop quark will contribute to the dilepton background. The production of a top antitop-quark pair can proceed via the annihilation of a quark and an antiquark or via the fusion of two gluons. In the process through annihilation of a quark-antiquark pair a virtual gluon is formed and immediately decays into a top antitop-quark pair. The related Feynman diagram at LO can be seen in figure 4.5. In the process through fusion of a gluon-gluon pair either a virtual gluon is formed and immediately decays into a top antitop-quark pair or a gluon-gluon scattering is taking place by mediating a quark and producing a top antitop-quark pair. The related Feynman diagrams at LO in the s-, t- and u-channel can be seen

Table 4.1: Values of the cross section σ_{Process}, the number of generated events N_{Events} and the integrated luminosity L_{Int} for the Drell-Yan process for specific regions of invariant mass m_{ll}.

m_{ll} [GeV]		σ_{Process} [nb]	N_{Events}		L_{Int} [fb^{-1}]	
min	max		$l \equiv e$	$l \equiv \mu$	$l \equiv e$	$l \equiv \mu$
60	120	$1.90 \cdot 10^{0}$	$7.91 \cdot 10^{7}$	$7.75 \cdot 10^{7}$	$4.16 \cdot 10^{1}$	$4.08 \cdot 10^{1}$
120	180	$1.75 \cdot 10^{-2}$	$4.98 \cdot 10^{5}$	$4.99 \cdot 10^{5}$	$2.85 \cdot 10^{1}$	$2.85 \cdot 10^{1}$
180	250	$2.92 \cdot 10^{-3}$	$2.50 \cdot 10^{5}$	$2.50 \cdot 10^{5}$	$8.56 \cdot 10^{1}$	$8.56 \cdot 10^{1}$
250	400	$1.08 \cdot 10^{-3}$	$1.49 \cdot 10^{5}$	$1.49 \cdot 10^{5}$	$1.38 \cdot 10^{2}$	$1.38 \cdot 10^{2}$
400	600	$1.96 \cdot 10^{-4}$	$1.00 \cdot 10^{5}$	$9.90 \cdot 10^{4}$	$5.10 \cdot 10^{2}$	$5.05 \cdot 10^{2}$
600	800	$3.74 \cdot 10^{-5}$	$1.45 \cdot 10^{5}$	$6.06 \cdot 10^{4}$	$3.88 \cdot 10^{3}$	$1.62 \cdot 10^{3}$
800	1000	$1.06 \cdot 10^{-5}$	$5.00 \cdot 10^{4}$	$5.00 \cdot 10^{4}$	$4.72 \cdot 10^{3}$	$4.72 \cdot 10^{3}$
1000	1250	$4.26 \cdot 10^{-6}$	$5.00 \cdot 10^{4}$	$5.00 \cdot 10^{4}$	$1.17 \cdot 10^{4}$	$1.17 \cdot 10^{4}$
1250	1500	$1.42 \cdot 10^{-6}$	$5.00 \cdot 10^{4}$	$4.98 \cdot 10^{4}$	$3.52 \cdot 10^{4}$	$3.51 \cdot 10^{4}$
1500	1750	$5.45 \cdot 10^{-7}$	$4.98 \cdot 10^{4}$	$4.96 \cdot 10^{4}$	$9.14 \cdot 10^{4}$	$9.10 \cdot 10^{4}$
1750	2000	$2.30 \cdot 10^{-7}$	$5.34 \cdot 10^{4}$	$5.00 \cdot 10^{4}$	$2.32 \cdot 10^{5}$	$2.17 \cdot 10^{5}$
2000	2250	$1.04 \cdot 10^{-7}$	$5.00 \cdot 10^{4}$	$5.00 \cdot 10^{4}$	$4.81 \cdot 10^{5}$	$4.81 \cdot 10^{5}$
2250	2500	$4.94 \cdot 10^{-8}$	$5.00 \cdot 10^{4}$	$4.98 \cdot 10^{4}$	$1.01 \cdot 10^{6}$	$1.01 \cdot 10^{6}$
2500	2750	$2.45 \cdot 10^{-8}$	$5.00 \cdot 10^{4}$	$4.98 \cdot 10^{4}$	$2.04 \cdot 10^{6}$	$2.03 \cdot 10^{6}$
2750	3000	$1.25 \cdot 10^{-8}$	$4.78 \cdot 10^{4}$	$5.00 \cdot 10^{4}$	$3.82 \cdot 10^{6}$	$4.00 \cdot 10^{6}$
3000	3500	$1.00 \cdot 10^{-8}$	$4.86 \cdot 10^{4}$	$5.00 \cdot 10^{4}$	$4.86 \cdot 10^{6}$	$5.00 \cdot 10^{6}$
3500	4000	$2.93 \cdot 10^{-9}$	$4.76 \cdot 10^{4}$	$5.00 \cdot 10^{4}$	$1.62 \cdot 10^{7}$	$1.71 \cdot 10^{7}$
4000	4500	$8.98 \cdot 10^{-10}$	$4.80 \cdot 10^{4}$	$4.90 \cdot 10^{4}$	$5.35 \cdot 10^{7}$	$5.46 \cdot 10^{7}$
4500	5000	$2.81 \cdot 10^{-10}$	$9.30 \cdot 10^{4}$	$5.00 \cdot 10^{4}$	$3.31 \cdot 10^{8}$	$1.78 \cdot 10^{8}$
5000	∞	$1.27 \cdot 10^{-10}$	$4.80 \cdot 10^{4}$	$5.00 \cdot 10^{4}$	$3.78 \cdot 10^{8}$	$3.94 \cdot 10^{8}$

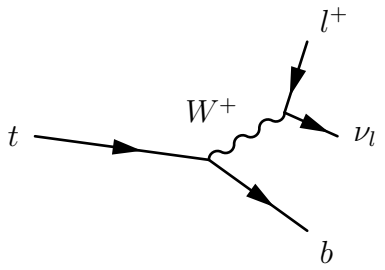

Figure 4.4: Feynman diagram of a top quark decaying into a W^+ boson and a bottom quark. The same process is valid by substituting all particles with their corresponding antiparticles.

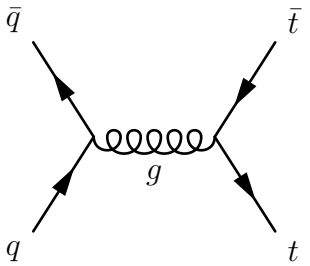

Figure 4.5: Feynman diagram of the leading order $t\bar{t}$ production process via quark-antiquark annihilation.

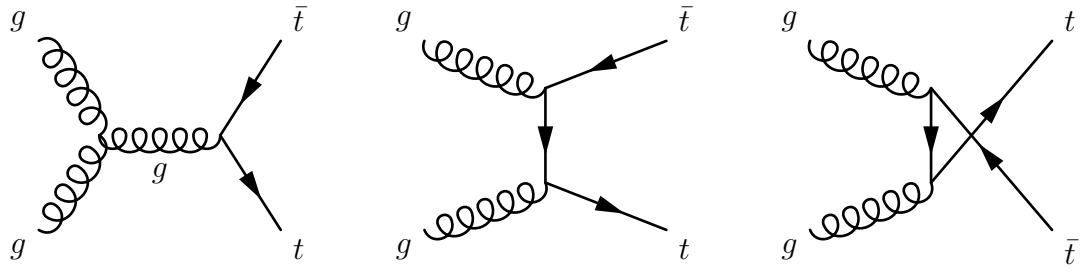

(a) s-channel (b) t-channel (c) u-channel

Figure 4.6: Feynman diagrams of the leading order $t\bar{t}$ production via gluon-gluon interactions.

in figure 4.6. At the LHC the dominant production mechanism of top-antitop quark pairs is the production via gluon-gluon fusion. At the Tevatron [104], in contrast, the dominant production mechanism of top-antitop quark pairs is the production via quark-antiquark annihilation. The differences between the Tevatron and the LHC are the beam energies as well as the beam particles. The beam energies of about 1 TeV at the Tevatron lead to a Bjorken-x of 0.17 when assuming the mass of a top/antitop quark for simplicity at around 170 GeV. At the LHC the beam energies are 6.5 TeV which leads to a Bjorken-x of around 0.03. Looking at figure 2.7 it can be seen that in case of the Tevatron Bjorken-x the PDFs of the valence quarks are dominating. For the LHC Bjorken-x, on the other hand, the gluon PDF is dominating. It has to be pointed out, that the gluon PDF is divided by a factor of 10 in figure 2.7. As a result, the top-antitop quark production via quark-antiquark annihilation is favored at the Tevatron while the production via gluon-gluon fusion is favored at the LHC. Another effect enhancing this scenario is the fact that the Tevatron has an antiproton beam which provides valence antiquarks. The LHC, due to proton beams only, can not provide valence antiquarks but only sea antiquarks. At the LHC, around 90 % of all top-antitop quark pairs are produced through gluon-gluon fusion. The Tevatron, on the other hand, produces about 85 % of all top-antitop quark pairs via quark-antiquark annihilation.
Another source of dilepton background through top processes arises from single top production. This can occur when the single top or antitop quark is accompanied by a W boson. The related Feynman diagrams at LO in the s- and t-channel can be seen in figure 4.7.

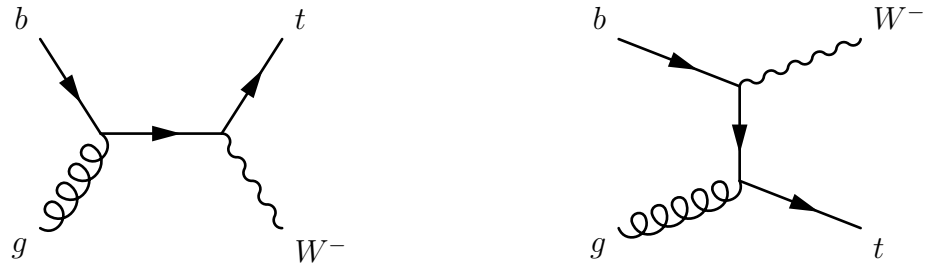

(a) s-channel (b) t-channel

Figure 4.7: Feynman diagrams of leading order single top production associated with a W boson.

The MC simulation of the $t\bar{t}$ process as well as the W boson associated single top

process is performed with the POWHEG BOX event generator in combination with PYTHIA 6.428 [105] for the hadronization and parton showering. The hard scattering is calculated at NLO using the CT10 PDF and the PERUGIA 2012 [106] tune under the assumption of a top quark mass of $m_t = 172.5\,\text{GeV}$. TOP++ 2.0 [107] has been used to correct the $t\bar{t}$ and W boson associated single top background to NNLO in QCD including resummation of next-to-next-to-leading logarithmic (NNLL) soft gluon terms. More information about studies on top quark MC modelling can be found in [108]. Single MC samples representing the full invariant mass spectrum are used. This results in a poor statistical uncertainty at high invariant masses. Thus the estimated top quark background will be extrapolated for higher invariant masses (see section 4.5.4). Each MC sample with the corresponding values of the cross section, the number of generated events and the integrated luminosity can be found in table 4.2.

Table 4.2: Values of the cross section σ_{Process}, the number of generated events N_{Events} and the integrated luminosity L_{Int} for all relevant top quark processes.

Process	σ_{Process} [nb]	N_{Events}	L_{Int} [fb^{-1}]
$pp \to t\bar{t} + X$	$7.33 \cdot 10^{-2}$	$1.98 \cdot 10^{7}$	$2.70 \cdot 10^{2}$
$pp \to W^{-}t + X$	$3.58 \cdot 10^{-3}$	$9.93 \cdot 10^{5}$	$2.77 \cdot 10^{2}$
$pp \to W^{+}\bar{t} + X$	$3.58 \cdot 10^{-3}$	$9.92 \cdot 10^{5}$	$2.77 \cdot 10^{2}$

4.2.3 Diboson Processes

As mentioned in the previous section a W boson decays into a lepton and the corresponding neutrino with a probability of around 11 % for each lepton flavor. A Z boson decays in a pair of same-flavor opposite-sign leptons in about 3 % for each lepton flavor. Hence, processes producing at least one Z boson or two W bosons can lead to final states including two real leptons. The relevant LO Feynman diagrams in the t-, u- and s-channel summarizing all these processes can be seen in figure 4.8 where $V \in \{Z, \gamma^*, W^{\pm}\}$.

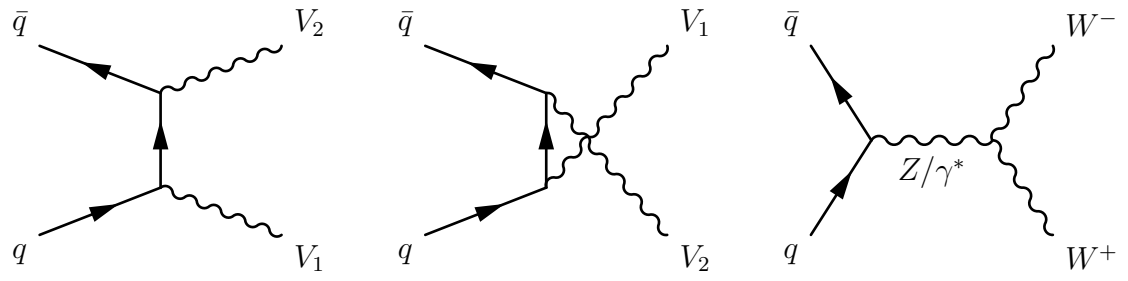

(a) t-channel (b) u-channel (c) s-channel

Figure 4.8: Feynman diagrams of leading order diboson production.

The MC simulation of the diboson processes is done with SHERPA 2.1.1 [48]. The calculation is performed at NLO with the CT10 PDF. Further information about the simulation of diboson processes can be found in [109]. Similarly to the MC simulation of the Drell-Yan process the simulation of the diboson processes is divided

into invariant mass ranges covering the entire dilepton invariant mass spectrum which ensures a small statistical uncertainty especially at high invariant masses. The MC simulation of each diboson process consists of eight samples which are listed in table 4.3 with the corresponding values of the cross section, the number of generated events and the integrated luminosity.

4.2.4 Fake Background

The fake background includes all processes with a maximum of only one real lepton in the final state while the remaining final state particles are fake leptons. A fake lepton is either a jet arising through the hadronization of a quark or a real lepton inside a b hadron decay. The main contribution to the fake background comes from higher order W boson production resulting in final states with a real lepton and a number of jets (see "Charged Current Drell-Yan Process" in section 4.2.5). Another contribution comes from any process that results in at least two jets but no real lepton in the final state. The fake background can therefore be denoted as contributions from W+jets and multi-jet production.

4.2.5 Additional Processes

Besides the above mentioned background processes which are significant for this analysis there are further processes that are either negligible or only significant in the context of the fake background estimation. The neglected background processes lead to a contribution that is extremely small compared to the background used in this analysis. Therefore these processes are rejected from the analysis.

Drell-Yan Process $q\bar{q} \to \tau^+\tau^-$
The nature of this process has been described in section 4.2.1. The difference is that the final state is not made up of two electrons or two muons but two taus. A tau has a mean lifetime of 2.9×10^{-13} s and thus immediately decays into lighter particles. With a probability of 17-18 % a tau decays into an electron, an electron antineutrino and a tau neutrino. Likewise a decay into a muon, a muon antineutrino and a tau neutrino is possible with approximately the same probability. These decays happen under the exchange of a W boson and are illustrated in figure 4.9. As a result this

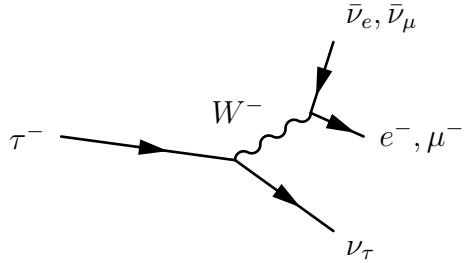

Figure 4.9: Feynman diagram of a tau decay. The same process is valid by substituting all particles with their corresponding antiparticles.

process becomes a background process for dielectron and dimuon final states. Due to the involved neutrinos in the tau decay the momentum of the electrons and muons is usually small compared to prompt electrons and muons from a Drell-Yan process.

Table 4.3: Values of the cross section σ_{Process}, the number of generated events N_{Events} and the integrated luminosity L_{Int} for all relevant diboson processes for specific regions of invariant mass m_{ll}.

m_{ll} [GeV]		σ_{Process} [nb]		N_{Events}		L_{Int} [fb^{-1}]	
min	max	$l \equiv e$	$l \equiv \mu$	$l \equiv e$	$l \equiv \mu$	$l \equiv e$	$l \equiv \mu$
Process: $pp \to l^+\nu_l l^-\nu_l + X$							
50	150	$8.28{\cdot}10^{-4}$	$8.30{\cdot}10^{-4}$	$1.90{\cdot}10^{5}$	$1.96{\cdot}10^{5}$	$2.29{\cdot}10^{2}$	$2.36{\cdot}10^{2}$
150	500	$2.32{\cdot}10^{-4}$	$2.34{\cdot}10^{-4}$	$4.80{\cdot}10^{4}$	$4.60{\cdot}10^{4}$	$2.07{\cdot}10^{2}$	$1.97{\cdot}10^{2}$
500	1000	$9.40{\cdot}10^{-6}$	$9.80{\cdot}10^{-6}$	$4.90{\cdot}10^{4}$	$4.90{\cdot}10^{4}$	$5.21{\cdot}10^{3}$	$5.00{\cdot}10^{3}$
1000	2000	$1.18{\cdot}10^{-6}$	$1.11{\cdot}10^{-6}$	$4.60{\cdot}10^{4}$	$5.00{\cdot}10^{4}$	$3.90{\cdot}10^{4}$	$4.50{\cdot}10^{4}$
2000	3000	$1.24{\cdot}10^{-7}$	$1.34{\cdot}10^{-7}$	$4.90{\cdot}10^{4}$	$4.90{\cdot}10^{4}$	$3.95{\cdot}10^{5}$	$3.66{\cdot}10^{5}$
3000	4000	$2.74{\cdot}10^{-8}$	$2.74{\cdot}10^{-8}$	$4.90{\cdot}10^{4}$	$4.90{\cdot}10^{4}$	$1.79{\cdot}10^{6}$	$1.79{\cdot}10^{6}$
4000	5000	$6.46{\cdot}10^{-9}$	$6.50{\cdot}10^{-9}$	$5.00{\cdot}10^{4}$	$5.00{\cdot}10^{4}$	$7.74{\cdot}10^{6}$	$7.69{\cdot}10^{6}$
5000	∞	$1.39{\cdot}10^{-9}$	$1.40{\cdot}10^{-9}$	$4.80{\cdot}10^{4}$	$5.00{\cdot}10^{4}$	$3.45{\cdot}10^{7}$	$3.57{\cdot}10^{7}$
Process: $pp \to l'^+l'^-l^+l^- + X$ with $l' \in \{e, \mu\}$							
50	150	$1.31{\cdot}10^{-3}$	$1.10{\cdot}10^{-3}$	$1.88{\cdot}10^{5}$	$2.00{\cdot}10^{5}$	$1.44{\cdot}10^{2}$	$1.82{\cdot}10^{2}$
150	500	$2.00{\cdot}10^{-5}$	$2.10{\cdot}10^{-5}$	$4.90{\cdot}10^{4}$	$4.80{\cdot}10^{4}$	$2.45{\cdot}10^{3}$	$2.58{\cdot}10^{3}$
500	1000	$6.50{\cdot}10^{-7}$	$6.28{\cdot}10^{-7}$	$5.00{\cdot}10^{4}$	$5.00{\cdot}10^{4}$	$7.69{\cdot}10^{4}$	$7.96{\cdot}10^{4}$
1000	2000	$4.93{\cdot}10^{-8}$	$6.39{\cdot}10^{-8}$	$4.50{\cdot}10^{4}$	$4.95{\cdot}10^{4}$	$9.13{\cdot}10^{5}$	$9.90{\cdot}10^{5}$
2000	3000	$1.40{\cdot}10^{-9}$	$1.60{\cdot}10^{-9}$	$5.00{\cdot}10^{4}$	$5.00{\cdot}10^{4}$	$3.57{\cdot}10^{7}$	$3.12{\cdot}10^{7}$
3000	4000	$8.24{\cdot}10^{-11}$	$9.40{\cdot}10^{-11}$	$4.70{\cdot}10^{4}$	$5.00{\cdot}10^{4}$	$5.70{\cdot}10^{8}$	$5.32{\cdot}10^{8}$
4000	5000	$6.31{\cdot}10^{-12}$	$7.63{\cdot}10^{-12}$	$4.45{\cdot}10^{4}$	$5.00{\cdot}10^{4}$	$7.05{\cdot}10^{9}$	$6.55{\cdot}10^{9}$
5000	∞	$5.44{\cdot}10^{-13}$	$6.98{\cdot}10^{-13}$	$4.40{\cdot}10^{4}$	$4.85{\cdot}10^{4}$	$8.09{\cdot}10^{10}$	$6.95{\cdot}10^{10}$
Process: $pp \to l'^{\pm}\nu_{l'}l^+l^- + X$ with $l' \in \{e, \mu\}$							
50	150	$6.84{\cdot}10^{-4}$	$6.87{\cdot}10^{-4}$	$1.85{\cdot}10^{5}$	$1.99{\cdot}10^{5}$	$2.70{\cdot}10^{2}$	$2.90{\cdot}10^{2}$
150	500	$8.63{\cdot}10^{-5}$	$8.53{\cdot}10^{-5}$	$4.90{\cdot}10^{4}$	$4.90{\cdot}10^{4}$	$5.68{\cdot}10^{2}$	$5.74{\cdot}10^{2}$
500	1000	$3.44{\cdot}10^{-6}$	$3.43{\cdot}10^{-6}$	$4.90{\cdot}10^{4}$	$4.80{\cdot}10^{4}$	$1.42{\cdot}10^{4}$	$1.40{\cdot}10^{4}$
1000	2000	$2.72{\cdot}10^{-7}$	$4.10{\cdot}10^{-7}$	$4.65{\cdot}10^{4}$	$4.90{\cdot}10^{4}$	$1.71{\cdot}10^{5}$	$1.20{\cdot}10^{5}$
2000	3000	$7.62{\cdot}10^{-9}$	$7.92{\cdot}10^{-9}$	$4.85{\cdot}10^{4}$	$4.90{\cdot}10^{4}$	$6.36{\cdot}10^{6}$	$6.19{\cdot}10^{6}$
3000	4000	$4.07{\cdot}10^{-10}$	$6.90{\cdot}10^{-10}$	$4.75{\cdot}10^{4}$	$4.95{\cdot}10^{4}$	$1.17{\cdot}10^{8}$	$1.22{\cdot}10^{8}$
4000	5000	$9.73{\cdot}10^{-9}$	$4.19{\cdot}10^{-11}$	$4.75{\cdot}10^{4}$	$4.85{\cdot}10^{4}$	$1.99{\cdot}10^{9}$	$2.03{\cdot}10^{9}$
5000	∞	$2.42{\cdot}10^{-9}$	$8.68{\cdot}10^{-12}$	$4.30{\cdot}10^{4}$	$4.75{\cdot}10^{4}$	$2.38{\cdot}10^{10}$	$2.62{\cdot}10^{10}$
Process: $pp \to q\bar{q}^{(\prime)}l^+l^- + X$							
50	150	$5.70{\cdot}10^{-3}$	$5.70{\cdot}10^{-3}$	$1.96{\cdot}10^{5}$	$2.00{\cdot}10^{5}$	$3.44{\cdot}10^{1}$	$3.51{\cdot}10^{1}$
150	500	$1.76{\cdot}10^{-4}$	$1.74{\cdot}10^{-4}$	$4.90{\cdot}10^{4}$	$4.90{\cdot}10^{4}$	$2.78{\cdot}10^{2}$	$2.82{\cdot}10^{2}$
500	1000	$4.08{\cdot}10^{-6}$	$4.05{\cdot}10^{-6}$	$4.90{\cdot}10^{4}$	$5.00{\cdot}10^{4}$	$1.20{\cdot}10^{4}$	$1.23{\cdot}10^{4}$
1000	2000	$3.16{\cdot}10^{-7}$	$3.11{\cdot}10^{-7}$	$4.90{\cdot}10^{4}$	$4.80{\cdot}10^{4}$	$1.55{\cdot}10^{5}$	$1.54{\cdot}10^{5}$
2000	3000	$1.00{\cdot}10^{-8}$	$1.01{\cdot}10^{-8}$	$4.90{\cdot}10^{4}$	$5.00{\cdot}10^{4}$	$4.90{\cdot}10^{6}$	$4.95{\cdot}10^{6}$
3000	4000	$6.60{\cdot}10^{-10}$	$6.62{\cdot}10^{-10}$	$4.80{\cdot}10^{4}$	$4.90{\cdot}10^{4}$	$7.27{\cdot}10^{7}$	$7.40{\cdot}10^{7}$
4000	5000	$5.35{\cdot}10^{-11}$	$5.44{\cdot}10^{-11}$	$4.60{\cdot}10^{4}$	$5.00{\cdot}10^{4}$	$8.60{\cdot}10^{8}$	$9.19{\cdot}10^{8}$
5000	∞	$4.85{\cdot}10^{-12}$	$4.83{\cdot}10^{-12}$	$4.95{\cdot}10^{4}$	$5.00{\cdot}10^{4}$	$1.02{\cdot}10^{10}$	$1.04{\cdot}10^{10}$

Therefore especially at high invariant masses the background from $q\bar{q} \to \tau^+\tau^-$ is negligible. This has been checked with a MC simulation revealing this contribution to be less than 1 ‰ over the entire m_{ll} spectrum compared to the full background.

Single Top Processes $q\bar{q}' \to \bar{b}\,t$, $pp \to \overset{(-)}{q}\,t$ and $pp \to \overset{(-)}{q}\,\bar{t}$
These processes are comparable to the W boson associated single top processes described in section 4.2.2 and figure 4.7. In contrast to the W boson associated processes, however, the final state does not contain a W boson but a quark accompanying the top quark. Figure 4.10 shows the LO Feynman diagrams of these processes. The quarks accompanying the top quark can decay into lighter quarks

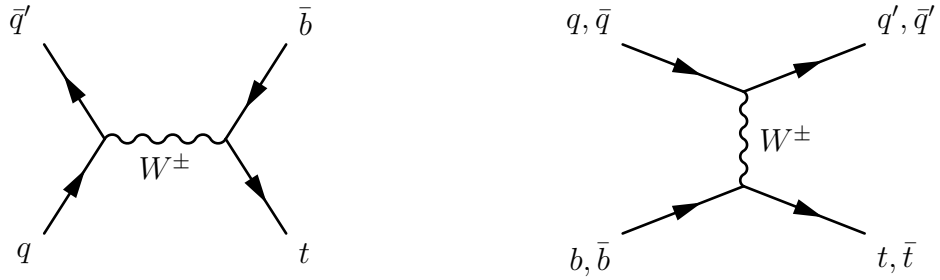

(a) s-channel (b) t-channel

Figure 4.10: Feynman diagrams of leading order single top production.

and a W boson. The W boson decay can then yield an electron or a muon. Together with the top quark decay a final state with two electrons or two muons can be formed. The contribution by the t-channel process has been checked with a MC simulation to be less than 1 ‰. Hence the t-channel process is neglected for the background with two real leptons in the final state. The quarks however can also hadronize and form a jet. The hadronization to a jet is more likely than a decay into lighter quarks and a W boson. A jet in turn can either fake a lepton or in case of a b hadron decay even contain a real electron. This leads to a small but non-negligible contribution to the fake background. Hence, this background will be used in the estimation of the fake background. The production cross section of the s-channel process [110] has been measured to be more than ten times smaller than the t-channel production cross section [111]. Therefore the s-channel process is fully neglected. Table 4.4 shows the MC simulation used in the fake background estimation with the corresponding values of the cross section, the number of generated events and the integrated luminosity.

Table 4.4: Values of the cross section σ_{Process}, the number of generated events N_{Events} and the integrated luminosity L_{Int} for all relevant single top quark processes via the t-channel.

Process	σ_{Process} [nb]	N_{Events}	L_{Int} [fb^{-1}]
$pp \to \overset{(-)}{q}\,t$	$4.37 \cdot 10^{-2}$	$4.99 \cdot 10^6$	$1.14 \cdot 10^2$
$pp \to \overset{(-)}{q}\,\bar{t}$	$2.58 \cdot 10^{-2}$	$4.99 \cdot 10^6$	$1.93 \cdot 10^2$

Charged Current Drell-Yan Process
The charged current Drell-Yan process in contrast to the so far described Drell-Yan

process is mediated by a W boson. The Drell-Yan process mediated by a Z/γ^* boson is therefore also called neutral current Drell-Yan process. A Feynman diagram of the LO charged current Drell-Yan process can be seen in figure 4.11. This LO

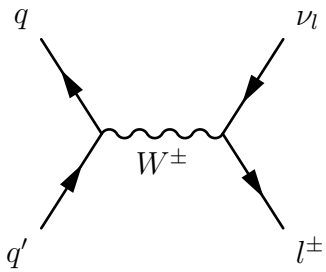

Figure 4.11: Feynman diagram of the leading order charged current Drell-Yan process. It shows the annihilation of two quarks with formation of a virtual W boson decaying into a lepton and a lepton antineutrino.

process does neither contribute to the real background nor to the fake background of a dilepton final state. However, the higher-order charged current Drell-Yan process results in jets in the final state making it the most important contribution to the fake background. Table 4.5 shows the MC simulation used in the fake background estimation with the corresponding values of the cross section, the number of generated events and the integrated luminosity. In order to gain a small statistical uncertainty especially at high $W^\pm$ boson masses the MC simulation is separated into 20 samples covering different $W^\pm$ boson mass ranges similarly to the MC simulation of the neutral current Drell-Yan process.

4.3 Signal Processes

The Feynman diagram of a possible signal process has already been shown in figure 4.1. The mediator X in this diagram depends on the theoretical model describing this process. In this work the models used are the Sequential Standard Model (SSM) as well as E_6 motivated models. Simulations of these models are costly because all possible pole masses of the mediator would need to be simulated. Therefore only four samples of the E_6 Z'_χ model at pole masses of 2 TeV, 3 TeV, 4 TeV and 5 TeV (see table 4.6) are available as a MC simulation while all other SSM and E_6 models with specific pole masses can be created with a reweighting procedure. This procedure is based on a Drell-Yan simulation at LO using Pythia 8.186 with the NNPDF23LO [112] PDF set and the ATLAS A14 [113] tune. Assuming that the Drell-Yan process and the signal processes have the same initial and final states one can calculate a SM cross section σ_{SM} as well as a BSM cross section $\sigma_{\text{SM + Signal}}$ for each invariant mass m_{ll}. The BSM cross section contains the SM Drell-Yan process and the desired signal process. For each event the reweighting factor

$$w_{\text{SM}\to\text{BSM}} = \frac{\sigma_{\text{SM + Signal}}}{\sigma_{\text{SM}}} \tag{4.1}$$

can be calculated and applied to the LO Drell-Yan simulation to create the desired signal. Interference effects between the signal model and the Drell-Yan production are not taken into account due to a large dependence on the model. Corrections to

Table 4.5: Values of the cross section σ_{Process}, the number of generated events N_{Events} and the integrated luminosity L_{Int} for the charged current Drell-Yan process for specific regions of $W^{\pm}$ boson mass $m_{W^{\pm}}$.

m_{W^c} [GeV]		σ_{Process} [nb]		N_{Events}		L_{Int} [fb^{-1}]	
min	max	$c \equiv +$	$c \equiv -$	$c \equiv +$	$c \equiv -$	$c \equiv +$	$c \equiv -$
60	120	$1.13 \cdot 10^{1}$	$8.28 \cdot 10^{0}$	$9.34 \cdot 10^{7}$	$1.12 \cdot 10^{8}$	$8.27 \cdot 10^{0}$	$1.35 \cdot 10^{1}$
120	180	$3.21 \cdot 10^{-2}$	$2.22 \cdot 10^{-2}$	$1.00 \cdot 10^{6}$	$1.00 \cdot 10^{6}$	$3.12 \cdot 10^{1}$	$4.50 \cdot 10^{1}$
180	250	$5.00 \cdot 10^{-3}$	$3.28 \cdot 10^{-3}$	$5.00 \cdot 10^{5}$	$5.00 \cdot 10^{5}$	$1.00 \cdot 10^{2}$	$1.52 \cdot 10^{2}$
250	400	$1.75 \cdot 10^{-3}$	$1.08 \cdot 10^{-3}$	$2.75 \cdot 10^{5}$	$3.00 \cdot 10^{5}$	$1.57 \cdot 10^{2}$	$2.78 \cdot 10^{2}$
400	600	$3.12 \cdot 10^{-4}$	$1.75 \cdot 10^{-4}$	$2.00 \cdot 10^{5}$	$2.00 \cdot 10^{5}$	$6.41 \cdot 10^{2}$	$1.14 \cdot 10^{3}$
600	800	$6.08 \cdot 10^{-5}$	$3.10 \cdot 10^{-5}$	$1.00 \cdot 10^{5}$	$1.00 \cdot 10^{5}$	$1.64 \cdot 10^{3}$	$3.23 \cdot 10^{3}$
800	1000	$1.77 \cdot 10^{-5}$	$8.29 \cdot 10^{-6}$	$1.00 \cdot 10^{5}$	$1.00 \cdot 10^{5}$	$5.65 \cdot 10^{3}$	$1.21 \cdot 10^{4}$
1000	1250	$7.29 \cdot 10^{-6}$	$3.16 \cdot 10^{-6}$	$9.50 \cdot 10^{4}$	$1.00 \cdot 10^{5}$	$1.30 \cdot 10^{4}$	$3.16 \cdot 10^{4}$
1250	1500	$2.51 \cdot 10^{-6}$	$1.00 \cdot 10^{-6}$	$1.00 \cdot 10^{5}$	$1.00 \cdot 10^{5}$	$3.98 \cdot 10^{4}$	$1.00 \cdot 10^{5}$
1500	1750	$9.86 \cdot 10^{-7}$	$3.68 \cdot 10^{-7}$	$1.00 \cdot 10^{5}$	$1.00 \cdot 10^{5}$	$1.01 \cdot 10^{5}$	$2.72 \cdot 10^{5}$
1750	2000	$4.25 \cdot 10^{-7}$	$1.49 \cdot 10^{-7}$	$8.00 \cdot 10^{4}$	$1.00 \cdot 10^{5}$	$1.88 \cdot 10^{5}$	$6.71 \cdot 10^{5}$
2000	2250	$1.95 \cdot 10^{-7}$	$6.53 \cdot 10^{-8}$	$1.00 \cdot 10^{5}$	$1.00 \cdot 10^{5}$	$5.13 \cdot 10^{5}$	$1.53 \cdot 10^{6}$
2250	2500	$9.33 \cdot 10^{-8}$	$3.02 \cdot 10^{-8}$	$1.00 \cdot 10^{5}$	$1.00 \cdot 10^{5}$	$1.07 \cdot 10^{6}$	$3.31 \cdot 10^{6}$
2500	2750	$4.63 \cdot 10^{-8}$	$1.45 \cdot 10^{-8}$	$1.00 \cdot 10^{5}$	$1.00 \cdot 10^{5}$	$2.16 \cdot 10^{6}$	$6.90 \cdot 10^{6}$
2750	3000	$2.35 \cdot 10^{-8}$	$7.26 \cdot 10^{-9}$	$1.00 \cdot 10^{5}$	$1.00 \cdot 10^{5}$	$4.26 \cdot 10^{6}$	$1.38 \cdot 10^{7}$
3000	3500	$1.84 \cdot 10^{-8}$	$5.67 \cdot 10^{-9}$	$1.00 \cdot 10^{5}$	$1.00 \cdot 10^{5}$	$5.43 \cdot 10^{6}$	$1.76 \cdot 10^{7}$
3500	4000	$5.10 \cdot 10^{-9}$	$1.60 \cdot 10^{-9}$	$1.00 \cdot 10^{5}$	$1.00 \cdot 10^{5}$	$1.96 \cdot 10^{7}$	$6.25 \cdot 10^{7}$
4000	4500	$1.43 \cdot 10^{-9}$	$4.72 \cdot 10^{-10}$	$1.00 \cdot 10^{5}$	$1.00 \cdot 10^{5}$	$6.99 \cdot 10^{7}$	$2.12 \cdot 10^{8}$
4500	5000	$4.01 \cdot 10^{-10}$	$1.43 \cdot 10^{-10}$	$9.50 \cdot 10^{4}$	$1.00 \cdot 10^{5}$	$2.37 \cdot 10^{8}$	$6.99 \cdot 10^{8}$
5000	∞	$1.53 \cdot 10^{-10}$	$6.16 \cdot 10^{-11}$	$1.00 \cdot 10^{5}$	$1.00 \cdot 10^{5}$	$6.54 \cdot 10^{8}$	$1.62 \cdot 10^{9}$

higher order in QCD are calculated with the same methodology as for the Drell-Yan process. Higher order EW corrections are not applied due to the large dependence on the model. The Z'_χ signal models are used to optimize the dilepton event selection while the reweighting procedure is used to create signal templates for the statistical interpretation.

Table 4.6: Values of the cross section σ_{Signal}, the number of generated events N_{Events} and the integrated luminosity L_{Int} for all simulated Z'_χ signals at specific pole masses $m_{Z'_\chi}$.

Pole Mass	σ_{Signal} [nb]		N_{Events}		L_{Int} [fb^{-1}]	
$m_{Z'_\chi}$ [TeV]	$l \equiv e$	$l \equiv \mu$	$l \equiv e$	$l \equiv \mu$	$l \equiv e$	$l \equiv \mu$
2	$8.85 \cdot 10^{-6}$	$8.84 \cdot 10^{-6}$	$1.98 \cdot 10^{4}$	$2.00 \cdot 10^{4}$	$2.24 \cdot 10^{3}$	$2.26 \cdot 10^{3}$
3	$8.10 \cdot 10^{-7}$	$8.05 \cdot 10^{-7}$	$1.96 \cdot 10^{4}$	$2.00 \cdot 10^{4}$	$2.42 \cdot 10^{4}$	$2.48 \cdot 10^{4}$
4	$1.04 \cdot 10^{-7}$	$1.04 \cdot 10^{-7}$	$1.98 \cdot 10^{4}$	$2.00 \cdot 10^{4}$	$1.90 \cdot 10^{5}$	$1.92 \cdot 10^{5}$
5	$1.83 \cdot 10^{-8}$	$1.84 \cdot 10^{-8}$	$1.80 \cdot 10^{4}$	$2.00 \cdot 10^{4}$	$9.84 \cdot 10^{5}$	$1.09 \cdot 10^{6}$

4.4 Selection of Events with Dilepton Final States

The selection of dilepton events is done in three stages. At the first stage, called event selection, criteria ensuring flawless event information are applied. At the second stage lepton selection criteria are applied to the electrons of the events that have passed the event selection and are removed in case the selection criteria are not fulfilled. Finally, at the third stage it is checked if a dilepton final state fulfilling the selection criteria can be found. The selection criteria are constructed in such a way that the signal efficiency gets maximized. The signal efficiency is defined as the number of dilepton events passing the selection criteria divided by the total number of dilepton events before the selection criteria.

4.4.1 Event Selection

The recorded data may include events that are corrupted and not usable for analyses. Therefore criteria preparing a flawless data set need to be applied as described below. Also part of the event selection is the trigger performing a preselection of events.

Data Quality
The data quality is ensured by a *GoodRunsList* (GRL). Each run is divided into several luminosity blocks in which the conditions of the beam and the detector can vary. For instance, since the beam intensity decreases with time the trigger prescales need to be adjusted. A luminosity block in which the trigger prescales have been changed can not be used for physics analyses and is therefore not listed in the GRL. Additionally a subsystem of the detector can develop a problem. Luminosity blocks affected by such a problem are not useful for analyses and hence are not listed in the GRL either. At the start of each event it is checked if the luminosity block in which the event has been recorded is listed in the GRL. In case the corresponding luminosity block is not listed the event is discarded.

Trigger
For the selection of dielectron final states a trigger requiring at least two electrons with a transverse momentum p_{T} of at least 17 GeV and an identification criterion of at least *LHLoose* is applied. (ATLAS notation: `2e17_lhloose`)
For the selection of dimuon final states two triggers are used in combination. Also a different combination of triggers is used for the data recorded in the year 2015 and the data recorded in the year 2016. The first trigger requires at least one muon with a p_{T} of at least 26 GeV and the muon to be isolated. For the data from 2015 this trigger has a slightly different isolation criterion compared to the trigger used for the 2016 data. Both first triggers have a high efficiency at low values of p_{T}. At very high p_{T} however the efficiency begins to drop. Therefore a second trigger without an isolation criterion but requiring at least one muon with a p_{T} of at least 50 GeV is used in combination for both 2015 and 2016 data. Only if none of the two combined triggers decides to keep the event it is discarded. (ATLAS notations: `mu26_imedium`, `mu26_ivarmedium` and `mu50`)

Event Cleaning
The event cleaning is a criterion checking for corrupted and incomplete events. Despite the check of the data quality via GRLs it can still happen to have a subdetector behaving corrupted within a run included in the GRL. Therefore the error states of the LAr calorimeter, the Tile calorimeter as well as the SCT are checked for corrupted events. The LAr calorimeter can end up with corrupted events due to noise bursts. The SCT can face corrupted events due to a recovery procedure which is necessary in case an SCT crate failed. All events with a corrupted error state are discarded. Incomplete events in contrast usually occur when a subdetector needs to be restarted during a data taking period. All events with incomplete event information are discarded as well.

Number of Leptons
In order to reconstruct a dilepton final state at least two lepton candidates are needed. Therefore it is checked that there are at least two electron candidates or at least two muon candidates in the event. The muon candidates in addition need to be of the type combined (see section 3.3.2).

4.4.2 Lepton Selection Criteria

From the remaining events leptons suitable for a dilepton final state will be selected. The following selection criteria are applied to each lepton candidate in the event. If one of these criteria is failed the lepton candidate is discarded. The whole event is discarded if the number of lepton candidates in the event reduces to less than two.

Pseudo-Rapidity η
For electron candidates the absolute value of the pseudo-rapidity has to be smaller than 2.47. This value is chosen because only within this region of pseudo-rapidity the ATLAS detector is equipped with tracking detectors. Since a high selection efficiency can only be assured within this region all electron candidates with a pseudo-rapidity of more than 2.47 are discarded. The transition region between the barrel and the

endcap calorimeter corresponding to an absolute value of the pseudo-rapidity of $1.37 < |\eta| < 1.52$ is excluded. This is due to a worse energy resolution in the transition region resulting in a worse selection efficiency.
For muon candidates the absolute value of the pseudo-rapidity has to be smaller than 2.5. However, the muon pseudo-rapidity criterion is not applied as a separate criterion. It is applied in the context of the identification criterion which will be introduced below.

Object Quality
The object quality is a set of requirements checking the energy deposition cluster of an electron candidate for the following problems:

- a failure of the Front End Board (FEB) in the first or second layer of the sampling calorimeter
- a region with high voltage failures affecting all three layers of the sampling calorimeter
- a calorimeter cell with its energy set to zero due to high noise in the 3×3 cells in the second layer of the sampling calorimeter of the sliding window cluster

If the energy deposition cluster of an electron candidate is facing one or more of the above problems the electron is discarded. The object quality is only applied for electron candidates.

Transverse Momentum $p_{\mathbf{T}}$
The transverse momentum of the lepton candidates has to be greater than 30 GeV. In case only the trigger requiring a muon candidate with at least 50 GeV has been triggered the transverse momentum of the muon candidate has to be greater than 50 GeV. These values arises due to the chosen triggers whose efficiencies are above 95 % for a transverse momentum of the lepton candidates of more than 30 GeV and 50 GeV respectively (see [114]).

Identification
The identification criterion for electron candidates is chosen to be *LHMedium* (see section 3.3.1). This choice has been studied with a Drell-Yan MC simulation to investigate the signal efficiency and a dijet MC simulation to investigate the background rejection efficiency. All identification criteria, namely *LHLoose*, *LHMedium* and *LHTight* have been tested to extract signal efficiencies and background rejection efficiencies. As a result the signal efficiency obtained with the *LHMedium* criterion is almost as good as the one obtained with the *LHLoose* criterion but with a better background rejection efficiency especially at high invariant masses.
In case of muon candidates the *High-p_T* identification (see section 3.3.2) is chosen. In addition the absolute value of the pseudo-rapidity of the muon candidates is checked to be smaller than 2.5. Despite the fact that the muon trigger system is only covering the absolute pseudo-rapidity region up to a value of 2.4 a muon can be identified up to a value of 2.5. This is due to the tracking detectors covering an absolute pseudo-rapidity region up to 2.5. Together with the information from the muon spectrometer covering an absolute pseudo-rapidity region up to 2.7 an identification of muon candidates in the pseudo-rapidity region up to 2.5 is possible

without a trigger.

Transverse Impact Parameter d_0
The transverse impact parameter is the closest distance between the primary vertex and the lepton candidates track component in the transverse plane. The discriminating variable used for this criterion is $|d_0|/\sigma_{d_0}$ where σ_{d_0} is the uncertainty of d_0. The uncertainty σ_{d_0} is used in this criterion to ensure that significant lepton candidates are not discarded due to a poor d_0 measurement with a large uncertainty. In general this criterion is used to sort out lepton candidates that are not associated to the primary vertex. The discriminating variable has to be smaller than 5 in case of electron candidates and smaller than 3 in case of muon candidates.

Longitudinal Impact Parameter z_0
The longitudinal impact parameter is the closest distance between the primary vertex and the lepton candidates track component along the beam line. The discriminating variable used for this criterion is $|z_0| \cdot \sin\theta$ where θ is the angle between the transverse momentum and the longitudinal momentum of the lepton candidates. The term $\sin\theta$ is multiplied to account for the diminishing resolution for small values of θ. The discriminating variable has to be smaller than 0.5 mm for both electron and muon candidates.

Isolation
For electron candidates the isolation criterion is defined by the level *Loose*, while muon candidates are discriminated by the level *LooseTrackOnly*. These are recommendations from the internal *ATLAS Isolation and Fake Forum* [115]. Both levels are designed to have an efficiency of at least 99 % over the whole invariant mass spectrum.

4.4.3 Selection of Dilepton Events

Applying the selection criteria discussed in the previous sections a set of events with at least two lepton candidates remains. In order to select these events as dilepton events the following steps are run through. First the two lepton candidates yielding the highest scalar sum of their transverse momenta are chosen. In case of muons the electric charge of the two candidates is checked to have an opposite sign. In case of electron candidates the electric charge is not used as a discrimination criterion due to a large systematic uncertainty at high transverse momenta. Lastly the invariant mass of the two candidates is evaluated via the four-momenta and required to be larger than 80 GeV. Table 4.7 shows a tabular overview of all applied selection criteria to gain the dilepton final states. The lepton with the higher p_{T} of the dilepton system is called leading lepton. Accordingly the lepton with the lower p_{T} is called subleading lepton.

Table 4.7: Overview of all selection criteria used to select dilepton final states.

Selection Criterion	ee	$\mu\mu$
GRL	applied	applied
Trigger	`2e17_lhloose`	2015: `mu26_imedium` or `mu50` 2016: `mu26_ivarmedium` or `mu50`
Event Cleaning	applied	applied
$N_{\text{Candidates}}$	> 2	> 2 (of type combined)
$\lvert\eta\rvert$	< 2.47 ($1.37 < \lvert\eta\rvert < 1.52$ excl.)	< 2.5 (applied in identification)
Object Quality	applied	— in identification
p_{T}	$> 30\,\text{GeV}$	$> 30\,\text{GeV}$ or $> 50\,\text{GeV}$ (depending on trigger)
Identification	*LHMedium*	*High-p_T*
$\lvert d_0\rvert/\sigma_{d_0}$	< 5	< 3
$\lvert z_0\rvert \cdot \sin\theta$	$< 0.5\,\text{mm}$	$< 0.5\,\text{mm}$
Isolation	*Loose*	*LooseTrackOnly*
Dilepton Selection	max. $\sum p_{\text{T}}$ no charge requirement $m_{ee} > 80\,\text{GeV}$	max. $\sum p_{\text{T}}$ opposite charge $m_{\mu\mu} > 80\,\text{GeV}$

4.5 Real Background Estimation

This section describes the estimation of the background processes leading to two real leptons in the final state. The MC samples discussed in section 4.2 of each background process are used for the estimate. The dilepton selection criteria as elaborated in the previous section are applied to estimate dilepton events from the MC simulations. The resulting set of dilepton events needs to be scaled and corrected for discrepancies between data and simulation as will be described in this section. Lastly the estimated background of each process will be discussed.

4.5.1 Luminosity Scale Factor

The luminosity scale factor is needed to match the magnitude of the MC simulations to the magnitude of data. This magnitude is described by the integrated luminosity which in case of data is fixed to what has been recorded with the ATLAS detector. The data used for this analysis has an integrated luminosity of $L_{\text{Int}}^{\text{Data}} = 36.1\,\text{fb}^{-1}$. Each MC sample has to be scaled such that its integrated luminosity L_{Int} matches with $L_{\text{Int}}^{\text{Data}}$. The values of L_{Int} for each MC simulation can be found in the corresponding tables in section 4.2. In order to account for this difference the scale factor

$$SF_{\text{Lumi}} = \frac{L_{\text{Int}}^{\text{Data}}}{L_{\text{Int}}} \tag{4.2}$$

is applied to each MC sample.

4.5.2 Correction Factors

In addition to the mandatory luminosity scale factor there are correction factors that are applied to the MC simulation in order to achieve a better agreement with data. These disagreements between data and the MC simulations result due to the models and predictions that have been used to create the MC simulation. Since the models and predictions are not fully accurate the following correction factors are introduced:

Theoretical Correction Factors
Theoretical correction factors in form of k-factors are applied to the MC simulation of the Drell-Yan process as described in section 4.2.1. Figure 4.12 shows the correction factor of each single theoretical correction as well as their combination which is the product of all correction factors. It can be seen that the correction due to the EW k-factor corrects the MC expectation to lower values while the PI k-factor corrects strongly in the opposite direction. The QCD k-factor adjusts the expectation to higher values up to an invariant mass of around 3 TeV and pulls the expectation to lower values for higher invariant masses. The combined theoretical correction to the Drell-Yan expectation for invariant masses of up to around 2 TeV is positive and in the order of 0-7 %. Above invariant masses of 2 TeV the combined theoretical correction is negative and in the range of 0-8 %. The top and diboson processes are corrected with global k-factors. For the $pp \to t\bar{t} + X$ contribution a k-factor of 1.19 is used while the $pp \to W^- t + X$ and $pp \to W^+ \bar{t} + X$ contributions are corrected with a factor of 1.05. For the diboson contributions the k-factor $0.91 \cdot k_{\text{Process}}$ is applied with $k_{\text{Process}} = 1.49$ for the $pp \to l'^{\pm}\nu_{l'} l^+ l^- + X$ contribution, $k_{\text{Process}} = 1.86$ for the $pp \to l'^+ l'^- l^+ l^- + X$ contribution, $k_{\text{Process}} = 1.54$ for the $pp \to l^+ \nu_l l^- \nu_l + X$ contribution and $k_{\text{Process}} = 0.80$ for the $pp \to q\bar{q}^{(\prime)} l^+ l^- + X$ contribution.

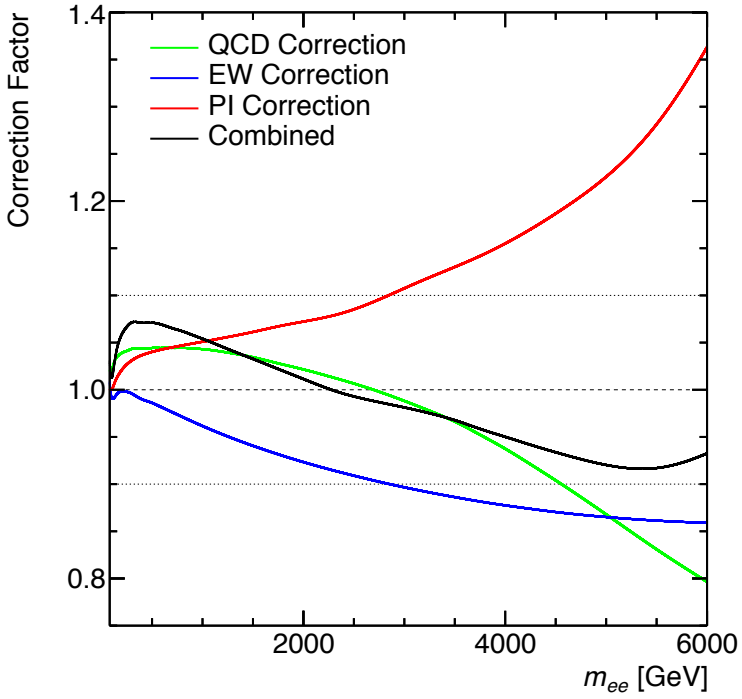

Figure 4.12: Magnitudes of the QCD, EW and PI k-factors as described in section 4.2.1. [116]

Pile-up Reweighting Correction Factor
Since the MC simulations are produced before or during the data taking period the pile-up conditions in data can only be guessed for the preceding MC simulations (see section 3.2.8). Therefore a reweighting of the simulated pile-up conditions to the conditions found in data has to be done. This is achieved with a correction factor reflecting the discrepancy between the measured and the simulated average number of interactions per beam crossing $\langle\mu_{\text{Data}}\rangle$ and $\langle\mu_{\text{MC}}\rangle$. One method to extract these values is to average the recorded $\langle\mu\rangle$ values for each event over a luminosity block and over all bunch crossing IDs (BCID). A second method is to only average the recorded $\langle\mu\rangle$ values over the lumi block but leave the dependence on the BCID. Due to dependencies amongst the BCIDs caused by different bunch currents and different emittances the second method is preferred over the first method.

Lepton Energy/Momentum Scale and Resolution Correction Factor
The electron energy scale and electron resolution show discrepancies between data and the MC simulation. This is observed using $Z \to ee$ events and comparing the resonant peak around 91 GeV in the invariant mass spectrum. The displacement of the position of the peak is corresponding to the electron energy scale correction factor while the difference in the width of the resonance is corresponding to the electron resolution correction factor. Both correction factors have been measured as a function of η and are extracted using multivariate algorithms [117]. Likewise to the electrons the muon momentum scale and muon resolution shows discrepancies between data and the MC simulation when comparing the resonant peak in the invariant mass spectrum using $Z \to \mu\mu$ events. Both correction factors are extracted using a maximum likelihood fit comparing templates of the invariant mass distribution of the MC simulation to the invariant mass distribution measured in data [118].

Lepton Efficiency Correction Factors
The lepton reconstruction, identification, isolation and trigger efficiencies show discrepancies between data and the MC simulations. This is observed when extracting the efficiencies in data and MC simulations using the Z resonance. The efficiencies are extracted with a tag-and-probe method. For both electrons and muons correction factors for the reconstruction efficiency, the isolation efficiency and the trigger efficiency are extracted. In case of electrons a correction factor for the identification efficiency is extracted. In case of muons a correction factor for the track to vertex association (TTVA) is extracted. Detailed information on the procedure can be taken from [119] for the electron efficiencies and from [118] for the muon efficiencies.

4.5.3 Drell-Yan Background Estimation

The Drell-Yan background is estimated using the MC simulations outlined in table 4.1. The simulation is split into 20 different bins of dilepton invariant mass covering the full spectrum with high statistics. Figure 4.13 shows the invariant mass spectrum of the dilepton and dimuon final states after applying the selection criteria discussed in section 4.4. Migrations from one invariant mass bin to a close by invariant mass bin occur due to resolution effects. The edges of the invariant mass bins of the MC simulations are set at generation level where the transverse

momenta of the particles are precisely known. At reconstruction level, however, the transverse momenta of the leptons have a finite resolution which allows the migration of some events into higher or lower bins of invariant mass. This effect is stronger for muons especially at high invariant masses since the resolution of the momenta gets worse in this range. Table 4.8 shows the number of events remaining after each

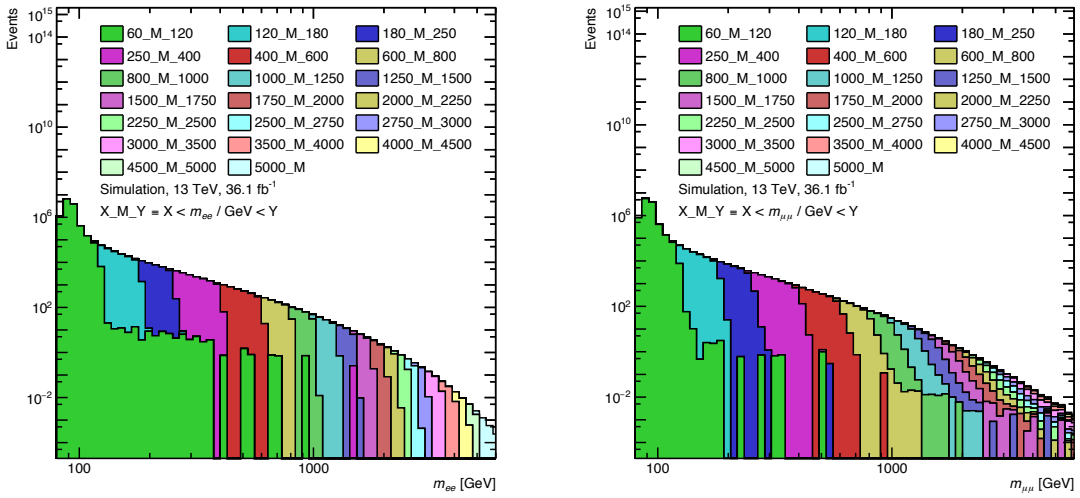

Figure 4.13: Drell-Yan background as a function of the invariant mass of the dielectron final states (left) and the dimuon final states (right).

criterion of the dilepton selection has been applied as well as the fraction of events remaining compared to the total number of events. The MC corrections discussed in section 4.5.2 and their impact on the number of combined dilepton events can be seen at the bottom of the table. As can be seen the GRL criterion as well as the event cleaning criterion do not have an impact on the MC simulation since these criteria are only applied on data. The different number of total events between the dielectron and the dimuon final states results due to a different number of simulated events as can be seen in table 4.1. The trigger has a large impact on the number of events by discarding almost two thirds of all dielectron events and more than 40 % of all dimuon events. The "number of leptons" criterion only has a small impact on dielectron events. This is due to the trigger which already discards events including only one electron with a high efficiency. Dimuon events, however, are discriminated by single muon triggers also leaving events with only one muon included. As a result the "number of leptons" criterion has a large impact on dimuon events. The pseudo-rapidity criterion as well as the object quality criterion are only applied on dielectron events but have a rather small impact. The transverse momentum criterion in contrast has a large effect on both types of final states discarding around one third of all remaining events. The identification criterion has a smaller impact on dielectron events but a larger impact on dimuon events by discarding almost 40 %. The following criteria namely both impact parameter, the isolation and the dilepton selection criteria only have a minor impact leaving almost 13 million dielectron events and slightly more than 12 million dimuon events of the Drell-Yan background. The largest correction for the dielectron final states is the identification efficiency correction factor correcting down the number of dielectron events by 5 %. The sec-

Table 4.8: Number of Drell-Yan events N_{Events} remaining after each selection criterion. The luminosity scale factor is applied such that N_{Events} corresponds to an integrated luminosity of $36.1\,\text{fb}^{-1}$. N_{Events} is rounded to be an integer. $\epsilon_{\text{Criterion}}$ is the number of events remaining after each criterion divided by the total number of events. $\epsilon_{\text{Correction}}$ is the number of events after each correction divided by the number of events after the dilepton selection.

Selection Criterion	N_{Events}		$\epsilon_{\text{Criterion}}$ [%]	
	ee	$\mu\mu$	ee	$\mu\mu$
Total	68590245	68590034	100.0	100.0
GRL	68590245	68590034	100.0	100.0
Trigger	23581329	40455466	34.4	59.0
Event Cleaning	23581329	40455466	34.4	59.0
$N_{\text{Candidates}}$	23549434	31190281	34.3	45.5
$\lvert\eta\rvert$	22812672	—	33.3	—
Object Quality	22753298	—	33.2	—
p_{T}	15327554	20273444	22.3	29.6
Identification	14028555	12896387	20.5	18.8
$\lvert d_0\rvert/\sqrt{\sigma_{d_0}}$	14001134	12736134	20.4	18.6
$\lvert z_0\rvert \cdot \sin\theta$	13894584	12699912	20.3	18.5
Isolation	13393763	12447315	19.5	18.1
Dilepton Selection	12956245	12000446	18.9	17.5
Corrections			$\epsilon_{\text{Correction}}$ [%]	
Pile-up	12923880	11966390	99.8	99.7
Reconstruction	12950068	11287177	100.0	94.1
Isolation	12948878	11955337	99.9	99.6
Trigger	12874496	12000432	99.4	100.0
Identification	12306284	—	95.0	—
TTVA	—	11698890	—	97.5
k-factor	13166226	12194692	101.6	101.6
Combined	12381687	11107771	95.6	92.6

ond largest correction is the k-factor acting in the opposite direction by 1.6 %. All corrections combined correct the number of dielectron events down by 4.4 %. The largest correction on dimuon events is the reconstruction efficiency correction factor correcting 5.9 % downwards. The TTVA efficiency correction factor has an impact of 2.5 % downwards. The combined number of dimuon events is corrected to be 7.4 % lower than the number of dimuon events passing the selection criteria.

4.5.4 Top Background Estimation

The top background estimate as a function of the invariant mass of the dilepton system can be seen in figure 4.14. In contrast to the Drell-Yan background the top background is estimated using the MC simulations from table 4.2 which are not simulated in separated regions of dilepton invariant mass. Therefore the statistics at high values of invariant mass are significantly lower. In fact above invariant masses of 2 TeV no dilepton events from the top background survive the selection criteria. Therefore the top background is extrapolated to higher invariant masses using the function

$$f(m_{ll}) = p_0 \left(1 - \frac{m_{ll}}{13\,\text{TeV}}\right)^{p_1} \left(\frac{m_{ll}}{13\,\text{TeV}}\right)^{p_2}. \tag{4.3}$$

This extrapolation function can be limited to be monotonically decreasing with higher values of m_{ll} by limiting the free parameters p_0, p_1 and p_2. Another important feature is that the function vanishes to zero at a mass of $m_{ll} = 13\,\text{TeV}$ which is the kinematically highest accessible value of the invariant mass of a dilepton event in the proton-proton collisions. The starting point of the fitted region is varied between 200 GeV and 400 GeV in 25 GeV steps while the ending point is fixed at 13 TeV. This yields nine different extrapolations as can be seen in figure 4.14. The arithmetic mean of all extrapolations is calculated and taken as the top background estimate from 800 GeV upwards. The extrapolation uncertainty can be seen in the lower plots of figure 4.14. It is estimated by taking the largest difference of the arithmetic mean and the highest or lowest extrapolation value in each bin. In table 4.9 the selected top background events after each selection criterion as well as after each correction can be seen. In contrast to the Drell-Yan background the top background does not feature the peak of the Z boson decay at an invariant mass of 91 GeV. Therefore the dielectron trigger does already discard more than 90 % of all dielectron events. In both channels only around 2 % of all top background events and a total number of around 74000 events in the dielectron channel and around 59000 events in the dimuon channel survive all selection criteria. The largest correction in both channels is the k-factor correcting the total numbers upwards by about 18 %.

4.5.5 Diboson Background Estimation

Similarly to the Drell-Yan background the diboson background is estimated using MC samples sliced in bins of invariant mass as can be seen in table 4.3. Eight samples are used in order to achieve a large statistic of diboson events especially at high invariant masses. This estimate can be seen in figure 4.15 where also the migration effect due to the resolution especially in the dimuon channel can be observed. Due to the $pp \to lll'l' + X$, $pp \to l\nu_l l'l' + X$ and $pp \to qql'l' + X$ processes contributing to the total diboson background a peak due to the Z boson decay is present in the diboson background. Table 4.10 shows the number of events remaining after

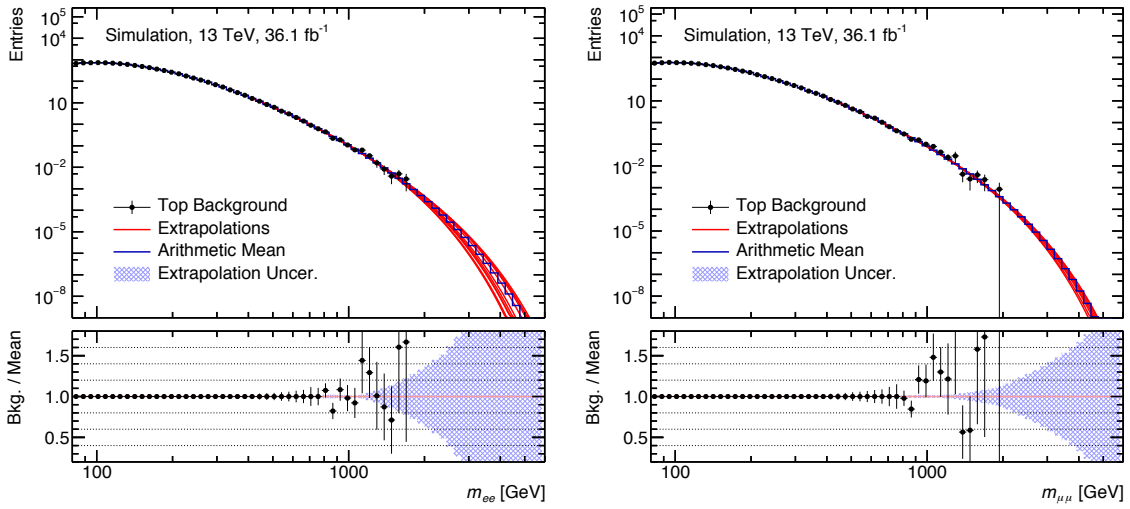

Figure 4.14: Top background as a function of the invariant mass of the dielectron final state (left) and the dimuon final state (right) and the corresponding extrapolations.

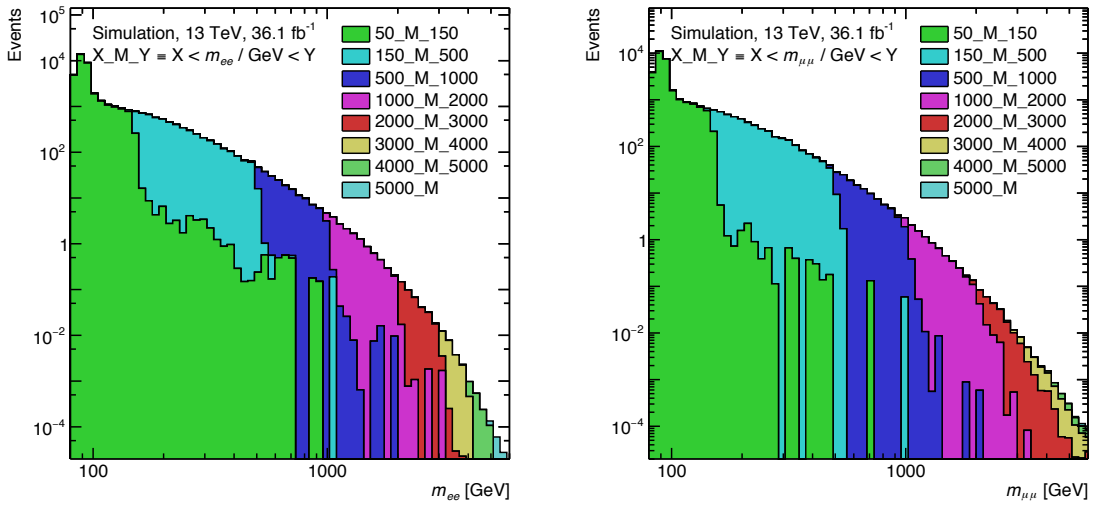

Figure 4.15: Diboson background as a function of the invariant mass of the dielectron final state (left) and the dimuon final state (right).

Table 4.9: Number of top events N_{Events} remaining after each selection criterion. The luminosity scale factor is applied such that N_{Events} corresponds to an integrated luminosity of 36.1 fb^{-1}. N_{Events} is rounded to be an integer. $\epsilon_{\text{Criterion}}$ is the number of events remaining after each criterion divided by the total number of events. $\epsilon_{\text{Correction}}$ is the number of events after each correction divided by the number of events after the dilepton selection.

Selection Criterion	N_{Events}		$\epsilon_{\text{Criterion}}$ [%]	
	ee	$\mu\mu$	ee	$\mu\mu$
Total	2903754	2903792	100.0	100.0
GRL	2903754	2903792	100.0	100.0
Trigger	200823	1016668	6.9	35.0
Event Cleaning	200823	1016668	6.9	35.0
$N_{\text{Candidates}}$	200813	610703	6.9	21.0
$\lvert\eta\rvert$	200439	—	6.9	—
Object Quality	200406	—	6.9	—
p_{T}	135393	159113	4.7	5.5
Identification	103728	99253	3.6	3.4
$\lvert d_0\rvert/\sqrt{\sigma_{d_0}}$	102542	86340	3.5	3.0
$\lvert z_0\rvert \cdot \sin\theta$	102464	86225	3.5	3.0
Isolation	95425	76631	3.3	2.6
Dilepton Selection	74407	59219	2.6	2.0
Corrections			$\epsilon_{\text{Correction}}$ [%]	
Pile-up	74300	59019	99.9	99.7
Reconstruction	74390	56414	100.0	95.3
Isolation	74308	59034	99.9	99.7
Trigger	74066	59217	99.5	100.0
Identification	71784	—	96.5	—
TTVA	—	57620	—	97.3
k-factor	87877	69950	118.1	118.1
Combined	84133	64411	113.1	108.8

each criterion of the dilepton selection has been applied as well as the fraction of events remaining compared to the total number of events. The MC corrections discussed in section 4.5.2 and their impact on the number of combined dilepton events can be seen at the bottom of the table. The number of dilepton events surviving the selection criteria is around 43000 in the dielectron channel and around 36000 in the dimuon channel which is around 13 % and 11 % of the total number of events respectively. The largest correction to the dielectron final states is the identification efficiency correction. The dimuon final states are mainly affected by the reconstruction efficiency correction.

Table 4.10: Number of diboson events N_{Events} remaining after each selection criterion. The luminosity scale factor is applied such that N_{Events} corresponds to an integrated luminosity of $36.1\,\text{fb}^{-1}$. N_{Events} is rounded to be an integer. $\epsilon_{\text{Criterion}}$ is the number of events remaining after each criterion divided by the total number of events. $\epsilon_{\text{Correction}}$ is the number of events after each correction divided by the number of events after the dilepton selection.

Selection Criterion	N_{Events}		$\epsilon_{\text{Criterion}}$ [%]	
	ee	$\mu\mu$	ee	$\mu\mu$
Total	326755	319311	100.0	100.0
GRL	326755	319311	100.0	100.0
Trigger	102032	177722	31.2	55.7
Event Cleaning	102032	177722	31.2	55.7
$N_{\text{Candidates}}$	101942	143944	31.2	45.1
$\lvert\eta\rvert$	99997	—	30.6	—
Object Quality	99828	—	30.6	—
p_{T}	58984	70920	18.1	22.2
Identification	51287	45303	15.7	14.2
$\lvert d_0\rvert/\sqrt{\sigma_{d_0}}$	51168	44310	15.7	13.9
$\lvert z_0\rvert \cdot \sin\theta$	50648	44095	15.5	13.8
Isolation	48135	42060	14.7	13.2
Dilepton Selection	42509	36054	13.0	11.3
Corrections			$\epsilon_{\text{Correction}}$ [%]	
Pile-up	42342	35862	99.6	99.5
Reconstruction	42493	34000	100.0	94.3
Isolation	42468	35928	99.9	99.7
Trigger	42269	36054	99.4	100.0
Identification	40645	—	95.6	—
TTVA	—	35136	—	97.5
k-factor	43676	36204	102.7	100.4
Combined	41283	32954	97.1	91.4

4.6 Fake Background Estimation

The fake background arises due to W+jets and multi-jet production as described in section 4.2.4. Since most of the energy of a jet is deposited in the electromagnetic

calorimeter a jet signature can be similar to an electron signature. In order to fake a muon, however, the jet needs to leave signatures in the muon spectrometer which is a rare scenario. By applying the above selection criteria for muons on a W+jets and a dijet sample it has been checked that the contribution is negligible compared to the total background. The fake background due to faked electrons in contrast has a non-negligible contribution. A data-driven method is used to estimate the electron fake background. A MC simulation of the fake background is not used due to two reasons. Firstly the necessary models are not describing the fake background sufficiently well. Secondly the computation of the MC simulation would need a lot of computing power and computing storage. This has to do with the fact that the probability of a jet faking an electron is typically small. As a result a lot of events need to be simulated in order to get a sufficient statistical set of fake background events. The following sections describe the strategy used for the estimate of the electron fake background.

4.6.1 General Idea

The general idea to estimate the fake background contribution is to use probabilities that describe how likely it is that a reconstructed electron is a true electron or an object faking an electron. These probabilities can be extracted from data and MC simulations as will be demonstrated in the next sections. A mathematical procedure called the *Matrix Method* is then used to extract a formula based on the above-mentioned probabilities to estimate the fake background contribution from data. In order to understand the general idea of this procedure in detail, a few definitions will be given first:

Real Electron (R)
A real electron is a reconstructed electron from which it is known that it is a true electron.

Fake Electron (F)
A fake electron is a reconstructed electron from which it is known that it is not a true electron.

Full Set of Selection Criteria
The full set of selection criteria contains all event selection criteria discussed in section 4.4.1 and all lepton selection criteria discussed in section 4.4.2. However, the "number of electrons" criterion is not applied since this selection aims at a set of leptons rather than a set of events. Note that also the dilepton selection criteria (see section 4.4.3) are not applied.

Loosened Set of Selection Criteria
The loosened set of selection criteria contains all selection criteria from the full set apart from the identification criterion and the isolation criterion. Instead the identification criterion is loosened to *LHLoose* while the isolation criterion is not applied at all.

Real Efficiency ϵ_r
The real efficiency is the probability that a real electron passing the loosened set of selection criteria also passes the full set of selection criteria.

Fake Efficiency ϵ_f
The fake efficiency is the probability that a fake electron passing the loosened set of selection criteria also passes the full set of selection criteria.

Figure 4.16 illustrates the different steps of the estimation procedure. First a set of real (fake) electrons has to be extracted which can be done with data or MC simulations. Then the loosened set and the full set of selection criteria are applied to the set of real (fake) electrons. This leads to the two subsets of real (fake) electrons after the loosened selection and after the full selection. The set of real (fake) electrons after the full selection is a subset of the set of real (fake) electrons after the loosened selection. In the next step the real (fake) efficiencies are calculated which serve as an input for the mathematical expressions of the Matrix Method. In the last step the Matrix Method uses the data from which the fake background estimate is extracted.

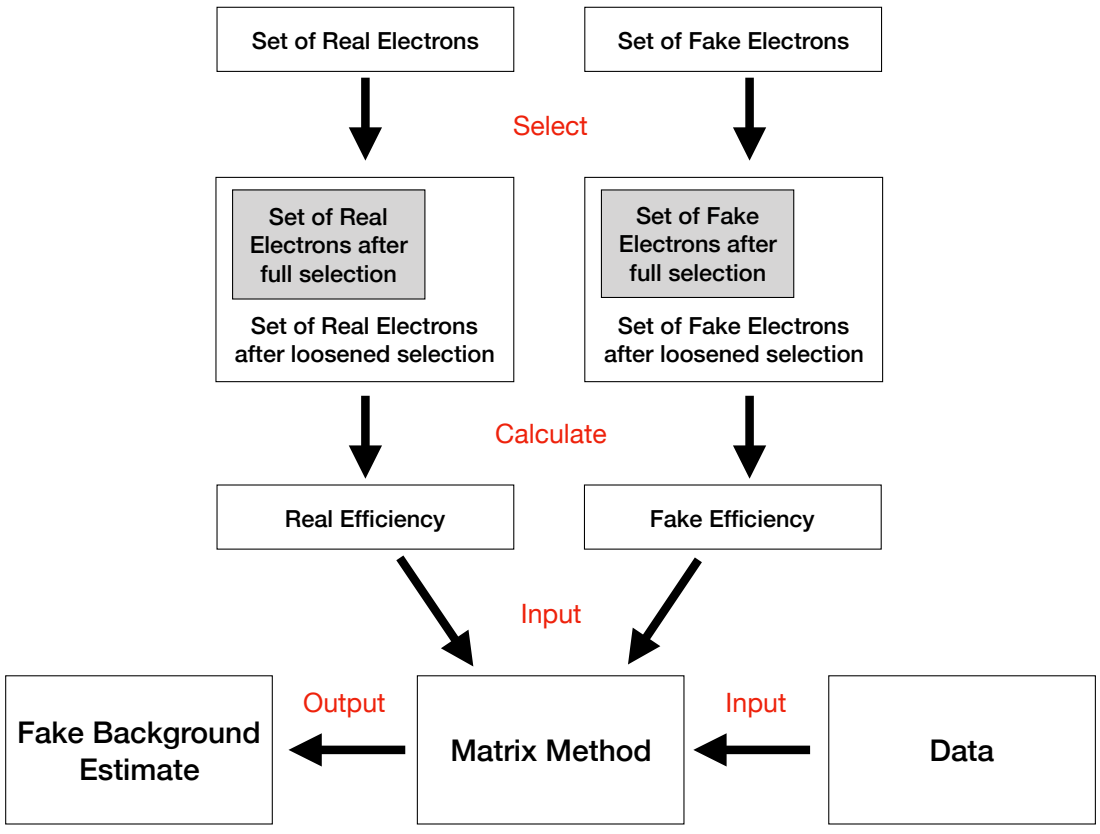

Figure 4.16: Schematic illustration reflecting the general idea of the procedure to estimate the fake background.

4.6.2 Real Efficiency Determination

The literal definition of the real efficiency ϵ_{r} has already been given in section 4.6.1. Formally this definition leads to

$$\epsilon_{\mathrm{r}} = \left.\frac{N_{\mathrm{full}}}{N_{\mathrm{loosened}}}\right|_{\text{real electrons}} \tag{4.4}$$

where N_{loosened} is the number of real electrons passing the loosened set of selection criteria and N_{full} is the number of real electrons passing the full set of selection criteria. The set of real electrons can be extracted from data or MC simulations. An extraction from data can be achieved by requiring the electrons to originate from a Z boson decay. Therefore a criterion checking for the reconstructed mass of the event to be close to the PDG value of the Z boson mass could be used. However, in data a truth level does not exist such that the extracted electrons could still be fake electrons. Thus, there would always be a small fraction of fake electrons contributing to the set of real electrons when using data. It is easier to gain the real electrons from a MC simulation which provides not only the information at the reconstruction level as in data but also the information at the truth level. In this case one can check for an electron at truth level and knows that the linked electron at reconstruction level is a real electron. A drawback of using MC simulations is of course that the data is not described perfectly. However, it is assumed that MC simulations are a more reliable approach to estimate the real efficiency. It has also been checked that the real efficiencies estimated with data are close to the ones estimated with MC simulations. A simulation of the Drell-Yan process has been used to estimate N_{loosened}, N_{full} and ϵ_{r} respectively. N_{loosened} and N_{full} have been determined as a function of p_{T} and $|\eta|$ and can be seen in figure 4.17. The left hand

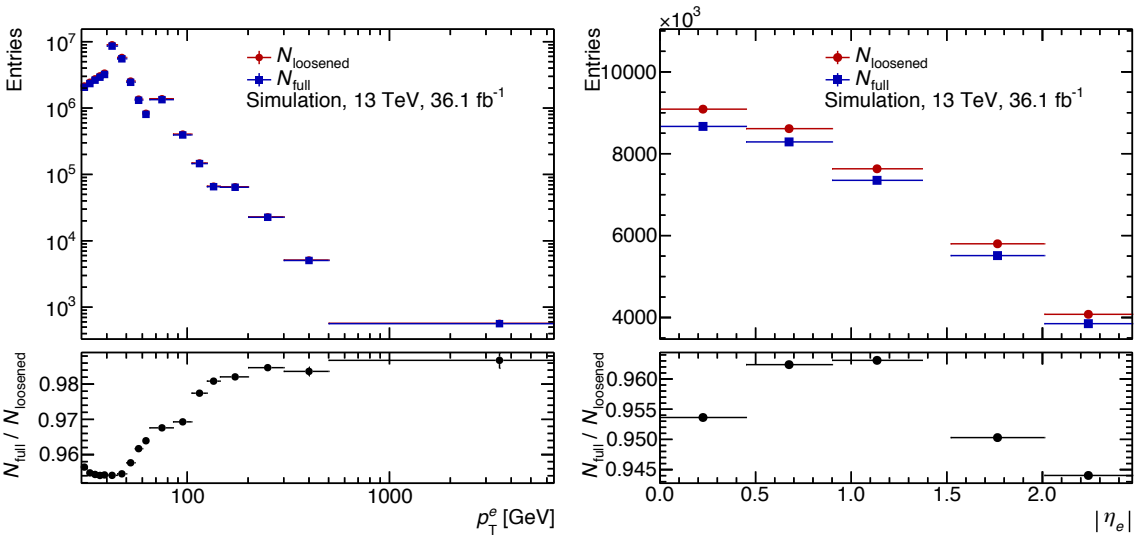

Figure 4.17: Number of real electrons passing the loosened set of selection criteria N_{loosened} and number of real electrons passing the full set of selection criteria N_{full} as a function of the transverse momentum p_{T} (left) and the absolute pseudo-rapidity $|\eta|$ (right). The lower plots show the ratio of both numbers which according to equation 4.4 is the real efficiency ϵ_{r}.

plot in figure 4.17 showing the dependence of N_{loosened} and N_{full} on the transverse

momentum has varying bin sizes. Therefore the number of entries per bin can change strongly when the bin size changes from one bin to another. An increase of the entries can be seen in both N_{loosened} and N_{full} up to a value of 45 GeV in p_{T}. For larger p_{T} values the entries keep decreasing. This is expected since electrons from Z boson decays predominantly carry a p_{T} of half the Z boson mass. The right hand plot in figure 4.17 shows the dependence of N_{loosened} and N_{full} on the absolute pseudo-rapidity. It can be observed that both values keep decreasing for higher values of $|\eta|$. The contribution to N_{loosened} and N_{full} at higher values of $|\eta|$ is predominantly due to boosted Z bosons meaning Z bosons with a high p_{T}. As a result since the Z boson p_{T} distribution decreases for higher p_{T} values the pseudo-rapidity distribution of N_{loosened} and N_{full} decreases as well for higher values of $|\eta|$. The lower plots of figure 4.17 show the real efficiency integrated over the whole range of p_{T} (left) and $|\eta|$ (right). In figure 4.18 the real efficiency in dependence on both p_{T} and $|\eta|$ can be seen together. The real efficiency has values from 94.5 % to 96 % below a p_{T}

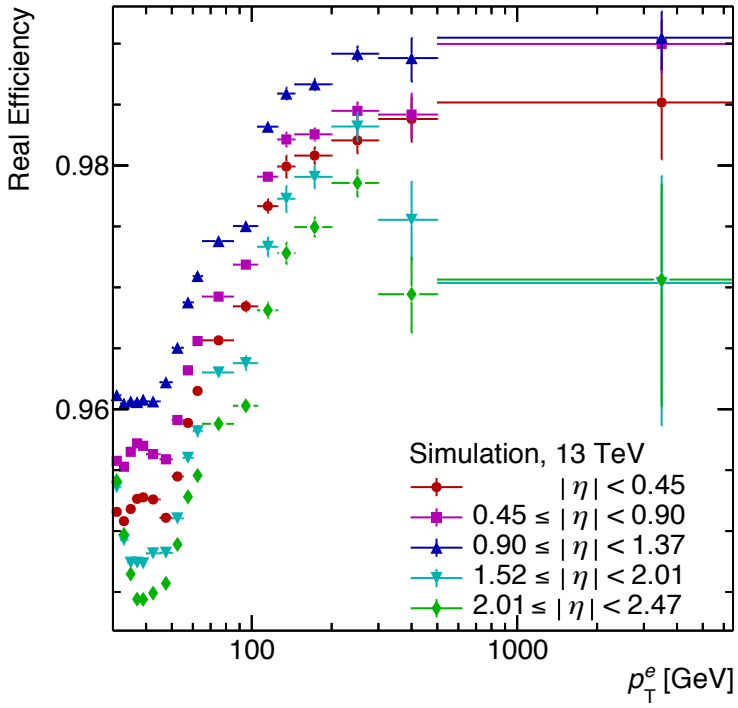

Figure 4.18: Real efficiency ϵ_{r} as a function of the transverse momentum p_{T} for different absolute pseudo-rapidity ranges of the electrons.

of 50 GeV. From a p_{T} of 50 GeV to 200 GeV the real efficiency rises and remains between 97 % and 99 % for p_{T} values of more than 200 GeV. It is also observed that the real efficiencies are smaller in the endcap region ($1.52 < |\eta| < 2.47$) than in the barrel region ($|\eta| < 1.37$). In the endcap region the real efficiency is lower for larger values of $|\eta|$ while in the barrel region the real efficiency is higher for larger values of $|\eta|$. The behavior may have to do with a slightly varying detector equipment in the different pseudo-rapidity regions. However, these effects have not been studied further.

4.6.3 Fake Efficiency Determination

The literal definition of the fake efficiency ϵ_{f} has already been given in section 4.6.1. Formally this definition leads to

$$\epsilon_{\mathrm{f}} = \left.\frac{N_{\mathrm{full}}}{N_{\mathrm{loosened}}}\right|_{\text{fake electrons}} \tag{4.5}$$

where N_{loosened} is the number of fake electrons passing the loosened set of selection criteria and N_{full} is the number of fake electrons passing the full set of selection criteria. The set of fake electrons is extracted from data with the additional use of MC simulations. A set of electrons enriched with fake electrons can be gained from data by suppressing all relevant processes leading to at least one real electron. Within this analysis these processes are the charged current Drell-Yan process or W boson decay as described in section 4.2.5 and the neutral current Drell-Yan process as described in section 4.2.1. Events from the Drell-Yan process are suppressed by a mass window according to

$$|m_{ee} - m_Z| < 20\,\mathrm{GeV} \tag{4.6}$$

where m_{ee} is the reconstructed invariant mass of the event and m_Z is the PDG value of the Z boson mass [120]. Additionally all events containing two or more electrons passing the full set of selection criteria are discarded as well. Events from $W^{\pm}$ boson decays are suppressed by requiring the missing transverse energy of the event to be smaller than 25 GeV. Applying the above mentioned criteria on data creates the sets of electrons $N^{\mathrm{Data}}_{\mathrm{loosened}}$ and $N^{\mathrm{Data}}_{\mathrm{full}}$ that are enriched with fake electrons but still contain a fraction of real electrons. In order to loose this real electron contribution MC simulations of all considered background processes discussed in section 4.2 are used. In the same way as on data the above criteria to suppress events from the Drell-Yan process and the decay of a $W^{\pm}$ bosons are also applied on these simulations. This creates the sets of real electrons $N^{\mathrm{Simulation}}_{\mathrm{loosened}}$ and $N^{\mathrm{Simulation}}_{\mathrm{full}}$ resembling the fraction of real electrons in the fake enriched sets of electrons. Hence subtracting the real electrons estimated with the MC simulations from the fake enriched set of electrons results in a pure set of fake electrons. Thus equation 4.7 needs to be altered to

$$\epsilon_{\mathrm{f}} = \frac{N^{\mathrm{Data}}_{\mathrm{full}} - N^{\mathrm{Simulation}}_{\mathrm{full}}}{N^{\mathrm{Data}}_{\mathrm{loosened}} - N^{\mathrm{Simulation}}_{\mathrm{loosened}}}. \tag{4.7}$$

The fake efficiency has been measured as a function of the transverse momentum p_{T} and the absolute pseudo-rapidity $|\eta|$ of the electrons. Figure 4.19 shows the set of fake enriched electrons extracted from data as well as the real electron contribution extracted from simulations for the loosened and the full set of selection criteria. The left hand plot of figure 4.19 shows the dependence of N^{Data} and $N^{\mathrm{Simulation}}$ for the loosened set of selection criteria (top) and the full set of selection criteria (bottom) as a function of p_{T}. The bin sizes can differ from one bin to another which causes the stepwise behavior. In general N^{Data} and $N^{\mathrm{Simulation}}$ decrease for higher values of p_{T} which is expected since fake electrons are predominantly caused by non-resonant jets. The right hand plot of figure 4.19 shows the dependence of N^{Data} and $N^{\mathrm{Simulation}}$ for the loosened set of selection criteria (top) and the full set of selection criteria (bottom) as a function of $|\eta|$. It can be seen that N^{Data} increases while $N^{\mathrm{Simulation}}$ stays rather constant as a function of $|\eta|$. The number of pure fake electrons which

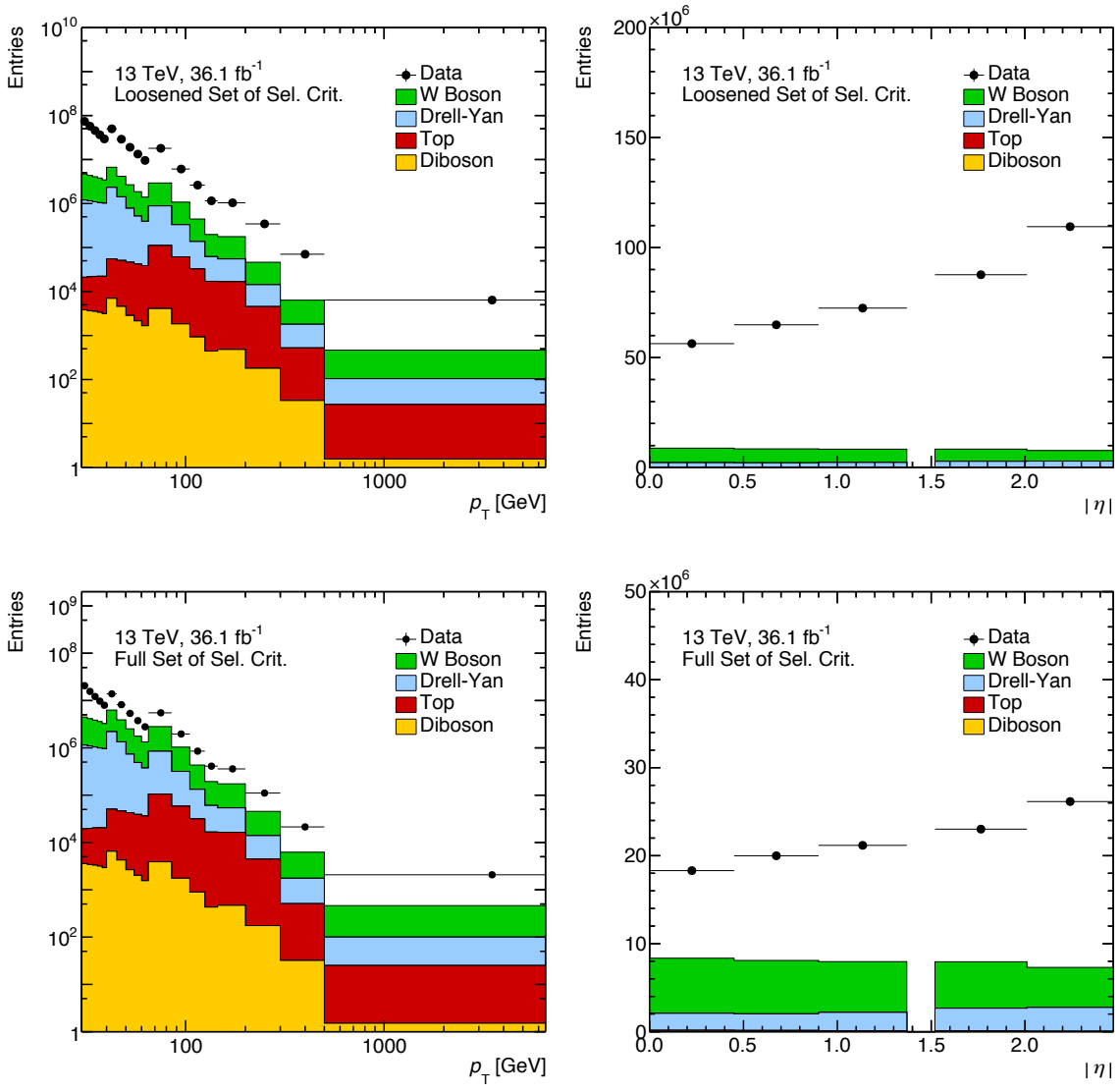

Figure 4.19: Measurement of the set of fake enriched electrons and their real contribution passing the loosened set of selection criteria (top) and the full set of selection criteria (bottom) as a function of the transverse momentum p_{T} (left) and the absolute pseudo-rapidity $|\eta|$ (right) of the electrons.

is the number of electrons enriched with fake electrons N^{Data} subtracted by the real electron contribution $N^{\text{Simulation}}$ is shown in figure 4.20. Both N_{loosened} and N_{full} show

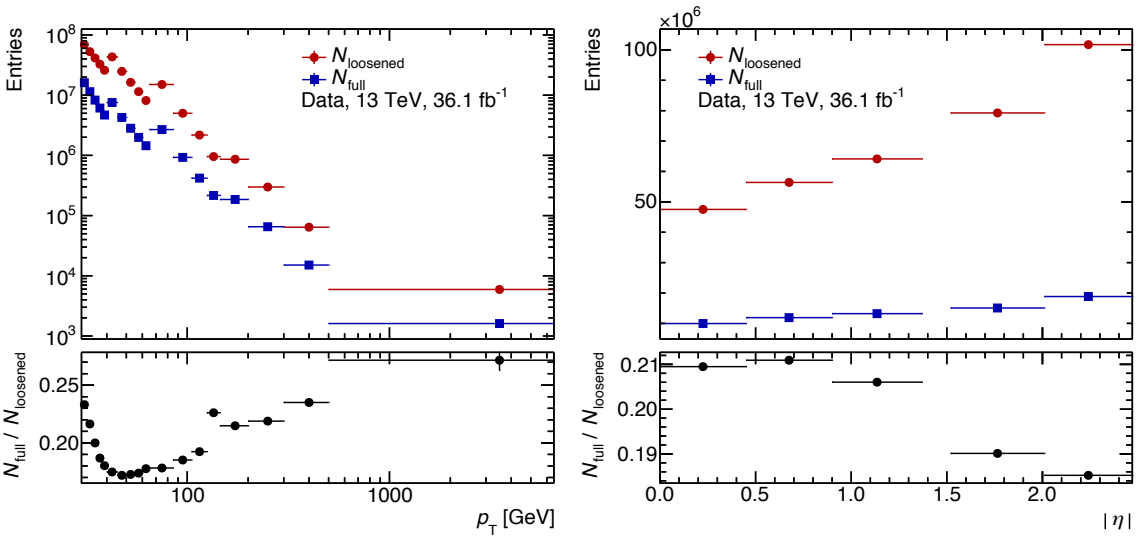

Figure 4.20: Measurement of the number of fake electrons as a function of the transverse momentum p_{T} (left) and the absolute pseudo-rapidity $|\eta|$ (right) of the electrons. The lower plots show the ratio of both numbers which according to equation 4.5 is the fake efficiency.

a decreasing behavior as a function of p_{T} and an increasing behavior as a function of $|\eta|$ as has been explained for figure 4.19. The lower plots of figure 4.20 only show the fake efficiency integrated over the whole range of p_{T} (left) and $|\eta|$ (right). In figure 4.21 the fake efficiency in dependence on both p_{T} and $|\eta|$ can be seen together. At a p_{T} of 30 GeV the fake efficiencies have values between 22 % and 25 %. From 30 GeV to 50 GeV the fake efficiencies drop to a level between 16 % and 18 %. From 50 GeV upwards the fake efficiencies keep rising to values between 22 % and 33 %. The dip of the fake efficiency between a p_{T} of 30 GeV and 50 GeV can be explained with the decays $Z \to q\bar{q}$ and $W^{\pm} \to q\bar{q}'$. These contributions are not suppressed by the above criteria on the dielectron invariant mass m_{ee} and the missing transverse energy. Both contributions are negligible outside the region of 30 GeV to 50 GeV in p_{T} since the quarks of the Z and $W^{\pm}$ decays will predominantly have a p_{T} of around 45 GeV and 40 GeV respectively. A dijet MC simulation has been used to check how many particles pass the full and the loosened set of selection criteria. As a result due to the stronger identification criterion and the applied isolation criterion the full set of selection criteria suppresses the $Z \to q\bar{q}$ and $W^{\pm} \to q\bar{q}'$ contributions stronger than the loosened set of selection criteria, especially in the discussed region of p_{T}. Hence when dividing N_{full} by N_{loosened} this leads to a dip in the fake efficiency in this region.

4.6.4 The Matrix Method

The Matrix Method is a procedure to estimate the fake background from data. The main ingredients are the real efficiency ϵ_{r} and the fake efficiency ϵ_{f}. These can be used to create a formalism that connects the number reconstructed events with the

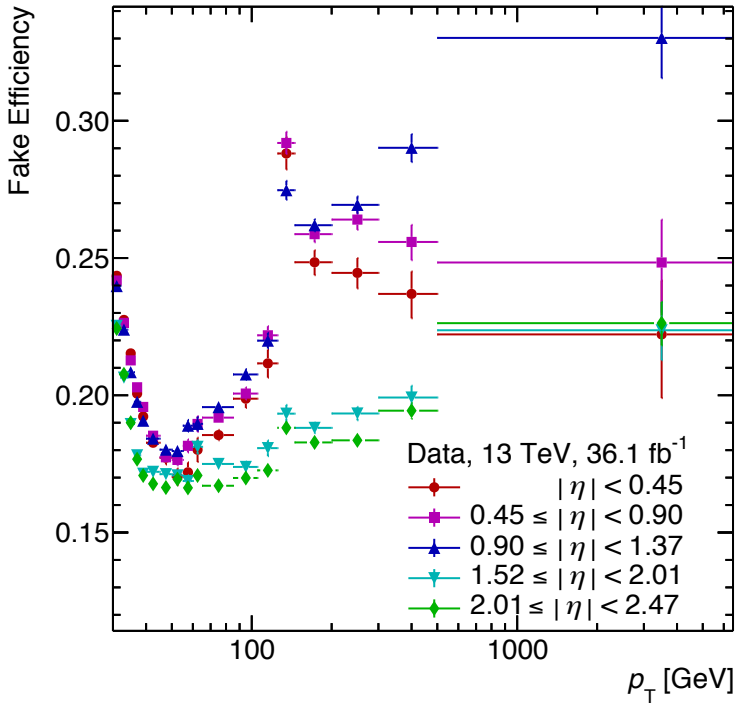

Figure 4.21: Measurement of the fake efficiency f as a function of the transverse momentum p_{T} and the absolute pseudo-rapidity $|\eta|$ of the electrons.

number of events containing a maximum of only one real electron and at least one fake electron. In order to build this formalism a few definitions will be needed first:

Loose Electron (L)
A loose electron is an electron passing the loosened set of selection criteria as defined in section 4.6.1 but failing the *LHMedium* identification or the *loose* isolation criteria additionally applied in the full set of selection criteria.

Tight Electron (T)
A tight electron is an electron passing the full set of selection criteria as defined in section 4.6.1.

With these definitions the reconstructed quantities N_{TT}, N_{TL}, N_{LT} and N_{LL} which denote the number of events with two tight electrons, one tight and one loose electron, one loose and one tight electron as well as two loose electrons can be measured in data. It is differentiated between the leading and the subleading electron such that the first index is labeling the leading electron and second index is labeling the subleading electron. In contrast to the reconstructed quantities there are the true quantities N_{RR}, N_{RF}, N_{FR} and N_{FF} which denote the number of events with two real electrons, one real and one fake electron, one fake and one real electron as well as two fake electrons. The aim is to gain an expression for N_{TT} in dependence of N_{RR}, N_{RF}, N_{FR} and N_{FF}. Since N_{TT} are the events entering the analysis this allows to extract the terms with the quantities N_{RF} and N_{FR} which describe the fake background due to one fake electron and the term with the quantity N_{FF} which describes the fake background due to two fake electrons. This can be achieved by

using the real and fake efficiencies to relate the reconstructed quantities to the true quantities. In the following the expressions

$$\tilde{x} = (1 - x) \quad \text{and} \quad \hat{x} = \frac{\tilde{x}}{x} \tag{4.8}$$

are used to shorten the equations for the mathematical formalism of the Matrix Method. In order to relate the reconstructed and the true quantities equation 4.9 can be build.

$$\begin{pmatrix} N_{\mathrm{TT}} \\ N_{\mathrm{TL}} \\ N_{\mathrm{LT}} \\ N_{\mathrm{LL}} \end{pmatrix} = \begin{pmatrix} \epsilon_{\mathrm{r}_1}\epsilon_{\mathrm{r}_2} & \epsilon_{\mathrm{r}_1}\epsilon_{\mathrm{f}_2} & \epsilon_{\mathrm{f}_1}\epsilon_{\mathrm{r}_2} & \epsilon_{\mathrm{f}_1}\epsilon_{\mathrm{f}_2} \\ \epsilon_{\mathrm{r}_1}\tilde{\epsilon}_{\mathrm{r}_2} & \epsilon_{\mathrm{r}_1}\tilde{\epsilon}_{\mathrm{f}_2} & \epsilon_{\mathrm{f}_1}\tilde{\epsilon}_{\mathrm{r}_2} & \epsilon_{\mathrm{f}_1}\tilde{\epsilon}_{\mathrm{f}_2} \\ \tilde{\epsilon}_{\mathrm{r}_1}\epsilon_{\mathrm{r}_2} & \tilde{\epsilon}_{\mathrm{r}_1}\epsilon_{\mathrm{f}_2} & \tilde{\epsilon}_{\mathrm{f}_1}\epsilon_{\mathrm{r}_2} & \tilde{\epsilon}_{\mathrm{f}_1}\epsilon_{\mathrm{f}_2} \\ \tilde{\epsilon}_{\mathrm{r}_1}\tilde{\epsilon}_{\mathrm{r}_2} & \tilde{\epsilon}_{\mathrm{r}_1}\tilde{\epsilon}_{\mathrm{f}_2} & \tilde{\epsilon}_{\mathrm{f}_1}\tilde{\epsilon}_{\mathrm{r}_2} & \tilde{\epsilon}_{\mathrm{f}_1}\tilde{\epsilon}_{\mathrm{f}_2} \end{pmatrix} \begin{pmatrix} N_{\mathrm{RR}} \\ N_{\mathrm{RF}} \\ N_{\mathrm{FR}} \\ N_{\mathrm{FF}} \end{pmatrix} \tag{4.9}$$

The coefficients ϵ_{r_1} (ϵ_{r_2}) and ϵ_{f_1} (ϵ_{f_2}) are the real efficiency and fake efficiency of the leading (subleading) electron, respectively. The number of events contributing to the signal N_{TT} can be expressed in equation 4.10 where $\mathcal{F}_{\mathrm{W+jets}}$ is describing the contribution due to W+jets production and $\mathcal{F}_{\mathrm{Multi\text{-}jet}}$ is describing the contribution due to multi-jet production.

$$N_{\mathrm{TT}} = \epsilon_{\mathrm{r}_1}\epsilon_{\mathrm{r}_2}N_{\mathrm{RR}} + \underbrace{\epsilon_{\mathrm{r}_1}\epsilon_{\mathrm{f}_2}N_{\mathrm{RF}} + \epsilon_{\mathrm{f}_1}\epsilon_{\mathrm{r}_2}N_{\mathrm{FR}}}_{=\mathcal{F}_{\mathrm{W+jets}}} + \underbrace{\epsilon_{\mathrm{f}_1}\epsilon_{\mathrm{f}_2}N_{\mathrm{FF}}}_{=\mathcal{F}_{\mathrm{Multi\text{-}jet}}} \tag{4.10}$$

The total fake background $\mathcal{F}$ is the sum of the W+jets and multi-jet contribution:

$$\mathcal{F} = \mathcal{F}_{\mathrm{W+jets}} + \mathcal{F}_{\mathrm{Multi\text{-}jet}} \tag{4.11}$$

As a result the true quantities N_{RF}, N_{FR} and N_{FF} need to be known in order to estimate the fake background $\mathcal{F}$. Expressions for these true quantities can be gained by inverting equation 4.9 as shown in equation 4.12.

$$\begin{pmatrix} N_{\mathrm{RR}} \\ N_{\mathrm{RF}} \\ N_{\mathrm{FR}} \\ N_{\mathrm{FF}} \end{pmatrix} = \frac{1}{\alpha} \begin{pmatrix} \tilde{\epsilon}_{\mathrm{f}_1}\tilde{\epsilon}_{\mathrm{f}_2} & -\tilde{\epsilon}_{\mathrm{f}_1}\epsilon_{\mathrm{f}_2} & -\epsilon_{\mathrm{f}_1}\tilde{\epsilon}_{\mathrm{f}_2} & \epsilon_{\mathrm{f}_1}\epsilon_{\mathrm{f}_2} \\ -\tilde{\epsilon}_{\mathrm{f}_1}\tilde{\epsilon}_{\mathrm{r}_2} & \tilde{\epsilon}_{\mathrm{f}_1}\epsilon_{\mathrm{r}_2} & \epsilon_{\mathrm{f}_1}\tilde{\epsilon}_{\mathrm{r}_2} & -\epsilon_{\mathrm{f}_1}\epsilon_{\mathrm{r}_2} \\ -\tilde{\epsilon}_{\mathrm{r}_1}\tilde{\epsilon}_{\mathrm{f}_2} & \tilde{\epsilon}_{\mathrm{r}_1}\epsilon_{\mathrm{f}_2} & \epsilon_{\mathrm{r}_1}\tilde{\epsilon}_{\mathrm{f}_2} & -\epsilon_{\mathrm{r}_1}\epsilon_{\mathrm{f}_2} \\ \tilde{\epsilon}_{\mathrm{r}_1}\tilde{\epsilon}_{\mathrm{r}_2} & -\tilde{\epsilon}_{\mathrm{r}_1}\epsilon_{\mathrm{r}_2} & -\epsilon_{\mathrm{r}_1}\tilde{\epsilon}_{\mathrm{r}_2} & \epsilon_{\mathrm{r}_1}\epsilon_{\mathrm{r}_2} \end{pmatrix} \begin{pmatrix} N_{\mathrm{TT}} \\ N_{\mathrm{TL}} \\ N_{\mathrm{LT}} \\ N_{\mathrm{LL}} \end{pmatrix} \tag{4.12}$$

$$\text{with} \quad \alpha = (\epsilon_{\mathrm{r}_1} - \epsilon_{\mathrm{f}_1})(\epsilon_{\mathrm{r}_2} - \epsilon_{\mathrm{f}_2})$$

By substituting N_{RF}, N_{FR} and N_{FF} in equation 4.10 with the expressions from equation 4.12 one gets to equation 4.13 which contains only the reconstructed quantities.

$$\mathcal{F} = \frac{\beta}{\alpha}\left[\left(\hat{\epsilon}_{\mathrm{r}_1}\hat{\epsilon}_{\mathrm{r}_2} - \hat{\epsilon}_{\mathrm{f}_1}\hat{\epsilon}_{\mathrm{r}_2} - \hat{\epsilon}_{\mathrm{r}_1}\hat{\epsilon}_{\mathrm{f}_2}\right) N_{\mathrm{TT}} + \hat{\epsilon}_{\mathrm{f}_1}N_{\mathrm{TL}} + \hat{\epsilon}_{\mathrm{f}_2}N_{\mathrm{LT}} - N_{\mathrm{LL}}\right] \tag{4.13}$$

$$\text{with} \quad \beta = \epsilon_{\mathrm{r}_1}\epsilon_{\mathrm{f}_1}\epsilon_{\mathrm{r}_2}\epsilon_{\mathrm{f}_2}$$

In the following it is assumed that the real efficiency and fake efficiency of the leading and the subleading electron is similar in such a way that the simplifications

$$\epsilon_{\mathrm{r}_1} = \epsilon_{\mathrm{r}_2}, \quad \epsilon_{\mathrm{f}_1} = \epsilon_{\mathrm{f}_2} \quad \text{and} \quad N_{\mathrm{TL}} = N_{\mathrm{LT}} \tag{4.14}$$

can be used. This reduces equation 4.13 to

$$\mathcal{F} = \frac{\epsilon_{\mathrm{r}}^2\epsilon_{\mathrm{f}}^2}{(\epsilon_{\mathrm{r}} - \epsilon_{\mathrm{f}})^2}\left[\left(\hat{\epsilon}_{\mathrm{r}}^2 - 2\hat{\epsilon}_{\mathrm{f}}\hat{\epsilon}_{\mathrm{r}}\right) N_{\mathrm{TT}} + 2\hat{\epsilon}_{\mathrm{f}}N_{\mathrm{TL}} - N_{\mathrm{LL}}\right]. \tag{4.15}$$

4.6.5 Result

The fake background estimated using the Matrix Method is shown on the left hand side of figure 4.22. Both the W+jets and the multi-jet contributions are shown separately as well as the total fake background. As expected the fake background

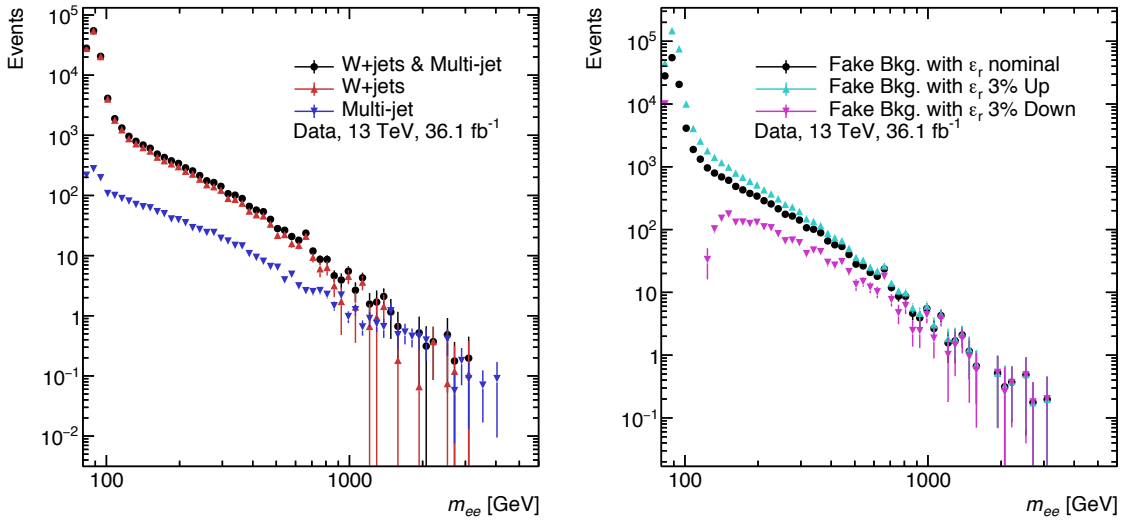

Figure 4.22: Estimate of the total fake background as well as the contributions from W+jets and multi-jet production as a function of the invariant mass m_{ee} (left) and the estimate of the total fake background with up and down variations of the real efficiency by 3 % (right).

component due to W+jets production is overall larger than the component due to multi-jet production. Both components decrease for larger values of invariant mass, however, the multi-jet component decreases slower than the W+jets component and becomes more and more important at higher invariant masses. In fact in some bins at high invariant masses the W+jets component is estimated with negative contributions by the Matrix Method. Therefore, only the multi-jet contribution can be seen in these bins on the left hand side of figure 4.22. Looking at equation 4.15 these negative contributions can be explained by an excess of events with two loose electrons which may happen due to small statistics. At low invariant masses it is observed that the fake background estimate by the Matrix Method yields a peak. The W+jets component, however, is not a resonant process leading to final states that can fake a dilepton final state. The multi-jet component contains the process $Z \to q\bar{q}$ which is a resonant process and which can fake a dilepton final state. In order to proof if this contribution could cause a peak a rough estimation of how many events can be expected by this process is performed. The cross section of the Z boson decay into a pair of electrons in a phase space similar to the one used in this analysis has been determined to be $\sigma_{Z\to e^+e^-} \approx 743\,\text{pb}$ at $\sqrt{s} = 13\,\text{TeV}$ [121]. The integrated luminosity is around $L_{\text{Int}} \approx 36\,\text{fb}^{-1}$. Via $N_{e^+e^-} = \sigma_{Z\to e^+e^-} L_{\text{Int}}$ a number of roughly 27 million $Z \to e^+e^-$ decays can be estimated. In order to extrapolate from $Z \to e^+e^-$ decays to $Z \to q\bar{q}$ decays the Z boson branching ratio $\Gamma(\text{hadrons})/\Gamma(e^+e^-) \approx 21$ [120] can be used. This leads to $N_{\text{hadrons}} = N_{e^+e^-}\Gamma(\text{hadrons})/\Gamma(e^+e^-) \approx 567\,\text{million}$. The efficiency to reject a jet with the event selection used in this analysis has been calculated to be $\epsilon_{\text{jet reject.}} > 99.9\,\%$ integrated over the full invariant mass range using a

dijet MC simulation. A contribution to the fake background only arises in case both jets are not rejected. Via $N_{\text{fake}} = N_{\text{hadrons}}(1 - \epsilon_{\text{jet reject.}})^2$ it can hence be calculated that less than 567 $Z \to q\bar{q}$ events are expected to pass the dielectron event selection. Compared to the several thousand events around an invariant mass of 90 GeV the contribution due to $Z \to q\bar{q}$ can not explain the resonance in the total fake background. An explanation for the resonance, however, can be found when introducing a small bias $d\epsilon_{\text{r}}$ in the formalism above. Transforming $\mathcal{F}$ with $\epsilon_{\text{r}} \to \epsilon_{\text{r}} + d\epsilon_{\text{r}}$ results in a bias term of $\mathcal{F}$ that is proportional to the number of real electrons. This can be seen much easier in the two-dimensional Matrix Method as formulated in [122]. Since the decay of Z bosons produces the conditions of much more real electrons than fake electrons at around 90 GeV the Matrix Method will always be affected by the bias term in this region. This has been checked by varying the real efficiency ϵ_{r} up and down globally by 3 %. The fake efficiency ϵ_{f} is not varied since the variation of the real efficiency has only minor effects on the fake efficiency. The result of this check can be seen on the right hand side of figure 4.22 which shows the fake background derived nominally as well as with the two variations of ϵ_{r}. It is observed that the results of the estimated fake background vary drastically in the region from 80 GeV to around 120 GeV. With increasing values of invariant mass the effects of the varied real efficiency become smaller. As a result the fake background for invariant masses of $m_{ee} < 120$ GeV will be discarded. Instead an extrapolation down to an invariant mass of 80 GeV will be performed. As has already been mentioned for high invariant masses the fake background has a lack of statistics with partially negative contributions. To counteract this, the extrapolation will also be performed to higher masses. Additionally the result of the fake background estimation will be rebinned in such a way that all negative contributions vanish. This can be achieved by merging bins together until the bin content at least reaches a specific number n_{content}. The resulting spectrum is then fitted in the region from $r_{\text{start}} = 120$ GeV up to the upper edge of the last bin with entries. The extrapolation is performed with the same function as used for the top background extrapolation (see equation 4.3). As already mentioned this extrapolation function can be limited to be monotonically decreasing with higher values of m_{ee} by limiting the free parameters p_0, p_1 and p_2. Furthermore the function vanishes to zero at a mass of $m_{ee} = 13$ TeV which are the relevant features to describe the fake background. The parameter r_{start} is the lower edge of the fitted region and is additionally varied from 120 GeV to 150 GeV in steps of 3 GeV. This is done in order to account for a possible influence of the resonance due to Z boson decays to the fake background in an expanded region up to 150 GeV as explained above. The required bin content n_{content} in the bin merging process is varied by the values 5, 10 and 15. These variations lead to 30 different extrapolations from which the arithmetic mean for each bin can be calculated. The result of this procedure can be seen in figure 4.23. The minimization of the extrapolation is performed by using the integral of the extrapolation function in each bin instead of the value at the bin center. The uncertainty of the extrapolation in a bin is the largest discrepancy between the arithmetic mean and the highest or lowest extrapolation value in a bin.

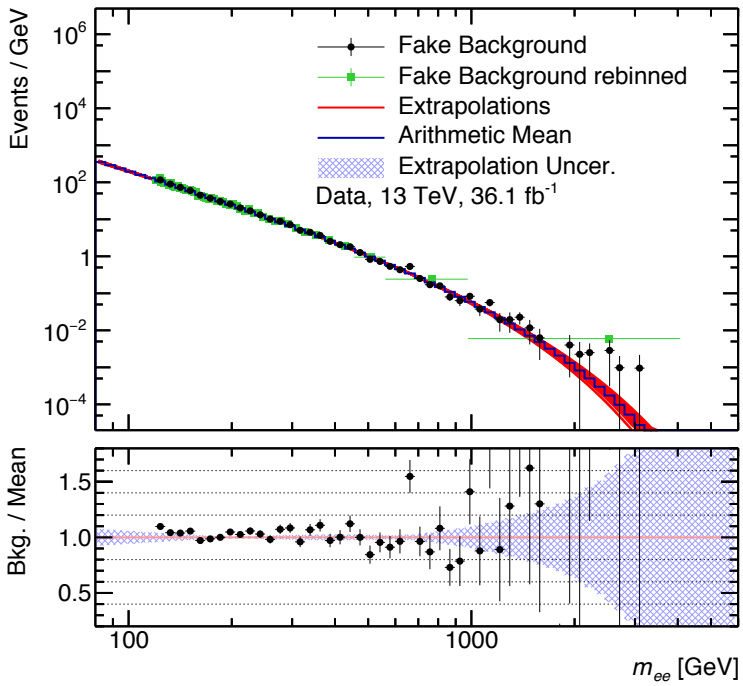

Figure 4.23: Extrapolations of the fake background estimate as a function of the invariant mass m_{ee}.

4.6.6 Systematic Uncertainties

Systematic uncertainties of the fake background can be estimated by a variation of the Matrix Method. Therefore the fake background is estimated under the assumption that the real efficiency is one. This variation will be called r_1-variation and yields a result with an additional real contribution. This real contribution in turn can be estimated using the r_1-variation of the Matrix Method on the simulations of the Drell-Yan, top quark and diboson processes. Eventually subtracting this real contribution from the estimated fake background with the r_1-variation of the Matrix Method is assumed to return a similar result as the nominal Matrix Method. The fake background spectrum obtained this way is then extrapolated in the same way as already described in the previous section. The differences between the nominal procedure and the r_1-variation can be expressed in a ratio as a function of m_{ee} as shown on the left hand side of figure 4.24.
Another systematic uncertainty can be estimated by analyzing the charge of the objects in the final state. Therefore it is defined that N_{os} is the number of events with a final state with two opposite-signed objects and N_{ss} is the number of events with a final state with two same-signed objects. The charge of a jet can be defined as the momentum-weighted sum of the charges of the associated tracks. This momentum-weighted sum of charges in turn is sensitive to the charge of the initiating quark or gluon. Since in the multi-jet contribution the amount of processes leading to opposite-sign and same-sign final states is the same the quantity

$$p_{\text{r}} = \frac{N_{\text{os}} - N_{\text{ss}}}{N_{\text{os}} + N_{\text{ss}}} \tag{4.16}$$

is expected to be zero if only a multi-jet contribution is prominent. Contributions leading to dilepton final states, however, have only opposite-signed final states which leads to the fact that p_{r} is one if only contributions with dilepton final states are prominent. Hence, p_{r} can be used to measure the dilution of the fake background by real dilepton final states. Again the estimated spectra by requiring opposite-signed and same-signed charge are extrapolated with the procedure from the previous section. The result is shown on the right hand side of figure 4.24.

The extrapolation uncertainty, the uncertainty due to the r_1-variation as well as

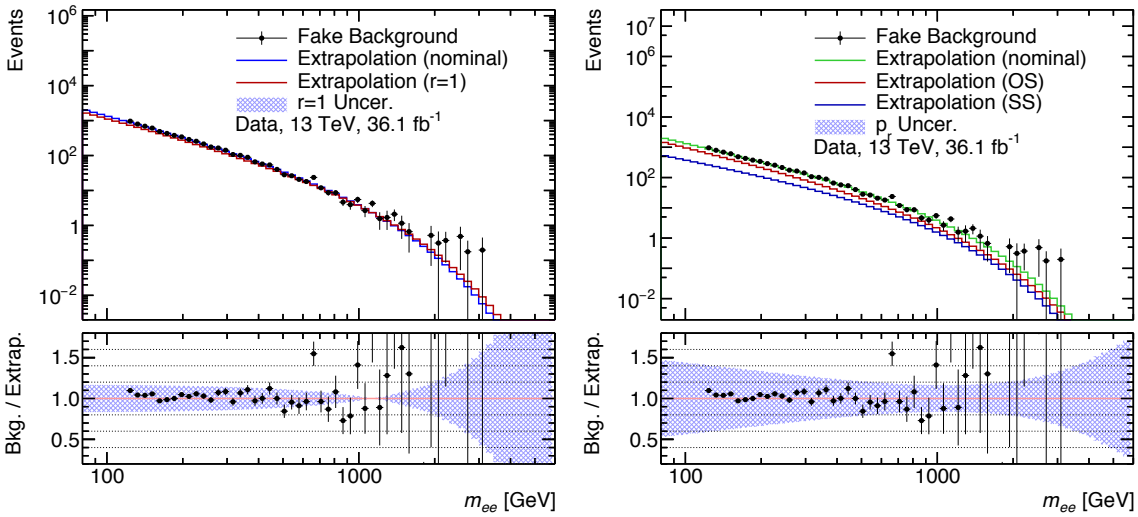

Figure 4.24: Systematic uncertainties due to the r_1-variation where the real efficiency is set to one and the real contribution is subtracted by simulations (left) and the p_r uncertainty measuring the dilution of the fake background by real dilepton final states (right) as a function of the invariant mass m_{ee}.

the p_r uncertainty are quadratically summed up to the total systematic uncertainty of the fake background. Figure 4.25 shows the final result. The smallest total uncertainty is reached in the region between 700 GeV and 1000 GeV with a value of 20 %. For high invariant masses of more than 3 TeV the total systematic uncertainty rises to more than 100 %. For the smallest invariant masses down to 80 GeV the total systematic uncertainty increases to about 50 %.

4.7 Systematic Uncertainties

The estimates of the different sources of real background are also affected by systematic uncertainties. These can arise from a theoretical nature as well as from an experimental nature. All uncertainties are assessed as a function of the dilepton invariant mass.

4.7.1 Theoretical Uncertainties

Theoretical uncertainties arise due to corrections of the cross sections of the simulated background processes to higher orders of perturbation theory. These corrections are calculated with VRAP0.9 relying on the quantities α_{s}, μ_{R} and μ_{F} and

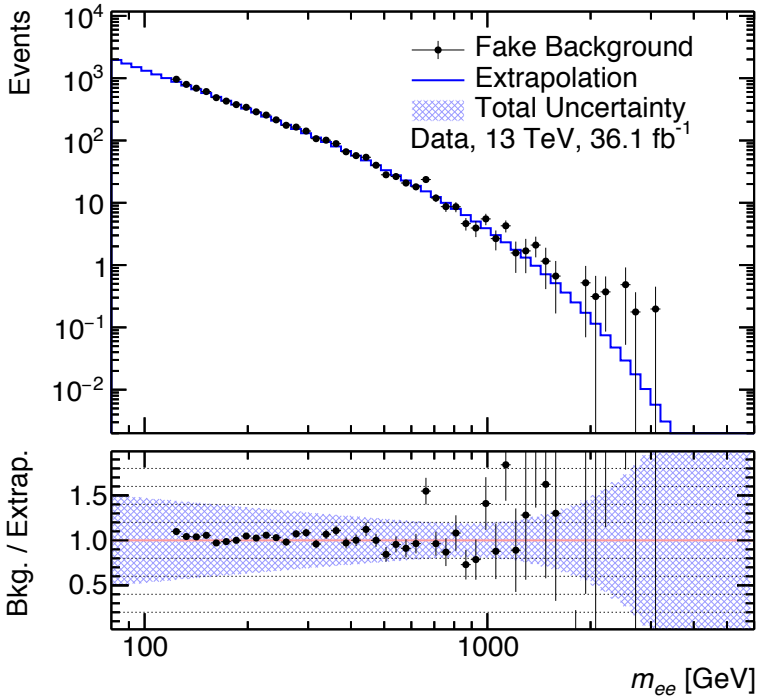

Figure 4.25: Total systematic uncertainty of the fake background estimate as a function of the invariant mass m_{ee}.

the choice of the PDF. The uncertainties on these quantities as well as the PDF propagate to the calculated corrections of the simulated background processes. In the following all theoretical uncertainties are discussed.

Strong coupling constant
The value of the strong coupling constant α_s is set to the nominal value of 0.118 in the calculations with VRAP0.9. Recommendations for the uncertainty are given by PDF4LHC [123] suggesting a value of ± 0.0015 corresponding to a confidence level of 68 %. Due to the high mass this search is aiming for, the more conservative value of ± 0.003 corresponding to a confidence level of 95 % is chosen. Up and down variations of the nominal value are performed using this uncertainty. The discrepancy of any of the variations compared to the nominal calculated correction is evaluated at each value of invariant mass where the largest discrepancy is taken as the uncertainty.

Renormalization and factorization scale
The value of the renormalization scale μ_R and the factorization scale μ_F are varied in the calculations with VRAP0.9. Both scales are varied simultaneously by a factor of 2 or 1/2. The largest differences of both variations compared to the nominal calculation for each value of invariant mass is taken as the uncertainty.

PDF
An uncertainty on the PDF arises due to the eigenvector error-set variations. Specifically for this search the 28 error-set variations of the eigenvectors have been rediagonalized to a set of 7 eigenvector variations by the authors of the CT14 PDFs.

A second uncertainty arises due to the specific choice of a PDF. Since there are several suitable PDFs the discrepancies observed compared to the nominally chosen CT14NNLO PDF result in an uncertainty. The PDF choice uncertainty is obtained by comparing the CT14NNLO PDF to the following set of PDFs:

- MMHT14 [124]
- NNPDF3.0 [125]
- ABM14 [126]
- JR14 [127]

In order to avoid any double counting of systematic uncertainties, the uncertainty due to the choice of the PDF is used in case it exceeds the uncertainty due to the eigenvector error-set variations of the CT14NNLO PDF. Otherwise the eigenvector error set variations are used as the uncertainty.

Combination of EW correction and QCD prediction
A complete prediction of the Drell-Yan cross section can only be obtained by a combination of the NLO EW correction calculated with MCSANC and the NNLO QCD prediction calculated with VRAP0.9. An additive as well as a factorized approach can be used for a combination. The following formulas are taken from [128] where further information is available. In the additive approach the absolute contribution of the EW correction is assumed to be independent of the order of the underlying QCD calculation. As a result the relative fraction of the higher order EW correction is different for each order of QCD. Defining

$$K_{\mathrm{QCD}} = \frac{\sigma^{\text{LO EW}}_{\text{NNLO QCD}}}{\sigma^{\text{LO EW}}_{\text{LO QCD}}} \quad \text{and} \quad K^{\mathrm{EW}} = \frac{\sigma^{\text{NLO EW}}_{\text{LO QCD}}}{\sigma^{\text{LO EW}}_{\text{LO QCD}}} \tag{4.17}$$

as the EW and QCD correction factor the additive approach can be expressed as

$$\begin{aligned} \sigma^{\text{NLO EW}}_{\text{NNLO QCD}} &= \sigma^{\text{LO EW}}_{\text{NNLO QCD}} + (\sigma^{\text{NLO EW}}_{\text{NNLO QCD}} - \sigma^{\text{LO EW}}_{\text{NNLO QCD}}) \\ &= \sigma^{\text{LO EW}}_{\text{NNLO QCD}} + (\sigma^{\text{NLO EW}}_{\text{LO QCD}} - \sigma^{\text{LO EW}}_{\text{LO QCD}}) \\ &= \sigma^{\text{LO EW}}_{\text{NNLO QCD}} + \sigma^{\text{LO EW}}_{\text{LO QCD}}(K^{\mathrm{EW}} - 1) \\ &= \sigma^{\text{LO EW}}_{\text{NNLO QCD}} \left(1 + \frac{K^{\mathrm{EW}} - 1}{K_{\mathrm{QCD}}}\right). \end{aligned} \tag{4.18}$$

From the first to the second line in equation 4.18 it has been exploited that the EW correction is independent of the order of the underlying QCD calculation. The factorized approach in contrast assumes that the fractional higher order EW correction K^{EW} is the same for each order of QCD. This can be expressed by

$$\begin{aligned} \sigma^{\text{NLO EW}}_{\text{NNLO QCD}} &= \sigma^{\text{LO EW}}_{\text{NNLO QCD}} K^{\mathrm{EW}} \\ &= \sigma^{\text{LO EW}}_{\text{LO QCD}} K_{\mathrm{QCD}} K^{\mathrm{EW}}. \end{aligned} \tag{4.19}$$

The uneven results of both approaches indicate a mixing of EW and QCD corrections that is not taken into account. This issue is handled by choosing the additive approach as the nominal procedure and the differences compared to the factorized

approach as the uncertainty of the procedure.

Photon-induced corrections
As described in section 4.2.1 the Drell-Yan process can be induced by two photons in the initial state. As an example photons can radiate from the protons and thus create a pair of leptons as shown in figure 4.3. The Drell-Yan cross section is corrected for photon-induced contributions by a mass-dependent k-factor calculated with MRST2004QED. This calculation comes with an uncertainty taken into account in this analysis.

Top and Diboson Background
A theoretical uncertainty on the top and diboson backgrounds arise due to the k-factors applied as discussed in section 4.5.2. In case of the top background a global uncertainty on the k-factor of 5.5 % is assumed while the k-factor of the diboson background is assumed to have an uncertainty of 10 %. The uncertainty on the background estimates is calculated by taking the difference between the nominal estimate and the estimate calculated with the k-factor and its uncertainty.

All theoretical uncertainties in the dielectron and the dimuon channel can be seen in figure 4.26. Up to an invariant mass of about 3 TeV the size of the theoretical uncertainties is almost the same in both channels. Up to 1 TeV the combined theoretical uncertainty varies around a value of 4 %. For larger values, however, the theoretical uncertainties in the dielectron channel grows to more than 30 % while the theoretical uncertainty in the dimuon channel grows up to a value of a maximum of 20 %. The combined theoretical uncertainty in both channels is driven by the PDF uncertainty. The increase of the PDF uncertainty at high invariant masses can be explained with the input data used for the global PDF fit (see section 2.3.2). The input data are measurements from other particle physics experiments. However, compared to the energies reached at the LHC these measurements were performed at smaller energies which also corresponds to smaller Bjorken-x values. The global PDF fit used to probe the higher values of Bjorken-x prevailing at the LHC can not be constrained since no input data for high Bjorken-x is available. As a consequence the PDF uncertainty grows strongly for high values of invariant mass. This increase is smaller in case of dimuon final states since the worse resolution causes migration effects. These effects lead to cases where muons produced at lower invariant masses with lower PDF uncertainties are reconstructed at higher invariant masses.

4.7.2 Experimental Uncertainties

Experimental uncertainties arise due to measurements of the detector as well as due to the correction factors discussed in section 4.5.2 that have been applied in order to get a better agreement between data and simulation.

Luminosity
The luminosity measurement of the recorded data by the ATLAS detector has an uncertainty that is important for the simulated MC samples used for the background expectation. These samples are scaled using the integrated luminosity of the recorded data according to equation 4.2. This results in an uncertainty on the

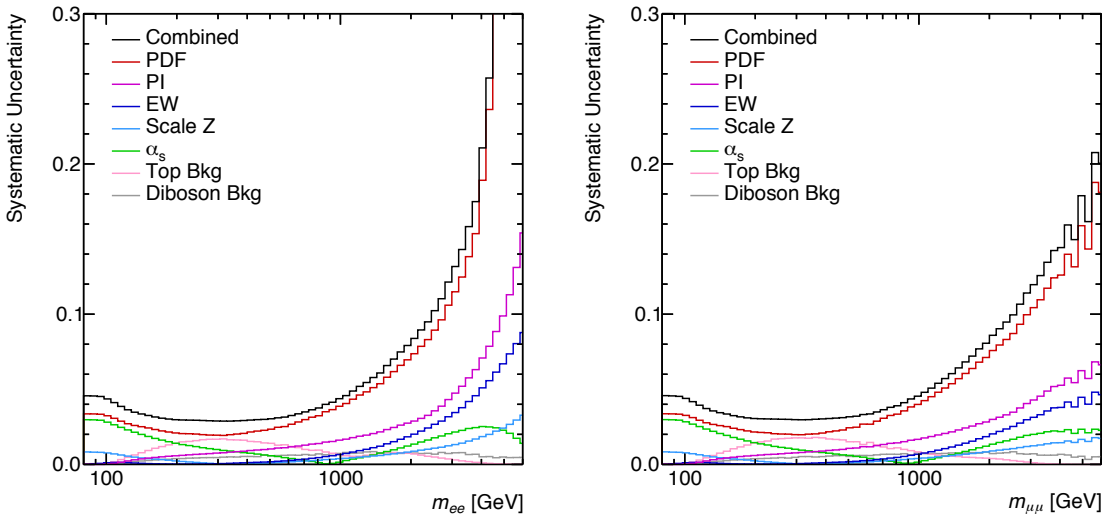

Figure 4.26: Theoretical uncertainties of the dielectron channel (left) and the dimuon channel (right) as a function of the invariant mass m_{ll}.

background expectation due to the luminosity measurement.

Beam Energy
Variations in the beam energy more specifically the energy of the protons have an impact on the cross section of all processes that can occur in a proton-proton collision. Official studies on the energy of the LHC beam have only been published at $\sqrt{s} = 8\,\text{TeV}$ related to a beam energy of 4 TeV [129]. The uncertainty has been determined to be 0.65 %. In order to estimate a beam uncertainty for $\sqrt{s} = 13\,\text{TeV}$ two assumptions have been made. The same fractional uncertainty as for $\sqrt{s} = 8\,\text{TeV}$ is assumed for $\sqrt{s} = 13\,\text{TeV}$ leading to an uncertainty of 1.06 %. The second assumption is that the correlation between the uncertainty at $\sqrt{s} = 8\,\text{TeV}$ and $\sqrt{s} = 13\,\text{TeV}$ is 100 %. The effects of the uncertainty are quantified using VRAP0.9. The NNLO QCD prediction of mass-dependent Drell-Yan production has been calculated for the nominal center of mass energy of $\sqrt{s} = 13\,\text{TeV}$ and for up and down variations according to the specified uncertainty. The deviations from the nominal prediction are used as an uncertainty on the simulated samples.

Correction Factors
As explained in section 4.5.2 the MC simulation has to be adjusted with correction factors to reproduce the conditions measured in data. The correction factors contain uncertainties that are propagated to the MC simulation and rise to the following systematic uncertainties:

- Lepton resolution uncertainty
- Lepton scale uncertainty
- Lepton reconstruction efficiency uncertainty
- Lepton isolation efficiency uncertainty

- Lepton trigger efficiency uncertainty
- Electron identification efficiency uncertainty
- Muon TTVA efficiency uncertainty
- Pile-up reweighting uncertainty

All experimental uncertainties of the dielectron and the dimuon channel can be seen in figure 4.27. In the dielectron channel the luminosity uncertainty is the most dominant uncertainty up to an invariant mass of about 1 TeV. For higher values of invariant masses the scale uncertainty is driving the total experimental uncertainty in the dielectron channel. In the dimuon channel the luminosity uncertainty is also the largest uncertainty at low invariant masses but only up to a value of around 500 GeV. For higher values of invariant mass the reconstruction uncertainty is the driving source of the combined experimental uncertainty in the dimuon channel. Both the dielectron and the dimuon combined experimental uncertainty has values between 4 % and 6 % up to an invariant mass of 1 TeV. Above 1 TeV the dielectron combined experimental uncertainty grows up to 14 % while the dimuon combined experimental uncertainty grows up to about 30 %. The systematic uncertainty due to the fake background has been included in left hand plot of figure 4.27 as well. As can be seen the impact on the combined experimental uncertainty is small.

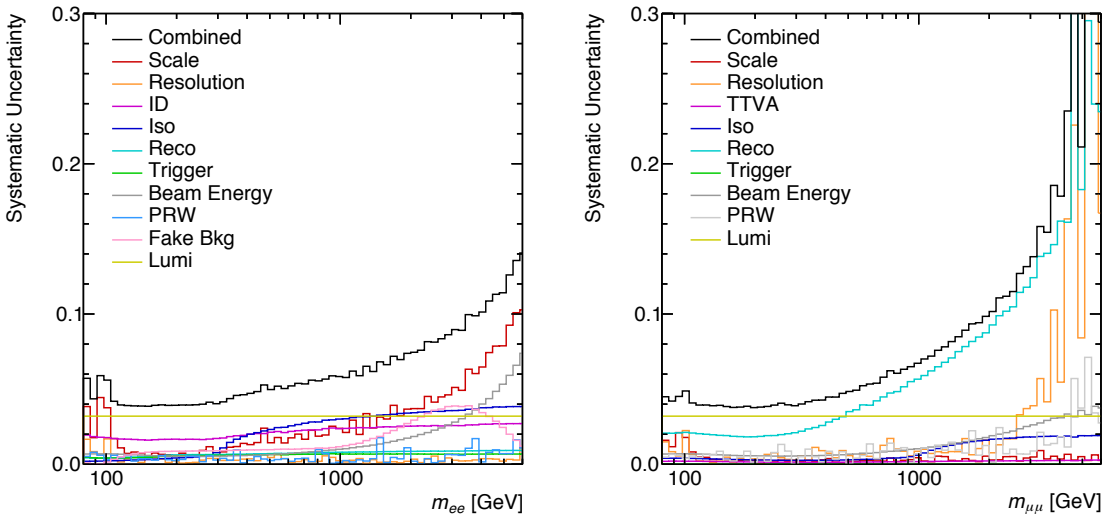

Figure 4.27: Experimental uncertainties of the dielectron channel (left) and the dimuon channel (right) as a function of the invariant mass m_{ll}.

4.8 Data and SM Expectation

This section discusses the selection of dilepton events from data and compares the final number of events to the number of expected events found in the backgrounds. Lastly the data and the background expectation will be compared differentially as a function of kinematical observables.

4.8.1 Data Selection

The recorded data corresponding to the $36.1\,\mathrm{fb}^{-1}$ is discriminated using the same selection criteria from section 4.4 that have been applied to all background expectations as well. Table 4.11 shows the number of events that remain after each selection criterion has been applied. The total number of data events is the number of events contained in the so called *main physics stream*. It contains all events recorded at a rate of around 200 Hz from the collision rate of 40 MHz provided by the LHC. The trigger reduces the number of dielectron events after the data quality criterion by about 70 %. In the dimuon channel the trigger accounts for a reduction of around 60 %. Another important criterion with a major impact in both channels is the transverse momentum. Additionally the identification criterion has a strong effect in the dimuon channel as well. Overall around 12.7 million dielectron events and 11.5 million dimuon events have been selected.

Table 4.11: Number of data events N_{Events} remaining after each selection criterion. $\epsilon_{\mathrm{Criterion}}$ is the number of events remaining after each criterion divided by the total number of events.

Selection Criterion	N_{Events}		$\epsilon_{\mathrm{Criterion}}$ [%]	
	ee	$\mu\mu$	ee	$\mu\mu$
Total	83695085	83695085	100.0	100.0
GRL	81520723	81520723	97.4	97.4
Trigger	23870885	34131923	28.5	40.8
Event Cleaning	23834461	34077736	28.5	40.7
$N_{\mathrm{Candidates}}$	23834152	33529535	28.5	40.1
$\lvert\eta\rvert$	23057150	—	27.5	—
Object Quality	22997398	—	27.5	—
p_{T}	15692991	23236004	18.8	27.8
Identification	13952157	13243109	16.7	15.8
$\lvert d_0\rvert/\sqrt{\sigma_{d_0}}$	13887625	12555060	16.6	15.0
$\lvert z_0\rvert \cdot \sin\theta$	13772301	12514900	16.5	15.0
Isolation	13256580	12038443	15.8	14.4
Dilepton Selection	12732720	11533585	15.2	13.8

4.8.2 Data to Background Comparison

The numbers of selected dilepton events in data and in the background processes are now compared to each other in different bins of invariant mass. Table 4.12 shows the results for the dielectron channel and table 4.13 shows the results for the dimuon channel. In both cases the Drell-Yan production is the largest contribution to the background. The second largest contribution is due to top quark production. This is true at least in the invariant mass range from 120 GeV to 1200 GeV. Below 120 GeV the contribution due to diboson production is equally strong as the contribution due to top quark production. For invariant masses larger than 1200 GeV the contribution due to diboson production becomes the second largest contribution. The fake background contribution in the dielectron channel is generally very low but relatively to the other contributions it is more and more important for higher invariant

masses. In both cases a good agreement between the total number of background events $N_{\text{Total Bkg}}$ and the number of data events N_{Data} is observed.

Table 4.12: Numbers of selected data and expected background dielectron events compared for different intervals of the invariant mass m_{ee}.

m_{ee} [GeV] min	max	$N_{\text{Drell-Yan}}$	N_{Top}	N_{Diboson}	N_{Fake}	$N_{\text{Total Bkg}}$	N_{Data}
80	120	$1.21 \cdot 10^{7}$	$3.37 \cdot 10^{4}$	$3.31 \cdot 10^{4}$	$9.53 \cdot 10^{3}$	$1.22 \cdot 10^{7}$	$1.25 \cdot 10^{7}$
120	300	$2.33 \cdot 10^{5}$	$5.07 \cdot 10^{4}$	$7.95 \cdot 10^{3}$	$5.71 \cdot 10^{3}$	$2.97 \cdot 10^{5}$	$2.95 \cdot 10^{5}$
300	500	$1.27 \cdot 10^{4}$	$6.01 \cdot 10^{3}$	$1.02 \cdot 10^{3}$	$6.63 \cdot 10^{2}$	$2.04 \cdot 10^{4}$	$1.99 \cdot 10^{4}$
500	700	$1.92 \cdot 10^{3}$	$6.67 \cdot 10^{2}$	$1.73 \cdot 10^{2}$	$1.30 \cdot 10^{2}$	$2.90 \cdot 10^{3}$	$2.76 \cdot 10^{3}$
700	900	$5.42 \cdot 10^{2}$	$1.23 \cdot 10^{2}$	$4.99 \cdot 10^{1}$	$4.17 \cdot 10^{1}$	$7.57 \cdot 10^{2}$	$7.29 \cdot 10^{2}$
900	1200	$1.98 \cdot 10^{2}$	$2.87 \cdot 10^{1}$	$1.94 \cdot 10^{1}$	$1.60 \cdot 10^{1}$	$2.62 \cdot 10^{2}$	$2.25 \cdot 10^{2}$
1200	1800	$7.31 \cdot 10^{1}$	$5.59 \cdot 10^{0}$	$7.31 \cdot 10^{0}$	$5.89 \cdot 10^{0}$	$9.19 \cdot 10^{1}$	$7.40 \cdot 10^{1}$
1800	3000	$1.06 \cdot 10^{1}$	$2.47 \cdot 10^{-1}$	$9.19 \cdot 10^{-1}$	$7.23 \cdot 10^{-1}$	$1.25 \cdot 10^{1}$	$1.20 \cdot 10^{1}$
3000	6500	$3.49 \cdot 10^{-1}$	$8.02 \cdot 10^{-4}$	$5.28 \cdot 10^{-2}$	$1.18 \cdot 10^{-2}$	$4.14 \cdot 10^{-1}$	$0.00 \cdot 10^{0}$

Table 4.13: Numbers of selected data and expected background dimuon events compared for different intervals of the invariant mass $m_{\mu\mu}$.

$m_{\mu\mu}$ [GeV] min	max	$N_{\text{Drell-Yan}}$	N_{Top}	N_{Diboson}	$N_{\text{Total Bkg}}$	N_{Data}
80	120	$1.09 \cdot 10^{7}$	$2.66 \cdot 10^{4}$	$2.68 \cdot 10^{4}$	$1.10 \cdot 10^{7}$	$1.13 \cdot 10^{7}$
120	300	$1.90 \cdot 10^{5}$	$3.82 \cdot 10^{4}$	$6.02 \cdot 10^{3}$	$2.34 \cdot 10^{5}$	$2.38 \cdot 10^{5}$
300	500	$8.76 \cdot 10^{3}$	$4.38 \cdot 10^{3}$	$7.15 \cdot 10^{2}$	$1.38 \cdot 10^{4}$	$1.35 \cdot 10^{4}$
500	700	$1.26 \cdot 10^{3}$	$4.75 \cdot 10^{2}$	$1.08 \cdot 10^{2}$	$1.84 \cdot 10^{3}$	$1.78 \cdot 10^{3}$
700	900	$3.37 \cdot 10^{2}$	$8.78 \cdot 10^{1}$	$3.09 \cdot 10^{1}$	$4.56 \cdot 10^{2}$	$4.12 \cdot 10^{2}$
900	1200	$1.23 \cdot 10^{2}$	$2.17 \cdot 10^{1}$	$1.10 \cdot 10^{1}$	$1.56 \cdot 10^{2}$	$1.55 \cdot 10^{2}$
1200	1800	$4.41 \cdot 10^{1}$	$4.36 \cdot 10^{0}$	$3.87 \cdot 10^{0}$	$5.23 \cdot 10^{1}$	$5.80 \cdot 10^{1}$
1800	3000	$6.58 \cdot 10^{0}$	$1.92 \cdot 10^{-1}$	$5.60 \cdot 10^{-1}$	$7.33 \cdot 10^{0}$	$6.00 \cdot 10^{1}$
3000	6500	$3.18 \cdot 10^{-1}$	$4.81 \cdot 10^{-4}$	$2.18 \cdot 10^{-1}$	$3.40 \cdot 10^{-1}$	$0.00 \cdot 10^{0}$

4.8.3 Kinematical Distributions

Distributions of kinematical observables are used to check that the analysis yields sensible results so far. Therefore the observables ϕ, η and p_{T} of the leading and the subleading lepton are examined. In case of dielectron final states a flat ϕ distribution is observed. This is expected since the electromagnetic calorimeter and the tracking detectors are equipped uniformly in the ϕ space. This can be seen clearly in the top plots of figure 4.28. In case of dimuon final states 8 dips can be seen in the ϕ distribution especially in case of the leading muon in the top left plot in figure 4.29. This is due to the coils of the toroidal magnet which causes an efficiency loss since less muon chambers are installed in these regions. This effect is not as prominent in the subleading muon ϕ distribution as can be seen in the top right plot in figure 4.29. The reason for this is a generally higher efficiency of lower p_{T} muons than of higher

p_{T} muons due to the stronger curvature of the lower p_{T} muons. However, at $\phi = -1$ and $\phi = -2$ two dips can also be seen in the subleading muon ϕ distribution. These correspond to the support structure between the ATLAS detector and the ground. The η distribution in case of dielectron final states has a maximum around $\eta = 0$ and decreases for larger values as can be seen in the middle plots of figure 4.28. A lack of events can be observed in the region from $1.37 < |\eta| < 1.52$ since this region has been excluded in the dielectron selection. In case of dimuon final states the η distributions shown in the middle plots of figure 4.29 are slightly lower in the central region compared to the η distributions of dielectron final states. This corresponds to a worse trigger efficiency in the barrel region than in the end-cap regions for muons. The dips in the muon η distributions are due to bad alignments of the muon spectrometer which are rejected in the *High-p_T* identification. The p_{T} distribution shown in the bottom plots of figure 4.28 and figure 4.29 feature a peak at around 45 GeV in both the dielectron and the dimuon final states. This is due to the decays of the Z bosons of which the mass is equally distributed to the two leptons. For higher transverse momenta the p_{T} distributions decrease such that at around 1 TeV only one event is expected. All observables show a good agreement within the systematic uncertainties between data and the expectation.

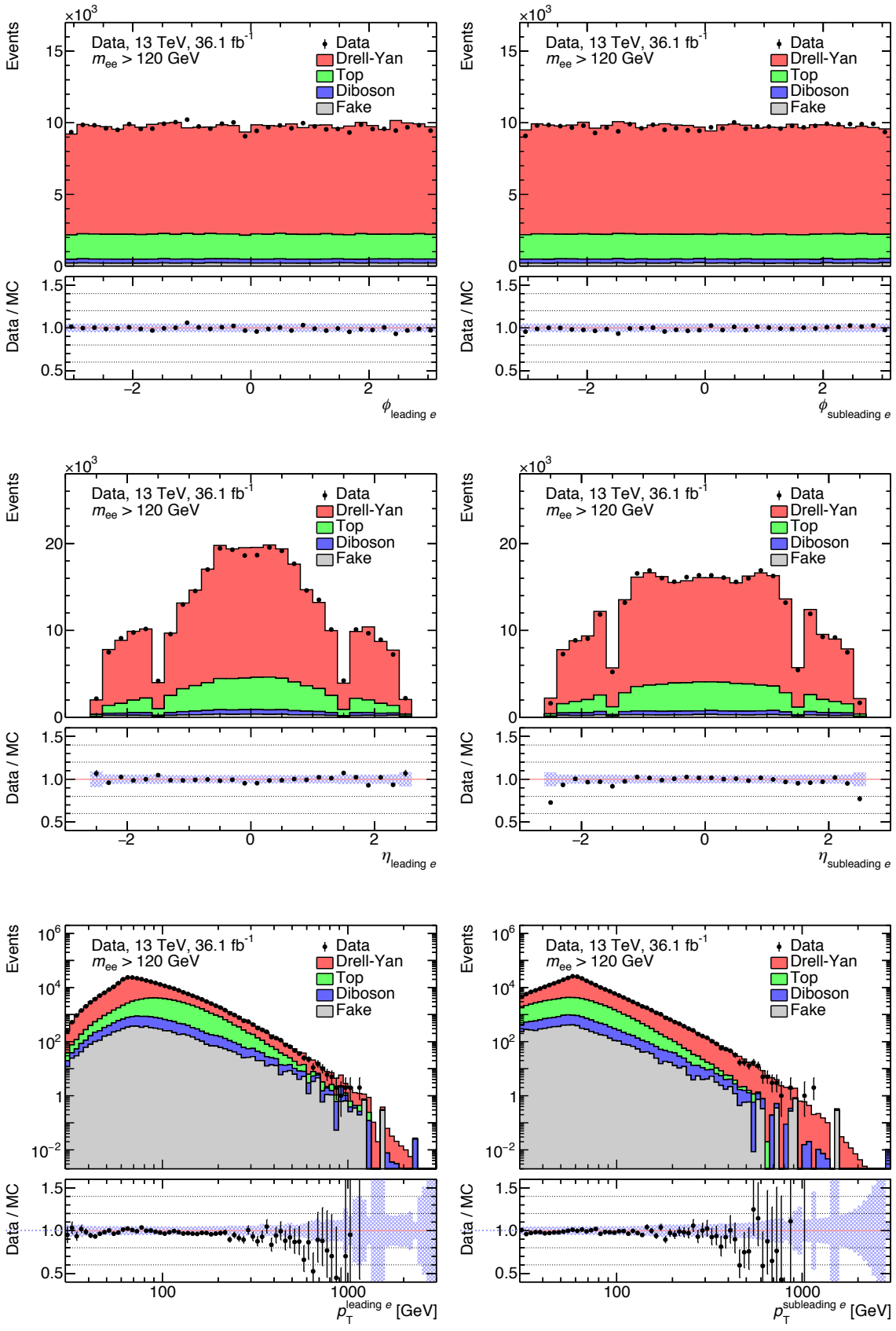

Figure 4.28: Kinematical distributions of ϕ, η and p_{T} of the leading electron (left) and the subleading electron (right).

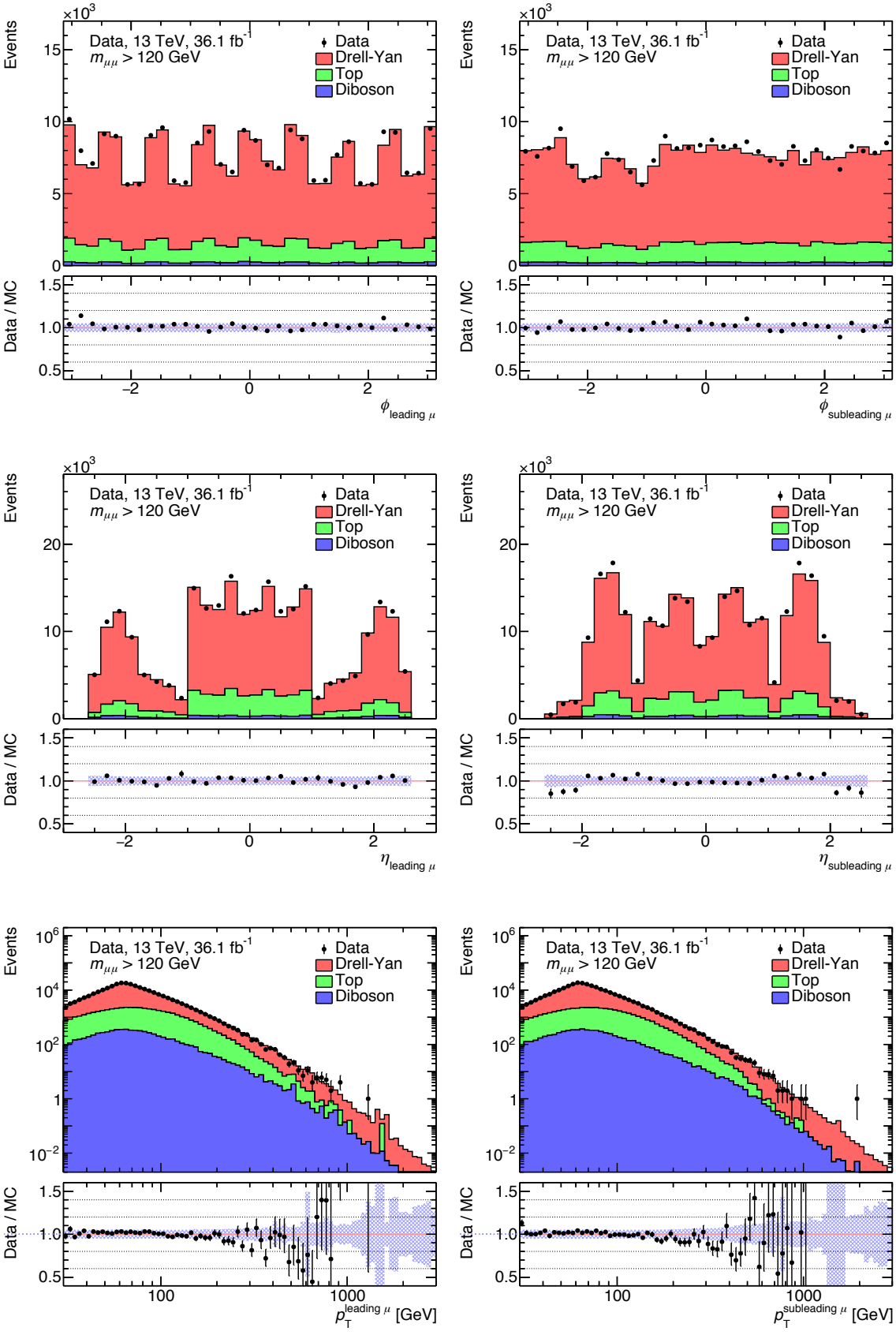

Figure 4.29: Kinematical distributions of ϕ, η and p_{T} of the leading muon (left) and the subleading muon (right).

Chapter 5

Statistical Interpretation

This chapter focuses on the statistical analysis of the invariant mass spectrum of the dilepton final states. First a search for resonances in the spectrum of the dilepton invariant mass is performed. Consequently the results are interpreted within specific models as well as in a model-independent way.

5.1 Search for Resonances

Applying the selection criteria discussed in section 4.4.1 on data and the background prediction the dilepton invariant mass spectrum as shown in figure 5.1 is obtained. In both spectra the resonance due to Z boson decays can be seen at around 90 GeV.

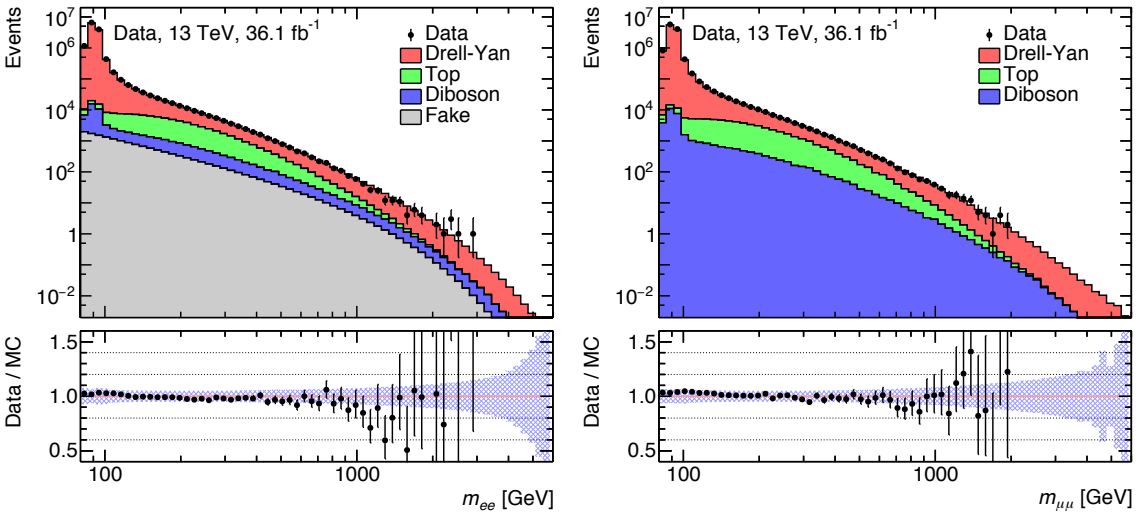

Figure 5.1: Spectra of the invariant mass of events with two electrons in the final state (left) and two muons in the final state (right).

The spectra decrease with larger values of m_{ll} such that at around 2 TeV only one event is expected. In both spectra the largest background contribution arises due to the Drell-Yan process, followed by top quark processes and diboson processes. In the electron channel an additional contribution due to processes faking electrons arises as the smallest background contribution. The main background in the Z boson

resonance region is due to Drell-Yan and diboson production. However, the contribution due to top quarks is equally strong to the diboson contribution even though it is not resonant in the Z boson resonance region. The observed data and the background prediction agree within the systematic and statistic uncertainties. Both the data in the dielectron spectrum as well as the data in the dimuon spectrum of the invariant mass do not show a significant deviation from the SM expectation. However, in order to search and quantify the most significant deviation the BumpHunter [130] method is used. The method scans over the spectrum of the dilepton invariant mass and quantifies the significance of the disagreement between the observed data and the predicted background within specific windows. Each of these windows is characterized by a position and a size. Testing the observed data against the background expectation within one specific window is called a hypothesis test. The BumpHunter method, testing several windows, is hence a multiple hypothesis test and therefore called hypertest. First the statistical formalism used in the BumpHunter method as well as the application of this formalism will be introduced. Subsequently the results will be shown and discussed.

5.1.1 Statistical Methodology of the BumpHunter

In the following it is assumed that d is the number of events observed in data while b is the number of expected background events. Since this analysis is based on a counting experiment d is always an integer while b, determined from MC simulations and the Matrix Method, is a real number. The observed data is therefore distributed according to a Poisson distribution. When expecting b events the probability to observe exactly d events can be calculated with the Poisson distribution

$$\text{Poisson}(d; b) = \frac{b^d}{d!} e^{-b} \quad \text{with} \quad b > 0 \quad \text{and} \quad d \in \mathbb{N}_0 \tag{5.1}$$

In the Poisson distribution the parameter b describes the expectation value and the variance at the same time. The interesting value in these hypothesis tests, however, is not the probability of measuring exactly d events when expecting b events but the probability describing how likely a possible discrepancy between d and b is. This can be expressed via the cumulative distribution function of the Poisson distribution. If d is larger or equal than b the probability P describing the discrepancy between d and b can be written as

$$P(d \geq b) = 1 - P(d - 1 \leq b) = 1 - \sum_{k=0}^{d-1} \text{Poisson}(k; b) \tag{5.2}$$

In order to evaluate this expression the following relation from [131] is used:

$$\Gamma(d, b) = (d - 1)! \sum_{k=0}^{d-1} \text{Poisson}(k; b). \tag{5.3}$$

$\Gamma(d, b)$ is called upper incomplete gamma function and is defined as

$$\Gamma(d, b) = \int_b^\infty t^{d-1} e^{-t} dt. \tag{5.4}$$

Using further that $\Gamma(d,0) \equiv \Gamma(d) = (d-1)!$ one can conclude that

$$P(d \geq b) = 1 - \frac{\Gamma(d,b)}{\Gamma(d)} \tag{5.5}$$

and

$$P(d-1 \leq b) = \frac{\Gamma(d,b)}{\Gamma(d)}. \tag{5.6}$$

Equation 5.5 and equation 5.6 are called lower and upper incomplete regularized gamma function respectively and are provided in the ROOT framework. Using this formalism the probability $\mathcal{P}(b,d)$ quantifying the discrepancy between the observed number of events d in data and the expected number of background events b for each hypothesis test can be written as

$$\mathcal{P}(d,b) = \begin{cases} 1 - \frac{\Gamma(d,b)}{\Gamma(d)} & d \geq b \\ \frac{\Gamma(d,b)}{\Gamma(d)} & d < b \end{cases}. \tag{5.7}$$

Out of all probabilities $\mathcal{P}$ from each hypothesis test the smallest probability $\mathcal{P}_{\text{min}}$ corresponds to the most significant discrepancy found in data compared to the background prediction. With this probability $\mathcal{P}_{\text{min}}$ the test statistic t of the hypertest is defined via

$$t = -\log \mathcal{P}_{\text{min}} \tag{5.8}$$

The test statistic is represented by a monotonically increasing function meaning that t gets larger if $\mathcal{P}_{\text{min}}$ gets smaller.

5.1.2 The BumpHunter Procedure

The BumpHunter procedure used within this analysis consecutively runs through the following steps:

1. Set the size of the window W to be at least 2 bins and a maximum of $\frac{N}{2}$ bins where N is the total number of bins.

2. Set the starting position of W as the bin with the lowest observed value of m_{ll}. The resonance of the Z boson will be excluded from the BumpHunter search. Hence the bin with the lowest observed value will be defined to be at 120 GeV.

3. Count the observed data d and determine the predicted background b inside the window W.

4. Evaluate $\mathcal{P}(d,b)$ according to equation 5.7.

5. Repeat step 2 to 4 by shifting the position of W by the number of bins

$$N_{\text{Step}} = \max\left\{1, \text{int}\left(\frac{W}{2}\right)\right\} \tag{5.9}$$

   as long as the upper edge of W is smaller or equal to the position of the bin with the highest observed value. This choice is made since especially tests with large window sizes and positions only differing by a few bins are highly correlated. Thus, adding these tests to the hypertest does not gain much new information.

6. Repeat step 2 to 5 for all values of the size of W as defined in step 1.

7. Calculate the test statistic t according to equation 5.8 where $\mathcal{P}_{\text{min}}$ is the smallest p-value found in all iterations of step 4.

5.1.3 The Look Elsewhere Effect

Since it is not known at which value of invariant mass a signal might show up the whole mass range has to be scanned within the above mentioned windows. This leads to the *multiple testing problem* or in high energy physics referred to as the *look elsewhere effect* [132]. Assuming one looks at specific different windows there is a chance that a statistically significant discrepancy has risen by a statistical fluctuation. Due to this problem the observed test statistic is not representing the actual significance since the *look elsewhere effect* has not yet been accounted for. In order to do so a large amount of pseudo-experiments has to be performed. In a pseudo-experiment the observed data is substituted by pseudo-data generated from the background expectation by applying fluctuations according to the Poisson distribution. The steps described in section 5.1.2 can then be repeated with the generated pseudo-data and thus yield a test statistic t. The actual significance of the observed test statistic t_0 is represented by the probability that the test statistic t from a pseudo-experiment is greater than t_0. This probability is called p-value. In order to calculate the p-value the probability density function which is achieved by the N pseudo-experiments is used. The p-value can then be estimated from a binomial success probability. Assuming S to be the number of pseudo-experiments with $t \geq t_0$ the most likely p-value is $\frac{S}{N}$.

5.1.4 Treatment of Systematic Uncertainties

The statistical methodology of the BumpHunter as described in section 5.1.1 does not incorporate the systematic uncertainties on the background estimation. As can be seen in equation 5.7 only the number of expected background events b but not the uncertainty of b denoted with σ_b is used to calculate $\mathcal{P}(d, b)$. The following formalism has first been introduced by Will Buttinger [133]. In order to incorporate the systematic uncertainties into the BumpHunter procedure the Gamma distribution as formulated in equation 5.10 can be used.

$$\text{Gamma}(x; \alpha, \beta) = \begin{cases} \frac{\alpha^\beta}{\Gamma(\beta)} x^{\beta-1} e^{-\alpha x} & x > 0 \\ 0 & x \leq 0 \end{cases} \quad \text{with} \quad \alpha > 0 \quad \text{and} \quad \beta > 0 \tag{5.10}$$

The Gamma distribution $\text{Gamma}(x; \alpha, \beta)$ is a probability density function and is not to be confused with the Gamma function as defined in equation 5.4. The Gamma distribution can be written in terms of an expectation value E and a variance V via

$$\alpha = \frac{E}{V} \quad \text{and} \quad \beta = \frac{E^2}{V}. \tag{5.11}$$

The expectation value E can be identified with the number of expected background events b while the variance V can be expressed through the uncertainty on the number of expected background events via $V = \sqrt{\sigma_b}$. There is no direct motivation to especially use the Gamma distribution for this purpose. However, it is one of the

easiest possibilities to incorporate an uncertainty on the background expectation into the BumpHunter procedure. The Gamma distribution described by b and σ_b can now be mixed with the Poisson distribution by integrating out x which will lead to the *Gamma-Poisson mixture* [134]:

$$\begin{aligned} F(k;\alpha,\beta) &= \int_0^\infty \text{Poisson}(k;x)\text{Gamma}(x;\alpha,\beta)dx \\ &= \frac{\alpha^\beta}{k!\Gamma(\beta)}\int_0^\infty x^{k+\beta-1}e^{-x(\alpha+1)}dx \\ &= \frac{\alpha^\beta}{k!\Gamma(\beta)}\frac{\Gamma(k+\beta)}{(\alpha+1)^{k+\beta}}\underbrace{\int_0^\infty \text{Gamma}(x;\alpha+1,\beta+k)dx}_{=1} \\ &= \frac{\Gamma(k+\beta)}{\Gamma(k+1)\Gamma(\beta)}\left(\frac{\alpha}{\alpha+1}\right)^\beta\left(\frac{1}{\alpha+1}\right)^k \end{aligned} \tag{5.12}$$

Using the Gamma-Poisson mixture $F(d;\alpha,\beta)$ instead of the plain Poisson distribution, equation 5.2 alters to

$$P(d \geq b) = 1 - P(d-1 \leq b) = 1 - \sum_{k=0}^{d-1} F(k;\alpha,\beta) \tag{5.13}$$

$$\text{with} \quad \alpha = \frac{b}{\sigma_b^2} \quad \text{and} \quad \beta = \frac{b^2}{\sigma_b^2}. \tag{5.14}$$

In order to evaluate this equation the following recursive formula which can be extracted from equation 5.12 is used:

$$F(k;\alpha,\beta) = F(k-1;\alpha,\beta)\frac{k-1+\beta}{k(\alpha+1)} \tag{5.15}$$

Since the above calculation takes a lot of computing time a condition is used to assess if the systematic uncertainty of the background can be ignored compared to the statistical uncertainty on data. This is done if the condition $\beta > 100d$ is true. In that case the probability $P(d \geq b)$ is calculated according to equation 5.5. The same is true for the probability $P(d < b)$.

5.2 Results

The BumpHunter formalism as described above is now applied to the invariant mass spectrum of the dielectron and dimuon final states. In order to achieve the most significant results the bin widths are chosen such that the highest possible discovery signal significance is yielded. Most optimal in this case would be infinitesimally small bins. Apart from the fact that this leads to a significant increase of the computing time a lower limit on the bin widths is already set by the mass resolution of the detector. The result of the BumpHunter procedure using this mass resolution binning can be seen in figure 5.2. Since the mass resolution for dimuon events is lower than the mass resolution for dielectron events the bin widths in the dimuon invariant mass spectrum are much larger than in the dielectron invariant

mass spectrum especially at high values of invariant mass. The red lines in figure 5.2 are the lower and upper border of the window with the most significant test statistic t_{observed}. In the dielectron spectrum this is $t^{ee}_{\text{observed}} = 5.67$ in the region from 2.35 TeV to 2.40 TeV. The dimuon spectrum results in $t^{\mu\mu}_{\text{observed}} = 2.42$ in the region from 1.28 TeV to 1.46 TeV. According to equation 5.8 the observed test

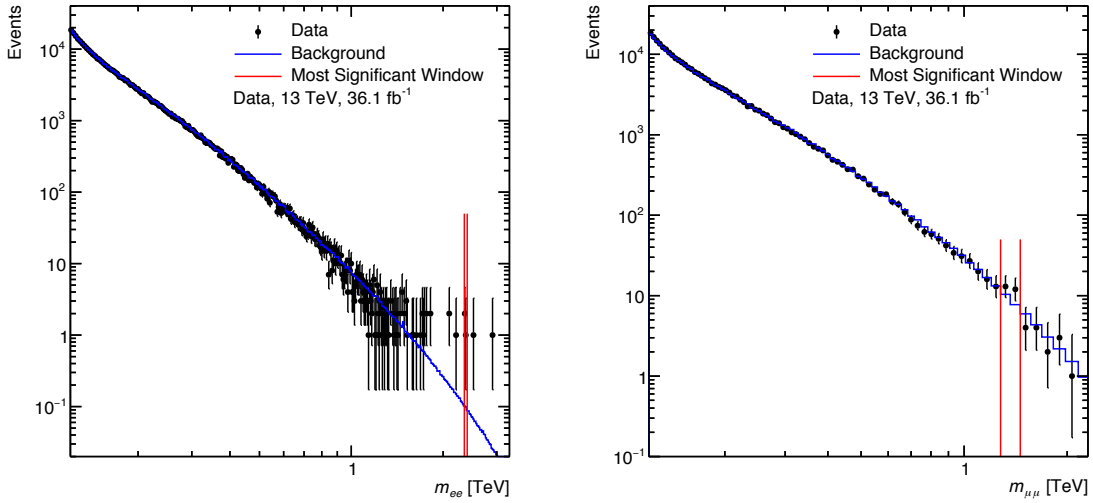

Figure 5.2: Result of the BumpHunter search procedure in the invariant mass spectrum of the dielectron final states (left) and the dimuon final states (right).

statistics lead to the minimal probabilities $\mathcal{P}^{ee}_{\text{min}} = 3.4 \times 10^{-3}$ in the dielectron case and $\mathcal{P}^{\mu\mu}_{\text{min}} = 8.9 \times 10^{-2}$ in the dimuon case. These probabilities $\mathcal{P}$ are usually called *local* p-values. Following [135] a p-value can be converted into a z-value denoting a number of standard deviations according to

$$\text{z-value} = \sqrt{2}\,\text{erf}^{-1}(1 - 2\,\text{p-value}) \tag{5.16}$$

where erf^{-1} is the inverse error function. The *local significances* expressed as a number of standard deviations corresponding to the *local* p-values yield 2.7σ in the dielectron channel and 1.4σ in the dimuon channel. In order to find the *global significances* the *look elsewhere effect* as explained in section 5.1.3 has to be taken into account. Hence, a large number of pseudo-experiments has to be performed. Figure 5.3 shows the probability density functions (PDFs) extracted from the pseudo-experiments as well as the observed test statistics indicated as a red line. As can be seen the value of the observed test statistic in both the dielectron and the dimuon case is relatively close to the position of the maximum of the test statistic PDF. Using the prescription from section 5.1.3 *global* p-values of 0.46 in the dielectron channel and 0.91 in the dimuon channel have been extracted. These values correspond to *global significances* of 0.1σ for dielectron final states and -1.3σ for dimuon final states. Equation 5.16 is defined in such a way that a p-value of 0.5 corresponds to a significance of 0. P-values larger than 0.5 correspond to negative significances. In the dimuon case this means that it is much more likely to find a more significant deviation in some invariant mass region in a pseudo-experiment than the most significant invariant mass region found in the observed data. In the dielectron case in contrast the *global* significance is positive but so small that a presence of new physics can be excluded.

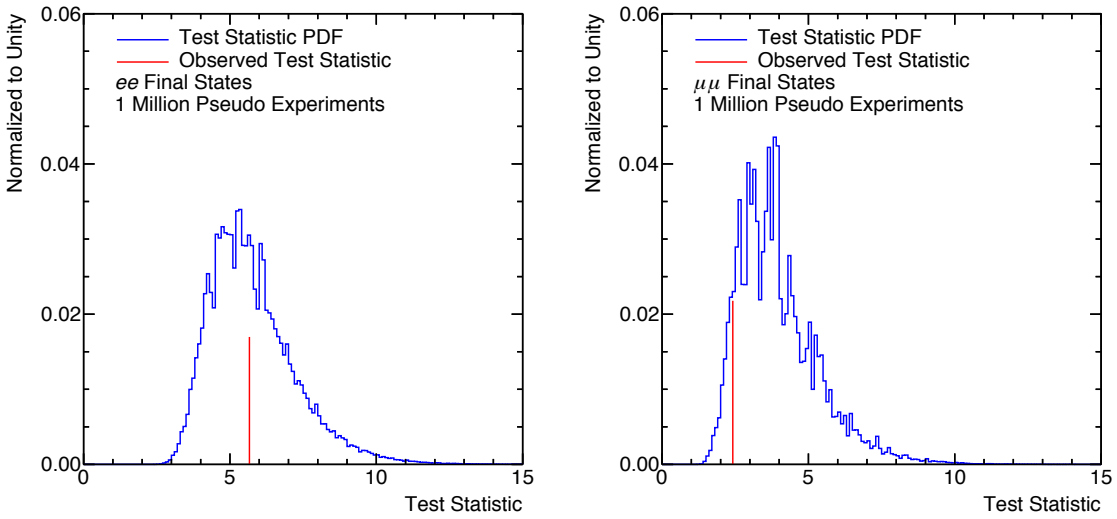

Figure 5.3: Test statistic probability density function determined from 1 million pseudo-experiments together with the observed test statistic in the dielectron final states (left) and the dimuon final states (right).

5.3 Exclusion Limits

Since no significant excess has been found limits are set on the signal strength Θ. The limit setting procedure relies on the number of measured events d_i as well as the number of expected events n_i determined from MC simulations and the Matrix Method in each bin i of the invariant mass spectrum. The quantity n_i consists of the number of expected background events b_i as well as the number of expected signal events s_i depending on the chosen model and hence Θ. Here the SSM as well as E_6 motivated models will be used. Another dependence of n_i arises due to the systematic uncertainties $\vec{u}$. The systematic uncertainties are different for dielectron and dimuon final states and will be denoted with $\vec{u}_{ee}$ and $\vec{u}_{\mu\mu}$ while the combined systematic uncertainties will be denoted with $\vec{u}_{\text{Comb}}$. However, in order to maintain simplicity the expressions $\vec{u}_{ee}$, $\vec{u}_{\mu\mu}$ and $\vec{u}_{\text{Comb}}$ are only used to preserve explicitness while $\vec{u}$ is used in general expressions. The number of expected events can thus be written as

$$n_i(\Theta, \vec{u}) = s_i(\Theta, \vec{u}) + b_i(\vec{u}). \tag{5.17}$$

In order to indicate the observed data over all bins of the invariant mass spectrum $\vec{d}$ will be used. The probability P of observing the data $\vec{d}$ under the assumption of a signal with strength Θ is called likelihood and given by the following product of Poisson probabilities:

$$P(\vec{d}|\Theta, \vec{u}) = \prod_{i=1}^{N_{\text{Bins}}} \frac{d_i^{n_i(\Theta,\vec{u})} e^{-n_i(\Theta,\vec{u})}}{d_i!}. \tag{5.18}$$

The probabilities are constructed separately for the dielectron channel and the dimuon channel. The combined probability is expressed by the product

$$P_{\text{Comb}}(\vec{d}|\Theta, \vec{u}_{\text{Comb}}) = P_{ee}(\vec{d}|\Theta, \vec{u}_{ee}) \cdot P_{\mu\mu}(\vec{d}|\Theta, \vec{u}_{\mu\mu}). \tag{5.19}$$

The interesting quantity, however, is not $P(\vec{d}|\Theta, \vec{u})$ but $P(\Theta, \vec{u}|\vec{d})$ which is the probability of observing a signal with strength Θ under the assumption that $\vec{d}$ has been measured. $P(\Theta, \vec{u}|\vec{d})$ is called posterior probability and is not defined in the frequentist approach where a probability only has a meaning as the limit of a number of successes in a sequence of trials. In order to obtain an expression for $P(\Theta, \vec{u}|\vec{d})$ BAYES' THEOREM can be used. The theorem states that

$$P(A|B) = \frac{P(B|A)P(A)}{P(B)} \quad \text{where} \quad P(B) \neq 0. \tag{5.20}$$

A and B are outcomes of an experiment assigned with a specific probability each. A can be identified with the observation of a signal with strength Θ while B can be identified with the measurement of the data $\vec{d}$. Applying BAYES' THEOREM the posterior probability can be expressed by

$$P(\Theta, \vec{u}|\vec{d}) = \frac{P(\vec{d}|\Theta, \vec{u})P(\Theta, \vec{u})}{P(\vec{d})}. \tag{5.21}$$

$P(\Theta, \vec{u})$ is the probability of observing a signal with strength Θ independently from the measured data $\vec{d}$. $P(\Theta, \vec{u})$ is called prior probability. $P(\vec{d})$ does not have a specific name and can be considered as a normalization constant. The systematic uncertainties $\vec{u}$ are assumed to be gaussian distributed and are called nuisance parameters. $P(\Theta, \vec{u})$ can thus be written as

$$P(\Theta, \vec{u}) = P(\Theta) \prod_{i=1}^{N_{\text{Sys}}} \frac{1}{\sqrt{2\pi}} e^{\frac{-u_i^2}{2}} \tag{5.22}$$

where N_{Sys} is the number of systematic uncertainties or simply the length of the vector $\vec{u}$. $P(\Theta)$ is chosen to be

$$P(\Theta) = \begin{cases} \text{const} & \Theta \geq 0 \\ 0 & \Theta < 0 \end{cases}. \tag{5.23}$$

The final expression for $P(\Theta|\vec{d})$ can be gained by integrating out all nuisance parameters. This integration is called marginalization and can be written as

$$P(\Theta|\vec{d}) = \int P(\Theta, \vec{u}|\vec{d}) d\vec{u} = N \int P_{ee/\mu\mu/\text{Comb}}(\vec{d}|\Theta, \vec{u}) \prod_{i=1}^{N_{\text{Sys}}} \frac{1}{\sqrt{2\pi}} e^{\frac{-u_i^2}{2}} d\vec{u} \tag{5.24}$$

$$\text{with} \quad N = \frac{P(\Theta)}{P(\vec{d})}.$$

$\vec{u}$ and N_{Sys} need to be chosen according to the dielectron case, the dimuon case or the combined case in equation 5.24. The normalization constant N can be determined by requiring

$$\int_0^\infty P(\Theta, \vec{d}) d\Theta = 1. \tag{5.25}$$

Equation 5.24 is calculated with the Bayesian Analysis Toolkit (BAT) [136] using a Markov chain MC technique. The limit on the signal strength Θ_{Limit} can finally be calculated by

$$\int_0^{\Theta_{\text{Limit}}} P(\Theta, \vec{d}) d\Theta = 1 - \alpha. \tag{5.26}$$

$1 - \alpha$ can be called confidence coefficient or confidence interval. In the Bayesian approach, however, one usually talks of credibility intervals instead of confidence intervals. In this limit setting procedure α is chosen to be 5 % which leads to a credibility interval of 95 %. Verbally this means that the posterior probability is included in a range of values on the posterior probability distribution including 95 % of the probabilities.

5.3.1 Model-Specific Cross Section and Mass Limits

Θ_{Limit} is directly related to s_{Limit} which is the limit on the number of signal events. s_{Limit} in turn can be transformed into a limit on the product of the cross section σ and the branching ratio B via

$$(\sigma B)_{\text{Limit}} = \frac{s_{\text{Limit}}}{L_{\text{Int}} \mathcal{A} \epsilon}. \tag{5.27}$$

L_{Int} is the integrated luminosity that has already been defined via equation 3.8. $\mathcal{A}$ is called the *acceptance* of the signal events while ϵ is called the *efficiency* of the signal events. The acceptance $\mathcal{A}$ is the fraction of the total signal events fulfilling certain restricted selection criteria at the truth level. These restricted selection criteria are constrains on the kinematical quantities of the signal events reducing the number of signal events in the total phase space $N_{\text{generated}}$ to a number of signal events in the restricted phase space $N_{\text{restricted}}$. The restricted selection consists of the following criteria:

$$p_{\text{T}} > 30\,\text{GeV} \quad \text{and} \quad |\eta| < 2.47 \quad (\text{with} \quad 1.37 < |\eta| < 1.52 \quad \text{excluded})\,. \tag{5.28}$$

Using the above notations the signal acceptance can be defined as

$$\mathcal{A} = \frac{N_{\text{restricted}}}{N_{\text{total}}}. \tag{5.29}$$

The efficiency ϵ is the fraction of the restricted signal events fulfilling all dilepton selection criteria as discussed in section 4.4.1. These criteria discriminate $N_{\text{restricted}}$ to the number of signal events in the reconstructed phase space $N_{\text{reconstructed}}$. Hence, the signal efficiency can be defined as

$$\epsilon = \frac{N_{\text{reconstructed}}}{N_{\text{restricted}}}. \tag{5.30}$$

The product of the signal acceptance and the signal efficiency is thus transferring the number of generated events to the total number of reconstructed events. This is necessary in order to gain a cross section limit $(\sigma B)_{\text{Limit}}$ that is corrected for the acceptance of the detector as well as the efficiency of the dilepton selection. This makes $(\sigma B)_{\text{Limit}}$ independent of the detector. The distribution of the product $\mathcal{A}\epsilon$ as a function of the signal pole mass $m_{Z'}$ can be seen in figure 5.4 for the SSM signal model in both the dielectron and the dimuon channel. The entry "Total Accepted" is identical with $\mathcal{A}$. All other entries show the development of the efficiency after the corresponding criterion has been applied. Hence, the entry "Dilepton Selection" is identical with $\mathcal{A}\epsilon$. The corresponding plots for the E_6 models can be found in appendix A. As expected $\mathcal{A}$ in both the dielectron and the dimuon case is very

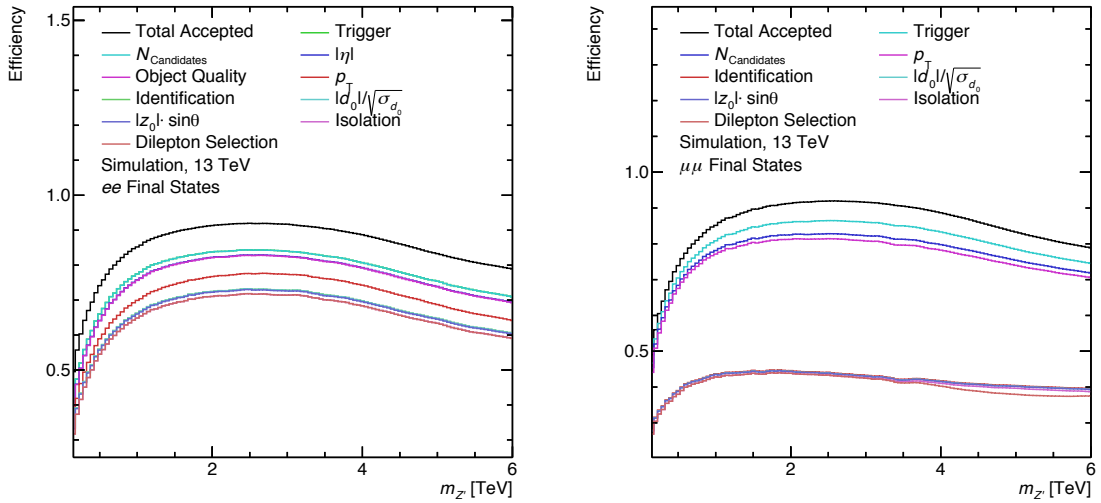

Figure 5.4: Product of signal acceptance and signal efficiency of the SSM signal model as a function of the signal pole mass for dielectron final states (left) and dimuon final states (right).

similar. The different criteria reduce the number of reconstructed events as has already been discussed in the previous chapter. After all criteria have been applied $\mathcal{A}\epsilon$ is generally larger in the dielectron channel than in the dimuon channel. The main reason for this is the strong identification criterion in the dimuon channel. At the lowest dielectron pole mass of 150 GeV $\mathcal{A}\epsilon$ rises from about 35 % and reaches a maximum of around 70 % at a pole mass of 3 TeV. For higher pole masses up to 6 TeV the value of $\mathcal{A}\epsilon$ decreases to about 60 %. Roughly the same behavior can be observed in the dimuon channel with a maximum $\mathcal{A}\epsilon$ value of around 42 % at a pole mass of 2 TeV. For higher pole masses a decrease of $\mathcal{A}\epsilon$ to around 30 % to 35 % can be seen.
Three exemplary signal templates used for the limit setting procedure can be seen in figure 5.5. Comparing the templates for the dielectron final states with the templates for the dimuon final states it can be seen that the worse resolution of the dimuon channel leads to broader signals. It can also be seen that the signal templates have a tail at lower values than the pole mass which is known as the parton luminosity tail. This tail arises due to the fact that the kinematic production limit is approached which leads to an increased fraction of the off-shell production for the signal events. As a result the impact of the parton luminosity tail becomes more significant for larger signal pole masses. The exclusion limits on σB are derived using the binning shown in figure 5.1 and can be seen in figure 5.6 for the SSM model. As can be seen the observed limit is within the $\pm 2\sigma$ of the expectation in both the dielectron and the dimuon case as well as in the combined case. For pole masses of around 4 TeV and higher the cross section limit gets larger due to the decreasing $\mathcal{A}\epsilon$ values. The theoretical cross section of the Z'_{SSM} model is shown in blue. The intersection of the observed and expected limit with the theoretical Z'_{SSM} define a lower limit on the mass $m_{Z'_{\mathrm{SSM}}}$. It is observed that the σB limit as well as the mass limit is stronger in the dielectron channel meaning that the limit on σB is smaller and hence the limit on $m_{Z'_{\mathrm{SSM}}}$ is larger than in the dimuon channel. The combined channel using

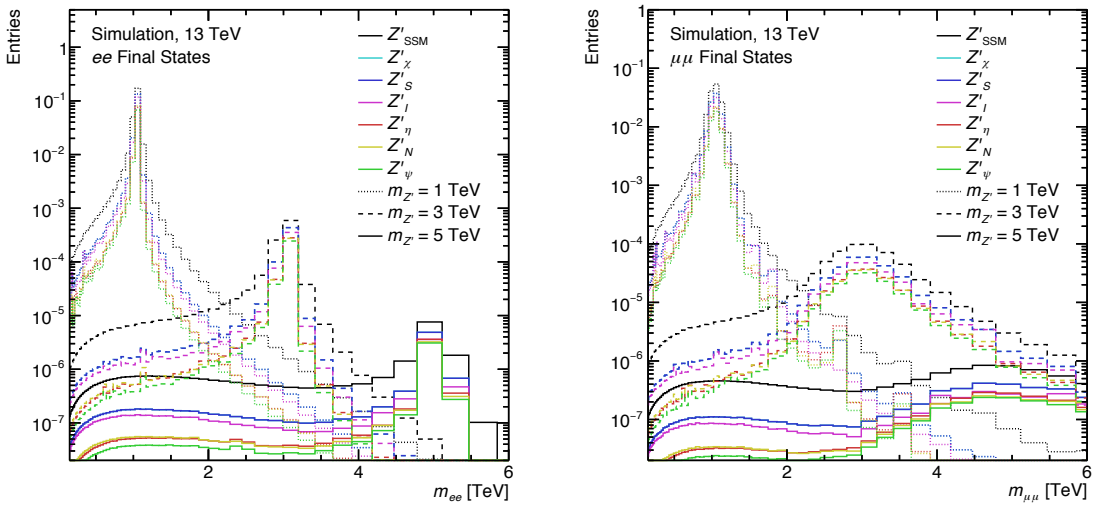

Figure 5.5: Signal templates for the SSM model and 6 different E_6 models at pole masses of 1 TeV, 3 TeV and 5 TeV for dielectron final states (left) and dimuon final states (right).

the information from both the dielectron channel and the dimuon channel has again stronger limits by construction. The lower mass limits for the Z' SSM model can be found in table 5.1. The limit on σB for the E_6 models are shown in figure 5.7. Only the combined case is shown while the σB limits for the dielectron channel and the dimuon channel can be found in appendix A. Only small differences in the σB limit are observed among the E_6 models. Generally it can be said that the limit is stronger the larger the width of the model is. Hence, the lower limit on the mass of the E_6 models is larger the larger the width of the model is. Table 5.1 shows the lower limit on the mass $m_{Z'}$ for all used models. The strongest lower mass limit by an E_6 model is given by the Z'_{χ} model with a value 4.06 TeV for the expected and observed limit in the combined case. The lower mass limit of the SSM model is stronger by about 300 GeV. Compared to the measurements presented in table 2.1 corresponding to an integrated luminosity of 3.2 fb^{-1} of proton-proton collisions the lower mass limits of the SSM model as well as the E_6 motivated models could be improved by around 1 TeV. Recent measurements from the CMS experiment, corresponding to an integrated luminosity of 36 fb^{-1} of proton-proton collision data at $\sqrt{s}$ = 13 TeV, have yielded lower mass limits of 4.50 TeV for the Z'_{SSM} model and 3.80 TeV for the Z'_{ψ} model at a credibility level of 95 % each [137]. In order to extract these limits CMS uses a Bayesian method with an unbinned extended likelihood function [138]. The lower mass limit for the Z'_{SSM} model is 150 GeV larger than the limit obtained in this work. However, a general agreement between both measurements can be observed.

5.3.2 Model-Independent Cross Section and Mass Limits

The model-independent exclusion limits are not extracted using resonances featured by specific models but by generic resonance shapes in the m_{ll} spectrum without an underlying model. In this case a generic resonance is a Breit-Wigner distribution

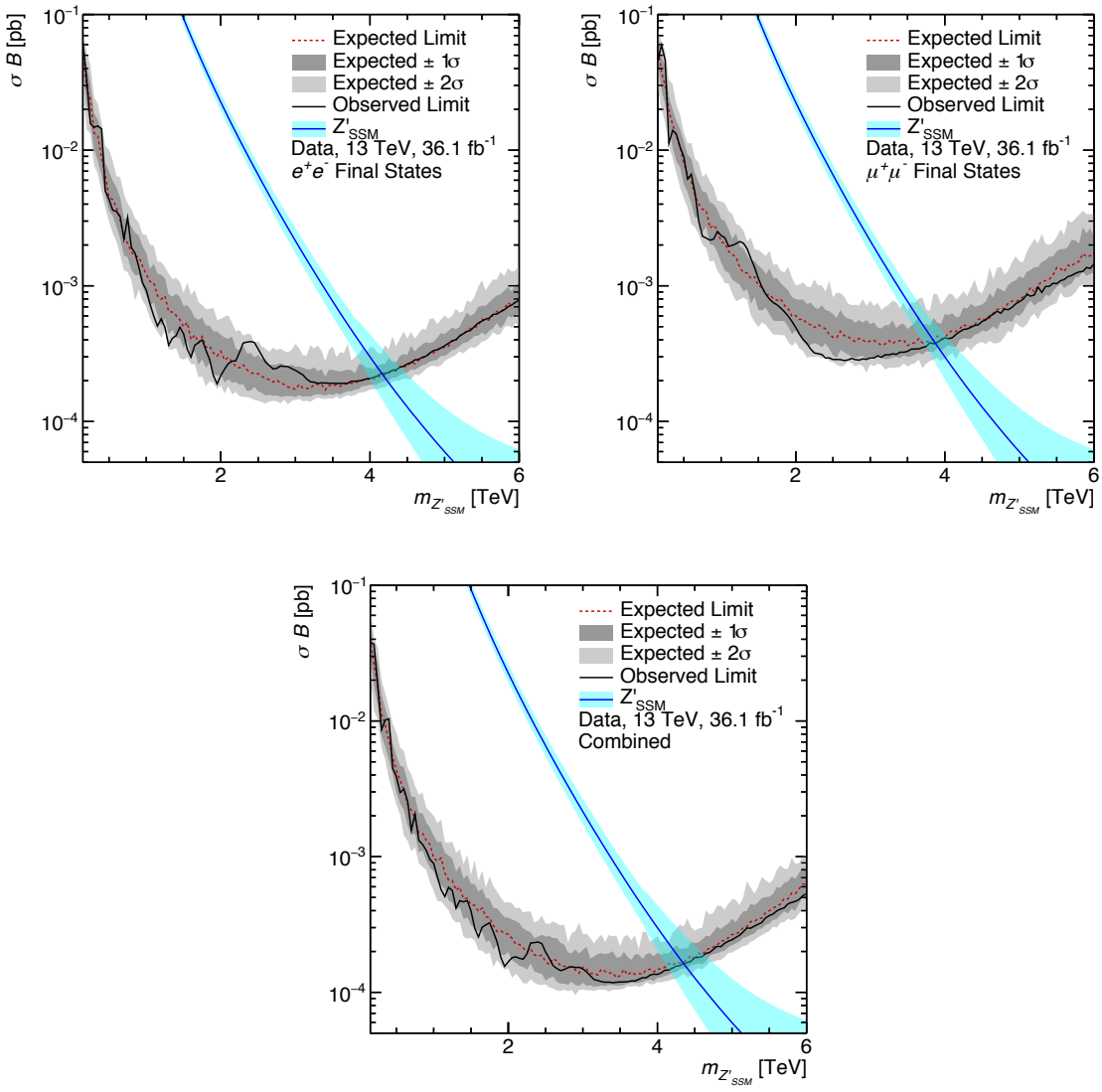

Figure 5.6: Expected and observed limit on σB for the SSM model as a function of the signal pole mass for dielectron channel (top left) the dimuon channel (top right) and the combined channel (bottom).

Table 5.1: Expected and observed lower limit on the pole mass of various Z' models for a credibility interval of 95 %.

Model	Expected Lower $m_{Z'}$ Limit [TeV]			Observed Lower $m_{Z'}$ Limit [TeV]		
	ee	$\mu\mu$	ll	ee	$\mu\mu$	ll
Z'_{SSM}	4.18	3.84	4.34	4.16	3.87	4.35
Z'_{χ}	3.91	3.53	4.06	3.90	3.59	4.06
Z'_{S}	3.84	3.48	3.99	3.84	3.53	4.01
Z'_{I}	3.77	3.41	3.93	3.77	3.48	3.94
Z'_{η}	3.69	3.33	3.85	3.70	3.39	3.87
Z'_{N}	3.67	3.31	3.81	3.66	3.37	3.84
Z'_{ψ}	3.63	3.26	3.77	3.62	3.32	3.80

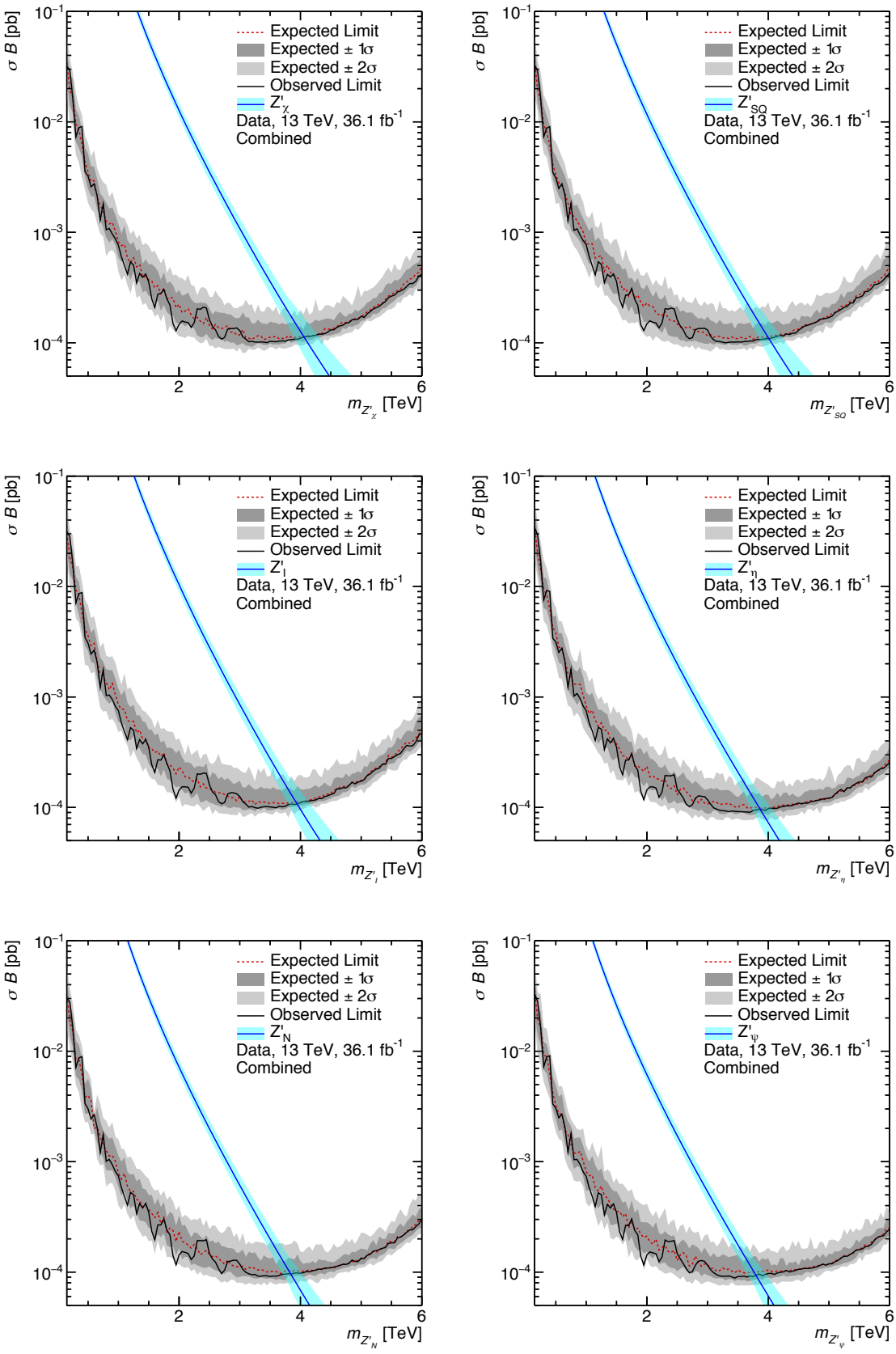

Figure 5.7: Expected and observed limit on σB as a function of the signal pole mass in the combined channel for the E_6^{χ} (top left), E_6^{S} (top right), E_6^{I} (middle left), E_6^{η} (middle right), E_6^{N} (bottom left) and E_6^{ψ} model (bottom right).

characterized by a pole mass $m_{Z'}$ and a width $\Gamma_{Z'}$. Using specific models like the SSM model and the E_6 models the value of $\Gamma_{Z'}$ is prescribed by the theory of the model. The benefit of model-independent exclusion limits is the ability that they can be reinterpreted in the context of other more specific models with a prescribed width $\Gamma_{Z'}$. In this approach the SSM model with differently adjusted widths is used as a generic resonance. In order to be as model-independent as possible only the peak of the resonance should be used. The effect of the parton luminosity tail which is model-dependent should not enter the generic resonance. Therefore the restricted phase space defined by the inequations 5.28 is supplemented with the mass window criterion

$$m_{Z'} - \Gamma_{Z'} < m_{ll} < m_{Z'} + \Gamma_{Z'}. \tag{5.31}$$

A second step to be more model-independent is to present the exclusion limits in the restricted phase space which is in contrast to the model-specific exclusion limits presented in the total phase space. As a result equation 5.27 alters to

$$(\sigma B\mathcal{A})_{\text{Limit}} = \frac{s_{\text{Limit}}}{L_{\text{Int}}\epsilon}. \tag{5.32}$$

The exclusion limits are hence presented as $(\sigma B\mathcal{A})_{\text{Limit}}$ which allows a reinterpretation of the exclusion limits to models with a strongly differing angular distribution. This is for instance the case when comparing spin 1 models like the SSM model and the E_6 models with a spin 2 model like a graviton.
The signal templates used for the limit setting procedure can be seen in figure 5.8. In contrast to the model-specific signal templates it can clearly be observed that the

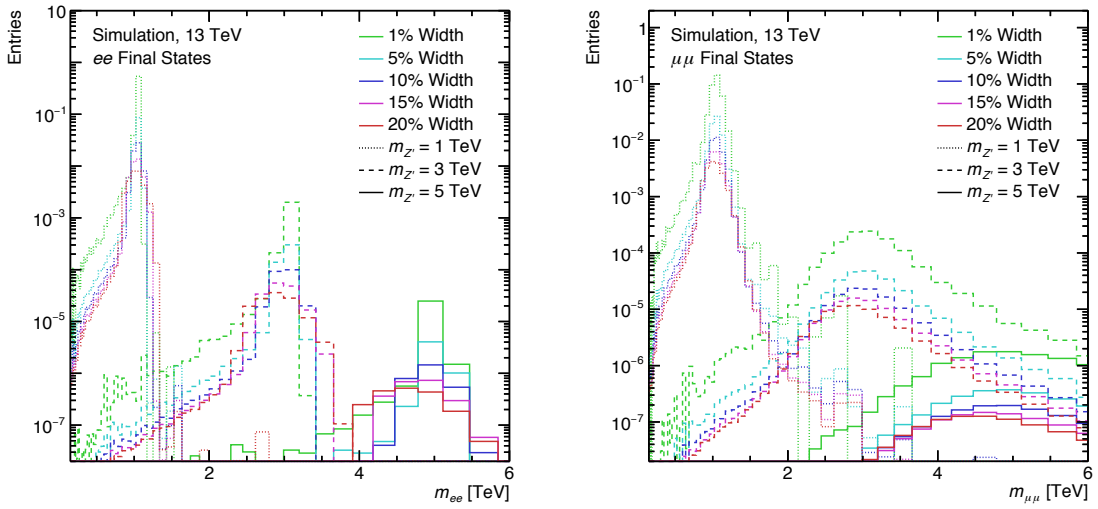

Figure 5.8: Signal templates for Breit-Wigner resonances with different widths at pole masses of 1 TeV, 3 TeV and 5 TeV for dielectron final states (left) and dimuon final states (right).

impact of the parton luminosity tail is reduced. Since the mass window is applied at the generation level a migration of events outside of the mass window can be seen at the reconstruction level as shown in figure 5.8. The extracted model-independent exclusion limits on $\sigma B\mathcal{A}$ as a function of the signal pole mass and signal width can be seen in figure 5.9. It is observed that the limits on $\sigma B\mathcal{A}$ for the dielectron case

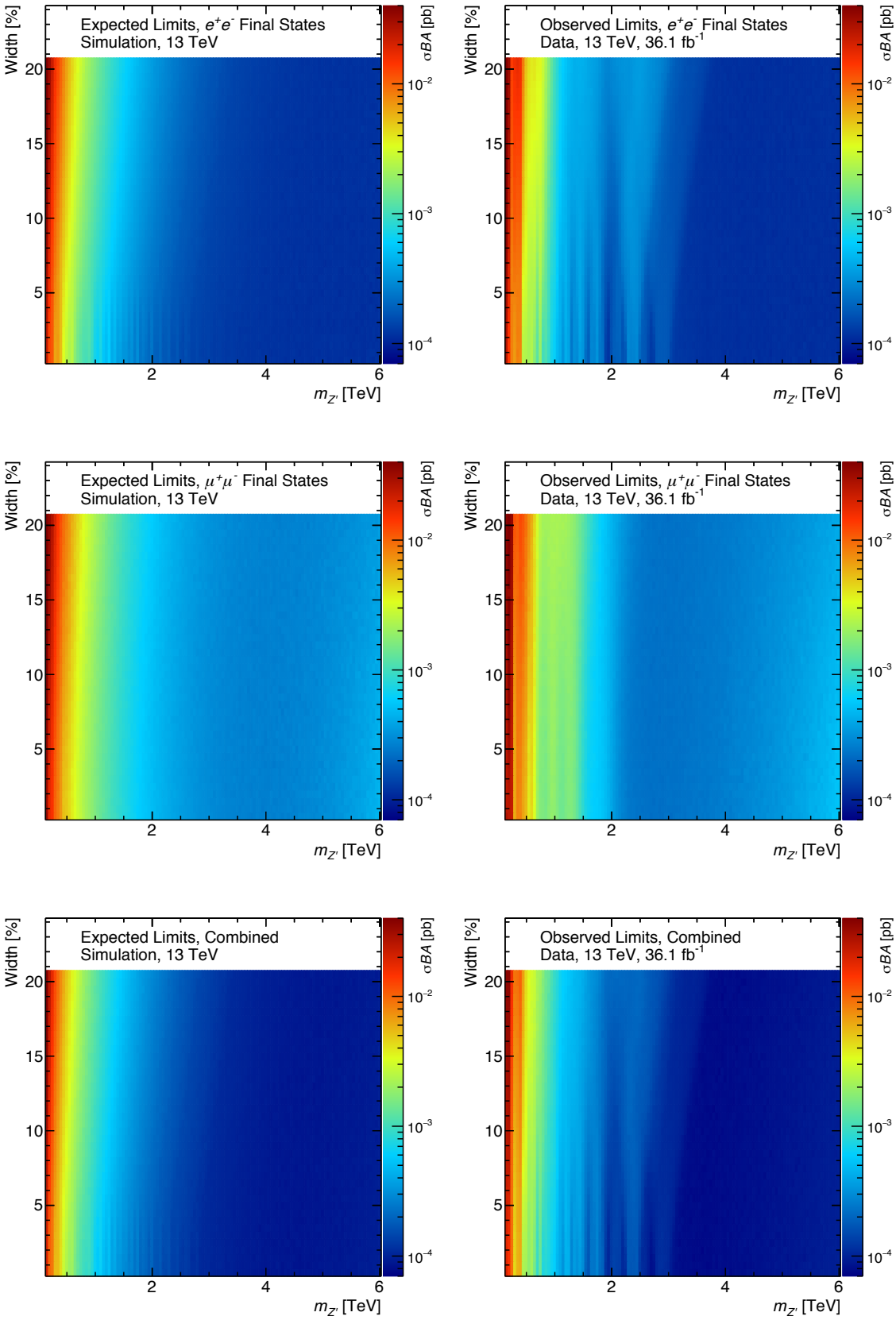

Figure 5.9: Expected and observed model-independent limits on $\sigma B\mathcal{A}$ as a function of the signal pole mass and the signal width for the dielectron case (top), the dimuon case (middle) and the combined case (bottom).

are smaller and hence stronger than the limits for the dimuon case. In contrast to the model-specific limits it is also observed that the limits stay low for increasing pole masses.
In order to reinterpret these limits into a specific model $\mathcal{M}$ featuring a resonance decaying in dilepton final states the following steps need to be done:

1. The acceptance of $\mathcal{M}$ in the restricted volume has to be calculated as a function of different pole masses.

2. The acceptance has to be multiplied with the total cross section of $\mathcal{M}$ again as a function of different pole masses.

3. The resulting theory curve needs to be overlaid with the model-independent limits. Therefore it is necessary to build the projections for specific widths. From table 7 to table 12 in [139] projections can be found for specific widths.

4. The intersection of the projection with the theory curve defines the lower mass limit in the context of $\mathcal{M}$. To be conservative, a projection for a width larger than the width of the resonance featured by $\mathcal{M}$ should be chosen.

So far there is no publication using this procedure yet. However, there are ongoing efforts to reinterpret the model-independent limits extracted in this work within the model of *Heavy Vector Triplets* [140] as well as within specific dark matter models assuming a potential mediator not only to couple to dark matter particles but also to leptons. An exemplary Feynman diagram of such a scenario can be seen in figure 5.10.

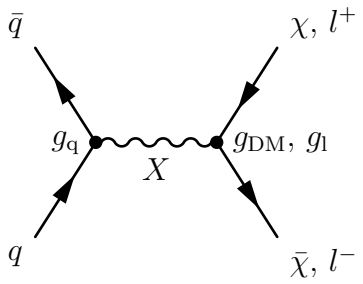

Figure 5.10: Feynman diagram of a quark-antiquark annihilation forming a potential mediator X with a coupling g_DM to dark matter particles as well as a coupling g_l to leptons at leading order.

Chapter 6

Search for Exotic Resonances

So far this analysis has been based on the search for resonances in the invariant mass spectrum of inclusive dilepton final states. This means that two leptons need to be in the final state while every other object in the final state remains unspecified. This is usually denoted with $pp \to l^+l^- + X$ where X is indicating the unspecified part of the final state. The search presented in this chapter focuses on the search for resonances in the invariant mass spectrum of more exclusive dilepton final states. This means that the unspecified part of the dilepton final states is further specified. In practise this will be a number n of jets besides the two leptons leading to the nomenclature $pp \to l^+l^- + n\,\text{jets} + X$. Hence, the set of more exclusive final states is a subset of the set of inclusive final states. Potential resonances in the invariant mass spectrum of more exclusive final states are referred to as exotic resonances. First the motivation and the strategy of this search is given. Afterwards the selection criteria as well as the background determination are discussed. Finally the results are statistically interpreted. The search for exotic resonances is performed within more exclusive invariant mass spectra of dielectron final states and dimuon final states.

6.1 Motivation and Strategy

The hidden valley model introduced in section 2.4.3 is a theoretical motivation for this search. This model suggests an interaction of so called v-quarks forming a Z' boson which can decay leptonically with a dielectron or a dimuon in the final state. The v-quarks as a final state of another preceding Z' boson decay can radiate v-gluons such that v-hadrons arise. It is assumed that some of the v-hadrons can decay to SM particles while others decay to v-particles which are invisible in the detector. Thus, the hidden valley model suggests a final state with a lepton-antilepton pair accompanied by either jets, missing transverse momentum or both. Another motivation for this search can be seen in figure 6.1. The left hand plot shows an exemplary invariant mass spectrum of inclusive dielectron final states as the SM background as well an exemplary signal corresponding to dielectron final states in addition with at least two jets. The signal has its maximum at around 500 GeV and seems to be negligible compared to the SM background as the ratio $\frac{\text{SM + Signal}}{\text{SM}}$ indicates. The right hand plot in figure 6.1 shows the same signal but the SM background is further constrained to include two electrons and at least 2 jets like the signal itself. It can be seen that the signal finally becomes visible in the more exclusive spectrum

as the ratio $\frac{\text{SM + Signal}}{\text{SM}}$ clearly indicates. As a consequence, an approach to search for exotic resonances in more exclusive final states has been developed. In order to

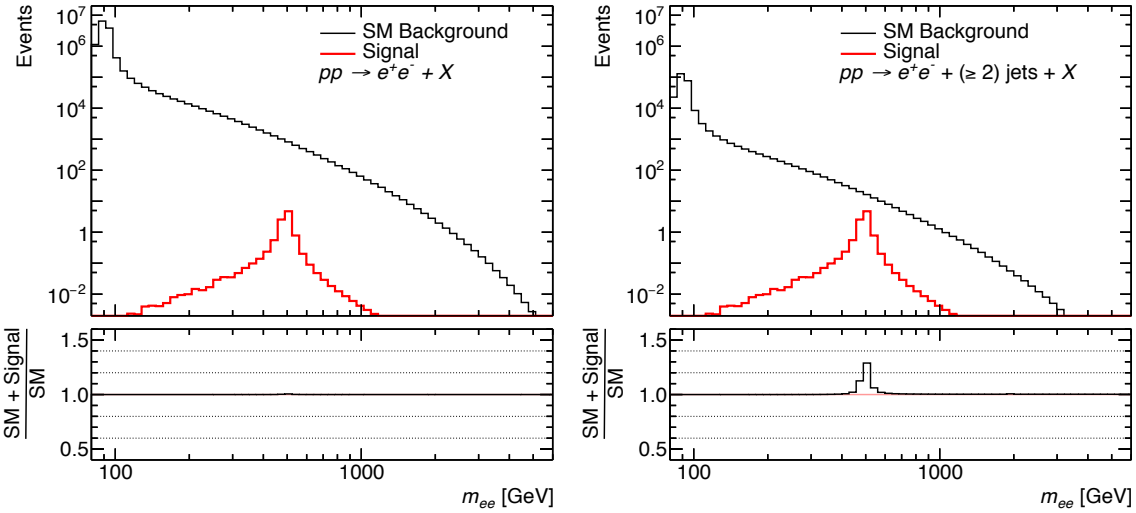

Figure 6.1: Exemplary spectra of the invariant mass of events with two electrons in the final state (left) and two electrons and at least two jets in the final state (right). Both plots contain an exemplary signal corresponding to a dielectron final state in addition with at least two jets.

investigate such exotic resonances dilepton events are selected exclusively depending on the number of jets. This yields different invariant mass spectra of specific final states with two leptons and a certain number of jets. In contrast to the inclusive analysis discussed in chapter 4 the background determination is not performed with MC simulations but with a data-driven approach. The reason for this is simply to reach a minimization of the effort. Additionally the data used for this search is from the LHC runs of 2015 only which correspond to an integrated luminosity of $3.2\,\text{fb}^{-1}$. The data-driven background determination is based on an extrapolation procedure performed on the invariant mass spectrum with a suitable function. It is assumed that a possible exotic resonance is not absorbed by the extrapolation. A statistical analysis will then be performed when comparing the extrapolation with data.

6.2 Selection Criteria

In order to select the more exclusive dilepton final states $l^+l^- + n\,\text{jets}$ a set of selection criteria needs to be defined. All of the final states need to fulfill the criteria defined in section 4.4.1. The leptons included in these final states need to fulfill all criteria discussed in section 4.4.2. The composition of dilepton events is performed as described in section 4.4.3. The jets included in these final states are reconstructed with the anti-k_t jet clustering algorithm [91]. The tracks clustered into the jet need to have a minimum p_T of 0.5 GeV. The following criteria need to be fulfilled by each jet in the more exclusive final states:

Pseudo-Rapidity η
The absolute pseudo-rapidity value of a jet candidate has to be smaller than 2.5.

Transverse Momentum $p_{\mathbf{T}}$
The transverse momentum of a jet candidate has to be greater than 30 GeV.

Suppression of Pile-up Jets
The transverse momentum of a reconstructed jet candidate associated with the interaction of the hard-scatter primary vertex PV_0 may include a significant contribution from interactions of the primary vertices PV_n with $n \geq 1$ due to pile-up (see section 3.2.8). These jet candidates referred to as *pile-up jets* can be discriminated by the following variable called *jet vertex fraction* (JVF) [141].

$$\mathrm{JVF} = \frac{\sum_k p_{\mathrm{T}}^{\mathrm{trk}_k}(\mathrm{PV}_0)}{\sum_k p_{\mathrm{T}}^{\mathrm{trk}_k}(\mathrm{PV}_0) + p_{\mathrm{T}}^{\mathrm{PU}}} \quad \text{with} \quad p_{\mathrm{T}}^{\mathrm{PU}} = \sum_{n\geq 1}\sum_i p_{\mathrm{T}}^{\mathrm{trk}_i}(\mathrm{PV}_n) \tag{6.1}$$

$\sum_k p_{\mathrm{T}}^{\mathrm{trk}_k}(\mathrm{PV})$ is the scalar sum of the transverse momenta of all tracks associated with the jet candidate and originated from the vertex PV. A JVF value of 1 means that there is no contribution due to pile-up jets while lower JVF values indicate such a contribution. Since the JVF value has the disadvantage to be depending on the number of primary vertices a new variable called *jet vertex tagger* (JVT) [142] has been developed. The JVT value is based on a corrected version *corrJVF* of the JVF value that is stable as a function of the number of primary vertices. In order to reach this stability the scalar sum of the tracks from pile-up interactions $p_{\mathrm{T}}^{\mathrm{PU}}$ in equation 6.1 is divided by the total number of pile-up tracks per event.
In addition the JVT value is based on the variable

$$R_{\mathrm{pT}} = \frac{\sum_k p_{\mathrm{T}}^{\mathrm{trk}_k}(\mathrm{PV}_0)}{p_{\mathrm{T}}^{jet}} \tag{6.2}$$

where p_{T}^{jet} is the fully calibrated jet p_{T} including pile-up subtraction. For pile-up jets R_{pT} peaks a 0 and falls steeply while for hard-scatter jets it resembles a distribution with a larger mean and a larger spread. The JVT discriminant is finally constructed using R_{pT} and *corrJVF* as a 2-dimensional likelihood that is based on a k-nearest neighbor algorithm [143]. The *ATLAS Jet and E_T^{miss} Combined Performance Group* [144] recommends to use JVT > 0.59 as a selection criterion.

Overlap Removal
In the processing of an event it can happen that the different physical objects are reconstructed by several algorithms instead of just one. This leads to overlapping event information in the reconstructed quantities which need to be removed. The overlap removal within this analysis is performed according to the following steps:

1. If an electron and a muon share a track the electron is removed.
2. If a jet is within $\Delta R < 0.2$ of an electron the jet is removed.
3. If an electron is within $\Delta R < \min\left(0.4, 0.04 + \frac{10\,\mathrm{GeV}}{p_{\mathrm{T}}^{\mathrm{electron}}}\right)$ of one of the remaining jets the electron is removed.
4. If a muon is within $\Delta R < \min\left(0.4, 0.04 + \frac{10\,\mathrm{GeV}}{p_{\mathrm{T}}^{\mathrm{muon}}}\right)$ of a jet and the jet has less than 3 tracks the jet is removed, otherwise the muon is removed.

6.3 Background Determination

The background determination is performed using the invariant mass spectra of more exclusive dilepton final states obtained from data by applying the selection criteria explained in the previous section. The final states are required to consist of an opposite-signed same-flavored pair of leptons l^+ and l^- and a specific number of jets n. Such a final state can be written shortly as $pp \to l^+l^- + n\,\text{jets} + X$ where X is indicating that every other object can be contained additionally in this final state. Since an exotic resonance present in $pp \to l^+l^- + n\,\text{jets} + X$ is assumed to be present in $pp \to l^+l^- + (n+1)\,\text{jets} + X$ as well the spectra from the final states $pp \to l^+l^- + (\geq n)\,\text{jets} + X$ will be used for this exotic resonance search. The extrapolation of these spectra will be performed with equation 4.3 which is the same equation used for the top background and the fake background extrapolation. This function is assumed to be flexible enough to describe the more exclusive spectra but inflexible enough to absorb a possible exotic resonance. However, a more sophisticated approach building upon this has been developed by introducing a sliding window procedure scanning over the full spectrum. This procedure assumes a specific shape with a pole mass $m_{Z'}$ and a width $\sigma_{Z'}$ as a hypothetical exotic signal. In a second step a simulation of such a specific signal is used in order to extract a signal mass region m_{Signal} that is excluded from the extrapolation procedure. For this approach the invariant mass spectrum of the simulated signal is binned very fine in bins of 0.1 GeV. Initially the signal mass region is the bin with the highest number of events. It is expanded by adding the neighboring bin with the highest amount of events. This process is repeated until the signal mass region contains at least 90 % of the signal events. The background in the signal mass region is finally determined by extrapolations based only on the data outside of the signal mass region. These extrapolations will be called *sideband fits*. Within the signal mass region a counting experiment will be performed using the measured data and the determined background in the signal mass region. A schematic illustration of this approach is shown in figure 6.2. Step 2 to 4 is repeated for every signal mass region tested. A systematic uncertainty is gained in a similar way as for the top background and fake background extrapolation. The spectrum is extrapolated starting from 120 GeV to avoid an influence of the resonance due to Z boson decays. This starting point of the sideband fits is varied up to 150 GeV in steps of 3 GeV. A second contribution to the systematic uncertainty is introduced by extending the extrapolation function to

$$f(m_{ll}) = p_0 \left(1 - \frac{m_{ll}}{13\,\text{TeV}}\right)^{p_1} \left(\frac{m_{ll}}{13\,\text{TeV}}\right)^{p_2 + p_3 \ln \frac{m_{ll}}{13\,\text{TeV}}} . \tag{6.3}$$

As can be seen the term $\left(\frac{m_{ll}}{13\,\text{TeV}}\right)^{p_3 \ln \frac{m_{ll}}{13\,\text{TeV}}}$ has been added compared to equation 4.3. This adaption gives the extrapolation function more flexibility especially at high invariant masses where the statistic is low. Overall these variations lead to 60 different sideband fits from which the arithmetic mean is used as the background expectation. Exemplary scenarios of the procedure for different spectra can be seen in figure 6.3. The upper two plots show scenarios with a lower pole mass $m_{Z'}$ while the bottom two plots show scenarios with a larger pole mass. The different behavior of the two extrapolation functions can clearly be seen at high invariant masses. Overall the 60 sideband fits lead to an envelope from which the outer most sideband fits determine the systematic uncertainty of the arithmetic mean. The normalized residuals are

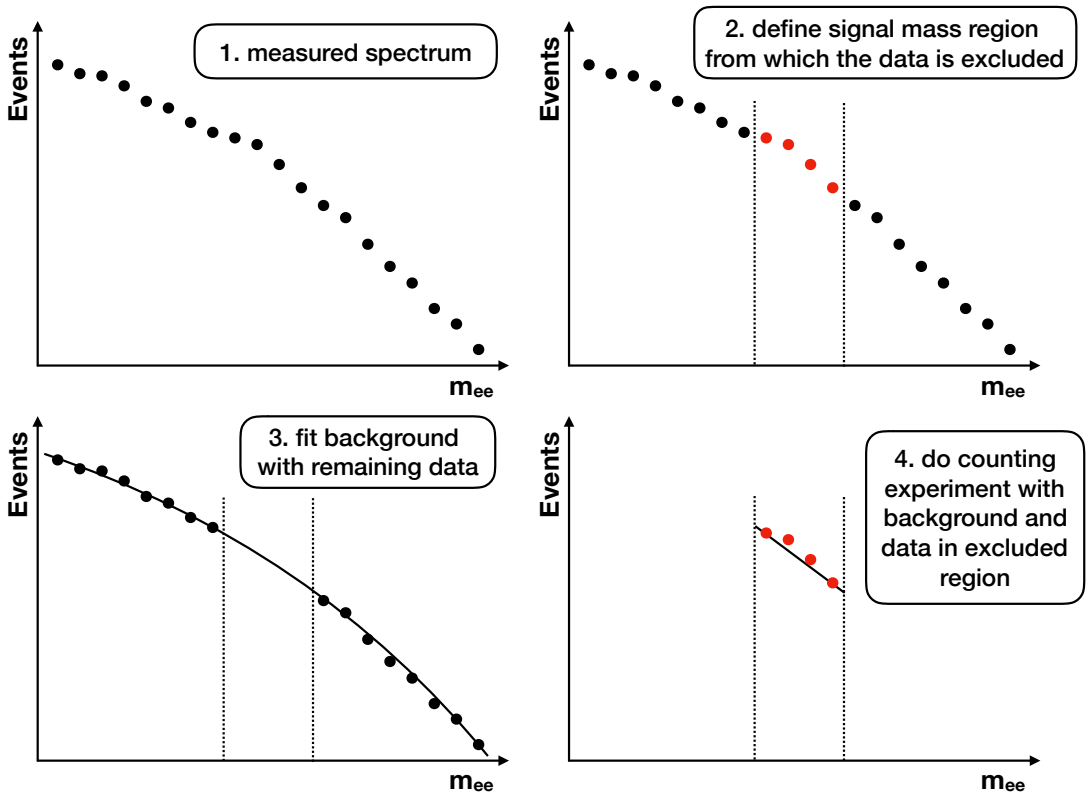

Figure 6.2: Schematic illustration of the sliding window procedure used to search for exotic resonances.

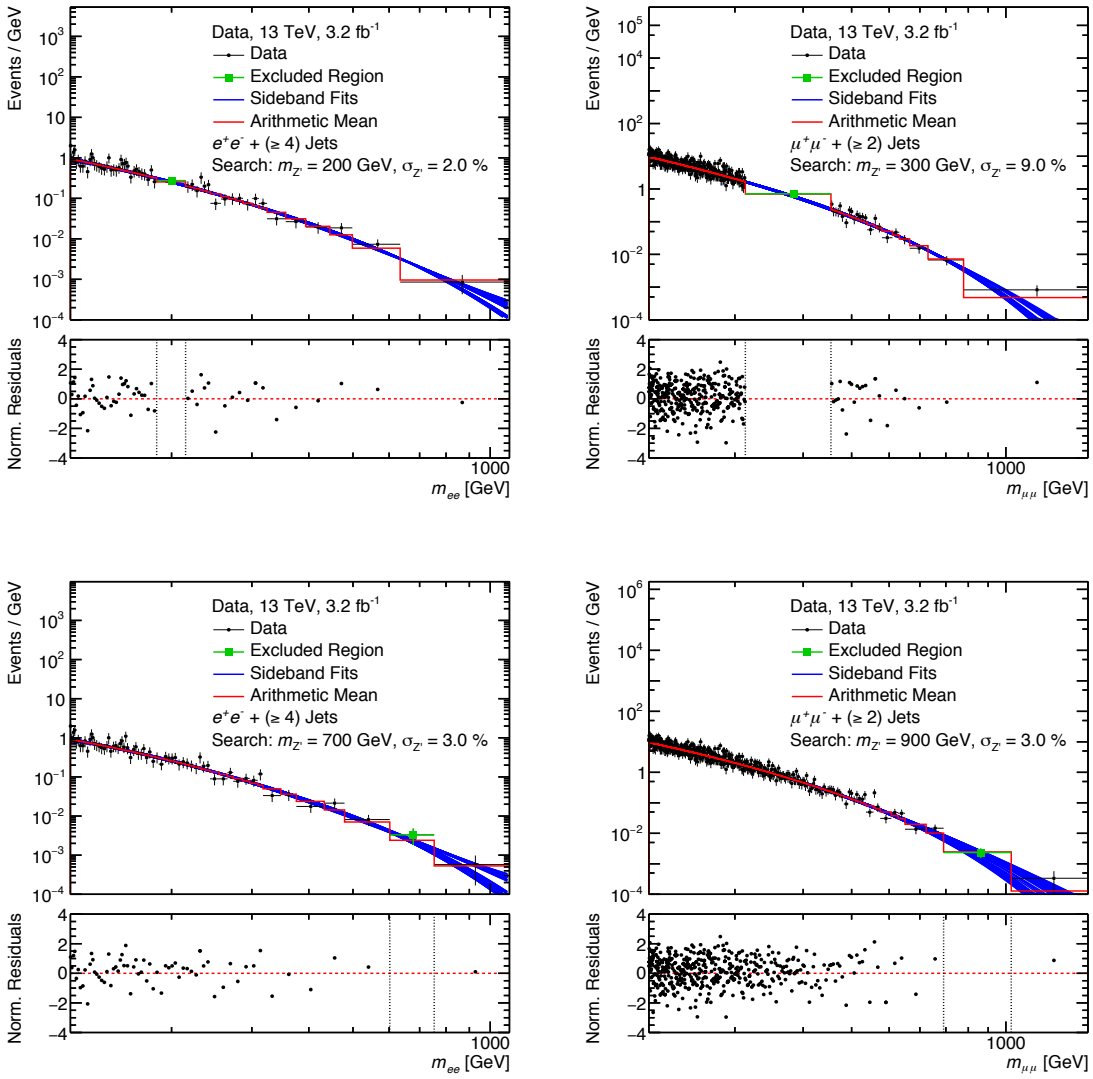

Figure 6.3: Exemplary scenarios of the background determination procedure for different spectra at various pole masses $m_{Z'}$ and widths $\sigma_{Z'}$ together with the normalized residuals.

defined as the difference of data and the determined background divided by the statistical errors of data. As can be seen the normalized residuals fluctuate equally around zero outside of the excluded region which is illustrated by the vertical dashed lines. This indicates that the extrapolation procedure yields backgrounds unbiased of systematic effects due to the extrapolation function. The data in the excluded region is merged in one bin displayed in green. For the statistical interpretation the data in the excluded region as well as the background determination in the excluded region is relevant and will be elaborated in the next section. The range of tested pole masses starts at 150 GeV in order to have the data from 120 GeV to 150 GeV as a guiding input for all sideband fits. The largest tested pole mass is depending on the highest recorded data event at around 1.6 TeV as well as on the excluded signal mass region defined by $m_{Z'}$ and $\sigma_{Z'}$. As long as the excluded signal mass region contains data events the pole mass $m_{Z'}$ is tested. In principle one could also extend the procedure to test even higher pole masses. However, this needs a more sophisticated treatment of the systematic uncertainties of the determined background at high invariant masses. The largest width tested is chosen to be 10 % since larger widths are considered to exclude too much data to guarantee a well performing fit.

6.4 Statistical Interpretation

In order to statistically evaluate a significance describing the agreement between the measured data and the determined background expectation the statistical tools from chapter 5 are used. More specifically the p-value for the excluded regions and hence the hypothetical exotic signals with pole mass $m_{Z'}$ and width $\sigma_{Z'}$ are calculated using equation 5.7. The *local significance* is calculated using equation 5.16 and referred to as z-value in the plots. The difference to the BumpHunter procedure is merely that the windows are set according to $m_{Z'}$ and $\sigma_{Z'}$. The procedure is tested first by using a spectrum with an injected signal. Therefore the $pp \to e^+e^- + (\geq 2)\,\text{jets} + X$ spectrum is used with an added signal with a pole mass of 500 GeV and a width of 3 %. Figure 6.4 shows the spectrum as well as the injected signal in red. The signal has been extracted from a simulation with large statistics. In order to match the statistical errors in data the extracted signal is fluctuated according to Poisson's law. The result of the procedure applied to the spectrum with the injected signal can be seen in the left hand plot of figure 6.5. It shows the local significances of the observed excesses and deficits for various combinations of pole mass and width of a hypothetical signal. As expected a fluctuation to larger local significances can be seen at a pole mass of around 500 GeV. The largest observed local significance is 4.6σ. However, the local significance does not account for the look elsewhere effect (see section 5.1.3). Therefore the procedure has been repeated 10000 times using poisson-fluctuated pseudo-data extracted from the determined background. The result in form of a test statistic can be seen in the right hand plot of figure 6.5. The observed test statistic is larger than most of the test statistics found in the pseudo-experiments which leads to a global significance of 2.5σ. Hence, the procedure is considered to be capable of detecting a fluctuation in the spectra of $pp \to e^+e^- + (\geq n)\,\text{jets} + X$. The results after applying the procedure to the raw spectra observed in data can be seen in figure 6.6 for dielectron final states and in figure 6.7 for dimuon final states. All four scenarios in the dielectron final states show small fluctuations around zero. These fluctuations are within a local

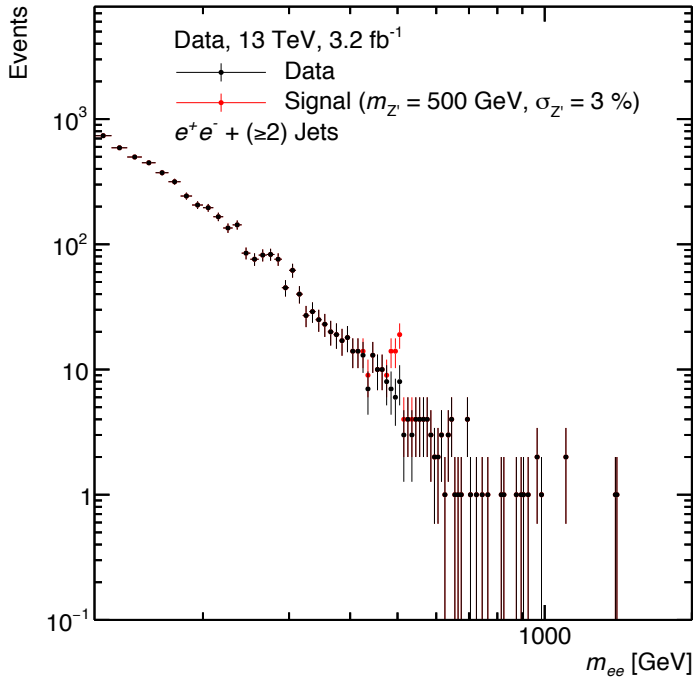

Figure 6.4: Data in the spectrum of $pp \to e^+e^- + (\geq 2)\,\text{jets} + X$ with an injected signal with a pole mass of 500 GeV and a width of 3 %.

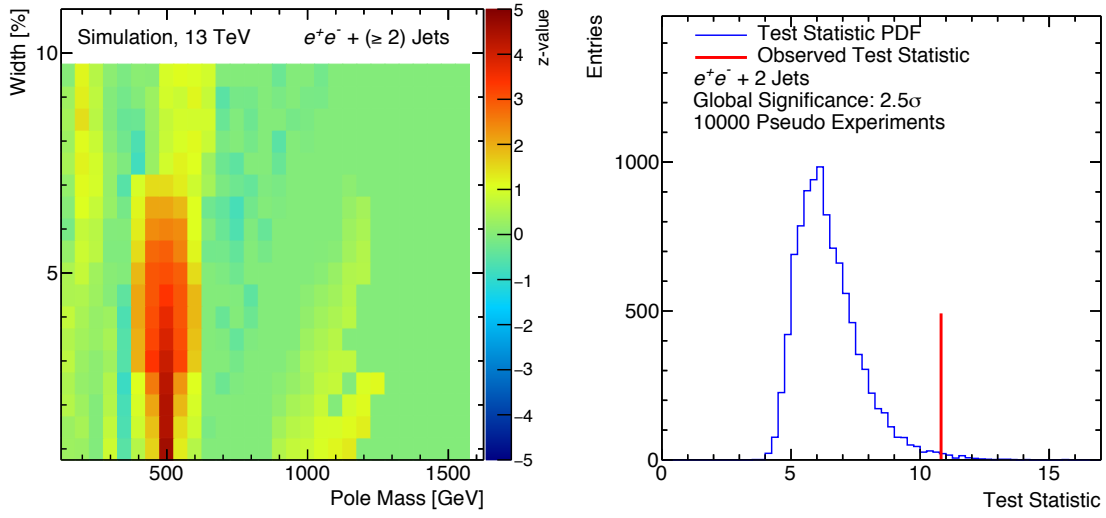

Figure 6.5: Local significances found in a simulation of the spectrum $pp \to e^+e^- + (\geq 2)\,\text{jets} + X$ with an injected hypothetical signal for various pole masses and widths (left) and the result of 10000 pseudo-experiments in form of a test statistic leading to the global significance (right).

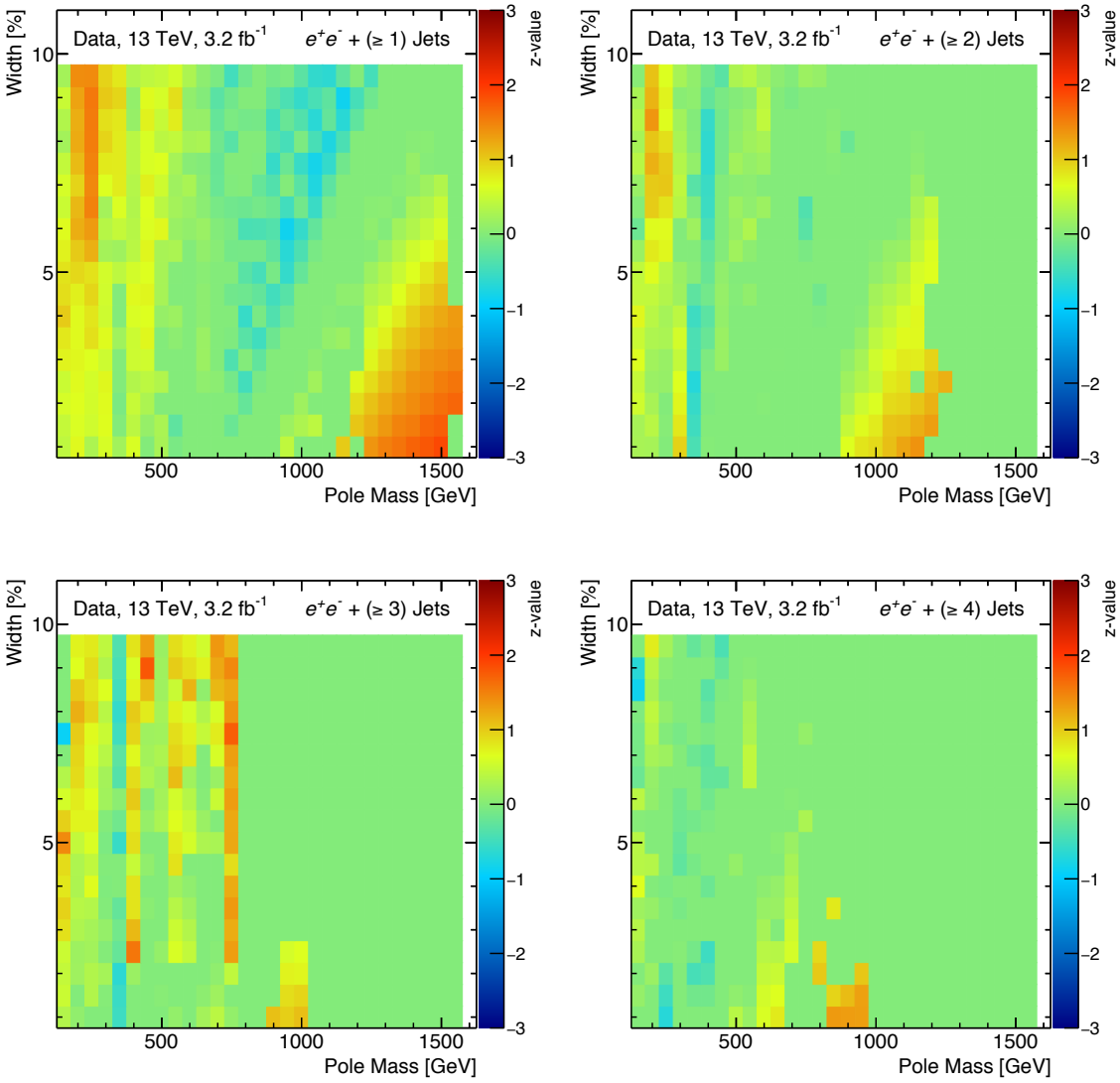

Figure 6.6: Local significances observed in data for several values of different pole masses $m_{Z'}$ and widths $\sigma_{Z'}$ characterizing the hypothetical exotic resonance in di-electron final states.

significance of 2σ and can be seen in detail in table 6.1. In the dimuon final states

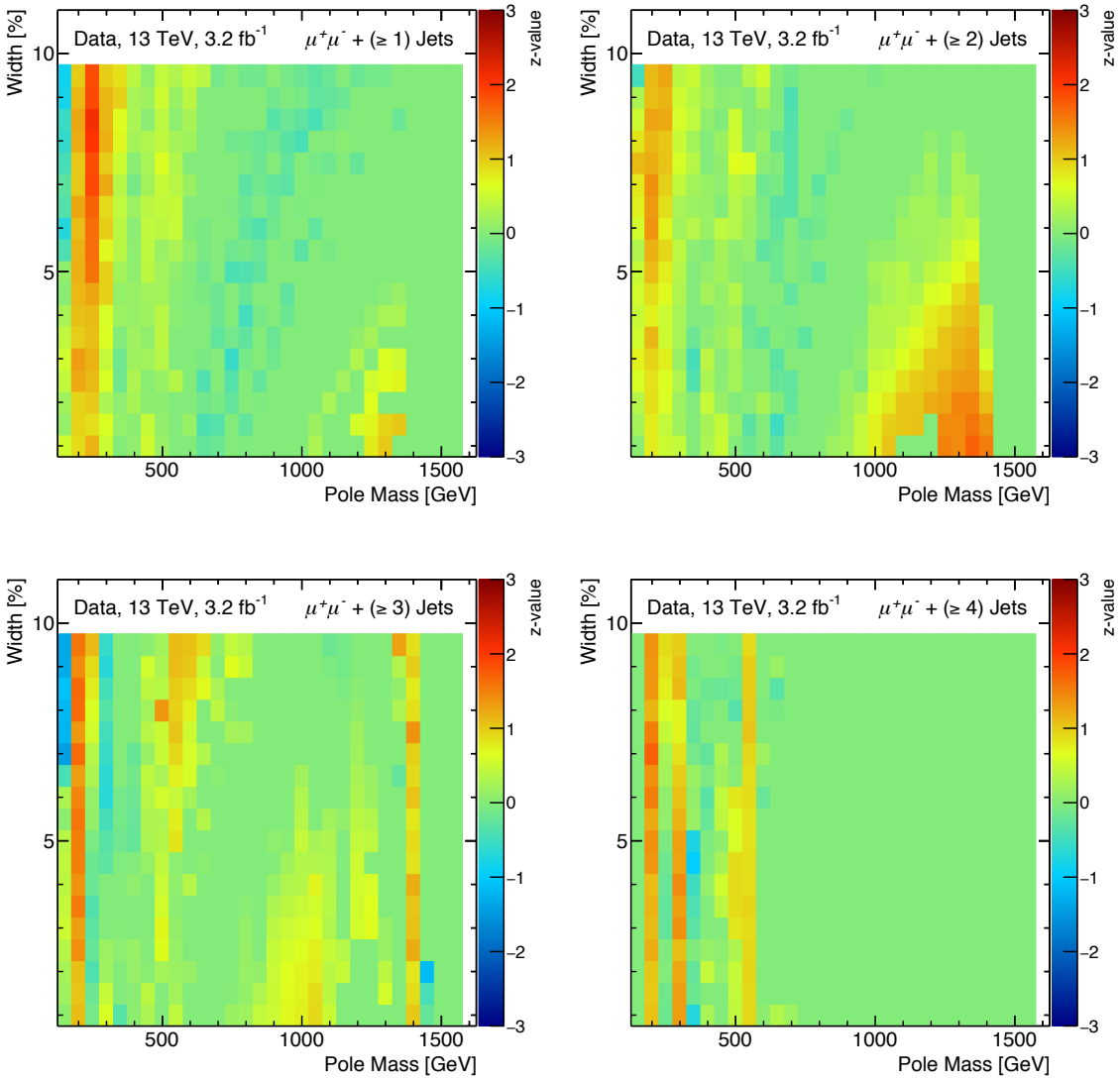

Figure 6.7: Local significances observed in data for several values of different pole masses $m_{Z'}$ and widths $\sigma_{Z'}$ characterizing the hypothetical exotic resonance in dimuon final states.

the fluctuations are in the same order as for the dielectron final states. Only in the spectrum of $pp \to \mu^+\mu^- + (\geq 1)\,\text{jets} + X$ a local significance of 2.1σ has been found in the signal mass region defined by $m_{Z'} = 250\,\text{GeV}$ and $\sigma_{Z'} = 8.5\,\%$. The background determination scenario for this region can be seen in figure 6.8. The results in form of global significances can be seen in table 6.1. In all eight scenarios the global significance is less than 0.1σ. This means that in almost all cases a significance larger than the largest observed significance in data has been found in one of the pseudo-experiments. As a result, no significant deviation from the SM expectation has been discovered in proton-proton collisions corresponding to an integrated luminosity of $3.2\,\text{fb}^{-1}$. As a next step for future efforts in this search the extracted results can be used to set model-specific as well as model-independent limits on the cross section of a heavy gauge boson decaying to two leptons and a number of jets similar to

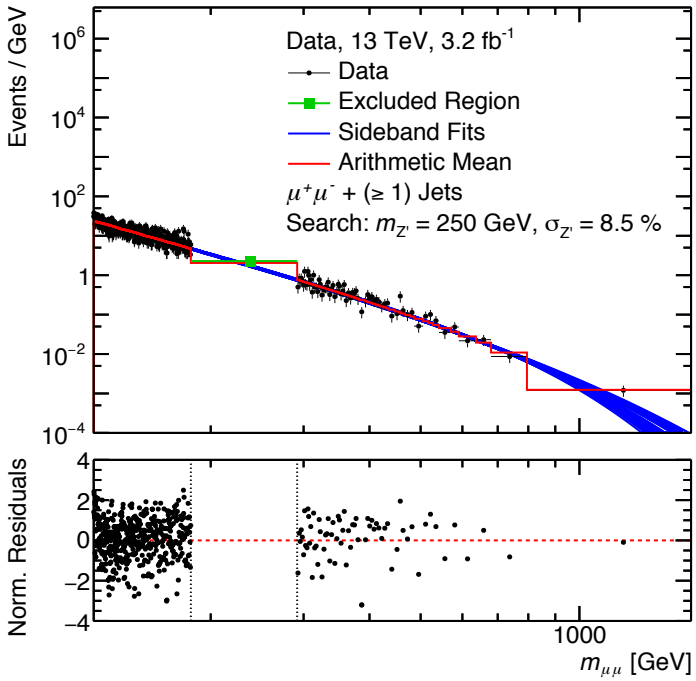

Figure 6.8: Background determination scenario for the spectrum $pp \to \mu^+\mu^- + (\geq 1)\,\text{jets} + X$ at a pole mass $m_{Z'} = 250\,\text{GeV}$ and widths $\sigma_{Z'} = 8.5\,\%$.

the approach from section 5.3.1 and section 5.3.2 respectively. Another approach to advance this search is to include missing transverse momentum as a specific part of the more exclusive final states. The fitting procedure used for this search could be improved by performing simultaneous fits to the investigated spectra. An improvement could also be gained by developing a MC based approach. In this case the HV1.0 Monte Carlo program [145] which is still in design and testing phase could be of special interest. It can simulate the process $q\bar{q} \to Z' \to Q\overline{Q}$ where $Q\,(\overline{Q})$ is a v-quark ($\bar{v}$-quark).

Table 6.1: Largest local significance and global significance in each investigated spectrum with dielectron and dilepton final states.

Spectrum	$m_{Z'}$ [GeV]	$\sigma_{Z'}$ [%]	Local Sig.	Global Sig.
$pp \to e^+e^- + (\geq 1)\,\text{jets} + X$	1500	1.0	1.9σ	$< 0.1\sigma$
$pp \to e^+e^- + (\geq 2)\,\text{jets} + X$	200	8.5	1.7σ	$< 0.1\sigma$
$pp \to e^+e^- + (\geq 3)\,\text{jets} + X$	450	9.0	1.8σ	$< 0.1\sigma$
$pp \to e^+e^- + (\geq 4)\,\text{jets} + X$	850	1.0	1.3σ	$< 0.1\sigma$
$pp \to \mu^+\mu^- + (\geq 1)\,\text{jets} + X$	250	8.5	2.1σ	$< 0.1\sigma$
$pp \to \mu^+\mu^- + (\geq 2)\,\text{jets} + X$	1350	1.0	1.7σ	$< 0.1\sigma$
$pp \to \mu^+\mu^- + (\geq 3)\,\text{jets} + X$	200	8.5	1.7σ	$< 0.1\sigma$
$pp \to \mu^+\mu^- + (\geq 4)\,\text{jets} + X$	200	7.0	1.7σ	$< 0.1\sigma$

Chapter 7

Conclusion

This work presents a search for new heavy resonances in the spectrum of processes with an electron-positron pair or a muon-antimuon pair in the final state. Such heavy resonances can be explained with neutral heavy Z' gauge bosons as predicted by several theories extending the SM in order to solve not understood phenomena of the microcosm. The theories used in the context of this search were the SSM (see section 2.4.1), E_6-motivated models (see section 2.4.2) as well as the hidden valley model (see section 2.4.3). The underlying data for this work has been produced in the LHC through proton-proton collisions at a center of mass energy of $\sqrt{s} = 13\,\text{TeV}$. The ATLAS detector recorded the data corresponding to an integrated luminosity of $36.1\,\text{fb}^{-1}$.
The search for new resonances has been performed using the electron-positron pair and the muon-antimuon pair invariant mass spectrum. The highest recorded invariant mass in events with an electron-positron pair in the final state is 2.90 TeV, while in events with a muon-antimuon pair in the final state 1.99 TeV has been found to be the highest recorded invariant mass. The real lepton background for both invariant mass spectra consists of Drell-Yan production, top quark production and diboson production which have been estimated with MC simulations. In the electron-positron pair invariant mass spectrum the background due to fake leptons can not be neglected and is estimated with a data-driven method. As a sanity check the data has been compared to the SM expectation for the variables ϕ, η and p_T of the leading and subleading leptons. A good agreement has been found in all three variables.
The search for new resonances is based on the comparison between data and the SM expectation of the invariant mass spectrum of the dilepton final states. For this the BumpHunter procedure (see section 5.1.2) has been used. The largest deviation between data and the SM expectation has been found at around 2.4 TeV for final states with an electron-positron pair and at around 1.3 to 1.4 TeV for final states with a muon-antimuon pair. The corresponding global p-values have been extracted to be 0.1σ and -1.3σ, respectively, such that no significant deviation has been found. As a result, exclusion limits have been set on the cross section times branching ratio from which an invariant mass limit has been extracted using different theoretical models. It has been found that for electron-positron (muon-antimuon) final states masses below 4.16 TeV (3.87 TeV) can be excluded with a credibility interval of 95 % when assuming a SSM Z' boson. For the E_6-motivated Z' bosons upper mass limits of 3.62 to 3.90 TeV (3.32 to 3.59 TeV) have been found for electron-positron (muon-

antimuon) final states with a credibility interval of 95 %. A combination of both final states leads to upper mass limits of 4.35 TeV (3.80 to 4.06 TeV) for the SSM Z' boson (E_6-motivated Z' bosons) with a credibility interval of 95 %. The extracted upper mass limits improve the upper mass limits given in table 2.1 by around 1 TeV in both the SSM Z' case and the E_6 Z' cases. Additionally, cross section limits have been extracted without specifying a theoretical model. These can be used to reinterpret other theoretical models in the context of dilepton final states.
Finally a search for more exotic resonances has been performed using lepton antilepton final states that are required to have additionally a specific number of jets. An exemplary model which could explain such a resonance is the hidden valley model. The search for exotic resonances is performed only with data and not using MC simulations as a background expectation. Instead, the background expectation is estimated via a fitting procedure. Different signal hypothesis characterized by a signal pole mass and a signal width have been used to test the invariant mass spectrum in data. The search has been performed with data collected in 2015 only which corresponds to $3.2\,\mathrm{fb}^{-1}$. In all investigated spectra the global significance has been extracted to be less than 0.1σ such that no significant deviation has been found.
Improvements of the analysis can be gained in general by refining the selection criteria which may result in an increase of the reconstruction efficiency or the background rejection. Mainly the identification and the isolation criteria for electrons and muons can be improved especially at high p_{T}. In case of muons an increase of the reconstruction efficiency for $|\eta| < 0.1$ can be gained by using calorimeter-tagged muons in addition to combined muons. Another area of improvement is the MC simulation which in case of the top background had a lack of statistics at high invariant masses such that an extrapolation procedure had to be used. In general a better statistical uncertainty of the MC simulation especially at high invariant masses will improve the analysis, however, more statistics will need more computing power and computing storage. Therefore performing the analysis completely data-driven could be an improvement when more data is available as a MC simulation would not match the demanded statistical uncertainty. The estimation of the fake background could be refined by using a Matrix Method based on Poisson likelihoods of the real and fake efficiencies [146]. Finally a reduction of the systematic uncertainties would improve the analysis as well. Especially at high invariant masses the uncertainties are dominated by the PDF uncertainty. Future analyses hence may improve by a better understanding and measurement of SM processes serving as an input for the determination of the PDF and its uncertainty.
The search for more exotic resonances can be expanded by investigating lepton-antilepton final states requiring additional missing transverse momentum instead of jets or in addition to jets. Furthermore the exotic search has only been performed with data corresponding to $3.2\,\mathrm{fb}^{-1}$ such that an improvement is already expected when using the data set corresponding to $36.1\,\mathrm{fb}^{-1}$.
In the upcoming years and decades the LHC will produce more and more proton-proton collisions such that either a resonance will be found or the limits on the invariant mass of Z' bosons can be pushed to higher values. An upgrade of the LHC planned for beyond 2025 is the *High Luminosity LHC* (HL-LHC) [147] which is designed to push the instantaneous luminosities a factor of five larger than the LHC nominal values. With this upgrade it is assumed that the LHC will deliver around $3000\,\mathrm{fb}^{-1}$. For the lower mass limit of a SSM W' boson a value of 7 TeV has

been estimated with this amount of data [122]. Empirically, the lower mass limit of a SSM Z' boson will have a similar value. Another project planned for the era after the HL-LHC is the *Future Circular Collider* [148]. The aim is to reach collision energies of 100 TeV. Scenarios of proton-proton, electron-positron or proton-electron collisions will be explored for a possible design. Assuming a proton-proton collider with $\sqrt{s} = 100\,\text{TeV}$ an exclusion reach of around 27 TeV is expected for the mass of a SSM Z' boson [149].

Appendix A

Additional Plots

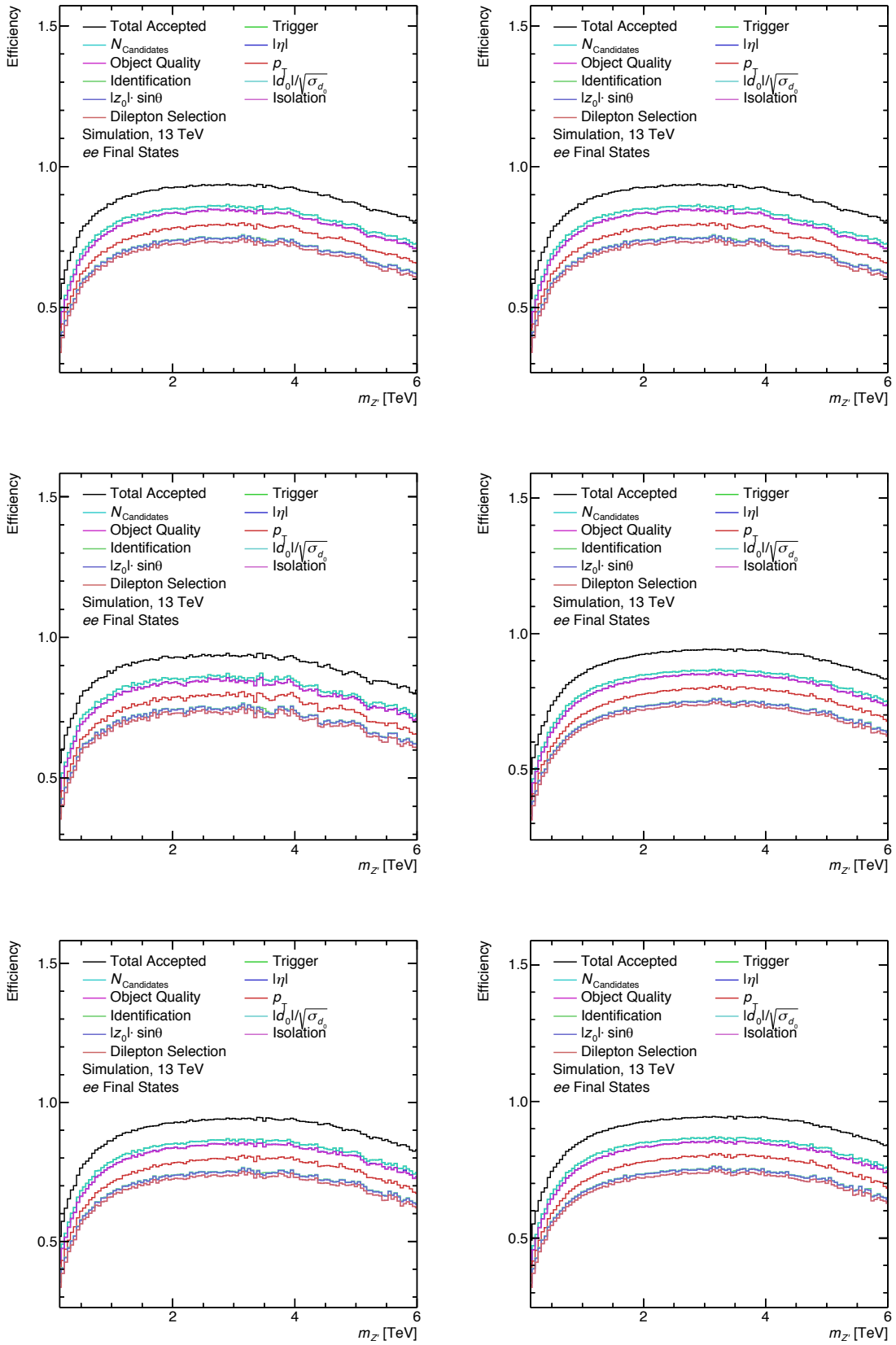

Figure A.1: Product of signal *acceptance* and signal *efficiency* of the E_6^χ (top left), E_6^S (top right), E_6^I (middle left), E_6^η (middle right), E_6^N (bottom left) and E_6^ψ model (bottom right) as a function of the signal pole mass for dielectron final states.

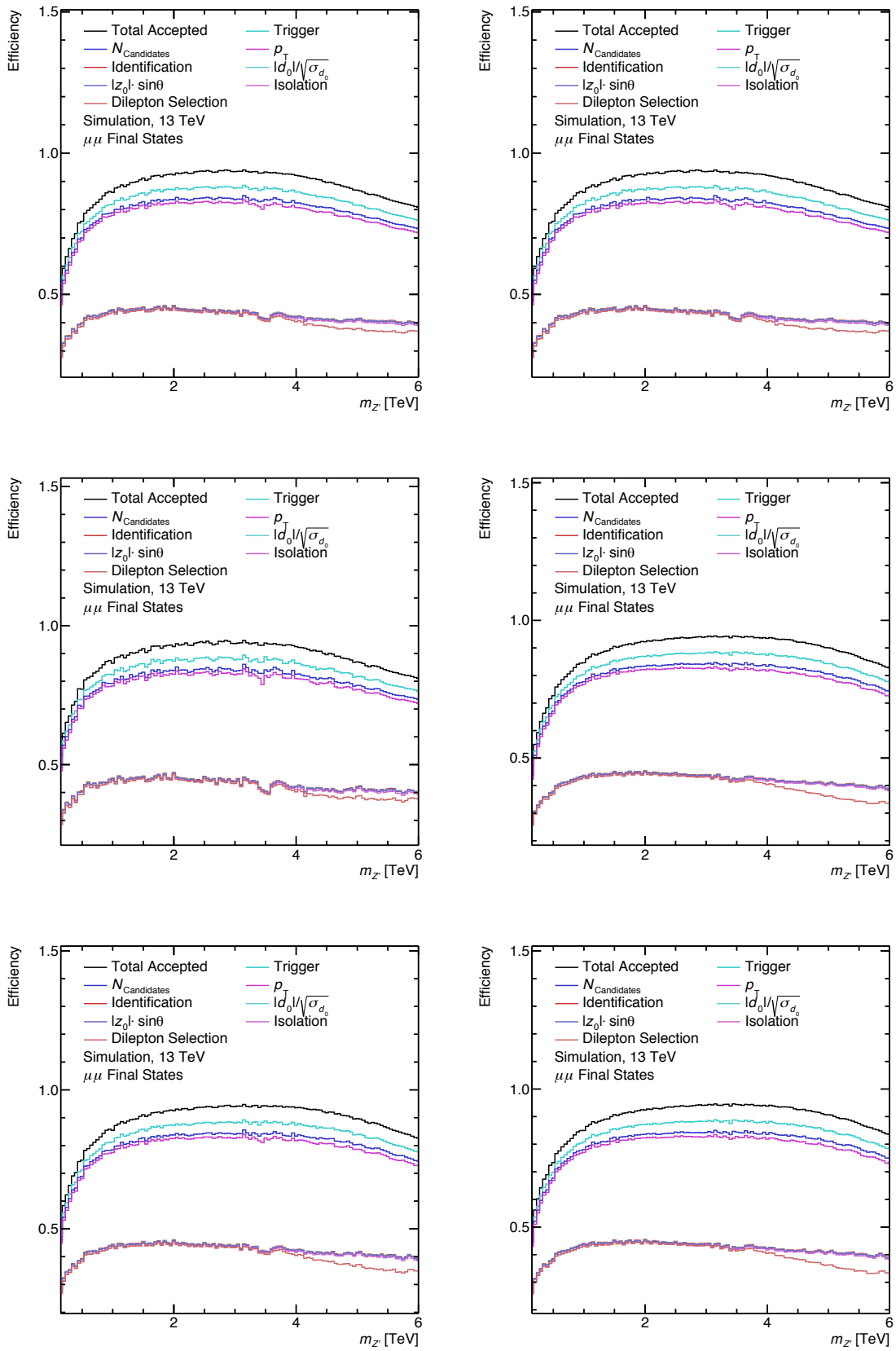

Figure A.2: Product of signal *acceptance* and signal *efficiency* of the E_6^χ (top left), E_6^S (top right), E_6^I (middle left), E_6^η (middle right), E_6^N (bottom left) and E_6^ψ model (bottom right) as a function of the signal pole mass for dimuon final states.

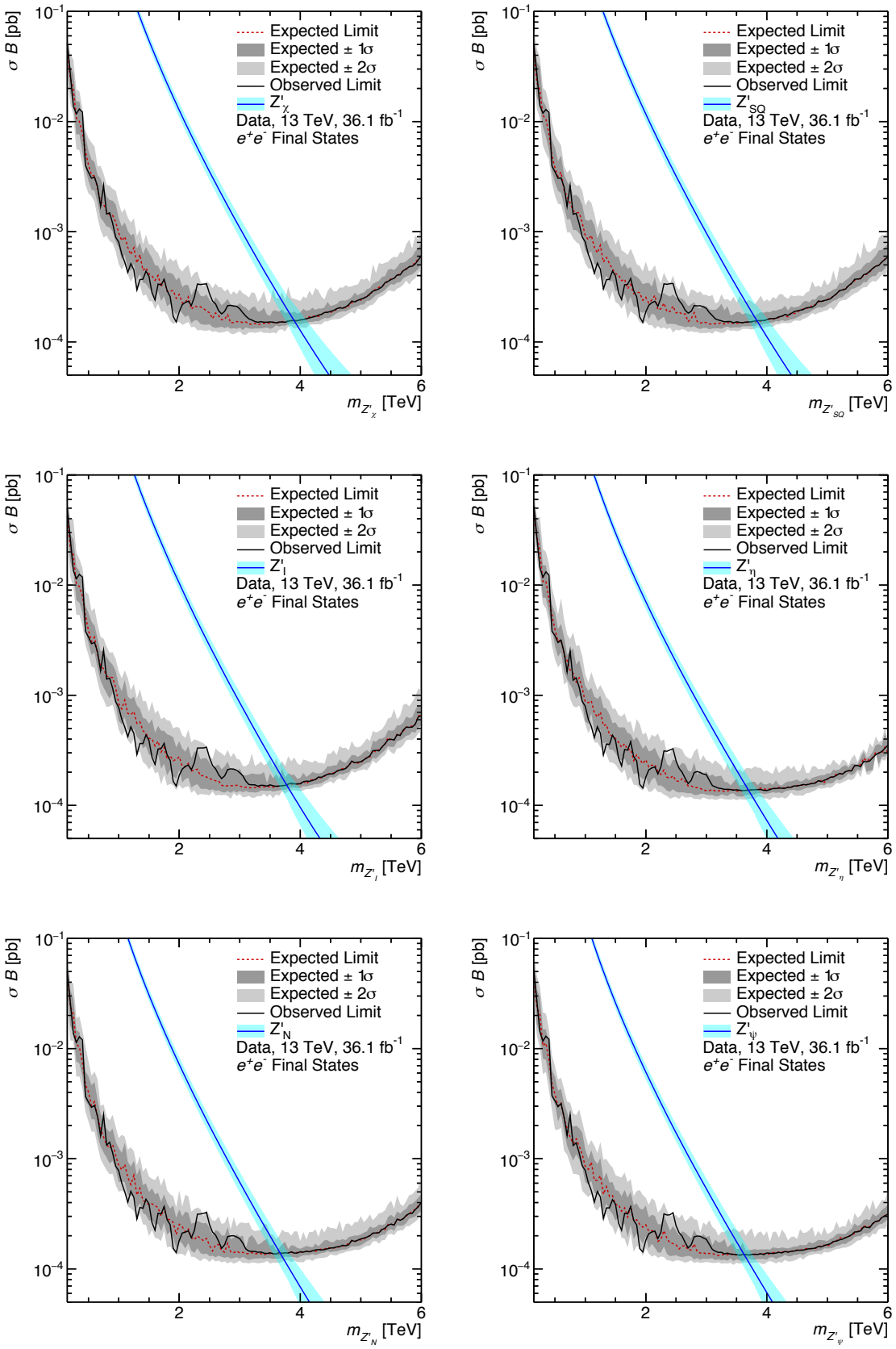

Figure A.3: Expected and observed limit on σB as a function of the signal pole mass in the electron channel for the E_6^χ (top left), E_6^S (top right), E_6^I (middle left), E_6^η (middle right), E_6^N (bottom left) and E_6^ψ model (bottom right).

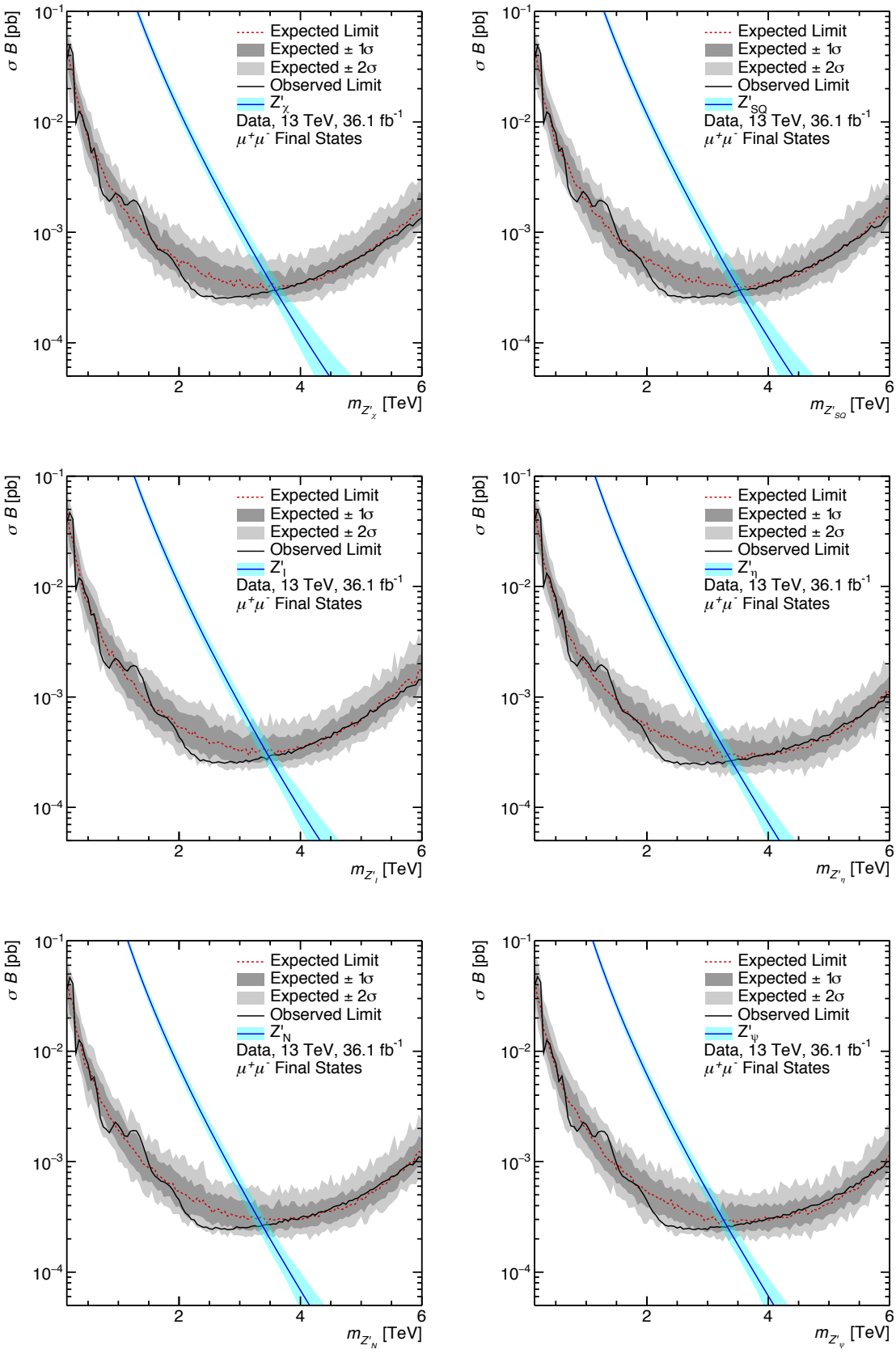

Figure A.4: Expected and observed limit on σB as a function of the signal pole mass in the muon channel for the E_6^χ (top left), E_6^S (top right), E_6^I (middle left), E_6^η (middle right), E_6^N (bottom left) and E_6^ψ model (bottom right).

Bibliography

[1] J. J. Thomson M.A. F.R.S. "XL. Cathode Rays". In: *The London, Edinburgh, and Dublin Philosophical Magazine and Journal of Science* 44.269 (1897), pp. 293–316. DOI: 10.1080/14786449708621070.

[2] Professor E. Rutherford F.R.S. "LXXIX. The scattering of α and β particles by matter and the structure of the atom". In: *The London, Edinburgh, and Dublin Philosophical Magazine and Journal of Science* 21.125 (1911), pp. 669–688. DOI: 10.1080/14786440508637080.

[3] J. Chadwick. "Possible Existence of a Neutron". In: *Nature* 129 (1932), p. 312. DOI: 10.1038/129312a0.

[4] M. Breidenbach et al. "Observed Behavior of Highly Inelastic Electron-Proton Scattering". In: *Phys. Rev. Lett.* 23 (16 Oct. 1969), pp. 935–939. DOI: 10.1103/PhysRevLett.23.935.

[5] E. D. Bloom et al. "High-Energy Inelastic $e-p$ Scattering at 6° and 10°". In: *Phys. Rev. Lett.* 23 (16 Oct. 1969), pp. 930–934. DOI: 10.1103/PhysRevLett.23.930.

[6] M. Gell-Mann. "A schematic model of baryons and mesons". In: *Physics Letters* 8.3 (1964), pp. 214–215. ISSN: 0031-9163. DOI: https://doi.org/10.1016/S0031-9163(64)92001-3.

[7] G. Zweig. "An SU(3) model for strong interaction symmetry and its breaking. Version 2". In: *DEVELOPMENTS IN THE QUARK THEORY OF HADRONS. VOL. 1. 1964 - 1978*. 1964, pp. 22–101. URL: http://inspirehep.net/record/4674/files/cern-th-412.pdf.

[8] Braunschweig Brandelik et al. "Evidence for planar events in e^+e^- annihilation at high energies". In: *Physics Letters B* 86.2 (1979), pp. 243–249. ISSN: 0370-2693. DOI: https://doi.org/10.1016/0370-2693(79)90830-X.

[9] Becker Barber et al. "Discovery of Three-Jet Events and a Test of Quantum Chromodynamics at PETRA". In: *Phys. Rev. Lett.* 43 (12 Sept. 1979), pp. 830–833. DOI: 10.1103/PhysRevLett.43.830.

[10] Genzel Berger et al. "Evidence for gluon bremsstrahlung in e^+e^- annihilations at high energies". In: *Physics Letters B* 86.3 (1979), pp. 418–425. ISSN: 0370-2693. DOI: https://doi.org/10.1016/0370-2693(79)90869-4.

[11] Canzler Bartel et al. "Observation of planar three-jet events in e^+e^- annihilation and evidence for gluon bremsstrahlung". In: *Physics Letters B* 91.1 (1980), pp. 142–147. ISSN: 0370-2693. DOI: https://doi.org/10.1016/0370-2693(80)90680-2.

[12] Astbury Arnison et al. "Experimental observation of isolated large transverse energy electrons with associated missing energy at $\sqrt{s} = 540\,\text{GeV}$". In: *Physics Letters B* 122.1 (1983), pp. 103–116. ISSN: 0370-2693. DOI: https://doi.org/10.1016/0370-2693(83)91177-2.

[13] Battiston Banner et al. "Observation of single isolated electrons of high transverse momentum in events with missing transverse energy at the CERN pp collider". In: *Physics Letters B* 122.5 (1983), pp. 476–485. ISSN: 0370-2693. DOI: https://doi.org/10.1016/0370-2693(83)91605-2.

[14] Astbury Arnison et al. "Experimental observation of lepton pairs of invariant mass around $95\,\text{GeV/c}^2$ at the CERN SPS collider". In: *Physics Letters B* 126.5 (1983), pp. 398–410. ISSN: 0370-2693. DOI: https://doi.org/10.1016/0370-2693(83)90188-0.

[15] Banner Bagnaia et al. "Evidence for $Z^0 \to e^+e^-$ at the CERN pp collider". In: *Physics Letters B* 129.1 (1983), pp. 130–140. ISSN: 0370-2693. DOI: https://doi.org/10.1016/0370-2693(83)90744-X.

[16] S. Abachi et al. "Observation of the top quark". In: *Phys. Rev. Lett.* 74 (1995), pp. 2632–2637. DOI: 10.1103/PhysRevLett.74.2632.

[17] Victor Mukhamedovich Abazov et al. "Measurement of the Electric Charge of the Top Quark in $t\bar{t}$ Events". In: *Phys. Rev.* D90.5 (2014), p. 051101. DOI: 10.1103/PhysRevD.90.051101,10.1103/PhysRevD.90.079904.

[18] Pushpalatha C. Bhat, Harrison Prosper, and Scott S. Snyder. "Top quark physics at the Tevatron". In: *Int. J. Mod. Phys.* A13 (1998), pp. 5113–5218. DOI: 10.1142/S0217751X98002389.

[19] Akimoto Abe et al. "Observation of Top Quark Production in $\overline{p}p$ Collisions with the Collider Detector at Fermilab". In: *Phys. Rev. Lett.* 74 (14 Apr. 1995), pp. 2626–2631. DOI: 10.1103/PhysRevLett.74.2626.

[20] Georges Aad et al. "A particle consistent with the Higgs Boson observed with the ATLAS Detector at the LHC". In: *Science* 338 (2012), pp. 1576–1582. DOI: 10.1126/science.1232005.

[21] Wim de Boer. "The Discovery of the Higgs Boson with the CMS Detector and its Implications for Supersymmetry and Cosmology". In: *Time and Matter 2013 (TAM2013) Venice, Italy*. 2013. arXiv: 1309.0721 [hep-ph].

[22] Robert Oerter. *The Theory of Almost Everything: The Standard Model, the Unsung Triumph of Modern Physics*. Pi Press, 2005. ISBN: 0132366789.

[23] *The Large Hadron Collider : Harvest of Run 1*. Cham: Springer International Publishing, 2015, Online–Ressource. ISBN: 9783319150000. DOI: 10.1007/978-3-319-15001-7.

[24] Wikimedia Commons. URL: https://commons.wikimedia.org/wiki/File:Standard_Model_of_Elementary_Particles.svg.

[25] L D Landau and E.M. Lifshitz. *Mechanics, Third Edition: Volume 1 (Course of Theoretical Physics S)*. Butterworth-Heinemann, 1976. ISBN: 0750628960.

[26] C. N. Yang and R. L. Mills. "Conservation of Isotopic Spin and Isotopic Gauge Invariance". In: *Phys. Rev.* 96 (1 Oct. 1954), pp. 191–195. DOI: 10.1103/PhysRev.96.191.

[27] Richard P. Feynman. *Quantum Electrodynamics (Advanced Books Classics)*. CRC Press, 1998. ISBN: 0201360756.

[28] Nicola Cabibbo. "Unitary Symmetry and Leptonic Decays". In: *Phys. Rev. Lett.* 10 (12 June 1963), pp. 531–533. DOI: 10.1103/PhysRevLett.10.531.

[29] Makoto Kobayashi and Toshihide Maskawa. "CP-Violation in the Renormalizable Theory of Weak Interaction". In: *Progress of Theoretical Physics* 49.2 (1973), pp. 652–657. DOI: 10.1143/PTP.49.652.

[30] Jeff Greensite. *An Introduction to the Confinement Problem (Lecture Notes in Physics, Vol. 821)*. Springer, 2011. ISBN: 9783642143816.

[31] R. P. Feynman. "Space-Time Approach to Quantum Electrodynamics". In: *Phys. Rev.* 76 (6 Sept. 1949), pp. 769–789. DOI: 10.1103/PhysRev.76.769.

[32] "The quantum theory of the emission and absorption of radiation". In: *Proceedings of the Royal Society of London A: Mathematical, Physical and Engineering Sciences* 114.767 (1927), pp. 243–265. ISSN: 0950-1207. DOI: 10.1098/rspa.1927.0039.

[33] B.H. Bransden and C.J. Joachain. *Quantum Mechanics (2nd Edition)*. Prentice Hall, 2000. ISBN: 0582356911.

[34] Enrico Fermi. *Nuclear Physics: A Course Given by Enrico Fermi at the University of Chicago*. University of Chicago Press, 1974. ISBN: 0226243656.

[35] Stefan Höche. "Introduction to parton-shower event generators". In: *Proceedings, Theoretical Advanced Study Institute in Elementary Particle Physics: Journeys Through the Precision Frontier: Amplitudes for Colliders (TASI 2014): Boulder, Colorado, June 2-27, 2014*. 2015, pp. 235–295. DOI: 10.1142/9789814678766_0005.

[36] Geoffrey T. Bodwin. "Factorization of the Drell-Yan Cross-Section in Perturbation Theory". In: *Phys. Rev.* D31 (1985), p. 2616. DOI: 10.1103/PhysRevD.34.3932,10.1103/PhysRevD.31.2616.

[37] John C. Collins, Davison E. Soper, and George F. Sterman. "Factorization for Short Distance Hadron - Hadron Scattering". In: *Nucl. Phys.* B261 (1985), pp. 104–142. DOI: 10.1016/0550-3213(85)90565-6.

[38] John C. Collins, Davison E. Soper, and George F. Sterman. "Soft Gluons and Factorization". In: *Nucl. Phys.* B308 (1988), pp. 833–856. DOI: 10.1016/0550-3213(88)90130-7.

[39] J. Beringer et al. "Review of Particle Physics". In: *Phys. Rev. D* 86 (1 July 2012), p. 010001. DOI: 10.1103/PhysRevD.86.010001.

[40] F. D. Aaron et al. "Combined Measurement and QCD Analysis of the Inclusive $e^+ - p$ Scattering Cross Sections at HERA". In: *JHEP* 01 (2010), p. 109. DOI: 10.1007/JHEP01(2010)109.

[41] S. Alekhin et al. "HERAFitter". In: *Eur. Phys. J.* C75.7 (2015), p. 304. DOI: 10.1140/epjc/s10052-015-3480-z.

[42] F. D. Aaron et al. "A precision measurement of the inclusive ep scattering cross section at HERA". In: *The European Physical Journal C* 64.4 (Dec. 2009), pp. 561–587. ISSN: 1434-6052. DOI: 10.1140/epjc/s10052-009-1169-x.

[43] A. D. Martin et al. "Parton distributions for the LHC". In: *Eur. Phys. J.* C63 (2009), pp. 189–285. DOI: 10.1140/epjc/s10052-009-1072-5.

[44] J. Pumplin et al. "Uncertainties of predictions from parton distribution functions. 2. The Hessian method". In: *Phys. Rev.* D65 (2001), p. 014013. DOI: 10.1103/PhysRevD.65.014013.

[45] Bo Andersson et al. "Parton Fragmentation and String Dynamics". In: *Phys. Rept.* 97 (1983), pp. 31–145. DOI: 10.1016/0370-1573(83)90080-7.

[46] D. Amati and G. Veneziano. "Preconfinement as a property of perturbative QCD". In: *Physics Letters B* 83.1 (1979), pp. 87–92. ISSN: 0370-2693. DOI: https://doi.org/10.1016/0370-2693(79)90896-7.

[47] Torbjorn Sjostrand, Stephen Mrenna, and Peter Z. Skands. "A Brief Introduction to PYTHIA 8.1". In: *Comput. Phys. Commun.* 178 (2008), pp. 852–867. DOI: 10.1016/j.cpc.2008.01.036.

[48] T. Gleisberg et al. "Event generation with SHERPA 1.1". In: *JHEP* 02 (2009), p. 007. DOI: 10.1088/1126-6708/2009/02/007.

[49] P. A. R. Ade et al. "Planck 2013 results. I. Overview of products and scientific results". In: *Astron. Astrophys.* 571 (2014), A1. DOI: 10.1051/0004-6361/201321529.

[50] Y. Fukuda et al. "Evidence for oscillation of atmospheric neutrinos". In: *Phys. Rev. Lett.* 81 (1998), pp. 1562–1567. DOI: 10.1103/PhysRevLett.81.1562.

[51] V. Barger et al. "Gauge coupling unification in the standard model". In: *Phys. Lett.* B624 (2005), pp. 233–238. DOI: 10.1016/j.physletb.2005.08.019.

[52] Paul Langacker. "The Physics of Heavy Z' Gauge Bosons". In: *Rev. Mod. Phys.* 81 (2009), pp. 1199–1228. DOI: 10.1103/RevModPhys.81.1199.

[53] David London and Jonathan L. Rosner. "Extra Gauge Bosons in E(6)". In: *Phys. Rev.* D34 (1986), p. 1530. DOI: 10.1103/PhysRevD.34.1530.

[54] Morad Aaboud et al. "Search for high-mass new phenomena in the dilepton final state using proton-proton collisions at $\sqrt{s} = 13$ TeV with the ATLAS detector". In: *Phys. Lett.* B761 (2016), pp. 372–392. DOI: 10.1016/j.physletb.2016.08.055.

[55] Matthew J. Strassler and Kathryn M. Zurek. "Echoes of a hidden valley at hadron colliders". In: *Phys. Lett.* B651 (2007), pp. 374–379. DOI: 10.1016/j.physletb.2007.06.055.

[56] Tao Han et al. "Phenomenology of hidden valleys at hadron colliders". In: *JHEP* 07 (2008), p. 008. DOI: 10.1088/1126-6708/2008/07/008.

[57] Matthew J. Strassler. "Why Unparticle Models with Mass Gaps are Examples of Hidden Valleys". In: (2008). arXiv: 0801.0629 [hep-ph].

[58] G. Aad et al. "The ATLAS Experiment at the CERN LHC". In: *JINST* 3 (2008), S08003. DOI: 10.1088/1748-0221/3/08/S08003.

[59] AC Team. "Computer-generated diagram of an LHC dipole. Schéma d'un dipôle du LHC". Sept. 1998. URL: https://cds.cern.ch/record/39731.

[60] C. Kourkoumelis and S. Vourakis. "HYPATIA—an online tool for ATLAS event visualization". In: *Phys. Educ.* 49 (2014), pp. 21–32. DOI: 10.1088/0031-9120/49/1/21.

[61] CERN AC. "Layout of ATLAS. Dessin representant le detecteur ATLAS". Mar. 1998. URL: https://cds.cern.ch/record/39038.

[62] *ATLAS inner detector: Technical Design Report, 1*. Technical Design Report ATLAS. Geneva: CERN, 1997. URL: https://cds.cern.ch/record/331063.

[63] Karolos Potamianos. "The upgraded Pixel detector and the commissioning of the Inner Detector tracking of the ATLAS experiment for Run-2 at the LHC". In: *PoS* EPS-HEP2015 (2015), p. 261. arXiv: 1608.07850 [physics.ins-det].

[64] *ATLAS liquid-argon calorimeter: Technical Design Report*. Technical Design Report ATLAS. Geneva: CERN, 1996. URL: https://cds.cern.ch/record/331061.

[65] Jiri Dolejsi. "Status of ATLAS and Preparation for the Pb-Pb Run". In: *Nucl. Phys.* A830 (2009), pp. 89C–96C. DOI: 10.1016/j.nuclphysa.2009.10.087.

[66] ATLAS Collaboration. *Technical Design Report for the Phase-II Upgrade of the ATLAS Muon Spectrometer*. Tech. rep. CERN-LHCC-2017-017. ATLAS-TDR-026. Geneva: CERN, Sept. 2017. URL: https://cds.cern.ch/record/2285580.

[67] E. Diehl. "Calibration and Performance of the ATLAS Muon Spectrometer". In: *Particles and fields. Proceedings, Meeting of the Division of the American Physical Society, DPF 2011, Providence, USA, August 9-13, 2011*. 2011. arXiv: 1109.6933 [physics.ins-det].

[68] *ATLAS level-1 trigger: Technical Design Report*. Technical Design Report ATLAS. Geneva: CERN, 1998. URL: http://cds.cern.ch/record/381429.

[69] Peter Jenni et al. *ATLAS high-level trigger, data-acquisition and controls: Technical Design Report*. Technical Design Report ATLAS. Geneva: CERN, 2003. URL: http://cds.cern.ch/record/616089.

[70] Aranzazu Ruiz-Martinez and ATLAS Collaboration. *The Run-2 ATLAS Trigger System*. Tech. rep. ATL-DAQ-PROC-2016-003. Geneva: CERN, Feb. 2016. URL: http://cds.cern.ch/record/2133909.

[71] Christoph Eck et al. *LHC computing Grid: Technical Design Report. Version 1.06 (20 Jun 2005)*. Technical Design Report LCG. Geneva: CERN, 2005. URL: https://cds.cern.ch/record/840543.

[72] R.W.L. Jones. "ATLAS computing and the GRID". In: *Nuclear Instruments and Methods in Physics Research Section A: Accelerators, Spectrometers, Detectors and Associated Equipment* 502.2 (2003), pp. 372–375. ISSN: 0168-9002. DOI: https://doi.org/10.1016/S0168-9002(03)00446-7.

[73] R. Brun and F. Rademakers. "ROOT: An object oriented data analysis framework". In: *Nucl. Instrum. Meth.* A389 (1997), pp. 81–86. DOI: 10.1016/S0168-9002(97)00048-X.

[74] Vladislav Balagura. "Notes on van der Meer Scan for Absolute Luminosity Measurement". In: *Nucl. Instrum. Meth.* A654 (2011), pp. 634–638. DOI: 10.1016/j.nima.2011.06.007.

[75] Oleksandr Viazlo and ATLAS LUCID Collaboration. *ATLAS LUCID detector upgrade for LHC Run 2*. Tech. rep. ATL-FWD-PROC-2015-004. Geneva: CERN, Oct. 2015. URL: https://cds.cern.ch/record/2062038.

[76] V Cindro et al. "The ATLAS Beam Conditions Monitor". In: *Journal of Instrumentation* 3.02 (2008), P02004. URL: http://stacks.iop.org/1748-0221/3/i=02/a=P02004.

[77] S. Agostinelli et al. "GEANT4: A Simulation toolkit". In: *Nucl. Instrum. Meth.* A506 (2003), pp. 250–303. DOI: 10.1016/S0168-9002(03)01368-8.

[78] Zachary Marshall. "Simulation of Pile-up in the ATLAS Experiment". In: *J. Phys. Conf. Ser.* 513 (2014), p. 022024. DOI: 10.1088/1742-6596/513/2/022024.

[79] ATLAS Collaboration. URL: https://twiki.cern.ch/twiki/bin/view/AtlasPublic/LuminosityPublicResultsRun2.

[80] *Electron efficiency measurements with the ATLAS detector using the 2015 LHC proton-proton collision data*. Tech. rep. ATLAS-CONF-2016-024. Geneva: CERN, June 2016. URL: https://cds.cern.ch/record/2157687.

[81] W Lampl et al. *Calorimeter Clustering Algorithms: Description and Performance*. Tech. rep. ATL-LARG-PUB-2008-002. ATL-COM-LARG-2008-003. Geneva: CERN, Apr. 2008. URL: http://cds.cern.ch/record/1099735.

[82] T G Cornelissen et al. "The global χ^2 track fitter in ATLAS". In: *Journal of Physics: Conference Series* 119.3 (2008), p. 032013. URL: http://stacks.iop.org/1742-6596/119/i=3/a=032013.

[83] *Improved electron reconstruction in ATLAS using the Gaussian Sum Filter-based model for bremsstrahlung*. Tech. rep. ATLAS-CONF-2012-047. Geneva: CERN, May 2012. URL: https://cds.cern.ch/record/1449796.

[84] Georges Aad et al. "Muon reconstruction performance of the ATLAS detector in proton–proton collision data at $\sqrt{s}$ =13 TeV". In: *Eur. Phys. J.* C76.5 (2016), p. 292. DOI: 10.1140/epjc/s10052-016-4120-y.

[85] J. Illingworth and J. Kittler. "A Survey of the Hough Transform". In: *Comput. Vision Graph. Image Process.* 44.1 (Aug. 1988), pp. 87–116. ISSN: 0734-189X. DOI: 10.1016/S0734-189X(88)80033-1.

[86] Georges Aad et al. "Measurements of Higgs boson production and couplings in the four-lepton channel in pp collisions at center-of-mass energies of 7 and 8 TeV with the ATLAS detector". In: *Phys. Rev.* D91.1 (2015), p. 012006. DOI: 10.1103/PhysRevD.91.012006.

[87] Georges Aad et al. "Search for high-mass dilepton resonances in pp collisions at $\sqrt{s}$ = 8 TeV with the ATLAS detector". In: *Phys. Rev.* D90.5 (2014), p. 052005. DOI: 10.1103/PhysRevD.90.052005.

[88] Georges Aad et al. "Search for new particles in events with one lepton and missing transverse momentum in *pp* collisions at $\sqrt{s} = 8$ TeV with the ATLAS detector". In: *JHEP* 09 (2014), p. 037. DOI: 10.1007/JHEP09(2014)037.

[89] Georges Aad et al. "Jet energy measurement with the ATLAS detector in proton-proton collisions at $\sqrt{s}$ = 7 TeV". In: *Eur. Phys. J.* C73.3 (2013), p. 2304. DOI: 10.1140/epjc/s10052-013-2304-2.

[90] A. Hrynevich. "ATLAS jet and missing energy reconstruction, calibration and performance in LHC Run-2". In: *JINST* 12.06 (2017), p. C06038. DOI: 10.1088/1748-0221/12/06/C06038.

[91] Matteo Cacciari, Gavin P. Salam, and Gregory Soyez. "The Anti-k(t) jet clustering algorithm". In: *JHEP* 04 (2008), p. 063. DOI: 10.1088/1126-6708/2008/04/063.

[92] Morad Aaboud et al. "Jet reconstruction and performance using particle flow with the ATLAS Detector". In: *Eur. Phys. J.* C77.7 (2017), p. 466. DOI: 10.1140/epjc/s10052-017-5031-2.

[93] Georges Aad et al. "Jet energy measurement and its systematic uncertainty in proton-proton collisions at $\sqrt{s}$ = 7 TeV with the ATLAS detector". In: *Eur. Phys. J.* C75 (2015), p. 17. DOI: 10.1140/epjc/s10052-014-3190-y.

[94] Georges Aad et al. "Topological cell clustering in the ATLAS calorimeters and its performance in LHC Run 1". In: *Eur. Phys. J.* C77 (2017), p. 490. DOI: 10.1140/epjc/s10052-017-5004-5.

[95] Georges Aad et al. "Performance of algorithms that reconstruct missing transverse momentum in $\sqrt{s}$= 8 TeV proton–proton collisions in the ATLAS detector." In: *Eur. Phys. J. C* 77.CERN-EP-2016-134. 4 (Sept. 2016), 241. 68 p. URL: http://cds.cern.ch/record/2220441.

[96] Simone Alioli et al. "A general framework for implementing NLO calculations in shower Monte Carlo programs: the POWHEG BOX". In: *JHEP* 06 (2010), p. 043. DOI: 10.1007/JHEP06(2010)043.

[97] Hung-Liang Lai et al. "New parton distributions for collider physics". In: *Phys. Rev.* D82 (2010), p. 074024. DOI: 10.1103/PhysRevD.82.074024.

[98] Georges Aad et al. "Measurement of the Z/γ^* boson transverse momentum distribution in pp collisions at $\sqrt{s}$ = 7 TeV with the ATLAS detector". In: *JHEP* 09 (2014), p. 145. DOI: 10.1007/JHEP09(2014)145.

[99] *Monte Carlo Generators for the Production of a W or Z/γ^* Boson in Association with Jets at ATLAS in Run 2*. Tech. rep. ATL-PHYS-PUB-2016-003. Geneva: CERN, Jan. 2016. URL: https://cds.cern.ch/record/2120133.

[100] Sayipjamal Dulat et al. "New parton distribution functions from a global analysis of quantum chromodynamics". In: *Phys. Rev.* D93.3 (2016), p. 033006. DOI: 10.1103/PhysRevD.93.033006.

[101] Charalampos Anastasiou et al. "High precision QCD at hadron colliders: Electroweak gauge boson rapidity distributions at NNLO". In: *Phys. Rev.* D69 (2004), p. 094008. DOI: 10.1103/PhysRevD.69.094008.

[102] Sergey G. Bondarenko and Andrey A. Sapronov. "NLO EW and QCD proton-proton cross section calculations with mcsanc-v1.01". In: *Comput. Phys. Commun.* 184 (2013), pp. 2343–2350. DOI: 10.1016/j.cpc.2013.05.010.

[103] A. D. Martin et al. "Parton distributions incorporating QED contributions". In: *Eur. Phys. J.* C39 (2005), pp. 155–161. DOI: 10.1140/epjc/s2004-02088-7.

[104] Stephen Holmes, Ronald S. Moore, and Vladimir Shiltsev. "Overview of the Tevatron Collider Complex: Goals, Operations and Performance". In: *JINST* 6 (2011), T08001. DOI: 10.1088/1748-0221/6/08/T08001.

[105] Torbjorn Sjostrand, Stephen Mrenna, and Peter Z. Skands. "PYTHIA 6.4 Physics and Manual". In: *JHEP* 05 (2006), p. 026. DOI: 10.1088/1126-6708/2006/05/026.

[106] Peter Zeiler Skands. "Tuning Monte Carlo Generators: The Perugia Tunes". In: *Phys. Rev.* D82 (2010), p. 074018. DOI: 10.1103/PhysRevD.82.074018.

[107] Michal Czakon and Alexander Mitov. "Top++: A Program for the Calculation of the Top-Pair Cross-Section at Hadron Colliders". In: *Comput. Phys. Commun.* 185 (2014), p. 2930. DOI: 10.1016/j.cpc.2014.06.021.

[108] *Studies on top-quark Monte Carlo modelling for Top2016*. Tech. rep. ATL-PHYS-PUB-2016-020. Geneva: CERN, Sept. 2016. URL: https://cds.cern.ch/record/2216168.

[109] *Multi-Boson Simulation for 13 TeV ATLAS Analyses*. Tech. rep. ATL-PHYS-PUB-2016-002. Geneva: CERN, Jan. 2016. URL: https://cds.cern.ch/record/2119986.

[110] Nikolaos Kidonakis. "NNLL resummation for s-channel single top quark production". In: *Phys. Rev.* D81 (2010), p. 054028. DOI: 10.1103/PhysRevD.81.054028.

[111] Nikolaos Kidonakis. "Next-to-next-to-leading-order collinear and soft gluon corrections for t-channel single top quark production". In: *Phys. Rev.* D83 (2011), p. 091503. DOI: 10.1103/PhysRevD.83.091503.

[112] Richard D. Ball et al. "Parton distributions with LHC data". In: *Nucl. Phys.* B867 (2013), pp. 244–289. DOI: 10.1016/j.nuclphysb.2012.10.003.

[113] *ATLAS Run 1 Pythia8 tunes*. Tech. rep. ATL-PHYS-PUB-2014-021. Geneva: CERN, Nov. 2014. URL: http://cds.cern.ch/record/1966419.

[114] Aranzazu Ruiz-Martinez et al. *Electron and photon trigger efficiency plots using the full 2016 dataset*. Tech. rep. ATL-COM-DAQ-2017-015. Geneva: CERN, Mar. 2017. URL: https://cds.cern.ch/record/2254973.

[115] ATLAS Isolation and Fake Forum. URL: https://twiki.cern.ch/twiki/bin/view/AtlasProtected/IsolationFakeForum.

[116] Uta Klein. URL: https://twiki.cern.ch/twiki/bin/view/AtlasProtected/HigherOrderCorrections2015.

[117] Georges Aad et al. "Electron and photon energy calibration with the ATLAS detector using LHC Run 1 data". In: *Eur. Phys. J.* C74.10 (2014), p. 3071. DOI: 10.1140/epjc/s10052-014-3071-4.

[118] Georges Aad et al. "Muon reconstruction performance of the ATLAS detector in proton–proton collision data at $\sqrt{s}$ =13 TeV". In: *Eur. Phys. J.* C76.5 (2016), p. 292. DOI: 10.1140/epjc/s10052-016-4120-y.

[119] The ATLAS collaboration. "Electron efficiency measurements with the ATLAS detector using the 2015 LHC proton-proton collision data". In: (2016).

[120] C. Patrignani et al. "Review of Particle Physics". In: *Chin. Phys.* C40.10 (2016), p. 100001. DOI: 10.1088/1674-1137/40/10/100001.

[121] Morad Aaboud et al. "Measurements of the production cross section of a Z boson in association with jets in pp collisions at $\sqrt{s} = 13$ TeV with the ATLAS detector". In: *Eur. Phys. J.* C77.6 (2017), p. 361. DOI: 10.1140/epjc/s10052-017-4900-z.

[122] Markus Zinser and Stefan Tapprogge. "Search for new heavy charged bosons and measurement of high-mass Drell-Yan production in proton-proton collisions". Aug. 2016. URL: https://cds.cern.ch/record/2239722.

[123] Jon Butterworth et al. "PDF4LHC recommendations for LHC Run II". In: *J. Phys.* G43 (2016), p. 023001. DOI: 10.1088/0954-3899/43/2/023001.

[124] Patrick Motylinski et al. "Updates of PDFs for the 2nd LHC run". In: *Nucl. Part. Phys. Proc.* 273-275 (2016), pp. 2136–2141. DOI: 10.1016/j.nuclphysbps.2015.09.347.

[125] Richard D. Ball et al. "Parton distributions for the LHC Run II". In: *JHEP* 04 (2015), p. 040. DOI: 10.1007/JHEP04(2015)040.

[126] S. Alekhin, J. Blumlein, and S. Moch. "The ABM parton distributions tuned to LHC data". In: *Phys. Rev.* D89.5 (2014), p. 054028. DOI: 10.1103/PhysRevD.89.054028.

[127] Pedro Jimenez-Delgado and Ewald Reya. "Delineating parton distributions and the strong coupling". In: *Phys. Rev.* D89.7 (2014), p. 074049. DOI: 10.1103/PhysRevD.89.074049.

[128] Morad Aaboud et al. "Precision measurement and interpretation of inclusive W^+ , W^- and Z/γ^* production cross sections with the ATLAS detector". In: *Eur. Phys. J.* C77.6 (2017), p. 367. DOI: 10.1140/epjc/s10052-017-4911-9.

[129] J Wenninger. *Energy Calibration of the LHC Beams at 4 TeV*. Tech. rep. CERN-ATS-2013-040. Geneva: CERN, May 2013. URL: https://cds.cern.ch/record/1546734.

[130] Georgios Choudalakis. "On hypothesis testing, trials factor, hypertests and the BumpHunter". In: *Proceedings, PHYSTAT 2011 Workshop on Statistical Issues Related to Discovery Claims in Search Experiments and Unfolding, CERN,Geneva, Switzerland 17-20 January 2011*. 2011. arXiv: 1101.0390 [physics.data-an].

[131] Milton Abramowitz. *Handbook of Mathematical Functions, With Formulas, Graphs, and Mathematical Tables,* Dover Publications, Incorporated, 1974. ISBN: 0486612724.

[132] Eilam Gross and Ofer Vitells. "Trial factors or the look elsewhere effect in high energy physics". In: *Eur. Phys. J.* C70 (2010), pp. 525–530. DOI: 10.1140/epjc/s10052-010-1470-8.

[133] Will Buttinger. URL: https://twiki.cern.ch/twiki/bin/view/Main/BumpHunter.

[134] S.A. Klugman, H.H. Panjer, and G.E. Willmot. *Loss Models: From Data to Decisions*. Wiley Series in Probability and Statistics. Wiley, 2012. ISBN: 9781118411650.

[135] G. Choudalakis and D. Casadei. "Plotting the differences between data and expectation". In: *The European Physical Journal Plus* 127.2 (Feb. 2012), p. 25. ISSN: 2190-5444. DOI: 10.1140/epjp/i2012-12025-y.

[136] A. Caldwell, D. Kollár, and K. Kröninger. "BAT - The Bayesian analysis toolkit". In: *Computer Physics Communications* 180 (Nov. 2009), pp. 2197–2209. DOI: 10.1016/j.cpc.2009.06.026.

[137] Albert M Sirunyan et al. *Search for high-mass resonances in dilepton final states in proton-proton collisions at $\sqrt{s}$ = 13 TeV*. Tech. rep. CMS-EXO-16-047. CMS-EXO-16-047-003. Geneva: CERN, Mar. 2018. URL: http://cds.cern.ch/record/2309470.

[138] V. Khachatryan et al. "Search for physics beyond the standard model in dilepton mass spectra in proton-proton collisions at $\sqrt{s} = 8$ TeV". In: *Journal of High Energy Physics* 2015.4 (Apr. 2015), p. 25. ISSN: 1029-8479. DOI: 10.1007/JHEP04(2015)025.

[139] *Search for new high-mass phenomena in the dilepton final state using 36.1 fb^{-1} of proton-proton collision data at $\sqrt{s}$ = 13 TeV with the ATLAS detector*. Data Collection. 2017. DOI: 10.17182/hepdata.79077.

[140] Duccio Pappadopulo et al. "Heavy Vector Triplets: Bridging Theory and Data". In: *JHEP* 09 (2014), p. 060. DOI: 10.1007/JHEP09(2014)060.

[141] *Pile-up subtraction and suppression for jets in ATLAS*. Tech. rep. ATLAS-CONF-2013-083. Geneva: CERN, Aug. 2013. URL: https://cds.cern.ch/record/1570994.

[142] *Tagging and suppression of pileup jets with the ATLAS detector*. Tech. rep. ATLAS-CONF-2014-018. Geneva: CERN, May 2014. URL: https://cds.cern.ch/record/1700870.

[143] A. Hoecker et al. "TMVA - Toolkit for Multivariate Data Analysis". In: *ArXiv Physics e-prints* (Mar. 2007). eprint: physics/0703039.

[144] ATLAS Jet and $E_{\mathrm{T}}^{\mathrm{miss}}$ Combined Performance Group. URL: https://twiki.cern.ch/twiki/bin/view/AtlasProtected/JetEtMiss.

[145] Peter Skands Steve Mrenna and Matthew Strassler. URL: http://www.physics.rutgers.edu/~strassler/hv/hv.htm.

[146] Erich W. Varnes. "A Poisson likelihood approach to fake lepton estimation with the matrix method". In: (2016). arXiv: 1606.06817 [hep-ex].

[147] Apollinari G. et al. "High-Luminosity Large Hadron Collider (HL-LHC)". In: (2017). DOI: 10.23731/CYRM-2017-004.

[148] Michael Benedikt and Frank Zimmermann. "Future Circular Colliders". In: *Proc. Int. Sch. Phys. Fermi* 194 (2016), pp. 73–80. DOI: 10.3254/978-1-61499-732-0-73.

[149] T. Golling et al. "Physics at a 100 TeV pp collider: beyond the Standard Model phenomena". In: *CERN Yellow Report* 3 (2017), pp. 441–634. DOI: 10.23731/CYRM-2017-003.441.